VOLUME 80 MAY 6, 1976 NUMBER 10

JPCHAx

THE JOURNAL OF PHYSICAL CHEMISTRY

PUBLISHED BIWEEKLY BY THE AMERICAN CHEMICAL SOCIETY

THE JOURNAL OF

PHYSICAL CHEMISTRY

Published by the
AMERICAN CHEMICAL SOCIETY
BOOKS AND JOURNALS DIVISION
D. H. Michael Bowen, Director

Editorial Department: Charles R. Bertsch, Head; Marianne C. Brogan, Associate Head; Celia B. McFarland, Joseph E. Yurvati, Assistant Editors
Graphics and Production Department: Bacil Guiley, Head
Research and Development Department: Seldon W. Terrant, Head

Advertising Office: Centcom, Ltd., 50 W. State St., Westport, Conn. 06880.

Published biweekly by the American Chemical Society at 20th and Northampton Sts., Easton, Pennsylvania 18042. Second class postage paid at Washington, D.C. and at additional mailing offices.

Editorial Information

Instructions for authors are printed in the first issue of each volume. Please conform to these instructions when submitting manuscripts.

Manuscripts for publication should be submitted to *The Journal of Physical Chemistry,* Department of Chemistry, University of Minnesota, Minneapolis, Minn. 55455. Correspondence regarding **accepted papers and proofs** should be directed to the Editorial Department at the ACS Easton address.

Page charges of $60.00 per page are assessed for papers published in this journal. Ability to pay does not affect acceptance or scheduling of papers.

Bulk reprints or photocopies of individual articles are available. For information write to Business Operations, Books and Journals Division at the ACS Washington address.

Requests for **permission to reprint** should be directed to Permissions, Books and Journals Division at the ACS Washington address. The American Chemical Society and its Editors assume no responsibility for the statements and opinions advanced by contributors.

Subscription and Business Information

1976 Subscription rates—including surface postage

	U.S.	PUAS	Canada, Foreign
Member	$24.00	$29.75	$30.25
Nonmember	96.00	101.75	102.25
Supplementary material	15.00	19.00	20.00

Air mail and air freight rates are available from Membership & Subscription Services, at the ACS Columbus address.

New and renewal subscriptions should be sent with payment to the Office of the Controller at the ACS Washington address. **Changes of address** must include both old and new addresses with ZIP code and a recent mailing label. Send all address changes to the ACS Columbus address. Please allow six weeks for change to become effective. **Claims** for missing numbers will not be allowed if loss was due to failure of notice of change of address to be received in the time specified; if claim is dated (a) North America—more than 90 days beyond issue date, (b) all other foreign—more than 1 year beyond issue date; or if the reason given is "missing from files". Hard copy claims are handled at the ACS Columbus address.

Microfiche subscriptions are available at the same rates but are mailed first class to U.S. subscribers, air mail to the rest of the world. Direct all inquiries to Business Operations, Books and Journals Division, at the ACS Washington address or call (202) 872-4444. **Single issues** in hard copy and/or microfiche are available from Special Issues Sales at the ACS Washington address. Current year $4.75. Back issue rates available from Special Issues Sales. **Back volumes** are available in hard copy and/or microform. Write to Special Issues Sales at the ACS Washington address for further information. **Microfilm** editions of ACS periodical publications are available from volume 1 to the present. For further information, contact Special Issues Sales at the ACS Washington address. **Supplementary material** must be ordered directly from Business Operations, Books and Journals Division, at the ACS Washington address.

Microfiche	U.S.	PUAS, Canada	Other Foreign
Photocopy	$2.50	$3.00	$3.50
1–7 pages	4.00	5.50	7.00
8–20 pages	5.00	6.50	8.00

Orders over 20 pages are available only on microfiche, 4 × 6 in., 24X, negative, silver halide. Orders must state photocopy or microfiche if both are available. Full bibliographic citation including names of all authors and prepayment are required. Prices are subject to change.

American Chemical Society
1155 16th Street, N.W.
Washington, D.C. 20036
(202) 872-4600

Member & Subscription Services
American Chemical Society
P.O. Box 3337
Columbus, Ohio 43210
(614) 421-7230

Editorial Department
American Chemical Society
20th and Northampton Sts.
Easton, Pennsylvania 18042
(215) 258-9111

Notice to Authors last printed in the issue of January 1, 1976

THE JOURNAL OF
PHYSICAL CHEMISTRY

Volume 80, Number 10, May 6, 1976

JPCHAx 80(10) 1031–1122 (1976)
ISSN 0022-3654

■ Supplementary and/or miniprint material for this paper is available separately (consult the masthead page for ordering information); it will also appear following the paper in the microfilm edition of this journal.

* In papers with more than one author, the asterisk indicates the name of the author to whom inquiries about the paper should be addressed.

AUTHOR INDEX

ANNOUNCEMENT

On the last two pages of this issue you will find reproduced the table of contents of the April 1976 issue of the Journal of Chemical and Engineering Data.

THE JOURNAL OF
PHYSICAL CHEMISTRY

VOLUME 80, NUMBER 10 MAY 6, 1976

Reaction of Hydrogen and Carbon Dioxide behind Reflected Shock Waves[1]

J. M. Brupbacher, R. D. Kern,* and B. V. O'Grady

Department of Chemistry, University of New Orleans, New Orleans, Louisiana 70122 *(Received December 1, 1975)*

Publication costs assisted by the National Science Foundation

A complementary shock tube system was used to study dilute mixtures of carbon dioxide and hydrogen in a 1:5 ratio reacting behind reflected shock waves to produce water and carbon monoxide over the temperature range 2275–3860 K. One shock tube was outfitted to record simultaneously the infrared emissions from water and carbon dioxide through interference filters centered at 3.8 and 4.2 μ, respectively. In order to minimize overlapping emissions, D_2 was employed instead of H_2. The formation of D_2O exhibited quadratic dependence with respect to reaction time. The appearance of CO_2 emission served primarily to mark time zero for the reaction and to establish the position of equilibrium. Argon was the inert diluent. The starting reactant percentages and the reflected shock zone pressure were varied for the purpose of determining the order dependencies for D_2 and the total gas density. The second shock tube was connected to a time-of-flight mass spectrometer which recorded the histories of reactants, products, and intermediates. One notable feature of the TOF experiments was the detection of a small peak at m/e 29 corresponding to the HCO radical which was formed at times previous to significant CO production when H_2 was used as a reactant. Runs performed on a CO_2–D_2 mixture under similar conditions revealed the presence of DCO. The mole fraction for water formation from both shock tubes was fit to the expression $(1 - f_{D_2O}/f_{D_2O,eq}) = \exp(-k[D_2]^{0.3}[M]^{0.7}t^2)$, where $k = 10^{20.0\pm0.2} \exp(-81.4 \pm 2.3/RT)$ cm^3 mol^{-1} s^{-2}. The units for the activation energy are kcal mol^{-1}. Product profiles computed from a selection of literature rate constants making up an atomic mechanism did not compare favorably with the experimental results. The possibility of a mechanism involving vibrational excitation of the reactants prior to transition state formation is discussed.

Introduction

Surprisingly little shock tube work has been devoted to the reaction of hydrogen and carbon dioxide.[2] The reverse reaction is the water gas shift which is of importance in combustion processes,[3] but is inconvenient to study in shock tubes because of the ready absorption of the reactant water on the walls before shock initiation. The same problem is present in studies of the decomposition of water.[4]

However, the high-temperature combination of hydrogen and carbon dioxide produces equilibrium amounts of water and carbon monoxide readily calculable from thermodynamic data[5] in an environment that is nearly ideal for shock tube work. The reaction is almost thermoneutral over the temperature range 2300–3800 K ($\Delta H_{2300} = 5.7$ and $\Delta H_{3800} = 3.5$ kcal mol^{-1}) and will produce an equilibrium mole fraction of water of 0.160 to 0.162 from an initial CO_2/H_2 ratio of 1:5. There exists then a method of introducing a known amount of water into a shock zone that has not been subjected to severe temperature changes caused by excessive heats of reaction. It is also possible to study the $H_2 + CO_2$ system by two independent analytical techniques; namely, infrared emission and time-of-flight (TOF) mass spectrometry. A shock tube coupled to a TOF ion source yields information about the time histories of reactants, products, and intermediates at 20-μs intervals. On the other hand, uninterrupted emission profiles may be obtained from an infrared shock tube. The two sources of data complement one another.

The $H_2 + CO_2 \rightleftharpoons CO + H_2O$ system is an attractive candidate for computer analysis since there are a limited number of reaction steps possible. Previous shock tube studies have reported rate constants for the dissociations of H_2 and CO_2 and many of the ensuing three center reaction rate constants have been measured.

Experimental Section

The complementary shock tube system has been described previously.[6] The usual precautions with regard to shock tube outgassing rates, ultimate vacuums, mixture preparation, and low impurity content of gas mixtures were observed.

A series of preliminary runs on the infrared emission facility using H_2 and CO_2 diluted in argon revealed a substantial amount of overlapping emission at 3.0 μ, the wavelength initially chosen to monitor the appearance of water. Substitution of D_2 for H_2 resulted in virtually clean emission from D_2O through an interference filter centered at 3.8 μ. A filter at 4.2 μ was selected for CO_2 emission although it was realized that emission from D_2O would contribute to the signal recorded at the 4.2-μ detector station. Since the CO_2 intensity was used primarily to mark reflected shock arrival, the D_2O contribution was of no consequence. However, it was necessary to determine the level of CO_2 emission at reaction equilibrium and for that reason a mixture of D_2 and O_2 was shocked in order to determine the amount of emission at 4.2 μ attributable to D_2O. Emissions at the two wavelengths mentioned passed through slit widths set at 0.5 mm. The respective interference filters (Infrared Industries) had ±0.10 μ bandpass at half-peak height. The detectors, transient recorders, and data handling process have been described elsewhere.[7] Polaroid pictures of each experiment were also taken.

Two reacting mixtures were prepared with the following reactant compositions: (A) 2% CO_2–10% D_2; and (B) 1% CO_2–5% D_2. A third mixture (C) consisting of 10% D_2–1% O_2 was used to measure the amount of D_2O contribution to the emission recorded at 4.2 μ. Linde argon (99.996%) comprised the balance of each of the three mixtures. Matheson CP grade deuterium (99.5%) was employed without further purification. Matheson commercial grade CO_2 (99.5%) was condensed, degassed, and subjected to bulb-to-bulb distillation. The reacting mixtures A and B displayed impurity levels of oxygen below the O_2 background of the TOF mass spectrometer which previously had been determined to be 30 ppm. Linde oxygen (99.5%) was utilized for mixture C. Mixtures A, B, and C were all shocked at an initial pressure of 5 Torr. In addition, mixture B was shocked at 10 Torr.

A fourth mixture (D) consisting of 2% CO_2–10% H_2 in a diluent of Matheson Research Grade Ne–1% Ar (99.995%) was shocked at 5 Torr initial pressure in the tube connected to the TOF mass spectrometer. The peak heights corresponding to m/e 18 (H_2O), 40 (Ar), and 44 (CO_2) were measured at 20-μs intervals. A small peak relative to parent CO at m/e 29 exhibited a noticeable variance during the observation period. The possibility that the peak might be composed of HCO in addition to ^{13}CO (natural abundance) was tested by shocking mixture D in which D_2 was used instead of H_2 at comparable temperatures and pressures. A peak at m/e 30 (DCO) was detected.

Linde hydrogen (99.95%) served as the reactant in mixture D and as the driver gas in all of the experiments performed.

Results

A photographic record of an infrared experiment is shown in Figure 1. The emission from D_2O is seen to be nonlinear with respect to reaction time. Records taken at higher temperatures (~3250 K) revealed a steady plateau for both the D_2O and CO_2 signals. At the highest temperatures achieved in this work, a measurable decay from the D_2O plateau was noted which was attributed to water decomposition.

The TOF experiments confirmed that all of the species could be accounted for by inclusion of H_2 (or D_2), CO, CO_2, and H_2O (or D_2O). The amount of HCO or (DCO) formed was too small for quantitative treatment and a reasonable mass balance and equilibrium position (within 3%) could be achieved without including the radical concentrations. This assumption was confirmed by the following two independent determinations of the equilibrium mole fraction of CO_2. The mole fraction of CO_2 at equilibrium was calculated by dividing the ratio of the peak heights corresponding to m/e 44/40 at equilibrium by six times the ratio of 44/40 at time zero. Since the initial mole fraction of CO_2 was in all experiments 1/6, subtracting the mole fraction of CO_2 at equilibrium from the initial mole fraction yielded a value for the equilibrium mole fraction of water. The value so obtained was equal to 0.157 which compared favorably to the value of 0.160 calculated from JANAF thermodynamic data.

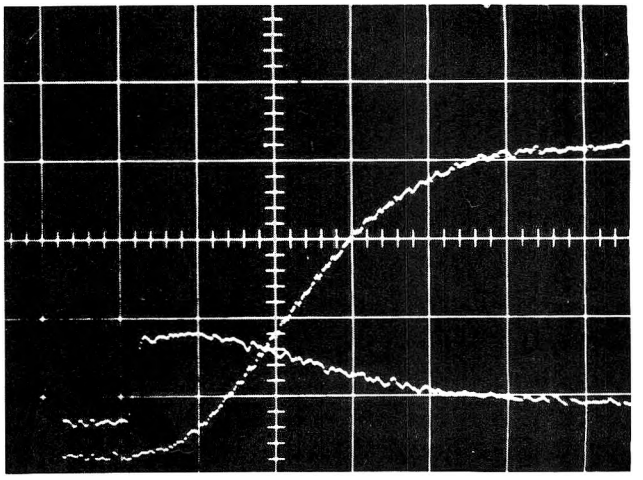

Figure 1. Infrared emission record from a 2% CO_2–10% D_2–88% Ar mixture reacting at 3110 K. Shock arrival at left of picture. Growth of D_2O emission recorded at 3.8 μ and decay of CO_2 at 4.2 μ. The sweep speed is 50 μs/cm.

A second determination was attained using the infrared facility and the following equation

$$f^{ir}_{CO_2,eq} = f^{ir}_{CO_2,i}\frac{(I^{tot}_{CO_2,\infty} - I^{int}_{D_2O,\infty})}{I_{CO_2,i}} \qquad (I)$$

where $f^{ir}_{CO_2,i}$ and $f^{ir}_{CO_2,eq}$ are the initial and equilibrium mole fractions of CO_2, $I^{tot}_{CO_2,\infty}$ is the total signal level at the CO_2 plateau at 4.2 μ, $I^{int}_{D_2O,\infty}$ is the contribution from the interfering emission of D_2O at 4.2 μ determined from shocks of mixture C at comparable temperatures and pressures, and $I_{CO_2,i}$ is the emission from the initial concentration of CO_2 at time zero. Substitution of the experimentally determined quantities in eq I yields a value for $f^{ir}_{CO_2,eq}$.

$$f^{ir}_{CO_2,eq} = 0.167\frac{(1.43 - 1.07)}{6.34} = 0.010$$

Using the stoichiometric relation $D_2 + CO_2 \rightleftharpoons D_2O + CO$, the mole fraction of D_2O at equilibrium may be calculated.

$$f^{ir}_{D_2O,eq} = 0.167 - 0.010 = 0.157$$

Kinetic data for the production of water from both shock tubes were fit to the following equation

$$(1 - f_{D_2O}/f_{D_2O,eq}) = \exp(-k't^2) \qquad (II)$$

Although the value of k' was determined by data up to a mole

TABLE I: Rate Constants for Water-Gas Reaction.

Mixture	T_5, °K	$\rho_5 \times 10^6$, mol cm^{-3}	$k \times 10^{-13}$, cc mol^{-1} sec^{-2}
A. 2% CO_2 - 10% D_2 - 88% Ar, P_1 = 5 Torr	2275.	3.20	0.26
	2447.	3.27	0.38
	2534.	3.30	0.80
	2584.	3.32	0.60
	2612.	3.32	1.93
	2667.	3.39	1.12
	2728.	3.36	1.44
	2731.	3.36	4.13
	2742.	3.05	1.84
	2786.	3.38	4.37
	2795.	3.38	1.49
	2855.	3.40	1.41
	2903.	3.42	6.21
	2916.	3.42	6.74
	2965.	3.43	5.69
	2968.	3.43	13.0
	2975.	3.44	7.62
	3007.	3.45	11.9
	3024.	3.45	10.1
	3030.	3.37	13.0
	3042	3.45	26.3
	3060	3.46	11.3
	3098	3.47	14.3
	3261.	3.51	50.4

TABLE I: Rate Constants for Water-Gas Reaction. (contd.)

Mixture	T_5, °K	$\rho_5 \times 10^6$, mol cm^{-3}	$k \times 10^{-13}$, cc mol^{-1} sec^{-2}
B. 1% CO_2 - 5% D_2 - 94% Ar, P_1 = 5 Torr	2563.	2.11	0.47
	2730.	2.16	5.55
	2753.	2.09	3.77
	2758.	2.17	3.28
	2799.	2.18	4.05
	2808.	2.18	3.92
	2845.	2.11	3.66
	2878.	2.12	10.5
	2970.	2.22	10.7
	3029.	2.24	16.3
	3045.	2.24	13.7
	3052.	2.16	10.6
	3105.	2.21	19.0
	3156.	2.26	15.9
	3749.	2.28	31.6
	3291.	2.29	45.3
	3330.	2.30	63.7
	3354.	2.26	54.1
	3451.	2.24	73.5
	3822.	2.30	239
	3857.	2.30	244

TABLE I: Rate Constants for Water-Gas Reaction. (contd.)

Mixture	T_5, °K	$\rho_5 \times 10^6$, mol cm^{-3}	$k \times 10^{-13}$, cc mol^{-1} sec^{-2}
B. 1% CO_2 - 5% D_2 - 94% Ar, P_1 = 10 Torr	2557.	4.22	1.48
	2587.	4.24	0.72
	2709.	4.31	2.46
	2723.	4.32	2.13
	2749.	4.33	3.37
	2756.	4.34	3.60
	2791.	4.36	4.82
	2792.	4.36	2.99
	2841.	4.38	6.67
	2853.	4.39	7.86
	2885.	4.40	11.6
	2921.	4.42	5.30
	2937.	4.43	8.33
	2939.	4.43	9.77
	2967.	4.44	8.19
	2991.	4.46	8.01
	3089.	4.50	18.3
	3167.	4.53	17.4
D. 2% CO_2 - 10% H_2 - 88% Ne, P_1 = 5 Torr	2410.	2.24	0.54
	2437.	2.25	0.78
	2512.	2.28	0.47
	2538.	2.29	1.25
	2573.	2.30	1.47
	2718.	2.35	2.19
	2900.	2.41	7.69
	3032.	2.44	11.2
	3066.	2.45	9.36

fraction of 0.1, the rest of the experimental points displayed a good fit to eq II also. The results from an infrared experiment are depicted in Figure 2. Variance of the initial reactant compositions and the initial shock tube pressure was accomplished with mixtures A and B. The order dependencies on the concentration of deuterium, which was approximately constant over the extent of reaction calculated ($f_{D_2O} = 0.1$), and the total gas density [M] were determined by a least-squares procedure to be 0.3 and 0.7, respectively. Hence, in eq II, $k' = k[D_2]^{0.3}[M]^{0.7}$. The Arrhenius parameters were calculated using the rate constants determined from mixtures A, B, and C, and are given in the following expression

$$k = 10^{20.0\pm0.2} \exp(-81.4 \pm 2.3/RT)$$

The units for k are cm^3 mol^{-1} s^{-2} and the units for the activation energy are kcal mol^{-1}. The rate constants are plotted in Figure 3 and are listed in Table I (miniprint material, see paragraph at end of text regarding miniprint material).

In several of the runs at the higher temperatures, decay from the plateau established by D_2O emission was noted. The maximum mole fraction attained was calculated as described previously and the amount of water decomposition over a 100-μs interval was determined and a pseudo-first-order rate constant was calculated. The values at 3417 and 3715 K were 4.56×10^2 and 1.53×10^3, respectively, which compare favorably with those obtained by other workers;[4] namely, 5.67×10^2 and 1.96×10^3 cm^3 mol^{-1} s^{-1}.

Discussion

The main findings of this work are the quadratic growth of the water profiles to a known mole fraction level that was confirmed by two independent techniques; the appearance of the HCO radical during the reaction period; the representation of the reaction profiles over a considerable temperature range by a single equation; and the feasibility of utilizing the reaction of carbon dioxide and hydrogen for the purpose of introducing a known amount of gaseous water from an essentially thermoneutral reaction source into the shock tube.

The detection of HCO and the nonlinear production of water suggests the possibility of an atomic mechanism. Since most of the plausible reaction steps have been measured and reported from many different laboratories, an attempt to fit the product profiles recorded for water from mixture B (5 Torr) at 2758, 3045, and 3822 K was made using the following sequence:

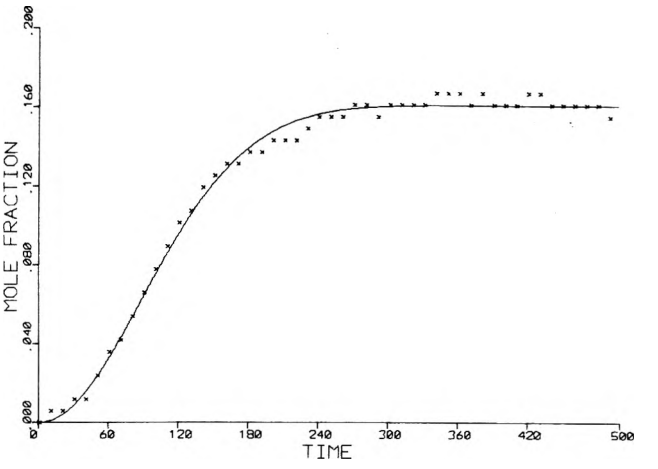

Figure 2. Fit of eq II to experimental data obtained from 1% CO_2–5% D_2–94% Ar mixture at 3045 K.

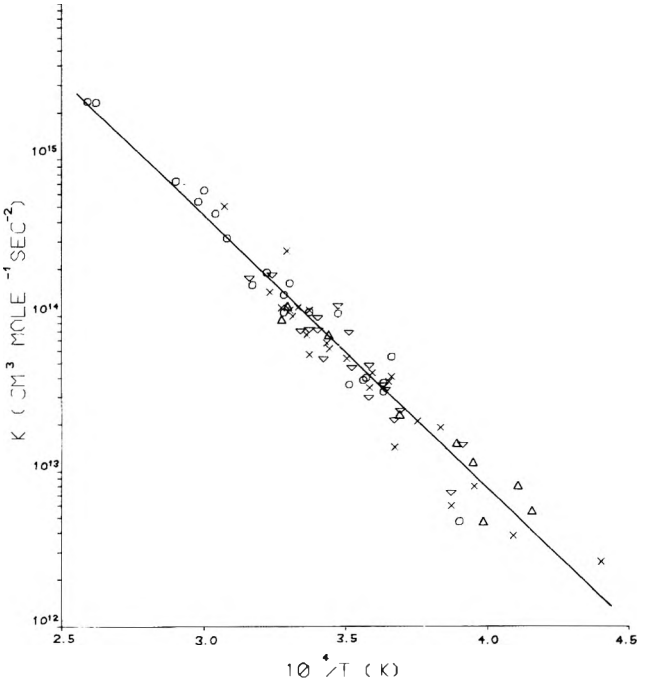

Figure 3. Arrhenius plot of the data in Table I: X, mixture A; O, B at 5 Torr; ∇, B at 10 Torr; △, D.

initiation

$$CO_2 + M \rightleftharpoons CO + O + M \quad (1)$$

$$H_2 + M \rightleftharpoons 2H + M \quad (2)$$

$$H_2 + H_2 \rightleftharpoons 2H + H_2 \quad (3)$$

$$H_2 + H \rightleftharpoons 3H \quad (4)$$

$$O + H_2 \rightleftharpoons OH + H \quad (5)$$

product formation

$$OH + H_2 \rightleftharpoons H_2O + H \quad (6)$$

$$H + CO_2 \rightleftharpoons CO + OH \quad (7)$$

intermediate formation

$$H + CO_2 \rightleftharpoons HCO + O \quad (8)$$

$$H_2 + CO_2 \rightleftharpoons HCO + OH \quad (9)$$

product decomposition

$$H_2O + M \rightleftharpoons H + OH + M \quad (10)$$

$$CO + M \rightleftharpoons C + O + M \quad (11)$$

Several of these reactions have different literature values for their Arrhenius parameters. For instance, the activation energy for the decomposition of CO_2 is reported to range from 74.1 to 107 kcal mol^{-1}. References to the various rate constants tried and a representative set of values are listed in Table II. When more than one reference is indicated, the first one pertains to the representative value. The computer programs for the calculation of the time dependent concentrations of the species found in steps 1–10 were run by Mr. James Hardy at the University of Texas and Dr. Tony Dean at the University of Missouri.[15] The amount of CO decomposition is negligible at the highest temperature achieved in this work and was not included.[16] The activation energies for reactions 8 and 9 were derived from thermochemical data[5] and the preexponential factors were estimated. The concentrations of HCO formed were small relative to the major species and their exclusion from the reaction scheme did not affect appreciably the calculated profiles for the major species.

It is interesting to note that the calculated values from the program for the mole fraction could be fit very well by the functional dependence found in eq II. However, the magnitude of k' differed markedly from the experimental values. The quadratic growth is a direct result of the fact that the initiation reactions 1–4 have not reached equilibrium in the time involved for the experiments (500–600 μs).

Comparison of the computer profiles calculated using the rate constants in Table II revealed that the representative set listed came closest to duplicating the experimental results but only at the higher temperature end. The observed mole fractions of water were greater than the calculated amounts by a factor of 2 at 2758 K and by a factor of 1.5 at 3045 K. These factors increased to 1000 at 2758 K and to 60 at 3045 K when the highest value[10] for the activation energy of step 1 was tried. Calculations were performed with starting amounts of 10, 20, and 30 ppm of O_2 using reactions 1–10 and adding the reaction[9]

$$H + O_2 \rightleftharpoons O + OH \quad (12)$$

in order to test for the effect of impurities[17] below the detectable background level. The amount of water predicted at 2758, 3045, and 3822 K remained well below that observed.

TABLE II: Representative Rate Constants[a]

Reaction	Rate constant	Ref
1	$3.80 \times 10^{-11} e^{-74.1/RT}$	8,9,10,11
2	$1.55 \times 10^{-10} e^{-88.9/RT}$	12
3	$5.48 \times 10^{-9} e^{-105.3/RT}$	12
4	$3.53 \times 10^{-9} e^{-87.2/RT}$	12
5	$3.65 \times 10^{-10} e^{-13.7/RT}$	13
6	$8.64 \times 10^{-11} e^{-6.45/RT}$	14
7	$1.18 \times 10^{-10} e^{-20.4/RT}$	9
8	$1.00 \times 10^{-10} e^{-104/RT}$	5
9	$1.00 \times 10^{-10} e^{-106/RT}$	5
10	$2.00 \times 10^{-9} e^{-105/RT}$	4

[a] Units of preexponential factor and activation energy are cm^3 molecule^{-1} s^{-1} and kcal mol^{-1}, respectively.

One possible explanation for the discrepancy might be that the rates of decomposition are severely affected by the presence of reactive species. For instance, decomposition of CO_2 in a hydrogen environment and/or decomposition of H_2 in a carbon dioxide environment could lower drastically the apparent rates of decomposition for either H_2 or CO_2 or both. Previous work on exchange systems argue indirectly against this proposal. The self-exchange of HD[18,19] and of CO[7,20] in inert gas diluents displayed activation energies far below the amount predicted by an atomic mechanism. In these systems the decomposition process was not affected by another species and it was concluded that the mechanism responsible for the large amounts exchange products formed was not atomic.

The complete details of the exchange mechanism are not known. The importance of the vibrational energy content of the reactants has been emphasized and the observed nonlinear time dependence for product formation supports the contention that there exists a nonequilibrium step(s) in the exchange mechanism.[21] The determination of non-zero-order dependencies for the inert gas diluent argues also for a multistep process involving excitation of the reactants prior to exchange.

Extending this line of reasoning to the present system and accepting the likely notion that the excitation consists primarily of vibrational energy, the following steps may be written

$$H_2 + M \rightarrow H_2^v + M \quad (13)$$

$$CO_2 + M \rightarrow CO_2^v + M \quad (14)$$

$$H_2^v + CO_2 \rightleftharpoons \left[\begin{matrix} H\cdot \\ H\cdot \end{matrix} O \text{–} C = O \right] \rightleftharpoons H_2O + CO \quad (15)$$

$$H_2^v + CO_2 \rightleftharpoons \left[O \text{–} C = O \right] \rightleftharpoons OH + HCO \quad (16)$$

Reactions 13 and 14 actually represent a sequence of steps leading to some vibrational energy manifold that is being depleted rapidly with respect to its equilibrium concentrations by the conversion reactions 15 and 16. The specific identification of this manifold is uncertain since it is the difference between the activation energy of step 15 and the experimental value, 81.4 kcal mol^{-1}. The activation energies for steps 15 and 16 are not known.

Similar ideas with regard to the importance of vibrational energy and the depletion of vibrational levels from their equilibrium amounts have been advanced to explain the experimental result that the activation energies for the decompositions of a large number of simple molecules are less than their respective bond energies.[22,23]

Current work in this laboratory on the reaction of H_2 + CNCl → HCN + HCl has produced similar results; namely, the production of HCN and HCl in amounts that far exceed those predicted by an atomic mechanism.

Acknowledgments. The assistance of Mr. David Wilbanks and Mr. Calvin Esneault in the data reduction process and the help of Dr. Tony Dean, Dr. W. C. Gardiner, and Mr. James Hardy in the computer calculations is greatly appeciated.

Miniprint Material Available: Full-size photocopies of Table I (3 pages). Ordering information is available on any current masthead page.

References and Notes

(1) (a) Paper presented at the 169th National Meeting of the American Chemical Society, Chicago, Ill., Aug, 1975. (b) Support of this work by the National Science Foundation, Grant No. MPS72-04717 A03, is gratefully acknowledged.
(2) J. C. Carter, Sc.D. Thesis, Washington University, St. Louis, Mo, 1965.
(3) G. A. Karim and D. Mohindra, *J. Inst. Fuel*, **47**, 219 (1974).
(4) J. B. Homer and I. R. Hurle, *Proc. R. Soc. London, Ser. A*, **314**, 585 (1970).
(5) "JANAF Thermochemical Tables", 2d ed, U.S. Department of Commerce, Washington, D.C., 1971.
(6) R. D. Kern and G. G. Nika, *J. Phys. Chem.*, **78**, 2549 (1974).
(7) A. F. Bopp, R. D. Kern, and B. V. O'Grady, *J. Phys. Chem.*, **79**, 1483 (1975).
(8) T. C. Clark, S. H. Garnet, and G. B. Kistiakowsky, *J. Chem. Phys.*, **51**, 2885 (1969).
(9) A. M. Dean, *J. Chem. Phys.*, **58**, 5202 (1973).
(10) J. H. Kiefer, *J. Chem. Phys.*, **61**, 244 (1974).
(11) W. A. Hardy, H. Vasatko, H. Gg. Wagner, and F. Zabel, *Ber. Bunsenges. Phys. Chem.*, **78**, 76 (1974).
(12) W. D. Breshears and P. F. Bird, *Symp. (Int.) Combust. [Proc.], 14th*, 211 (1973).
(13) G. L. Schott, R. W. Getzinger, and W. A. Seitz, *Int. J. Chem. Kinet.*, **6**, 921 (1974).
(14) W. C. Gardiner, Jr., W. G. Mallard, and J. H. Owen, *J. Chem. Phys.*, **60**, 2290 (1974).
(15) Dr. Dean kindly furnished us with a copy of his program which has been adapted by Mr. David Wilbanks to run on the DEC PDP-10 computer at the University of New Orleans.
(16) R. K. Hanson, "Recent Developments in Shock Tube Research", Stanford University Press, Stanford, Calif., 1973.
(17) T. Just and S. Stepanek, *Shock Tubes, Proc. Int. Shock Tube Symp., 7th, 1969*, 626 (1970).
(18) D. Lewis and S. H. Bauer, *J. Am. Chem. Soc.*, **90**, 5390 (1968).
(19) R. D. Kern and G. G. Nika, *J. Phys Chem.*, **75**, 2541 (1971).
(20) A. Bar-Nun and A. Lifshitz, *J. Chem. Phys.*, **51**, 1826 (1969).
(21) S. H. Bauer, D. M. Lederman, E. L. Resler, and E. R. Fisher, *Int. J. Chem. Kinet.*, **5**, 93 (1973).
(22) J. H. Kiefer, H. P. G. Joosten, and W. D. Breshears, *Chem. Phys. Lett.*, **30**, 424 (1975).
(23) H. S. Johnston and J. Birks, *Acc. Chem. Res.*, **5**, 327 (1972).

Rare Gas Sensitized Radiolysis of Hydrogen Sulfide in the Low Concentration Range

Mieczysław Forys,* Antoni Jówko, and Iwona Szamrej

Chemistry Department, University Teachers College, 08-110 Siedlce, Poland *(Received September 18, 1975)*

Hydrogen and sulfur yields have been determined in the rare gas sensitized radiolysis of hydrogen sulfide. A decrease in $G(H_2)$ and $G(S)$ has been discovered in each of the three mixtures examined: H_2S–Ar, H_2S–Kr, and H_2S–Xe. A mechanism has been proposed including (1) competition between a charge transfer to H_2S and Ar_2^+ formation in the H_2S–Ar system, and (2) competition between an excitation transfer to H_2S and formation of excited rare gas molecules in H_2S–Xe and H_2S–Kr mixtures. Rate constants of the charge and excitation transfer have been estimated: $k_{Ar^+ + H_2S} = 1.8 \times 10^{-9}$ cm^3 s^{-1}, $k_{Kr^* + H_2S} = (0.6\text{–}1.5) \times 10^{-9}$ cm^3 s^{-1}, and $k_{Xe^* + H_2S} = 2.7 \times 10^{-9}$ cm^3 s^{-1}. The relevance of Franck–Condon transitions in the charge-transfer processes has been shown. The maximum recombination energy values of the rare gas molecular ions were estimated as 14.0, 12.7, and 10.8 eV for Ar_2^+, Kr_2^+, and Xe_2^+, respectively.

Introduction

The rare gas sensitized radiolysis of hydrogen sulfide has been the object of several investigations using γ[1–5] and pulse[6] radiolysis techniques.

Jezierska and Forys[2] have reported results on $G(H_2)$ in H_2S–Xe, H_2S–Kr, and H_2S–Ar systems in a full range of concentrations. The main experimental feature observed was the fact that $G(H_2)^R$ (R denotes the rare gas) varied slowly at large concentration of hydrogen sulfide in all systems and decreased sharply at small amounts of hydrogen sulfide in argon and krypton containing mixtures. The lowering of $G(H_2)^R$ was not observed in the xenon–hydrogen sulfide mixture.

On these grounds, the mechanism of hydrogen formation has been proposed including reaction 1 in the case of argon and krypton

$$R^+ + H_2S \longrightarrow HS^+ + H + R \quad (1a)$$

$$\longrightarrow S^+ + H_2 + R \quad (1b)$$

this reaction being in competition with

$$R^+ + 2R \longrightarrow R_2^+ + R \quad (2)$$

followed by

$$R_2^+ + H_2S \longrightarrow H_2S^+ + 2R \quad (3)$$

It should be here pointed out that only a few points were obtained in the region of lowering $G(H_2)$ (below ca. 2 mol % of H_2S) in each case.

Woodward et al.[3] have measured $G(S)$ in an H_2S–Ar mixture as well as $G(S)$ and $G(H_2)$ in a H_2S–Xe mixture. The hydrogen and sulfur yields in the last system generally sup-

ported the data of ref 2, but $G(S)$ from H_2S–Ar mixtures was enormously large (about 20) and was in contradiction with $G(H_2) = 7$ from ref 2.

So, the aim of this investigation was to measure $G(H_2)$ and $G(S)$ in all three systems of interest to solve the discrepancy between the data of ref 2 and 3, and obtain more detailed results on hydrogen and sulfur yields at small (below 2 mol %) concentrations of hydrogen sulfide. In the course of the experiment it has been observed that $G(H_2)$ decreases also in the mixture H_2S–Xe, where formation of hydrogen from ionic processes is not possible.[5] Thus, it was necessary to propose a mechanism which would be able to explain a decrease in $G(H_2)$ in all three mixtures.

Experimental Section

The experimental technique was exactly the same as in ref 5, 7, and 8.

Briefly, the ^{60}Co γ ray source of the Institute of Applied Radiation Research at Łódź was used for irradiations. Hydrogen sulfide has been used as a dosimeter, taking[9] $G(H_2) = 7.1$. The dose rate in hydrogen sulfide was 9.0×10^{15} eV g^{-1} s^{-1}, unless mentioned otherwise. The maximum absorbed dose was 1×10^{20} eV g^{-1}. At low concentrations of hydrogen sulfide the conversion corresponded to formation ca. 0.01 mol % of hydrogen in the mixture.

$G(\text{prod})^R$, a radiation yield from the sensitization processes, was calculated using[2]

$$G(\text{prod})^R = \frac{G(\text{prod})^t - G(\text{prod})^{H_2S} F_{H_2S}}{F_R} \qquad \text{(I)}$$

Here $G(\text{prod})^t$ is a measured product (hydrogen or sulfur) yield per total absorbed dose; $G(\text{prod})^{H_2S} = 7.1$ is that produced by the dose absorbed in hydrogen sulfide. We assume that $G(H_2)^{H_2S}$ is not influenced by a rare gas. F_{H_2S} and F_R are the fractions of the dose absorbed in hydrogen sulfide and rare gas, respectively. They were calculated, taking $F_R + F_{H_2S} = 1$, from

$$F_{H_2S} = \frac{x_{H_2S}}{x_{H_2S} + x_R(S_R/S_{H_2S})} \qquad \text{(II)}$$

Here x_{H_2S} and x_R denote corresponding molar fractions and S_{H_2S}/S_R = the stopping power ratios. Woodward's data[10] were used for calculations: $S_{Xe}/S_{H_2S} = 2.45$, $S_{Kr}/S_{H_2S} = 1.70$, and $S_{Ar}/S_{H_2S} = 0.96$.

At molar fractions of H_2S below 0.01 (the range of interest) $G(\text{prod})^R$ was practically equal $G(\text{prod})^t$. At low mole fractions of hydrogen sulfide its conversion was relatively large. Thus, the mean value of the mole fraction, x'_{H_2S}, was used for calculations: $x'_{H_2S} = x_{H_2S} - 0.5\,x_{H_2}$, where x_{H_2} denotes the mole fraction of hydrogen produced. The sensitivity limit of the sulfur determination is equal that formed when ca. 0.1 mol % of hydrogen is produced in the mixture. Thus, sulfur yields were not measured at low concentrations of hydrogen sulfide in the irradiated mixture because of a too low H_2S conversion required (corresponding to formation ca. 0.01 mol % of hydrogen in the mixture). Hence we measured hydrogen yields and in the discussion we assumed that sulfur is produced stoichiometrically, which has been shown in the higher concentration range.

Results

In the preliminary analysis of the data it has been stated that $G(H_2)^R$ depends not only on the $[H_2S]/[Ar]$ ratio but also on rare gas pressure. So, the effect of the $[H_2S]/[Ar]^2$ ratio on $G(H_2)^R$ and $G(S)^R$ is shown in Figures 1–3 for the H_2S–Ar, H_2S–Kr, and H_2S–Xe mixtures, respectively. The overall pressure used in the experiments varied in the range 300–700 Torr. It is seen that the hydrogen yield stoichiometrically corresponds to the sulfur yield in all mixtures within the range of experimental error. Particularly, unlike the observations in ref 3, $G(S)$ from the H_2S–Ar mixture does not exceed the value of $G(H_2) = 7$ and is much less than 20, the figure obtained in ref 3. As all parameters of Woodward's and our experiments were the same except for dose rates (Woodward's dose rate was 7.4×10^{14} eV g^{-1} s^{-1} in pure H_2S), we have performed the experiment at a dose rate of 5.0×10^{14} eV g^{-1} s^{-1}. However, the results (Figure 1) were not altered and thus the reason for the discrepancy is not yet understood.

$G(H_2)$ decreases sharply at low concentrations of hydrogen sulfide in all three systems: from 7.0 to ca. 4 in H_2S–Ar; from 5.5 to 3.5 in H_2S–Kr; and from 5.4 to 1.8 in H_2S–Xe in the range of H_2S concentrations 2–0.05 mol % in Ar and 0.5–0.05 mol % in Kr and Xe. This is essentially the same result as in ref 2, keeping in mind that a H_2S–Xe mixture was not investigated in the range below 0.5 mol % of hydrogen sulfide.

It should be noted here that Perner and Franken[6] observed lowering in $G(H_2)$ in the pulse radiolysis of the H_2S–Xe mixture. They have found $G(H_2)$ to equal 1.8 and 5.7 at 0.13 and 1.6 mol % of H_2S respectively.[11] Woodward et al.[3] have obtained $G(H_2) = 3.7$ at 0.5 mol % of H_2S compared to 4.7 and 5.2 at 2.5 and 12 mol % of H_2S, respectively. Also, Jonsson and Lind[12] have observed a sharp decrease in $G(-CH_3SH)$ from 30 ± 10 to 10 ± 2 when the methanethiol concentration had been changed from 1 to 0.02% in argon-sensitized radiolysis of methanethiol.

Discussion

When a mixture containing a large excess of rare gas is irradiated, the main primary processes can be written in the following manner:

$$R + e^- \longrightarrow R^+ + 2e^- \qquad (4)$$

$$\longrightarrow R^* + e^- \qquad (5)$$

Ion recombination has been shown[8] not to be a source of hydrogen or sulfur in the rare gas–hydrogen sulfide systems. Thus, only the processes of charge and energy transfer should allow to the formation of these products.

Resulting ions are produced in their ground ($^2P_{3/2}$) and excited ($^2P_{1/2}$) states, and excited atoms are formed in higher excited Rydberg states, low-lying resonance ($^3P_1$ and $^1P_1$), and metastable ($^3P_{2,0}$) states. When hydrogen sulfide is present in the mixture

$$R^+ + H_2S \longrightarrow R + H_2S^+ \qquad (6)$$

simple and dissociative charge transfer, reactions 1a and 1b, as well as excitation transfer can occur which results in observed hydrogen and sulfur yields. These processes are in competition with the formation of molecular ions from atomic ions (reaction 2) and from atoms in higher excited states (Hornbeck–Molnar processes)

$$R^{**} + R \longrightarrow R_2^+ + e^- \qquad (7)$$

Hornbeck–Molnar processes are very fast ($k = (1\text{–}2) \times 10^{-9}$ cm^3 s^{-1}) and prevent higher excited states from being involved in a reaction with low concentration (of the order of 1 mol %) admixtures.

At near atmospheric pressures a radiation from the resonance states $^3P_1$ and $^1P_1$ is thought to be reabsorbed by

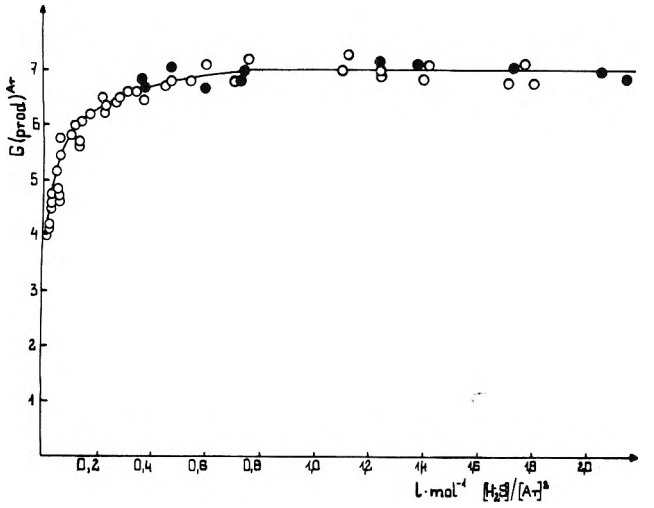

Figure 1. The plot of hydrogen and sulfur yields from sensitization with argon, $G(\text{prod})^{Ar}$, as a function of the $[H_2S]/[Ar]^2$ ratio: (O) $G(H_2)^{Ar}$; (●) $G(S)^{Ar}$.

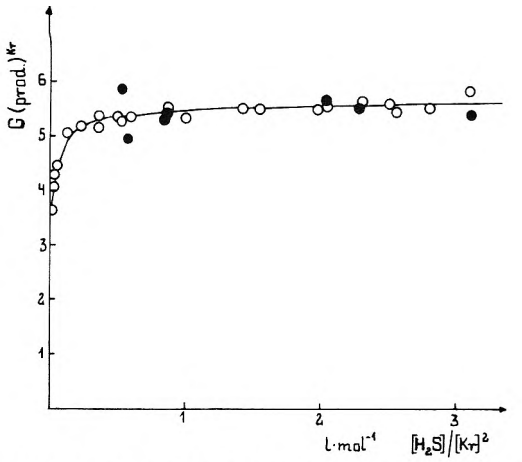

Figure 2. The plot of hydrogen and sulfur yields from sensitization with krypton, $G(\text{prod})^{Kr}$, as a function of the $[H_2S]/[Kr]^2$ ratio: (O) $G(H_2)^{Kr}$; (●) $G(S)^{Kr}$.

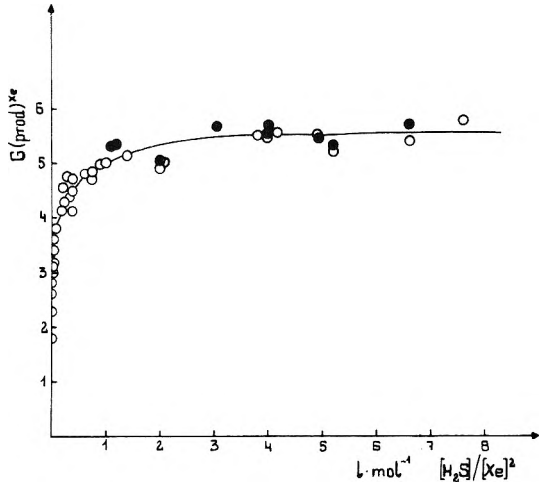

Figure 3. The plot of hydrogen and sulfur yields from sensitization with xenon, $G(\text{prod})^{Xe}$, as a function of the $[H_2S]/[Xe]^2$ ratio: (O) $G(H_2)^{Xe}$; (●) $G(S)^{Xe}$.

ground-state rare gas atoms so that they decay by a cascade of transitions to the metastable states, as well as by collisional conversions between states of nearly the same energy.[13,14]

Ellis and Twiddy[15] have shown that both the metastables of argon $^3P_0$ and $^3P_2$ have similar rate constants for a deactivation in a three-body reaction

$$R^*(^3P_{2,0}) + 2R \longrightarrow R_2^*(^{3,1}\Sigma_u^+) + R \qquad (8)$$

$k_8(^3P_2) = 1.7 \times 10^{-32}$ cm^6 s^{-1} and $k_8(^3P_0) = 1.2 \times 10^{-32}$ cm^6 s^{-1}. Also rate constants for an excitation transfer from $^3P_2$ and $^3P_0$ to small molecules are similar, as measured in discharge flow[16] experiments. On this basis it may be stated that both states take part in reaction 8 and an excitation transfer to molecules with similar rate constants and a composite rate constant for the $^3P_{2,0}$ state can be found in radiolysis experiments, as it has been observed in pulse radiolysis.[17] Measured rate constants of the reaction 8 are 2.8×10^{-34} (He),[18a] 5×10^{-34} (Ne),[18b] 6×10^{-33} (Ar),[16] 4×10^{-32} (Kr),[19] 9×10^{-32} cm^6 s^{-1} (Xe).[20]

Le Calvé and Bourène[17] have shown that Ar_2 molecules are unable to excite the $(C^3\Pi_u)$ state of nitrogen ($v' = 0$ at 11.2 eV).

It could be supposed similarly that observed lowering in $G(H_2)$ is caused by a competition between the reaction of a dissociative excitation transfer to hydrogen sulfide

$$R^*(^3P_{2,0}) + H_2S \longrightarrow R + H + HS \qquad (9a)$$

$$\longrightarrow R + 2H + S \qquad (9b)$$

$$\longrightarrow R + H_2 + S \qquad (9c)$$

and reaction 8 followed by

$$R_2(^{3,1}\Sigma_u) + H_2S \longrightarrow 2R + H_2S^* \not\longrightarrow H \qquad (10a)$$

$$\longrightarrow 2R + H + HS \qquad (10b)$$

$$\longrightarrow 2R + H_2 + S \qquad (10c)$$

Among the reactions 9 and 10, processes 9c and 10c may be excluded owing to the results of our experiments with butadiene[8,21] which have shown that (1) S^+ ions are absent and, (2) molecular hydrogen is not produced in the primary processes.

Besides reactions 9 and 10 two additional processes should be considered at low concentrations of hydrogen sulfide. (1) At concentration of hydrogen sulfide of order of 0.1 mol %, the product hydrogen is present in the system at relatively high concentration ($[H_2]/[H_2S] \simeq 0.1$) and the energy transfer from a rare gas to hydrogen might occur. Fortunately, Hotop and Niehaus[22] have shown that Ar and Kr (and presumably Xe) react with hydrogen only in their high Rydberg states. Because these are quickly removed in the Hornbeck–Molnar reaction 7, hydrogen may be taken to be nonreactive under our conditions. (2) The most reactive possible impurity is oxygen. It was removed below 0.01 mol % (a limit of sensitivity of chromatographic detection). Because of the fact that at low concentrations (below $[O_2]/[H_2S] = 0.1$) oxygen only slightly influences $G(H_2)$ from hydrogen sulfide,[23] it also cannot cause the observed decrease in $G(H_2)$.

Additionally, if the effect were caused by any impurity, an enlarged spread of the experimental results at low concentrations of H_2S should have been observed. This was not discovered in the performed experiment. Thus, the observed decrease in $G(H_2)$ should be ascribed to the changes in the charge and/or excitation transfer from the rare gas to the hydrogen sulfide molecule.

Hydrogen Sulfide–Argon Mixture. In the hydrogen sulfide–argon mixture the reaction scheme of hydrogen formation may be written as follows:

$$Ar + e^- \longrightarrow Ar^+ + 2e^- \quad (11)$$

$$\longrightarrow Ar^* + e^- \quad (11a)$$

$$Ar^+ + H_2S \longrightarrow Ar + H + HS^+ \quad (12)$$

$$\hookrightarrow H_2$$

$$Ar^+ + 2Ar \longrightarrow Ar_2^+ + Ar \quad (13)$$

$$Ar_2^+ + H_2S \longrightarrow H_2S^{+*} + 2Ar \quad (14)$$

$$\hookrightarrow H_2$$

$$Ar^* + H_2S \longrightarrow H_2S^+ + Ar + e^- \quad (15a)$$

$$\longrightarrow H(2H) + HS(S) + Ar \quad (15b)$$

$$Ar^* + 2Ar \longrightarrow Ar_2^* + Ar \quad (16)$$

$$H + H_2S \longrightarrow H_2 + HS \quad (17)$$

Rate constants of reactions 16 and 15 have been rather well established and are equal to 6×10^{-33} cm^6 s^{-1} [16] and 8×10^{-10} cm^3 s^{-1},[24] respectively.

It can be calculated that the rate of reaction 15 will be equal to that of reaction 16 at 1.2×10^{-2} mol % of H_2S at the radiolysis pressure (500 Torr). It follows from Figure 1 that $G(H_2)^{Ar}$ decreases by $0.5\Delta G(H_2)$ actually at ca. 0.2 mol % of H_2S (500 Torr total pressure). Hence, competition between the reactions 15b and 16 cannot be responsible for the observed decrease. It is also known from Woodward's[3] experiments that reaction 15a occurs consuming $G(Ar^*) = 2.0$. Taking $G(ion)^{Ar} = 3.8$ and $AP(Ar^+) = 15.8$ eV[14] one can obtain the lowest value of energy necessary to ion formation 60.0 eV, hence the maximum $G(Ar^*)$ is 3.5 (supposing 11.7 eV[14] for the energy level of the ^3P state of argon). From that, only 3.5 − 2.0 = 1.5 excited argon atoms may transfer energy to hydrogen sulfide via excitation transfer, reaction 15b, even without taking into account subexcitation electrons. This is less than that necessary to cause the observed lowering $G(H_2)^{Ar}$ by more than 3.1 (Figure 1) even if two hydrogen atoms are formed in reaction 15b. This supports our assumption that competition between reactions 15 and 16 is not responsible for the observed effect.

The rate constant of reaction 13 is[24,25] 2×10^{-31} cm^6 s^{-1}. The rate constant of reaction 12 has not been measured as yet using the primary method but was evolved from the previous Ar–H_2S radiolysis data[2] as 1.0×10^{-10} cm^3 s^{-1}. The value $k_{13} = 6 \times 10^{-32}$ cm^6 s^{-1} has been taken.[2] If the value 2×10^{-31} is used for k_{13} the rate constant of reaction 12 becomes 3.3×10^{-10} cm^3 s^{-1}. Also, an estimation can be made by the comparison of data for charge transfer from Ar^+ to other small molecules. These lie usually between 1×10^{-9} and 10×10^{-9} cm^3 s^{-1}. In this case a decrease in $G(H_2)$ by $0.5\Delta G(H_2)$ should take place (at 500 Torr of Ar) in the range 0.3–3 mol %. Our experimental value is 0.2 mol %. So, the present refined results support ionic mechanism proposed previously.[2] A steady-state treatment of the scheme leads to

$$\frac{1}{G(H_2)^{Ar} - G(H_2)^*} = \frac{1}{G(Ar^+)}\left(1 + \frac{k_{13}[Ar]^2}{k_{12}[H_2S]}\right) \quad (III)$$

The corresponding plot is shown in Figure 4. Here $G(H_2)^*$ is the hydrogen yield from reaction 15b, taken constant in the entire range of concentrations used (see above comparison of the rate constant of reactions 15 and 16). It has been calculated as 3.2, a difference between the plateau value of $G(H_2)^{Ar} = 7.0$ and $G(Ar^+) = 3.8$.[14] From the slope and intercept of the line

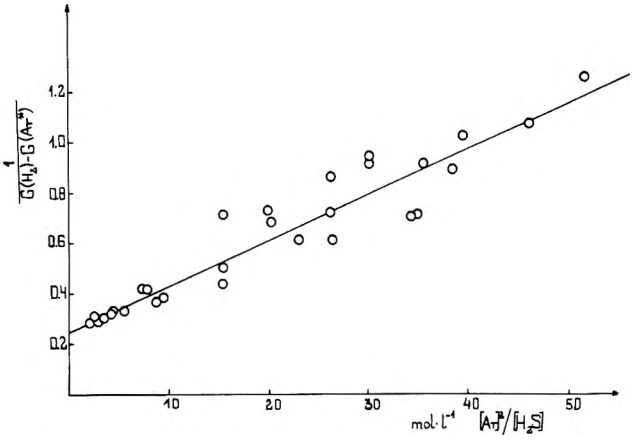

Figure 4. A Stern–Volmer-like plot for a hydrogen sulfide–argon mixture.

the rate constants ratio is $k_{13}/k_{12} = 1.1 \times 10^{-22}$ cm^3. Taking[24,25] $k_{13} = 2 \times 10^{-31}$ cm^6 s^{-1} one can obtain $k_{12} = 1.8 \times 10^{-9}$ cm^3 s^{-1}. This value is somewhat larger than the previous[2] value of 3.3×10^{-10} cm^3 s^{-1}, but is in good agreement with that of the reaction[26] $He^+ + H_2S$ ($k = 4.4 \times 10^{-9}$ cm^3 s^{-1}).

We wish to note here that reaction 14 implies charge transfer to hydrogen sulfide without destruction of a molecule of H_2S. It is not obvious, because $AP(Ar_2^+) = 14.71$ eV[14] just as $AP(HS^+) = 14.3 - 14.4$ eV and $AP(S^+) = 13.4$ eV[27] and both reactions 14a and 14b seem energetically possible.

$$Ar_2^+ + H_2S \longrightarrow H + HS^+ + 2Ar \quad (14a)$$

$$\longrightarrow H_2 + S^+ + 2Ar \quad (14b)$$

To understand this feature (1) more detailed information about the Ar_2^+ ion, and (2) consideration of the kinetics of charge-transfer processes is required. Here we shall consider Ar_2^+ recombination energy and later on with the kinetics of charge transfer.

So, a well depth of the Ar_2^+ ion has been calculated[28] as $\epsilon = 1.25$ eV, being consistent with the data on rainbow scattering for $Ar^+ + Ar$.

This allows $RE(Ar_2^+) = RE(Ar^+) - \epsilon = 15.76 - 1.25 = 14.51$ eV, below $AP(Ar_2^+)$ by 0.2 eV. Moreover, R_2 vacuum-ultraviolet fluorescence data[29] show that the equilibrium distance of the lowest bonding states ($^{1,3}\Sigma_u^+$) of R_2 is shorter than that of the $^1\Sigma_g^+$ ground state and transition from the lowest vibrational levels of $^{1,3}\Sigma_u^+$ states occurs in the repulsive part of the $^1\Sigma_g^+$ ground state potential. This lowers the transitions energy by several tenths of an electron volt in the case of Xe_2. The equilibrium radius in R_2^+ is even smaller than in $R_2(^{1,3}\Sigma_u^+)$ (in the case of Xe 3.1[28] and 3.4,[29] respectively). It forces us to suppose that the actual electronic energy released in the Franck–Condon (FC) transition during the charge transfer is less by at least several tenths of electron volt (for Xe more than 0.3 eV) than that calculated from $RE(R^+)$ and the well depth of the molecular ion, R_2^+. This means that the actual value of RE is below ca. 14.0 eV for Ar_2^+. It is less than $AP(SH^+)$ but yet more than that of the S^+ ion. Taking[28] $\epsilon = 1$ eV for Kr_2^+ and Xe_2^+, $RE(Kr^+) = 14.0$ eV, $RE(Xe^+) = 12.1$ eV,[14] and the height of the repulsive part of the ground state potential corresponding an FC transition of 0.3 eV, we can obtain $RE(Kr_2^+) = 12.7$ eV and $RE(Xe_2^+) = 10.8$ eV. Both values lie below[27] the AP of HS^+ and S^+ ions.

Hydrogen Sulfide–Krypton Mixture. In the krypton-containing mixture two states of the Kr^+ ion are formed, $^2P_{3/2}$

(RE = 14.00 eV) and $^2P_{1/2}$ (RE = 14.67 eV)[14] with relative abundances[30] 0.67 and 0.33, respectively, both of them being energetically able to cause a dissociative charge transfer to hydrogen sulfide. However, it has been noted that S^+ ions and molecular hydrogen are not produced in the hydrogen sulfide–krypton mixture. This is not an unusual result because there are known energetic ranges ("gaps") where the probability of the charge transfer is relatively low.[30] This seems to be connected with the postulate that high vibrational excitation in the charge transfer reactions has relatively low cross section.[31] It appears to be the case for the charge transfer resulting in the formation of an H–H bond in reactions of the type 1b.

This problem was considered in detail in the recent study of Laudenslager, Huntress, and Bowers.[32] They have shown that for the thermal energy charge transfer reaction to be fast, an energy resonance should exist with a level of the molecular ion that has a large FC factor connecting it with the ground state neutral molecule. They have also pointed out that photoelectron peaks may be considered as experimental FC factors.

There are a number of papers dealing with photoelectron spectra of hydrogen sulfide.[31-38] Figure 5 shows the photoelectron spectrum (HeI 584-Å radiation) of hydrogen sulfide from ref 34. From this, it is seen that in the range 14.0–14.7 eV there is a low probability of the formation of both $^2A_1$ and $^2B_2$ states, the vertical IP of the first being 13.4 eV and second 15.5 eV. Thus, only ions having RE in the vicinity of these values should be expected to have a large cross section of charge transfer to hydrogen sulfide with formation of $^2A_1$ or $^2B_2$ states of H_2S^+. Of the rare gas ions of interest (RE in parentheses) $Ar^+(^2P_{1/2}$ 15.9 eV, $^2P_{3/2}$ 15.7 eV), Ar_2^+ (ca. 14.0 eV), $Kr^+(^2P_{1/2}$ 14.7 eV, $^2P_{3/2}$ 14.0 eV), Kr_2^+ (12.8 eV), $Xe^+(^2P_{1/2}$ 13.5 eV, $^2P_{3/2}$ 12.1 eV), Xe_2^+ (10.8 eV), only Ar^+ and $Xe^+(^2P_{1/2})$ have appropriate RE's. However, Fiquet-Fayard and Guyon[27] have shown that none of the $^2A_1$ and $^2B_2$ states of the molecular ion H_2S^+ can be correlated directly with ground state fragments ($S^+ + H_2$ or $SH^+ + H$). They considered potential surfaces and claimed that fragmentation involves predissociation through a quartet, ^4A, state. This is in good agreement with the work of Dibeler and Liston[39] on photoionization efficiency. From their data it follows that the probability of S^+ ion formation becomes different from zero at a photon energy of 13.36 eV but is very small and reaches its maximum value (still much smaller that that for H_2S^+ formation) at 14.2 eV. The HS^+ ion appears at 14.3 eV with a low intensity up to 14.7 eV and a maximum intensity at 16 eV.

Thus, we may conclude that of the listed rare gas ions the only one which can cause a destruction of the H_2S molecule in a charge-transfer process is the $Ar^+(^2P_{1/2}$ and $^2P_{3/2})$ ion. The Ar_2^+ ion is expected to form $H_2S^+(^2A_1)$ without noticeable predissociation; the $Kr^+(^2P_{1/2}, ^2P_{3/2})$ ion apparently reacts with krypton with formation of Kr_2^+ rather than with hydrogen sulfide; the Kr_2^+ and $Xe^+(^2P_{1/2})$ ions give the $H_2S^+(^2A_1)$ ion without predissociation and Kr_2^+, $Xe^+(^2P_{3/2})$ and Xe_2^+ ions produce the H_2S^+ ion in its ground $^2B_1$ state.

Thus, it seems that in the case of krypton we may propose that the sole process in the mechanism of hydrogen formation is an excitation transfer from $Kr(^3P_{2,0})$ metastables to hydrogen sulfide molecule. Energy levels of these states are 9.91 and 10.56 eV.[14]

Owing to a slight excess of energy of $^3P_0$ state compared to $AP(H_2S^+)$ = 10.4 eV the Jesse effect may be expected to play a minor role in this mixture. However, because of the high excess energy available (9.91 eV vs. D(H–SH) = 3.7 eV) a high degree of destruction of the H_2S molecule should be expected. Thus, reaction 9a is rather improbable. It is also improbable from the energy balance. In fact, if reaction 9a were operating, then $G(Kr^*)$ should equal a plateau value of $G(H_2)$ = 5.7. Taking $G(Kr^+)$ = 4.2, abundances of $^2P_{1/2}$ and $^2P_{3/2}$ 0.33 and 0.67, respectively,[30] $G(Kr^*)$ = 5.7, and a mean energy of the ^3P state 10 eV, we obtain an energy required for their formation of 117 eV, a value much more than 100 eV, even without taking into account energy taken by subexcitation electrons. Thus, reaction 9b seems to be a main process of energy transfer from atomic krypton to hydrogen sulfide. Figure 6 shows Stern–Volmer-like plots for the competition between processes 9b and 8 followed by 10a (upper curve) as well as processes 9b and 8 followed by 10b (lower curve).

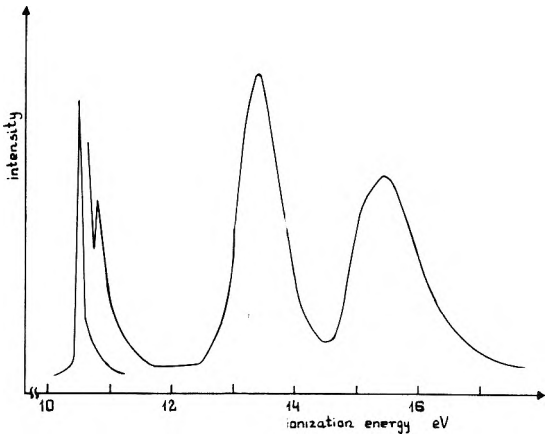

Figure 5. A photoelectron spectrum of hydrogen sulfide[34] (HeI 58.4-nm radiation).

Unfortunately, a scattering of our results does not allow us to make a choice between two mechanism (probably both of them are partially operating). Nevertheless for each case a constant ratio can be calculated. It is equal respectively to $k_8/k_{9b} = 2.2 \times 10^{-23}$ cm^3 (reaction 10a assumed) and 6×10^{-23} cm^6 s^{-1} (reaction 10b assumed). Taking $k_8 = 4 \times 10^{-32}$ cm^6 s^{-1} one obtains $k_{9b} = 0.6 \times 10^{-9}$ and 1.5×10^{-9} cm^3 s^{-1}. Both values are in the range of measured excitation transfer rate constants for $Ar(^3P_2)$ and $Xe(^3P_2)$ atoms.[24,40]

Hydrogen Sulfide–Xenon Mixture. Xenon has a recombination energy of the $Xe^+(^2P_{3/2})$ state of RE = 12.13 eV and the $^2P_{1/2}$ state of RE = 13.44 eV.[14,40] The first value is below appearance potential of the S^+ ion $AP(S^+)$ = 13.40 eV and $AP(SH^+)$ = 14.27 eV,[27,34,39] the second one below $AP(SH^+)$ and just equal to $AP(S^+)$. The higher $^2P_{1/2}$ state is rather slowly converted into the ground $^2P_{3/2}$ state. Hence, energetically reaction 1b could occur. However, it was mentioned above that (1) it is improbable from the view of FC transitions and, (2) molecular hydrogen and S^+ ion are not formed in the primary processes of the xenon-sensitized radiolysis of hydrogen sulfide.[21] Additionally, relative abundances of the $^2P_{1/2}$ and $^2P_{3/2}$ states are known to be 0.33 and 0.67, respectively,[30] and the expected maximum decrease caused by reaction 1b was $\Delta G(H_2) = (1/3)G(Xe^+) = (1/3)(4.6) = 1.5$. This is much less than the lowering in $G(H_2)$ observed in Figure 3.

Thus, excitation transfer from xenon to hydrogen sulfide, reactions 9 and 10, should be taken as responsible for hydrogen formation. Because reactions 9c and 10c have been eliminated, the lowering in $G(H_2)$ can be accounted for if any one of three following sets of reactions are operating: (1) reaction 9a competing with (8) followed by (10a); (2) reaction 9b competing with (8) followed by (10a); and (3) reaction 9b

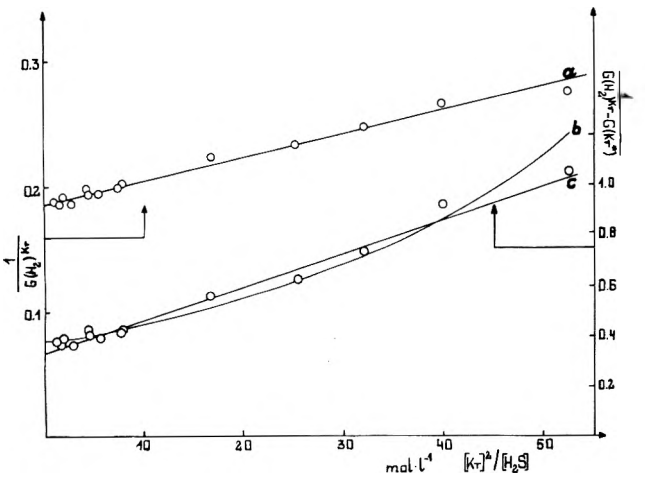

Figure 6. A Stern–Volmer-like plot for a hydrogen sulfide–krypton mixture: (upper points) competition of processes 9b and 8 followed by 10a; (lower points) competition of processes 9b and 8 followed by 10b. Curve b is the upper line a when transformed to the right-hand ordinate.

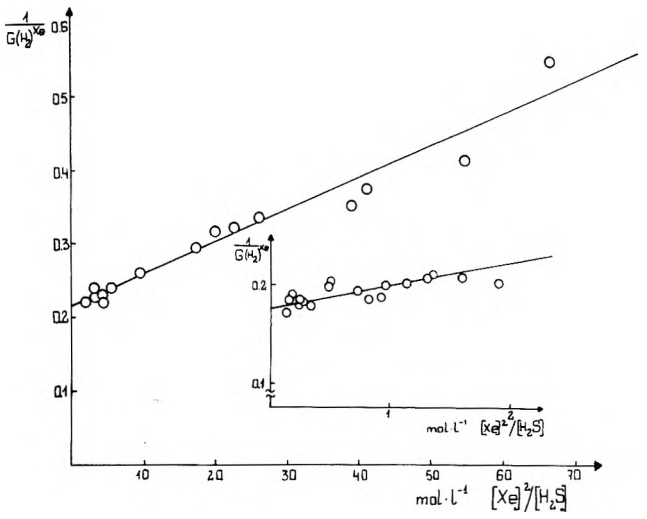

Figure 7. A Stern–Volmer-like plot for a hydrogen sulfide–xenon mixture.

competing with (8) followed by (10b). Sets 1 and 2 are kinetically identical. The first mechanism implies $G(Xe^*) = G(H_2)_{plateau} = 5.5$, the second one $G(Xe^*) = 0.5G(H_2)_{plateau} = 2.8$.

The value 5.5/100 eV is rather improbable from the energetic view. If we take the mean excitation energy of Xe equal ca. 9 eV, $G(Xe^+) = 4.6$,[14] $AP(Xe^+ {}^2P_{3/2}) = 12.1$, and $AP(Xe^+ {}^2P_{1/2}) = 13.5$ eV then we obtain the energy required equal to 106 eV, more than 100 eV. So it is improbable that mechanism 1 is the only one operating. However, it may not be fully excluded, because previous experiments in our laboratory[5] have shown that at least a fraction of the hydrogen atoms formed in the radiolysis of a xenon–hydrogen sulfide mixture has kinetic energies higher than 1 eV.

Mechanism 3 requires the lowest value of $G(H_2)$ to be equal $0.5G(H_2)_{plateau} = 2.8$. Our experimental value is 1.8; on this basis mechanism 3 may be excluded.

Steady-state approximation for mechanism 1 or 2 gives

$$\frac{1}{G(H_2)^{Xe}} = \frac{1}{G(Xe^*)}\left(1 + \frac{k_8[Xe]^2}{k_{9a,b}[H_2S]}\right) \qquad \text{(IV)}$$

It is seen from Figure 7 that experimental data fit eq IV rather well. The rate constant ratio $k_8/k_{9a,b}$ evolved from the intercept and slope of the straight line in Figure 7 is equal 3.3×10^{-23} cm^3. Taking[10] $k_8 = 9 \times 10^{-32}$ cm^6 s^{-1} one obtains $k_{9a,b}{}^{Xe} = 2.7 \times 10^{-9}$ cm^3 s^{-1}. This value is comparable to that for Ar ($k_{12} = 8 \times 10^{-10}$ cm^3 s^{-1})[24] as well as to the rate constants of excitation transfer from xenon to other small molecules which are as a rule somewhat larger than the corresponding values for argon,[40] keeping in mind that the value of k_8 used is the only one available as yet.

The proposed mechanism of the excitation transfer from the rare gas to hydrogen sulfide involves the supposition that the Xe_2 molecule in excited $^{1,3}\Sigma_u^+$ states does not decompose the hydrogen sulfide molecule (reaction 9a). It implies that either the $Xe_2(^{1,3}\Sigma_u^+)$ molecule transfers the excitation without decomposition of the H_2S molecule, or it radiates without absorption of radiation by H_2S molecule. The rate constants of the unimolecular relaxation

$$R_2(^{3,1}\Sigma_u^+) \longrightarrow 2R + h\nu \qquad (18)$$

are 0.3×10^6, 3×10^6, and 2×10^7 s^{-1} for Ar_2, Kr_2, and Xe_2 molecules, respectively.[41,42] The rate constant of the collisional deactivation of R_2, k_{10}, is not known, but for estimation purposes it may be supposed similar to k_9 and taken as 1×10^{-9} cm^3 s^{-1}. If so, reaction rate ratios v_{18}/v_{10} at the highest point of the H_2S concentration range where a sharp decrease in $G(H_2)$ (Figures 1–3) is observed (0.3 mol % of H_2S at 500 Torr overall pressure) are 0.4, 0.06, and 0.006 for Xe_2, Kr_2, and Ar_2, respectively; and those at lowest point of $G(H_2)$ measured (0.1 mol %, 300 Torr) are 2, 0.3, and 0.03. Thus, the rate of unimolecular spontaneous decay (18) is negligibly small compared to that of collisional decomposition (10) in the entire range for Ar (0.006–0.03), is small for Kr (0.06–0.3), and is significant for Xe (0.4–2).

The energy of the Xe_2 radiation at maximum intensity is 7.7 eV,[29] enough for reaction 10b to occur. The pressure of H_2S corresponding to 0.5–0.1 mol % of H_2S at 500 Torr overall pressure is equal 2.5–0.5 Torr and the mean path to the wall of the vessel is 1–2 cm. It seems that emitted light may not be entirely absorbed by H_2S under these conditions.

Concluding, the excitation transfer from R_2^* molecules to H_2S should be expected to occur mainly via a collisional mechanism in the case of argon and krypton. In the xenon-containing mixture spontaneous decay of the Xe_2 molecule without decomposition of the hydrogen sulfide molecule seems possible.

Conclusions

The foregoing discussion emphasizes the complexity of energy transfer processes from the rare gas ions and excited atoms and/or molecules to the molecule even when the latter is a simple one like hydrogen sulfide. Nevertheless, if the FC rule requirement is involved and correct RE's of rare gas molecular ions are taken the experimental results are consistent with the supposition that hydrogen and obviously sulfur is produced both in charge- and excitation-transfer processes in the H_2S–Ar mixture, and in the excitation-transfer processes alone in the H_2S–Xe and H_2S–Kr mixtures. Rate constants of charge and excitation transfer evolved from present experimental data using the proposed mechanism are quite consistent with other available data. Thus, our evidence strongly supports the relevance of the FC rule for the kinetics of charge-transfer reactions as proposed by Laudenslager, Huntress, and Bowers.[32]

The recombination energy of the rare gas molecular ions is estimated to be equal to or less than 14.0, 12.7, and 10.8 eV for the Ar_2^+, Kr_2^+, and Xe_2^+ ions, respectively.

Excitation transfer appears to be the sole process of the $^3P_{2,0}$ state decay in argon in the range of H_2S concentrations covered, and to be in competition with the $Xe_2^*(^{3,1}\Sigma_u^+)$ and $Kr_2^*(^{3,1}\Sigma_u^+)$ molecular formation in other mixtures. The Kr_2^* molecule is expected to transfer the excitation energy via a collisional mechanism with at least partial destruction of hydrogen sulfide. The Xe_2^* is believed to decompose most likely by spontaneous radiative decay, the radiation not being absorbed by hydrogen sulfide in the concentration range corresponding to the observed decrease in $G(H_2)^{Xe}$.

Acknowledgment. The authors are greatly indebted to Professor A. Suszko-Purzycka for her interest in this work.

References and Notes

(1) K. Jezierska, *Nukleonika*, **16**, 213 (1971).
(2) K. Jezierska and M. Foryś, *Nukleonika*, **17**, 23 (1973).
(3) M. Ahmad, D. W. Huyton, and T. W. Woodward, *J. Chem. Soc., Faraday Trans. 1*, **68**, 1857 (1972).
(4) K. Jezierska and M. Foryś, *Nukleonika*, **17**, 451 (1972).
(5) M. Foryś, *Radiat. Effects*, **25**, 111 (1975).
(6) D. Perner and Th. Franken, *Ber. Bunsenges. Phys. Chem.*, **73**, 897 (1969).
(7) A. Jówko, I. Szamrej, and M. Foryś, *Radiochem. Radioanal. Lett.*, **15**, 353 (1973).
(8) I. Szamrej, A. Jówko, and M. Foryś, *Radiat. Effects*, **25**, 191 (1975).
(9) M. Foryś and K. Wojciechowski, *Radiochem. Radioanal. Lett.*, **10**, 277 (1972).
(10) D. W. Huyton and T. W. Woodward, *Radiat. Res. Rev.*, **2**, 205 (1970).
(11) For their dosimetry see footnote 2 in C. Willis, A. W. Boyd, and O. A. Miller, *Can. J. Chem.*, **49**, 1677 (1971).
(12) B. Ö. Jonsson and I. Lind, *J. Chem. Soc., Faraday Trans. 2*, **70**, 1399 (1974).
(13) P. M. Becker and F. W. Lampe, *J. Chem. Phys.*, **42**, 3857 (1965).
(14) B. Brocklehurst, *Radiat. Res. Rev.*, **1**, 223 (1968).
(15) E. Ellis and N. D. Twiddy, *J. Phys. B*, **2**, 1366 (1969).
(16) L. G. Piper, W. C. Richardson, G. W. Taylor, and D. W. Setser, *Discuss. Faraday Soc.*, **53**, 100 (1972).
(17) J. Le Calvé and M. Bourène, *J. Chem. Phys.*, **58**, 1446 (1973); see also other values for Ar in this reference.
(18) (a) K. H. Ludlum, L. P. Larson, and J. M. Caffrey, *J. Chem. Phys.*, **46**, 127 (1967); (b) A. V. Phelps, *Phys. Rev.*, **114**, 1011 (1959).
(19) (a) V. Čermak, *J. Chem. Phys.*, **44**, 1318 (1966); (b) D. S. Smith and R. Turner, *Can. J. Phys.*, **41**, 1949 (1963).
(20) P. R. Timpson and J. M. Anderson, *Can. J. Phys.*, **48**, 1817 (1970).
(21) A. Jówko, I. Szamrej, and M. Foryś, *J. Phys. Chem.*, submitted for publication.
(22) H. Hotop and A. Niehaus, *Z. Phys.*, **215**, 395 (1968).
(23) M. Foryś and E. Midgal, *Khim. Vys. Energ.*, **5**, 228 (1971).
(24) M. Bourène and J. Le Calvé, *J. Chem. Phys.*, **58**, 1452 (1973).
(25) W. F. Liu and D. C. Conway, *J. Chem. Phys.*, **60**, 784 (1974); D. Hyatt and P. F. Knewstubb, *J. Chem. Soc., Faraday Trans. 2*, **68**, 202 (1972).
(26) (a) J. K. Kim and W. T. Huntress, Jr., *Int. J. Mass Spectrom. Ion Phys.*, **16**, 451 (1975). (b) It is noteworthy here that the rate constant ratio $k_{12}/k_{He^+ + H_2S} = 0.4$ is equal to that for $k_{Ar^+ + H_2O}/k_{He^+ + H_2O}$ ($k_{He^+ + H_2O} = 4.4 \times 10^{-10}$ cm^3 s^{-1} [26a] and $k_{Ar^+ + H_2O} = 1.5 \times 10^{-10}$ cm^3 s^{-1} from W. Lindinger, *Phys. Rev. A*, **7**, 328 (1973)).
(27) F. Fiquet-Fayard and P. M. Guyon, *Mol. Phys.*, **11**, 17 (1966).
(28) D. C. Lorents, R. E. Olson, and G. M. Conklin, *Chem. Phys. Lett.*, **20**, 589 (1973).
(29) E. M. Fink and F. J. Comes, *Chem. Phys. Lett.*, **30**, 267 (1975).
(30) G. Sahlstrom and I. Szabo, *Ark. Fys.*, **38**, 145 (1968); E. Lindholm, I. Szabo, and P. Wilmenius, *ibid.*, **25**, 417 (1963); H. Sjörgen, *ibid.*, **29**, 565 (1965).
(31) D. L. Smith and L. Kevan, *J. Am. Chem. Soc.*, **93**, 2113 (1971).
(32) J. B. Laudenslager, W. T. Huntress, Jr., and M. T. Bowers, *J. Chem. Phys.*, **61**, 4600 (1974).
(33) J. E. Collin, J. Delwiche, and P. Natalis, "Electron Spectroscopy", D. A. Shirley, Ed., North Holland Publishing Co., Amsterdam, London, 1972.
(34) A. W. Potts and W. C. Price, *Proc. R. Soc. London, Ser. A*, **326**, 181 (1972).
(35) D. C. Frost, A. Katrib, C. A. McDowell, and R. A. N. McLean, *Int. J. Mass Spectrom Ion Phys.*, **7**, 485 (1971).
(36) S. Durmaz, G. H. King, and R. J. Suffolk, *Chem. Phys. Lett.*, **13**, 304 (1972).
(37) J. Delwiche, P. Natalis, and J. E. Collin, *Int. J. Mass Spectrom Ion Phys.*, **5**, 443 (1970).
(38) J. W. Rabalais, T. P. Debies, J. L. Berkosky, J-T. J. Huang, and F. O. Ellison, *J. Chem. Phys.*, **61**, 516 (1974).
(39) V. H. Dibeler and S. K. Liston, *J. Chem. Phys.*, **49**, 482 (1968).
(40) J. E. Velazco and D. W. Setzer, *Chem. Phys. Lett.*, **25**, 197 (1974).
(41) A. W. Johnson and J. B. Gerardo, *J. Chem. Phys.*, **59**, 1738 (1973).
(42) T. Oka, K. V. S. Rama Rao, J. L. Redpath, and R. F. Firestone, *J. Chem. Phys.*, **61**, 4740 (1974).

Mass Spectrometric Observation of Difluorocarbene and Its Reactions in Inhibited Methane Flames

Joan C. Biordi,* Charles P. Lazzara, and John F. Papp

Pittsburgh Mining and Safety Research Center, Bureau of Mines, U.S. Department of the Interior, Pittsburgh, Pennsylvania 15213
(Received November 14, 1975)

Publication costs assisted by the U.S. Bureau of Mines

Difluorocarbene has been identified in methane–oxygen–argon flames initially containing ≤1% CF_3Br and burning at 0.04 atm. Profiles of the concentration of this species (maximum 10^{14} molecules cm^{-3}) through the reaction zone of the flame have been determined, and from these, profiles of the net chemical reaction rates have been calculated. These data, combined with knowledge of the complete microstructure of the flames studied, suggest that CF_2 is formed in this flame principally by the reaction $CF_3 + H \rightarrow HF + CF_2$ (2), and $k_2 = 2 \times 10^{14}$ cm^3 mol^{-1} s^{-1} at 1540 K. The decay of CF_2 is via reactions with the major flame radicals, $CF_2 + (O, H, OH) \rightarrow$ products, with rate constants of the order of (1–5) $\times 10^{13}$ cm^3 mol^{-1} s^{-1}. The implication of these reactions for the mechanism of flame inhibition by fluorocarbons is discussed.

Introduction

The reactivity of difluorocarbene continues to be of interest in the field of carbene chemistry in general,[1] and it is of direct practical interest from the viewpoint of the mechanism of the high-temperature pyrolysis and oxidative degradation of fluorocarbons and fluorocarbon polymers.[2,3] The CF_2 radical has been produced by photolyses,[4–6] pyrolyses,[1,7,8] and by hot atom[9] and shock tube[2,10–15] techniques. It has been reported as a product of hydrocarbon–fluorine flames[16] and has been investigated spectroscopically using a matrix isolation technique.[17] The radical has been generated in or introduced into the ion source of mass spectrometers by several techniques, and its appearance potential is well established.[18–20] Spectrophotometric monitoring of CF_2 in flash photolyses and shock tube studies has provided the most direct determinations of rate constants for recombination of CF_2[4,5] and, recently, for reaction with O_2 at high temperature.[15] Rate data are also available for reaction between CF_2 and HX,[9] C_2F_4,[5,6] and CF_3H.[14] There have been little data reported on reactions of CF_2 with atomic and radical species;[21] it appears that such reactions are important in high-temperature C/F/O systems.[15]

We report here observations of difluorocarbene in low-pressure methane flames to which small amounts of CF_3Br have been added. Considerable information is available for radical and stable species composition profiles for these flames as well as aerodynamic and temperature profiles.[22] This information, together with the fact that the data permit a quantitatively meaningful kinetic analysis, leads to mechanisms for the formation and decay of CF_2 in the flame and to estimates of rate coefficients for reactions between difluorocarbene and the major flame radicals. The mechanism implies that H atom scavenging reactions by the fluorocarbon part of the CF_3Br molecule contribute to its observed effectiveness as a flame inhibitor.

Experimental Section

The apparatus used was constructed to study the chemical microstructure of low-pressure flat flames. The details of construction and its performance have been described,[22–26] so only a limited description will be given here.

Near stoichiometric methane–oxygen–argon flames and their analogues containing ≤1% CF_3Br are burned on a cooled, porous plug copper burner with a diameter of 10 cm. The pressure is maintained at 32 (±0.02) Torr. Under these conditions, the flame appears as a steady luminous disk about 3 mm thick and sitting about 2–3 mm above the surface of the burner. The burner can be moved vertically, and its distance from a fixed sampling cone can be measured precisely. This sampling cone, constructed from quartz, has an outside angle of about 38°, and the orifice at its tip has a diameter of 87 μ. It is fixed to a cooled flange, which forms the interface between the low-pressure flame housing and a differentially pumped two stage quadrupole mass spectrometer (Extranuclear Laboratories EMBA II).

As the flame gases expand into the low-pressure ($\sim 5 \times 10^{-5}$ Torr) region downstream of the orifice, their temperature drops rapidly, and chemical reactions are effectively quenched. The expansion, initially in the slip-transition flow regime, makes the transition to molecular flow upstream of a second cone, through which the central portion of the molecular beam is admitted to the mass spectrometer proper. The beam is modulated by a toothed chopper wheel upstream of the electron impact ionizer. An electron multiplier (14-stage Cu–Be or Channeltron) is used to detect the mass analyzed ions. Detection of signals in phase with a reference signal from the chopper wheel permits distinction between ions originating from molecules within the beam and those randomly scattered off surfaces in the mass spectrometer.

Temperature profiles were determined using fine wire (0.0025 cm) Pt/Pt–10% Rh thermocouples coated with silica to reduce catalytic reactions on the metal surface. Radiation corrections were calculated using the formulation by Kaskan;[27] the emissivity of the coated wire was measured to be 0.22 ± 0.02. Area expansion ratios, required for velocity profile calculations, were measured on unignited gas using hot wire anemometers calibrated in situ.[28]

The sampling system mass spectrometer is calibrated directly for the major stable species from mixtures of known composition passed through the burner without ignition, and otherwise sampled in exactly the same manner as with the flame. The procedures used to identify, calibrate for, or estimate the concentration of minor stable species are specified

elsewhere.[29] The procedure for estimating radical concentrations will be discussed presently.

Cylinder gases (Ar, O_2, CH_4, and CF_3Br) were of the highest purity available commercially; all had stated purities of 99.99% except CF_3Br (99%). The gases passed through Drierite and molecular sieve traps before entering the critical flow system, and their purities were checked periodically by mass spectrometric analyses.

The use of molecular beam sampling techniques allows the possibility of sampling atom and radical species, as well as highly reactive stable species, in addition to the normal flame gases. We routinely sample quantitatively species such as H, OH, CH_3, and O from flames, and others have successfully applied similar techniques to flames as well as a variety of dynamic sampling problems.[30-33] In flame-microstructure studies, species concentration, temperature, and gas velocity are determined along an axis, here called z, perpendicular to the flame front as a function of distance from a fixed reference point in the flame,[34] here taken to be the burner surface. Meaningful analyses of these profiles for rate data require either that the sampling probe presents acceptably small perturbation to the flame, or that quantitative corrections be made for the perturbation. In either case, it is necessary to demonstrate, by calculation or experiment, the perturbing effect of the probe. We have empirically characterized the molecular-beam probe used in this study[25] and have assessed the accuracy with which one might expect to determine rate constants for elementary reactions at flame temperatures using this sampling technique.[26] A properly constructed probe offers no visual perturbation to the flame and shows concentrations of species and temperature at a given point in the flame to be those characteristic of a position slightly upstream of the actual physical location of the probe tip.[34] For certain well-known flame reactions for which the radical concentrations can be determined to ±50% or better (e.g., $H + O_2 \rightarrow OH + O$) rate constants can be evaluated in good agreement with literature values measured in the same temperature range.[29] For other, less well-defined reactions, the limitations of accuracy for the rate constants are dominated by the lack of definition of the mechanism and the uncertainties in knowledge of the absolute radical concentrations involved.[26] The limitations specific to the reactions examined here will be noted as those reactions are discussed.

Identification of the CF_2 Radical

An unignited mixture of CH_4 (10.1%)–O_2 (21.2%)–Ar (67.6%)–CF_3Br (1.1%), passed through the burner and sampled in the usual fashion, gives no signal at 50 amu with an electron energy of 14.5 eV and other adjustable instrument parameters optimized for high sensitivity. When the flame is ignited without CF_3Br, no signal is observed at 50 amu, 14.5 eV, anywhere across the flame front. When CF_3Br is added to the flame, a signal is easily detected at mass 50. The variation of the intensity of the signal at mass 50 was measured as a function of distance from the burner surface using several electron energies. These profiles are shown in Figure 1. The 70-eV profile is typical of the CF_3Br decay profile[22] usually monitored at the base peak, 69 amu, and the intensity of the signal at mass 50 at 70 eV is everywhere directly proportional to that at mass 69. The CF_2^+ ion is a fragment ion in the normal electron impact spectrum of CF_3Br and at high electron energy dominates the profile of mass 50. At lower electron energy, the 50-amu profile has the character of an intermediate flame species, but with some contribution from CF_3Br close to the burner. Finally, at low enough electron energy, a

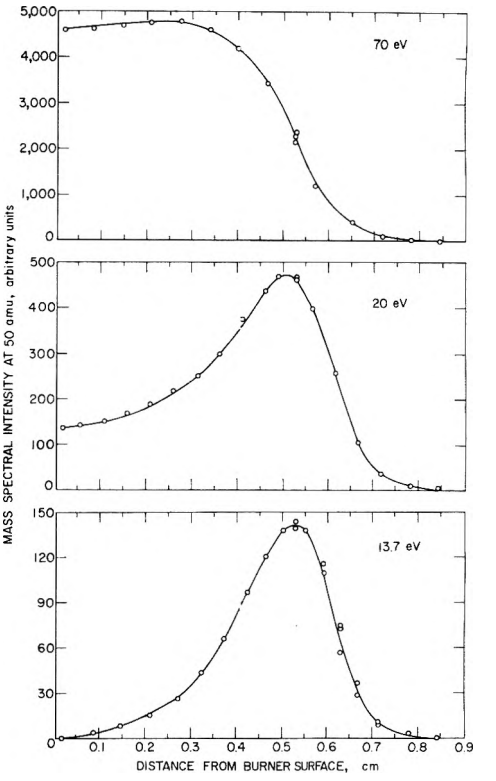

Figure 1. Profiles of the mass spectral intensity at 50 amu at various energies of the ionizing electrons. The initial composition of the flame gases was 10.1% CH_4–21.2% O_2–67.6% Ar–1.1% CF_3Br; pressure, 32 Torr; initial linear flow velocity, 48 cm s^{-1}.

profile is observed of a species initially absent from the reacting mixture, maximizing in the primary reaction zone, and decaying to zero. Thus, the signal at 50 amu at low electron energy is associated with the presence of CF_3Br in the flame, but does not arise from dissociative ionization of the inhibitor molecule. Similar results were obtained from a flame containing 0.3% CF_3Br.

To further characterize the source of the signal at 50 amu, a number of appearance potential measurements were made. The electron energy distribution in the high efficiency ion source of the mass spectrometer is broad relative to that of conventional ionizers, and it has been previously demonstrated[24] that the accuracy of appearance potential measurements using a simple linear extrapolation is about ±0.5 eV. This will also be apparent from the succeeding discussion. The argon constituent of the flames provides a convenient reference gas for calibration of the electron energy scale, and its ionization efficiency curve was determined simultaneously with that of the species in question.

An ionization-efficiency curve determined at $z \sim 0.5$ cm, where the maximum occurs in the profile, is shown in Figure 2. At this point in the flame, the appearance potential for the species observed at 50 amu was found to be 11.6 ± 0.2 eV, where the limits refer to the precision of the measurement. This is in good agreement with values expected for ionization of CF_2. The ionization potential for the CF_2 radical has been recently reported to be 11.5 eV,[20] and appearance potential measurements with conventional ion sources have yielded values of 11.7 eV.[18,19] The ionization efficiency curve of Figure 2 shows distinct structure, suggesting contributions to mass 50 from other sources above approximately 20 eV, presumably CF_2^+ from CF_3Br. To verify this, an ionization efficiency curve was determined for 50 amu at a point in the flame close to the

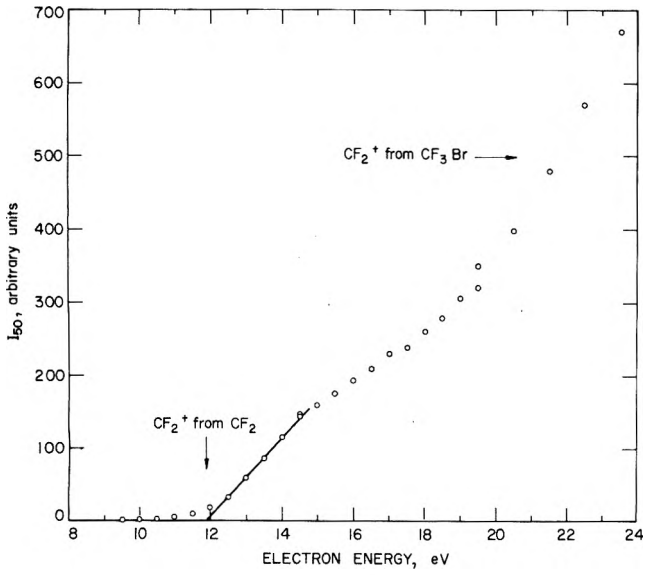

Figure 2. Ionization efficiency curve for 50 amu determined at $z \sim 0.5$ cm for the flame described in Figure 1.

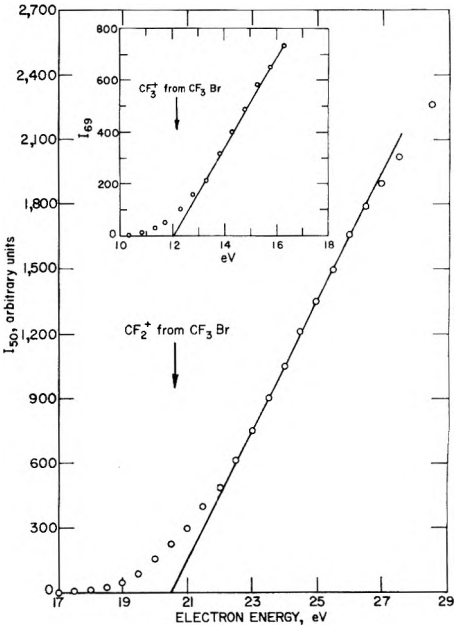

Figure 3. Ionization efficiency curve for 50 amu determined at $z \sim 0.06$ cm for the flame described in Figure 1. The insert shows an ionization efficiency curve for 69 amu determined near the $[CF_2]$ maximum.

burner surface, where the low electron volt profile data (Figure 1) indicate that $[CF_2] = 0$. This curve is shown in Figure 3. The low-energy contributor is clearly absent from the curve and the appearance potential measured is 20.5 eV, within the range of literature values quoted for formation of CF_2^+ from CF_3Br (18.3, 21.4 eV).[35] Shown as an insert in Figure 3 is an appearance potential measurement for 69 amu, CF_3^+, determined where the CF_2 is at a maximum. The value measured is 12.1 eV, compared with 12.1–12.5 eV reported for the formation of CF_3^+ from CF_3Br.[35]

In methane flames containing CF_3Br, several intermediate stable species associated with the inhibitor have been observed;[22] these species might be expected to make some contribution to the mass 50 peak at normal electron energies. It is necessary to examine the possibility that they might be responsible for or contribute to the low electron energy signal at 50 amu. The species in question are CH_2CF_2, F_2CO, and, if sufficient inhibitor is present, CF_3H. For the flames containing 1% CF_3Br initially, the maximum mole fractions observed (and the distance from the burner surface at which the maximum occurs) for these intermediates are 1.0×10^{-3} ($z = 0.52$ cm), 1.8×10^{-3} ($z = 0.68$ cm), and 6.5×10^{-5} ($z = 0.57$ cm), for CH_2CF_2, F_2CO, and CF_3H, respectively. Appearance potential measurements for CF_2^+ from these species have been reported only for CF_3H (14.7 eV, 20.2 eV),[35] and these are well outside the experimental error of the appearance potential measurements made here. Furthermore, the intensity at 51 amu, which is about seven times that of 50 in the "pattern" of CF_3H,[36] is zero everywhere across the flame front under the measurement conditions of the CF_2 profile. Therefore, no contribution is made by CF_3H to the signal at 50 amu at 14.5 eV.

Appearance potentials for CF_2^+ from CH_2CF_2 and F_2CO can be estimated from enthalpy of formation data. For CH_2CF_2, $AP(CF_2^+, CH_2CF_2) = \Delta H°_f(CF_2^+) + \Delta H°_f(CH_2) - \Delta H°_f(CH_2CF_2)$. Using the values recommended by Lifshitz and Long[37] for the enthalpies of formation, $AP(CF_2^+, CH_2CF_2)$ is about 17.5 eV compared with 11.6 eV observed.

The CF_2^+ ion is a very minor species in the fragmentation of excited $CH_2CF_2^+$ ion[38] and, in fact, is not reported at all in standard compilations of mass spectral data.[36] Using the patterns reported by Lifshitz and Long, and taking into account the discrimination of our mass filter over the range 50–64 amu, we estimate that the contribution to 50 amu from CH_2CF_2 *at 70 eV* is less than one-third the signal actually observed at 14.5 eV, and is bound to be negligible at the lower electron energy.

Finally, one can calculate the appearance potential for CF_2^+ from F_2CO to be 19.3 eV when $\Delta H°_f$ for O and F_2CO are taken from Benson.[39] The CF_2^+ ion is also reported to be a very minor species in the F_2CO mass spectrum.[36] However, in this case, the profiles for mass 50 and for mass 47 or 66 (i.e., F_2CO) are sufficiently different that it is clear by inspection alone that they do derive from the same species in the flame. The F_2CO profile reaches a maximum around $z = 0.7$, well downstream of that for 50 amu; the maximum is broad and the decay is slow, so that the profile has a long tail on the downstream side, reaching zero at $z \sim 2$ cm. All of these characteristics are in contrast to the profile shown in Figure 4.

In summary, the appearance-potential measurements, together with a consideration of the profiles and nature of other possible interfering species, lead to the conclusion that the species observed at low electron energy at 50 amu is the CF_2 radical. As will be shown later, the absolute concentration of this radical in this system is low, about two orders of magnitude lower than in the shock tube[10] and photolytic[4] studies, where the radical was monitored via its optical absorption. Optical detection of CF_2 in flames might be possible under certain optimum conditions, but for our system it would require instrumentation sufficiently stable and sensitive to detect a 0.5% attentuation.

Estimation of Concentration of CF_2

The concentration of CF_2 can be estimated using a technique that has been applied previously to the major flame radicals.[24] It is assumed that the ionization cross sections for the species in question and another chemically similar species have the same ratio at equivalent energies above their appearance potentials as they have at 70 eV. With a knowledge of those cross sections and by measuring the relative intensi-

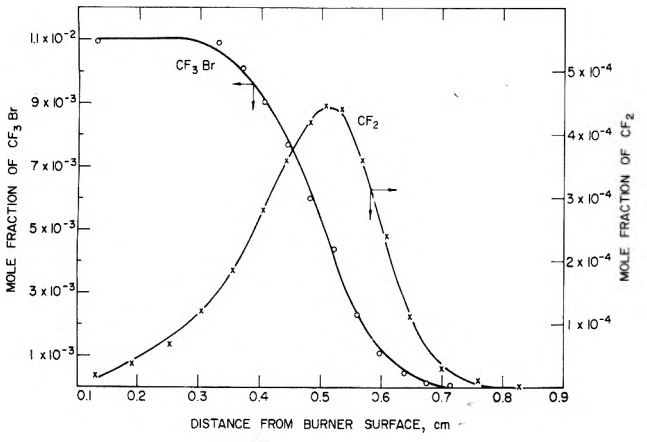

Figure 4. Concentration profile for CF_2 and CF_3Br. The flame is that described for Figure 1.

ties at the appropriate electron energies, the relative concentrations can be calculated. In this case, we chose CO_2 for comparison with CF_2. This may not be an optimum choice from the viewpoint of similar chemistries (although it is not as bad as it might, at first, appear because of the remarkably low reactivity of the radical[4]), but an equally critical requirement in this quadrupole system is that ions with nearly the same mass are compared. There is the additional advantage to using CO_2 that the required total ionization cross section for CO_2, Q_{CO_2}, has been measured directly. The cross section for CF_2 must be estimated. A simple additivity calculation using Mann's[41] atomic cross sections gives a value of 4.82×10^{-16} cm^2 (based on 70 eV and $Q_{Ar} = 3.62 \times 10^{-16}$ cm^2). However, Beran and Kevan have found that perfluorocarbons generally have measured ionization cross sections less than additivity calculations predict. Using their empirical correlation, eq III, a value of 3.39×10^{-16} cm^2 is calculated for Q_{CF_2}, and is taken to be the better approximation. Then

$$X_{CF_2} \sim X_{CO_2} \frac{Q_{CO_2}(70\text{ eV})}{Q_{CF_2}(70\text{ eV})} \frac{I_{50}(E^\circ + b)}{I_{44}(E^\circ + b)}$$

where X denotes mole fraction; E°, the appearance potential; and b, a constant. The mole fraction of CO_2 is known from calibration, and (I_{50}/I_{44}) was measured to be 0.017 ± 0.001 at the maximum of the CF_2 profile. This gives $X_{CF_2}(\text{max}) \sim 4.5 \times 10^{-4}$ in the 1% CF_3Br containing flame. This value is used, together with argon as an internal standard, to generate a concentration profile from the intensity profiles. It is difficult to accurately estimate the uncertainty in this value but, considering the various assumptions made, a factor of 2 would be appropriate. Figure 4 shows the concentration profile for CF_2 in the 1% flame together with that of CF_3Br for orientation purposes.

The maximum X_{CF_2} in the flame containing 0.3% CF_3Br was estimated by comparing intensities at 50 amu directly with that of the 1% flame, both measured under the same conditions. The maximum CF_2 mole fraction in this flame was 1.6×10^{-4}.

Kinetic Analyses

In order to obtain rate data from a profile such as that shown in Figure 4, it is necessary to take into account the fact that in a system with concentration and temperature gradients as large as in the flame, mass and thermal diffusion contribute importantly to the observed concentration at a point. The net chemical reaction rate, K_i, of a flame species can be determined by evaluation of the following equation:

$$K_i(z) = \frac{\rho_0 v_0}{A(z)M_i} \frac{dG_i(z)}{dz}$$

where

$$G_i(z) = \frac{M_i}{\sum_i X_i M_i}\left[X_i(z) - \frac{D_{i-Ar}}{v(z)}\left(\frac{dX_i(z)}{dz} + \frac{k_{T_i}}{T(z)}\frac{dT(z)}{dz}\right)\right]$$

In these equations, ρ is the mean density; v, the bulk flow velocity; A, the area expansion ratio; M, the molecular weight; X, the mole fraction; T, the temperature; D, a binary diffusion coefficient; and k_T, the thermal diffusion ratio. The subscript i associates the quantity with the species i, and subscript 0 refers to unburnt gas conditions. The development of these equations from physical modeling of the flame may be found in standard reference books,[34,43] the specific computational techniques used to analyze profiles from low-pressure flames have been documented,[44] and some results for reaction rate coefficients are also available.[22,26] We apply the techniques here to the CF_2 radical and use the derived information to construct a mechanism for the formation and decay of CF_2 in the flame and to estimate rate coefficients for some of the reactions involved. D_{CF_2-Ar} and $k_{T(CF_2)}$ were evaluated using the Lennard-Jones potential with the parameters suggested by Svehla.[45] The net reaction rate for CF_2 calculated in the flame containing 1% CF_3Br is shown as a function of distance from the burner surface in Figure 5. The same quantity for CF_3Br is also shown.

It has been found that in stoichiometric flames containing 0.3% CF_3Br,[22] the reaction responsible for 90% of the disappearance of the inhibitor is

$$CF_3Br + H \rightarrow HBr + CF_3 \quad (1)$$

We have been unable to detect unambiguously the CF_3 radical in these or the 1% CF_3Br containing flames. The CF_2 radical is readily detectable in both cases, however; this, together with the fact that in the 0.3% flame, no species is observed containing the CF_3 group intact, leads to the conclusion that the CF_3 radical is rapidly destroyed. It seems reasonable to suppose that CF_2 is a product of this destruction and, further, that it is the principal source of CF_2 in the early part of the flame. Of all of the reactions that can be written forming CF_2 from CF_3 in this system (including those with CH_4, OH, O, Br, and HO_2), only

$$CF_3 + H \rightarrow HF + CF_2 + 40.5\text{ kcal mol}^{-1} \quad (2)$$

is exothermic and therefore may be fast. Since H atoms diffuse rapidly into the low-temperature region of the flame and since H is the dominant radical in these flames, reaction 2 is probably the most important source of CF_2. Two other reactions could conceivably contribute to the formation of CF_2:

$$CF_3H \rightarrow HF + CF_2 \quad (3)$$

and

$$CH_2CF_2 + O \rightarrow H_2CO + CF_2 \quad (4)$$

Small amounts of CF_3H were observed in the 1% CF_3Br containing flames. However, reaction 3 is unlikely to be anywhere near its high-pressure limit under the conditions of the flame;[14] therefore, the use of the reported rate coefficient[14] for (3) will overestimate its importance in this system. In fact, we can estimate the rate constant for (3) in our system from the minimum value of K_{CF_3H}, where reactions forming CF_3H can be considered negligible. The rate constant so calculated is six times less than that expected from the literature value.

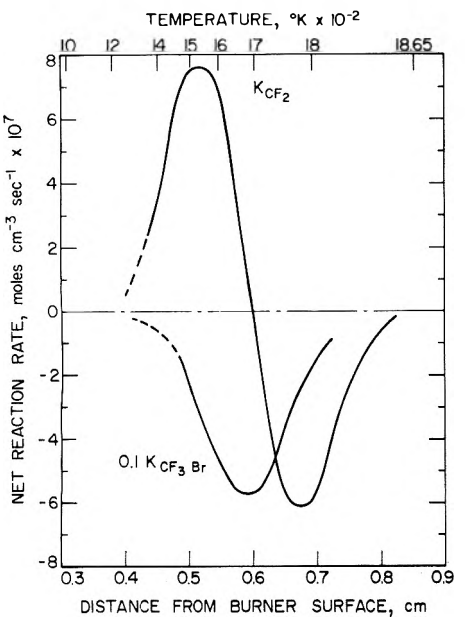

Figure 5. The net chemical reaction rate profiles for CF_2 and CF_3Br determined from analyses of the profiles shown in Figure 4.

Reaction 4 is assumed to occur with a rate coefficient equal to that of the parallel reaction giving $F_2CO + CH_2$ as product; this coefficient has been estimated at flame temperature from previous studies.[22] Using these rate coefficients and the measured reactant concentrations and temperatures, it is found that reaction 3 could account for 4% and reaction 4 for 19% of the observed maximum net formation rate of CF_2. Thus, reaction 2 accounts for >75% of the CF_2 formation.

If the concentration of CF_3 can be determined, then an estimate for the rate coefficient of reaction 1 can be made. The observation of CF_3H in the 1% CF_3Br containing flame provides a means of determining $[CF_3]$ if the reactions of CF_3H can be properly evaluated. CF_3H is formed by H atom abstraction reactions between the CF_3 radical and species such as H_2, CH_4, H_2O, and HBr in the flame. Rate constants for all these abstraction reactions except H_2O are available.[46,47] We take the rate constant for the analogous reaction with H_2S[47] as a reasonable approximation to that with H_2O. A direct recombination of CF_3 with H has also been postulated as a formation route in these systems.[48] The consumption of CF_3H is most likely via reaction with H atom since the decay occurs relatively early in the flame, where the concentration of that atom is large relative to O, OH, and HO_2. A rate coefficient for this reaction was calculated by Skinner and Ringrose.[49,56] Reaction 3 also contributes to the net rate of reaction of CF_3H. Assuming these seven are the only important reactions involving CF_3H in the flame, and with a knowledge of the net reaction rate of CF_3H calculated from the profile data, X_{CF_3} can be estimated. Its maximum value was found to be 3×10^{-5} at $z \sim 0.5$ cm. The value changes by about a factor of 2 for an order of magnitude change in the rate coefficient for either the recombination reaction, $CF_3 + H \rightarrow CF_3H$, or the abstraction reaction with water, $CF_3 + H_2O \rightarrow CF_3H + OH$, the two reactions that are the least well defined. Based on our maximum sensitivity for radicals species in general[24] and on the fact that, to avoid interference from CF_3Br, it is necessary to work at electron energies only a few tenths of an electron volt above the appearance potential for CF_3^+ from CF_3 in the search for this radical, it is not surprising that we were unable to detect CF_3, even in the flame containing 1% CF_3Br.

Using the calculated X_{CF_3}, we evaluate the rate coefficient, k_2, of reaction 2 at the point of maximum net formation of CF_2 to be 2×10^{14} cm^3 mol^{-1} s^{-1} at 1540 K. For this calculation, all of the uncertainty in the determination of X_{CF_2}, K_{CF_2}, and X_{CF_3} propagate into k_2, so that this number is good only to within an order of magnitude. Since the calculated value corresponds to the reaction occurring about every tenth gas kinetic collision, it probably errs on the high side.

The decay of CF_2 in the flame can proceed by several routes. We have considered the possibility of CF_2 reacting with all the major and minor observed constituents of the flame, and the results of these considerations are summarized in Table I. The table is divided into three parts, and each will be discussed in turn. Part A lists those reactions that are primarily responsible for the consumption of CF_2 in the flame. These reactions are all thermodynamically favorable and although there is no quantitative information available regarding their rates, there is qualitative evidence that they can be fast. Bauer et al.[2] in their shock tube studies of the oxidation of perfluoroethylene suggest that reaction 7 has a rate constant very much larger than that for the reaction of CF_2 and molecular oxygen, reaction 11. Other shock-tube studies of the C_2F_4–O_2 system have led to similar conclusions, but favor reaction 6[10] or reaction 8[15] as the dominant reaction path for $CF_2 + O$. Reactions of CF_2 with H and OH have not been characterized, but must be considered here since H and OH concentrations are appreciable (actually greater than [O] everywhere in the flame) and, sterically, reaction with H should be more favorable than with O. It is not possible to distinguish among reactions 5–10 because they do not lead to unique products in this system. At the point in the flame where CF_2 is disappearing rapidly, there are parallel reactions forming HF, F_2CO, and CO.[22]

Part B of Table I lists reactions that could occur but can be shown quantitatively to be unimportant. For each of the reactions shown, some rate constant data are available, and are found in the references cited. This data, together with the measured concentrations of the reactants, permit calculation of the rate of disappearance of CF_2 in the flame by the reaction in question. The calculated rate may be compared with the observed rate of disappearance of CF_2. None of the reactions 11–17 can account for as much as 1% of the observed decay rate and usually not even 0.1%. For example, the most important of these, reaction 12, has a rate constant of 1.1×10^{10} cm^3 mol^{-1} s^{-1} $\sim$ 1800 K,[15] where K_{CF_2} is a minimum (see Figure 5). The mole fraction of CF_2 at this point in the flame is 8×10^{-5} and of O_2, 6.9×10^{-2}. The rate of disappearance of CF_2 via reaction 11 is 5.3×10^{-9} mol cm^{-3} s^{-1}. The observed rate of decay of CF_2 of 6.2×10^{-7} mol cm^{-3} s^{-1} and thus reaction 11 is of negligible importance in this flame. Analogous calculations for the other reactions listed in part B lead to similar conclusions.

Part C of Table I lists those possible reactions that are considered to be slow, but for which it is not possible to quantitatively demonstrate that fact. Some of these reactions are assumed to be relatively slow because of their endothermicity.

That CF_2 is remarkably unreactive toward alkanes, olefins, and gases such as O_2, H_2, and CO has been noted by various investigators.[4,5,50] The rate constant for the reaction of CF_2 with either C_2F_4[5] or C_2H_4[4] is found to be smaller than that for reaction with O_2 at room temperature.

Even at 500 K, little reaction was observed between CF_2 produced in a discharge and reagents such as C_3H_8, CO, or H_2, although small amounts of the recombination product, C_2F_4,

TABLE I: Possible Reactions of CF_2 in Inhibited Methane Flames

		Ref
	A. Major Reactions Consuming CF_2	
(5)	$CF_2 + H \rightarrow HF + CF$	
(6)	$CF_2 + O \rightarrow CO + F + F$	
(7)	$\rightarrow F_2CO$	
(8)	$\rightarrow FCO + F$	
(9)	$CF_2 + OH \rightarrow CO + HF + F$	
(10)	$\rightarrow F_2CO + H$	
	B. Reactions that Are Quantitatively Slow	
(11)	$CF_2 + O_2 \rightarrow F_2CO + O$	15
(12)	$\rightarrow CO + 2F + O$	15
(13)	$CF_2 + CF_2 \rightarrow C_2F_4$	4, 5, 6
(14)	$CF_2 + M \rightarrow CF + F + M$	11
(15)	$CF_2 + HF \rightarrow CF_3H$	9
(16)	$CF_2 + HBr \rightarrow CF_2HBr$	9
(17)	$CF_2 + CF_3H \rightarrow C_2F_4 + HF$	14
	C. Reactions that Are Qualitatively Slow	
(18)	$CF_2 + CH_3 \rightarrow HF + CFCH_2$	Endothermic
(19)	$CF_2 + Br \rightarrow CF + BrF$	Endothermic
(20)	$CF_2 + CF_3Br \rightarrow C_2F_4 + BrF$	Endothermic
(21)	$CF_2 + \left\{\begin{matrix} CH_4 \\ H_2O \\ CO \\ CO_2 \end{matrix}\right\} \rightarrow$ products	50
(22)	$CF_2 + CH_2CF_2 \rightarrow H_2C(\text{—}CF_2\text{—})C(F_2)$	5, 6
(23)	$CF_2 + F_2CO \rightarrow CF_3 + FCO$	Endothermic
(24)	$CF_2 + O \rightarrow CF + FO$	Endothermic
(25)	$CF_2 + OH \rightarrow CF + FOH$	Endothermic
(26)	$CF_2 + H_2CO \rightarrow$ products	
(27)	$CF_2 + CH_3Br \rightarrow$ products	

were observed.[50] There appear to be no data reported on the reactions of CF_2 with H_2CO or CH_3Br, for which exothermic reactions can be written. However, even if these reactions were to have rate coefficients equal to that of reactions with the major radical species, it is unlikely that they could be significant in this system since, at the point of the maximum rate of CF_2 decay, the concentrations of CH_3Br and H_2CO are 100 and 10 times smaller, respectively, than any one of the major radical species.

Although it is not possible to distinguish among reactions 5–10, we can estimate a rate constant for reaction of CF_2 with H, O, and/or OH as follows. We consider that at 1800 K, where K_{CF_2} is a minimum, the observed net reaction rate is the rate of decay of CF_2, i.e., CF_2 is no longer being formed. This is reasonable since $[CF_3] \sim 0$ at this point in the flame. If we assume that the rate coefficient for reaction with each of the radicals are equal, then

$$K_{CF_2} = -d[CF_2]/dt = k_r[CF_2] \sum_i [i] \qquad i = H, O, OH$$

and k_r can be calculated. It is found to be 1.0×10^{13} cm^3 mol^{-1} s^{-1}. Alternatively, we may assume that reaction with a single radical dominates the decay of CF_2. Then

$$K_{CF_2} = k_i[CF_2][i] \qquad i = H, O, \text{or } OH$$

We find that k_i is 2.4×10^{13}, 4.9×10^{13}, or 2.5×10^{13} when the dominant radical reactant is assigned to H, O, or OH, respectively. The results of these two types of calculations permit a bracketing of the rate coefficient for the reaction between CF_2 and these species. It should be noted that errors in the absolute concentration of CF_2 do not propagate into the rate constant here because of the $K_{CF_2}/[CF_2]$ term. However, the net reaction rate for CF_2 does depend upon the value of the diffusion coefficient for CF_2 in argon, and, by necessity, this is calculated from a model for molecular interactions that is not very realistic for radical species. We estimate that the rate constants calculated for CF_2 + H, O, or OH, an average between the two types of calculations, are good to a factor of 5 or better.

TABLE II: Rate Coefficients Determined for Reactions of CF_2 in Inhibited Methane Flames

Reaction	T, K	k, cm^3 mol s^{-1}
$CF_3 + H \rightarrow HF + CF_2$	1540	2×10^{14}
$CF_2 + (H,O,OH) \rightarrow$ products	1800	1×10^{13}, if $k_H = k_O = k_{OH}$
$CF_2 + H \rightarrow$ products	1800	2×10^{13}, if $k_H \gg k_O, k_{OH}$
$CF_2 + O \rightarrow$ products	1800	5×10^{13}, if $k_O \gg k_H, k_{OH}$
$CF_2 + OH \rightarrow$ products	1800	3×10^{13}, if $k_{OH} \gg k_O, k_H$

A summary of the rate coefficients determined for reactions relating to CF_2 in the flame is given in Table II. There are no literature data available for comparison of the rate coefficients for CF_2 reactions estimated here, formation or decay. Keating and Matula[15] conclude that the reaction $CF_2 + O \rightarrow FCO + F$ can be important in shock tube studies of C_2F_4–O_2 oxidation as the oxygen concentration is increased. The (gas kinetic) value for the reaction rate constant of this reaction used by them in modeling their experiments is ten times higher than that found here.

Comments on the Involvement of the Fluorocarbon Adduct in Flame Inhibition

The use of chemical extinguishants for fire protection is now common. These agents are considered effective by virtue of their interference with the normal chain reactions responsible for flame propagation. The exact nature of this interference has been the object of a number of investigations (see, e.g., ref 51 and the references therein). Until very recently the fluorine containing part of the halohydrocarbon inhibitors was viewed as an essentially nonreactive adduct whose function was to transport bromine to the flame reaction zone; bromine is considered to be the principal reactive agent in retarding flame propagation. For some time, CF_3Br has been known to be rather more effective than one might expect on the basis of its bromine content[52] and, in that sense, has been described as a synergistic system.[53]

In this discussion, it is important to bear in mind that there are significant differences between flames maintained at low pressure and at atmospheric pressure, but they are differences that are understood and can be modeled. Once the basic chemistry of the system is identified, the relative importance of any reaction under a variety of imposed conditions can be assessed.

The reactions proposed for the formation and decay of CF_2 are relevant to the mechanism of inhibition of CF_3Br to the extent that inhibition does involve the fluorocarbon adduct. Reactions such as (2) and (5) are true atom scavenging reactions since, once formed, HF does not react further in the flame. Reaction 7 could also have a similar effect since the decay of F_2CO is relatively slow in the flame and could itself provide for a relatively rapidly bimolecular route to remove H atoms from the secondary reaction zone.[22] The early appearance of both HF and F_2CO in the flame is consistent with the notion that these three reactions are important.[22] The fact

that the CF_2Br_2 is only as effective as CH_2Br_2 and Br_2 in reducing the burning velocity of atmospheric methane flames[52] suggests that, for inhibition, reaction 2 is the most significant of the three.

However, other reactions proposed for the decay of CF_2, those producing F atoms, e.g., could result in promotion, rather than inhibition. Rapid F-atom abstraction reactions, such as $F + CH_4 \rightarrow HF + CH_3$, could hasten the decay of fuel. Promotion of fuel reaction at low temperature has been observed in HBr–propane flames burning at 1 atm[54] and was partly attributed to reaction of Br atoms with C_3H_8. We are unable to observe F atoms, supposing they are present in detectable concentrations, because of interference at 19 amu by H_2O, which has an appearance potential well below that for F^+ from F atoms and whose concentration is relatively large throughout the flame. Since we do observe inhibition at low pressures[55] where, according to current ideas regarding the Br mechanism,[51] the effectiveness of the Br part of the molecule should be greatly reduced, such promotion reactions are unlikely to be important in this system. This further implies that reactions 6, 8, and 9 are not important here, or that the F atoms produced react so rapidly that their concentration in the region where methane is being attacked remains very low.

References and Notes

(1) R. Mitsch and A. Rodgers, *Int. J. Chem. Kinet.*, **1**, 439 (1969).
(2) S. H. Bauer, K. C. Hou, and E. L. Resler, Jr., *Phys. Fluids, Suppl. I*, **12**, I-125 (1969).
(3) R. E. Kupel, M. Nolan, R. G. Keenan, M. Hite, and L. D. Scheel, *Anal. Chem.*, **36**, 386 (1964).
(4) F. W. Dalby, *J. Chem. Phys.*, **41**, 2297 (1964).
(5) W. J. R. Tyerman, *Trans. Faraday Soc.*, **65**, 1188 (1969).
(6) N. Cohen and J. Heicklen, *J. Chem. Phys.*, **43**, 871 (1965).
(7) G. R. Barnes, R. A. Cox, and R. F. Simmons, *J. Chem. Soc. B*, 1176 (1971).
(8) R. A. Cox and R. F. Simmons, *J. Chem. Soc. B*, 1625 (1971).
(9) T. Smail and F. S. Rowland, *J. Phys. Chem.*, **74**, 1866 (1970).
(10) A. P. Modica and J. E. LaGraff, *J. Chem. Phys.*, **43**, 3383 (1965).
(11) A. P. Modica, *J. Chem. Phys.*, **44**, 1585 (1966).
(12) A. P. Modica and S. J. Sillers, *J. Chem. Phys.*, **48**, 3283 (1968).
(13) G. A. Carlson, *J. Phys. Chem.*, **75**, 1625 (1971).
(14) E. Tschuikow-Roux and J. E. Marte, *J. Chem. Phys.*, **42**, 2049 (1965).
(15) E. L. Keating and R. A. Matula, paper presented at the 1973 Fall Meeting of the Eastern States Section of the Combustion Institute, McGill University, Montreal, Quebec, Canada, Oct 11–12, 1973.
(16) E. S. Fleming, D. I. MacLean, and J. M. Smist, paper presented at the 169th National Meeting of the American Chemical Society, Philadelphia, Pa., Apr 4–11, 1975.
(17) D. E. Milligan, D. E. Mann, and M. E. Jacox, *J. Chem. Phys.*, **41**, 1199 (1964).
(18) I. P. Fisher, J. B. Homer, and F. P. Lossing, *J. Am. Chem. Soc.*, **87**, 957 (1965).
(19) T. C. Ehlert, *J. Phys. Chem.*, **73**, 949 (1969).
(20) D. L. Hildenbrand, *Chem. Phys. Lett.*, **30**, 32 (1975).
(21) M. C. Lin, paper presented at the 169th National Meeting of the American Chemical Society, Philadelphia, Pa., Apr 4–11, 1975.
(22) J. C. Biordi, C. P. Lazzara, and J. F. Papp, *Symp. (Int.) Combust., [Proc.], 15th*, 917–931 (1975).
(23) J. C. Biordi, C. P. Lazzara, and J. F. Papp, U.S. Bureau of Mines RI 7723, 1973.
(24) J. C. Biordi, C. P. Lazzara, and J. F. Papp, *Combust. Flame*, **21**, 371 (1973).
(25) J. C. Biordi, C. P. Lazzara, and J. F. Papp, *Combust. Flame*, **23**, 73 (1974).
(26) J. C. Biordi, C. P. Lazzara, and J. F. Papp, *Combust. Flame*, **26**, 57 (1976).
(27) W. E. Kaskan, *Symp. (Int.) Combust., [Proc.], 6th*, 134–143 (1957).
(28) J. Peeters and G. Mahnen, *Symp. (Int.) Combust., [Proc.], 14th*, 133–141 (1973).
(29) J. C. Biordi, C. P. Lazzara, and J. F. Papp, U.S. Bureau of Mines RI 8029, 1975.
(30) E. L. Knuth in "Engine Emissions: Pollutant Formation and Measurement", G. Springer and D. J. Patterson, Ed., Plenum Press, New York, N.Y., 1973, pp 319–363.
(31) G. J. Williams and R. G. Wilkins, *Combust. Flame*, **21**, 325 (1973).
(32) K. H. Homan and D. I. MacLean, *J. Phys. Chem.*, **75**, 3645 (1971).
(33) H. Gg. Wagner, C. Zetzsch, and J. Warnatz, *Ber. Bunsenges. Phys. Chem.*, **76**, 526 (1972).
(34) R. M. Fristrom and A. A. Westenberg, "Flame Structure", McGraw-Hill, New York, N.Y., 1965.
(35) F. H. Field and J. F. Franklin, "Electron Impact and Ionization Phenomena", Revised edition, Adademic Press, New York, N.Y., 1970, pp 239–493.
(36) A. Cornu and R. Massut, "Compilation of Mass Spectral Data", Heyden and Son, Ltd., London, 1966.
(37) C. Lifshitz and F. A. Long, *J. Phys. Chem.*, **69**, 3731 (1965).
(38) C. Lifshitz and F. A. Long, *J. Phys. Chem.*, **67**, 2463 (1963).
(39) S. W. Benson, "Thermochemical Kinetics", Wiley, New York, N.Y., 1968.
(40) D. Rapp and P. Englander-Golden, *J. Chem. Phys.*, **43**, 1464 (1965).
(41) J. B. Mann, *J. Chem. Phys.*, **46**, 1646 (1967).
(42) J. A. Beran and L. Kevan, *J. Phys. Chem.*, **73**, 3866 (1969).
(43) J. O. Hirschfelder, C. F. Curtiss, and R. B. Bird, "Molecular Theory of Gases and Liquids", Wiley, New York, N.Y., 1965.
(44) J. F. Papp, C. P. Lazzara, and J. C. Biordi, U.S. Bureau of Mines RI 8019, 1975.
(45) R. A. Svehla, NASA Technical Report R-132, 1962.
(46) V. N. Kondratiev, National Bureau of Standards, No. COM-72-10014 (1972).
(47) A. F. Trotman-Dickenson and G. S. Milne, *Natl. Stand. Ref. Data. Ser., Natl. Bur. Stand.*, **No. 9** (1967).
(48) G. B. Skinner, *ACS Symp. Ser.*, **No. 16**, 295–312 (1975).
(49) G. B. Skinner and G. H. Ringrose, *J. Chem. Phys.*, **43**, 4129 (1965).
(50) W. Fielding and H. O. Pritchard, *J. Phys. Chem.*, **64**, 278 (160).
(51) R. G. Gann, Ed., *ACS Symp. Ser.*, **No. 16** (1975).
(52) W. A. Rosser, H. Wise, and J. Miller, *Symp. (Int.) Combust., [Proc.], 7th*, 175–182 (1959).
(53) J. W. Hastie and C. L. McBee, *ACS Symp. Ser.*, **No. 16**, 118–146 (1975).
(54) C. Pownall and R. F. Simmons, *Symp. (Int.) Combust., [Proc.], 13th* 585–592 (1971).
(55) J. C. Biordi, C. P. Lazzara, and J. F. Papp, *Combust. Flame*, **24**, 401 (1975).
(56) Skinner[48] has recently reanalyzed these data and recommends a substantially higher activation energy than in the earlier work. The change has negligible effect on the calculated maximum $[CF_3]$ here, since at this point in the flame primarily CF_3H is being formed; decay is relatively very slow.

Reduction of Mercuric Halides and Pseudohalides in Aqueous Solution. Formation and Some Physicochemical Properties of HgCl, HgBr, HgI, HgSCN, and HgCN Radical Molecules

H. Jungbluth, J. Beyrich, and K.-D. Asmus*

Hahn-Meitner-Institut für Kernforschung Berlin GmbH, Bereich Strahlenchemie, 1 Berlin 39, Germany *(Received December 1, 1975)*

Publication costs assisted by Hahn-Meitner-Institut Berlin GmbH

Reduction of HgX_2 (X = Cl, Br, I, SCN, or CN) in aqueous solutions by hydrated electrons or $(CH_3)_2\dot{C}OH$ radicals yields transient HgX radical molecules. The optical absorption spectra of HgX, except for HgCN, exhibit two bands: a long wavelength band the position of which is dependent on the nature of X (λ_{max} 330, 350, 355, and 415 nm for X = Cl, Br, I, and SCN, respectively) and an approximately three times stronger band which peaks independently of X around 240–250 nm. HgCN shows only one distinct peak at 285 nm and no comparable absorption at shorter wavelengths. The HgX radical molecules readily reduce tetranitromethane and *p*-benzoquinone. In the absence of suitable reaction partners two HgX combine to form the stable Hg_2X_2 except for HgCN which disproportionates. Differences between HgCN and the other HgX are also observed in their reactions with molecular oxygen. While HgCN transfers an electron to form $O_2\cdot^-$, the other HgX add oxygen to form primarily a peroxy radical, $\cdot O_2HgX$. Based on these findings and the optical absorption characteristics the following electronic structures of HgX are proposed: The cyano compound seems to be best described by a three electron bond between the mercury atom and the cyano group, Hg.:.CN, with the third electron in a σ^* orbital. A hybrid structure, ·Hg··X, is assigned to the other species (X = Cl, Br, I, and SCN) with one of the orbitals participating in the σ bond to the halide and the other containing the unpaired electron.

Introduction

Mercuric halides and pseudohalides predominantly exist as undissociated molecules HgX_2 in aqueous solution if X = Cl, Br, I, SCN, and CN. Reduction eventually leads to the rather insoluble precipitates Hg_2X_2. Only the corresponding mercurous cyanide, $Hg_2(CN)_2$, cannot be isolated owing to spontaneous disproportionation of the Hg^+ oxidation state in this particular compound.[1]

A transient intermediate HgCl resulting from dissociative electron capture during the reduction of mercuric chloride

$$HgCl_2 + e_{aq}^- \rightarrow HgCl + Cl^- \quad (1)$$

has recently been identified and characterized in a pulse radiolysis study.[2] The reduction was not only achieved by hydrated electrons, but also by other reducing species such as $(CH_3)_2\dot{C}OH$ radicals. The HgCl exhibited radical character, for example, it readily reacted with oxygen, transferred an electron to tetranitromethane, and in the absence of suitable reaction partners dimerized

$$2HgCl \rightarrow Hg_2Cl_2 \quad (2)$$

to the stable form of mercurous chloride. The HgCl showed optical absorption with two distinguishable maxima at 245 nm (ϵ 7 × 10^3 M^{-1} cm^{-1}) and 330 nm (ϵ 2.3 × 10^3 M^{-1} cm^{-1}), respectively. Evidence for HgCl as an intermediate in the reduction of $HgCl_2$ has also been found in gas phase investigations[3] and is discussed in polarographic studies of chloride containing systems.[4] Very recently, also HgCN from the reduction of $Hg(CN)_2$ has been proposed.[30]

The present paper is concerned with the formation and characterization of other HgX radical species in aqueous solution. From our earlier work with HgCl it became evident that electronic excitation of this radical molecule does not only involve electrons located at the mercury atom.[2] No absorption corresponding to the 330 nm band is found for either Hg_2^{2+} or its precursor Hg^+, i.e. for mercury ions in the +1 oxidation state which are not attached to a hetero-atom.[5] Based on the absorption spectra and some chemical reactions of the various HgX, possible electronic structures of this radical species are proposed.

Experimental Section

The experimental details of optical and conductivity pulse radiolysis measurements have already been described.[6–9] The pulse experiments were done with high-energy electrons from a 1.6-MeV Van de Graaff generator (10 mA) at pulse lengths of 0.5–3 μs and an absorbed dose of ca. 700 rads/1 μs pulse duration. The experiments were carried out under commonly used radiation chemical conditions. Solutions were prepared from reagent grade compounds and triply distilled or "Millipore" filtered water. Deoxygenation whenever required was achieved by bubbling with either argon or N_2O. The latter was used if e_{aq}^- were to be converted to OH radicals ($N_2O + e_{aq}^- \rightarrow N_2 + OH^- + OH\cdot$). Reactions involving O_2 were usually investigated in air saturated solutions or 1:1 mixtures of air-saturated solutions with solutions saturated with N_2O or argon.

Dosimetry was based on optical measurements of $C(NO_2)_3^-$ ions (ϵ_{350} 1.5 × 10^4 M^{-1} cm^{-1}) formed during the reduction of tetranitromethane (TNM) by e_{aq}^- and $(CH_3)_2\dot{C}OH$ in deoxygenated solutions of 10^{-3} M TNM and 10^{-1} M 2-propanol. This process occurs with a yield of $G(C(NO_2)_3^-)$ = 5.6.[8–10] The dosimetry solution also served as a reference standard for the conductivity data.[8,9] For every neutral TNM molecule which is reduced one $C(NO_2)_3^-$ plus the associated positive counter ion, H_{aq}^+, is formed. The observed conductivity signal V which is observed on the oscilloscope as a result

of this reduction process is proportional to the yield (G or concentration) and the specific conductivity of the ions (Λ in Ω^{-1} cm^2).[7] The product $(G\Lambda)_X$ for an unknown system X is given by

$$(G\Lambda)_X = \frac{V_X}{V_{TNM}} G_{TNM}\Lambda_{TNM} \quad (3)$$

With G_{TNM} = 5.6 [$C(NO_2)_3^-$ + H_{aq}^+ ion pairs formed per 100 eV absorbed energy] and $\Lambda_{TNM} = \Lambda_{C(NO_2)_3^-} + \Lambda_{H_{aq}^+}$ = 360 Ω^{-1} cm^2 the pulse induced changes in conductivity of the unknown system can be interpreted quantitatively.

All data given in this paper refer to room temperature.

Results

Formation and Spectral Properties of HgX. Reduction of HgX_2 (X = Cl, Br, I, SCN, and CN) by hydrated electrons or other strongly reducing agents lead to transient species showing significant absorption bands in the near uv and sometimes also the visible range. Figure 1a shows, for example, an absorption–time curve traced at 420 nm in a deoxygenated (Ar saturated) pulsed solution of 10^{-3} M $Hg(SCN)_2$ and 5 × 10^{-1} M 2-methyl-2-propanol. The latter was added to remove OH· radicals which are produced simultaneously with about the same yield as the reducing e_{aq}^-. Under these conditions the one-electron reduction of the mercuric compound is completed during the ca. 1 μs electron pulse, i.e., maximum absorption of the primary reduction product has developed during this time period. A different picture is seen at 270 nm (Figure 1b). Only the initial fast increase in optical absorption is due to the transient species. Formation of a more strongly absorbing stable product in the decay reaction of the transient species is responsible for the second slow increase. Details on this process will be discussed later.

Assignment of the transient absorption from Figure 1a to the radical molecule HgSCN and corresponding absorptions to HgX in similar experiments with the other mercuric compounds is based on the same grounds as presented for HgCl in our previous paper.[2] Spectral considerations exclude complete separation of the mercury from the halide, i.e., Hg^+ or $X_2^{\cdot -}$ formation since the absorption spectra of the latter are significantly different. In addition kinetic salt effect experiments on the bimolecular decay of the absorption in the absence of other scavengers indicates that the transient species carries no charge. Finally conductometric measurements are in agreement with simultaneous X^- ion elimination, for example, during the reduction of $Hg(CN)_2$ an anion is observed with a pK = 9.3 identical with that of HCN. The underlying process for the HgX formation is therefore generally the dissociative electron capture

$$HgX_2 + e_{aq}^- \rightarrow HgX + X^- \quad (4)$$

The bimolecular rate constants for the reaction given in eq 4 was determined by kinetic analysis of the decay of the strong e_{aq}^- absorption at 700 nm and the formation of the HgX absorption in pulsed deoxygenated solutions of various low concentrations of HgX_2. The results are summarized in Table I; that for $HgCl_2$ is taken from our previous investigation.[2] The reduction of HgX_2 by hydrated electrons is seen to occur essentially by diffusion controlled processes.

Reduction of HgX_2 by the α-hydroxy radical from 2-propanol

$$HgX_2 + (CH_3)_2\dot{C}OH \rightarrow HgX + X^- + H_{aq}^+ + (CH_3)_2CO \quad (5)$$

was followed through the formation of the HgX absorption at appropriate wavelengths in pulsed N_2Osaturated solutions of 10^{-1} M 2-propanol and various low concentrations of HgX_2. Under these conditions 85% of the primary radiolysis products of water (e_{aq}^-, OH·, and H·) are converted to the reducing species $(CH_3)_2\dot{C}OH$[10] which then react according to eq 5 (the remaining 15% result in chemically inert β-hydroxy radicals).[10] The bimolecular rate constants for these electron transfer processes are also listed in Table I. No such reaction could be observed for $Hg(CN)_2$ + $(CH_3)_2\dot{C}OH$. The electron transfer reaction in this case presumably is too slow to compete with the combination and disproportionation of two $(CH_3)_2\dot{C}OH$ radicals.

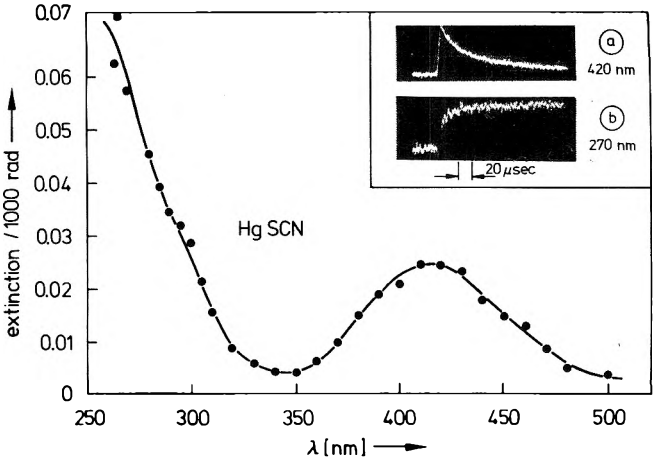

Figure 1. Optical absorption spectrum of HgSCN and absorption–time traces at 420 nm (a) and 270 nm (b). Solution: N_2O saturated, 10^{-1} M 2-propanol, 10^{-3} M $Hg(SCN)_2$. Dose per pulse: ca. 600 rads (HgSCN is formed with G = 5.6 molecules per 100 eV absorbed energy).

TABLE I: Bimolecular Rate Constants for the Reduction of HgX_2 by Hydrated Electrons and $(CH_3)_2\dot{C}OH$ Radicals

HgX_2	$k(HgX_2 + e_{aq}^-)$, M^{-1} s^{-1}	$k(HgX_2 + (CH_3)_2\dot{C}OH)$, M^{-1} s^{-1}
$HgCl_2$[a]	(4.0 ± 0.3) × 10^{10}	(2.0 ± 0.2) × 10^9
$HgBr_2$	(3.4 ± 0.4) × 10^{10}	(2.4 ± 0.6) × 10^9
HgI_2	(3.0 ± 0.5) × 10^{10}	(2.0 ± 0.5) × 10^9
$Hg(SCN)_2$	(4.5 ± 0.5) × 10^{10}	(2.2 ± 0.5) × 10^9
$Hg(CN)_2$	(1.6 ± 0.3) × 10^{10} [b]	

[a] Taken from ref 2. [b] k = 1.3 × 10^{10} M^{-1} s^{-1} reported in ref 30.

Reaction 5 was generally used to obtain the optical absorption spectra of HgX. The spectra were obtained from the change in optical density immediately after the pulse in N_2O saturated solutions of 10^{-3} M HgX_2 and 10^{-1} M 2-propanol. Only the HgCN spectrum was measured in argon degassed solutions containing 5 × 10^{-1} M 2-methyl-2-propanol instead of 2-propanol as OH· scavenger.

The spectrum of HgSCN is shown in Figure 1. Its shape is essentially that of HgCl reported in our previous paper,[2] i.e., two absorption bands are observable. The weaker band at longer wavelengths is, however, shifted considerably toward the red as compared to that of HgCl and peaks at 415 nm (ϵ_{415} 4.4 × 10^3 M^{-1} cm^{-1}). The uv peak could not be resolved since $Hg(SCN)_2$ itself increasingly absorbs with decreasing wavelength. It seems to be very similar though to that of HgCl. The absorption steadily increases toward shorter wavelengths and may also have a maximum around 245 nm with an extinction coefficient which is about 2–3 times higher than that of the long wavelength band.

Similar characteristics have been found for the absorption spectra of HgBr and HgI, i.e., a long wavelength band, the position of which depends on the nature of the halide, and a comparatively 2–3 times stronger uv band, the position of which appears to be independent of the halide around 240–250 nm.

A significant difference is observed for the absorption spectrum of HgCN. As can be seen from Figure 2 only one peak is found with λ_{max} 285 nm, and an extinction coefficient (ϵ_{285} 3.5 × 10^3 M^{-1} cm^{-1}) similar to that of the long wavelength band of the other HgX. No absorption occurs around 245 nm, i.e., the absorption band which was independent of the halide function does not exist.

The corresponding λ_{max} and ϵ_{max} for the long wavelength absorptions are listed in Table II. Since the uv bands could not be resolved quantitatively except for HgCl only their existence or nonexistence is noted in the same table.

Reactions of HgX. In Figure 1a it can be seen that the absorption at 420 nm decays to its prepulse value. At shorter wavelengths, e.g., 270 nm, the initial fast rise in optical absorption due to HgSCN is followed by a slower second increase indicating the formation of a strongly absorbing and stable product (Figure 1b). The kinetics of this second process are identical with that of the 420-nm decay both following second-order rate laws. The final absorption in Figure 1b is therefore attributed to the stable form of mercurous thiocyanate formed in the dimerization process

$$2HgSCN \rightarrow Hg_2(SCN)_2 \qquad (6)$$

Similarly the formation of Hg_2Cl_2 from HgCl[2] and the other Hg_2X_2 (X = Br and I) from the corresponding HgX could be observed at shorter wavelengths. No such stable absorption was observed during the reduction of $Hg(CN)_2$. This, however, was to be expected since, as mentioned above,[1] the hypothetical $Hg_2(CN)_2$ does not exist in aqueous solution. Nevertheless the transient HgCN absorption also decays by a second-order process. Since radiation chemical yields, i.e., concentrations of the HgX radical molecules are calculable (G values and dose are known) the rate constants for their bimolecular decay can be derived from the measured half-lives at various doses. The corresponding results for $2k_2$ are listed in Table III.

The HgX radical molecule is also very reactive toward other compounds. As has been established already for HgCl in our previous study it readily reduces tetranitromethane.[2] The reaction

$$HgX + C(NO_2)_4 \rightarrow C(NO_2)_3^- + HgX^+ + NO_2 \qquad (7)$$

can be observed by following either the decay of the HgX absorption or the formation of the strongly absorbing $C(NO_2)_3^-$ ion at suitable wavelengths. The solutions used for these experiments were N_2O saturated and also contained 10^{-1} M 2-propanol, high concentrations of HgX_2 (10^{-2} M or saturated solutions) and comparatively small concentrations of TNM. For the cyano compound argon and 2-methyl-2-propanol (5 × 10^{-1} M) were used instead of N_2O and 2-propanol. Under these conditions HgX is formed via reactions 5 or 4 within the period of the pulse prior to any possible direct reaction of $(CH_3)_2\dot{C}OH$ or e_{aq}^- with TNM. The bimolecular rate constants for the electron transfer reaction 7 are listed in Table III and indicate essentially diffusion controlled processes.

A fast electron transfer is also observed for the reaction of HgX with p-benzoquinone which at pH 5–5.5 leads to the formation of the semiquinone anion

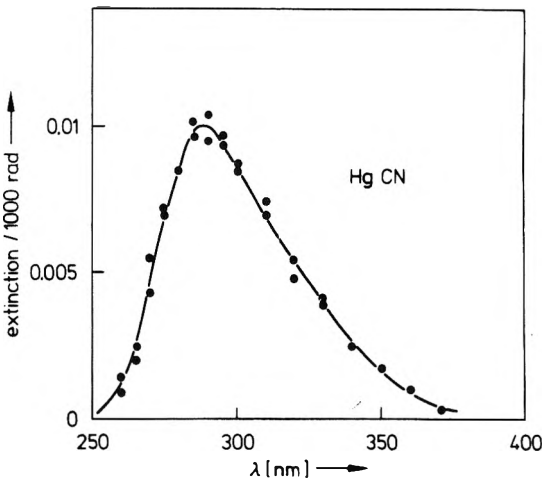

Figure 2. Optical absorption spectrum of HgCN. Solution: argon saturated, 5 × 10^{-1} M 2-methyl-2-propanol, 10^{-3} M $Hg(CN)_2$ (HgCN is formed with G = 2.7 molecules per 100 eV absorbed energy).

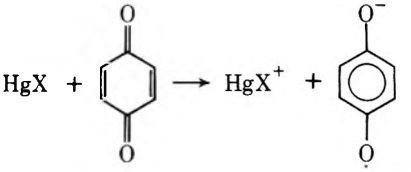

(8)

The latter may be observed directly through its absorption at 410 nm.[11,12] The bimolecular rate constants have been determined for HgCl and HgCN (see Table III); because of too much overlapping absorptions by the radicals involved only estimates of the order of magnitude of the reaction rates of the other HgX were possible.

The fate of the HgX^+ ion, by the way, is mostly determined by the equilibrium $HgX_2 \rightleftharpoons HgX^+ + X^-$. As has been mentioned already the dissociation constant of HgX_2 is very low in aqueous solutions and thus the majority of HgX^+ will be neutralized by X^- (from reaction 4 or 5). This may be observed through pulse radiolysis conductivity experiments and has been discussed in detail already for the chloro compound elsewhere.[2]

The radical character of HgX is also demonstrated by its reaction with molecular oxygen. In air saturated solutions (≈2 × 10^{-4} M O_2) of up to 10^{-2} M HgX_2 (depending on solubility) the HgX absorptions decay with half-lives of ≤1 μs. This allows estimates of ≥10^9 M^{-1} s^{-1} for the rate constant of the reaction HgX + O_2 (Table III). A significant difference between HgCl, HgBr, HgI, and HgSCN on the one hand and HgCN on the other hand appears to exist with respect to the reaction product. In case of the cyano compound clearly an electron transfer occurs:

$$HgCN + O_2 \rightarrow HgCN^+ + O_2^{\cdot -} \qquad (9)$$

The $O_2^{\cdot -}$ radical anion was identified optically by its known absorption spectrum and its lifetime in neutral solution.[13] In addition the formation of a negatively charged species in reaction 9 has been observed in conductivity measurements. If the solution was increasingly acidified the spectrum of $O_2^{\cdot -}$ was replaced by that of HO_2· and the yield of the conducting species dropped according to the equilibrium $HO_2 \rightleftharpoons O_2^{\cdot -} + H_{aq}^+$, i.e., a p$K$ curve with pK = 4.8[14] was obtained.

No such reaction seems to occur with the other HgX. Optical measurements which could be conducted with $HgCl_2$ and $HgBr_2$ solutions in the interesting wavelength range did not

TABLE II: Spectral Characteristics of HgX and $X_2^{\cdot-}$

HgX	240–250 absorption	Long wavelength absorption λ_{max}, nm	ϵ_{max}, M^{-1} cm^{-1}	$X_2^{\cdot-}$	λ_{max}, nm	Ref
HgCl[a]	+	330	2.3×10^3	$Cl_2^{\cdot-}$	345	16
HgBr	+	350	4.3×10^3	$Br_2^{\cdot-}$	365	17
HgI	+	355	3.2×10^3 [b]	$I_2^{\cdot-}$	380	18, 19
HgSCN	+	415	4.4×10^3	$(SCN)_2^{\cdot-}$	475	19, 20
HgCN	−	285	3.5×10^3 [c]	$(CN)_2^{\cdot-}$	290	21

[a] Taken from ref 2. [b] This is a lower limit. Owing to the low solubility of HgI_2 reduction possibly is not quantitative. [c] ϵ 3.8×10^9 M^{-1} cm^{-1} reported in ref 30.

TABLE III: Rate Constants (in M^{-1} s^{-1}) for Reactions of HgX

HgX	$2k_2$(HgX + HgX)	k(TNM + HgX)	k(O_2 + HgX)	k(PBQ + HgX)	k(PBQ + $\cdot O_2$HgX)
HgCl[a]	0.8×10^{10}	4.5×10^9	1×10^9	3.0×10^9	0.6×10^9
HgBr	0.8×10^{10}	2.2×10^9	$\geq 10^9$	$>10^9$	0.7×10^9
HgI	0.5×10^{10}	1.4×10^9	$\geq 10^9$	$>10^9$	
HgSCN	0.6×10^{10}	2.8×10^9	$\geq 10^9$	$>10^9$	1.0×10^9
HgCN	1.2×10^{10}	3.1×10^9	4×10^9	3.5×10^9	

[a] Partially taken from ref 2.

show any absorption attributable to $O_2^{\cdot-}$ or $HO_2^{\cdot}$. Furthermore, no conductivity signal indicating $O_2^{\cdot-}$ ion formation could be detected in the appropriate pH range. A different mechanism therefore has to apply and the most likely initial step would be addition of the oxygen to the HgX radical:

$$HgX + O_2 \rightarrow \cdot O_2HgX \rightarrow \text{products} \qquad (10)$$

Such a reaction, i.e., formation of a peroxy radical, has been established for most of the organic radicals in their reaction with oxygen.[15]

$O_2^{\cdot-}$ radical ions are known to transfer their electron to *p*-benzoquinone (PBQ) in the forward reaction of the equilibrium

$$O_2^{\cdot-} + PBQ \rightleftharpoons O_2 + PBQ^{\cdot-} \qquad (11)$$

while most of the organic peroxy radicals do not.[12] It was hoped that the formation of $O_2^{\cdot-}$ from reaction 9 and $\cdot O_2HgX$ from reaction 10 could be distinguished through their reaction with *p*-benzoquinone. However, both $O_2^{\cdot-}$ and $\cdot O_2HgX$ readily transfer their electron to PBQ with even similar rate constants (see Table III). Such reducing properties of peroxy radicals are not unusual though: α-hydroxy-peroxy-radicals

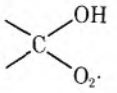

for example, have been found to reduce suitable electron acceptors, such as, tetranitromethane with rate constants being only slightly lower than for the corresponding reaction of $O_2^{\cdot-}$.[15b]

Discussion

In the reduction process of HgX_2 the mercury may be regarded as being formally reduced from the +2 to the +1 oxidation state. The absorption spectra of the transient HgX, however, not only show the optical characteristics of an isolated mercurous ion, Hg^+, which absorbes at 250 nm and below,[5] but also indicate a strong influence of the halide/pseudohalide group. A covalent structure similar to HgX_2[1] is therefore attributed to the HgX radical. Owing to the different electron affinity of X the HgX bond may exhibit more or less ionic character (Hg^+X^-) as has been suggested for HgCl, for example, from EPR data.[29] Electronic excitation of HgX in any case could involve electrons which are not just located at the mercury atom.

It is interesting to compare the long wavelength absorption bands listed in Table II with those of the $X_2^{\cdot-}$ radical ions.[16-21] The HgX bands are seen to be shifted in the same direction as the $X_2^{\cdot-}$ bands with varying X. Differences exist only in the quantitative extent, in that the shift is larger for the $X_2^{\cdot-}$ absorptions. Also extinction coefficients are higher for the latter.

Based on EPR measurements on, for example, $Cl_2^{\cdot-}$ in solid matrices, the electronic structure of $X_2^{\cdot-}$ is described by a three electron bond between the two halide atoms

$$|\overline{X}\therefore\overline{X}|$$

with the third electron being located in a σ^* (antibonding) orbital.[22] From anisotropic spin coupling data it appears that essentially only p and no d orbitals participate in the formation of σ^*. Such three electron bonds are also indicated by looking at optical absorptions and EPR spectra of mixed halide radical ions XY^-, e.g., $Br(SCN)^{\cdot-}$,[23] complex thioether radical cations, $(R_2S)_2^{\cdot+}$,[24,25] and their seleno analogues, $(R_2Se)_2^{\cdot+}$.[26] A similar structure

$$Hg\therefore\overline{X}|$$

may therefore be attributed to the HgX radical molecule. A trial to obtain more information through EPR measurements using the pulse sampling technique by Fessenden and Schuler[27] failed, however, where no signal at all could be detected, presumably mainly on account of too short a lifetime of HgX in aqueous solution.

On the other hand, mercury is known to accommodate electrons in 6s 6p hybrids, particularly in covalent molecules such as HgX_2.[1] Accordingly the HgX could equally well exist as

$$\begin{matrix}\cdot Hg\text{--}\overline{X}| \\ \text{II}\end{matrix}$$

with one hybrid orbital forming the σ bond, the other containing the unpaired electron.

The most likely process responsible for the long wavelength absorption band, i.e., the one which depends on the halide function, appears to be an n,σ^* transition of a nonbonding electron of the halide or of the sulfur in the SCN group. The absorption of HgCN is almost identical with that of $(CN)_2^{\cdot-}$. This would indicate that it is an electron of the CN group which is excited, which could be either a nonbonding electron from the nitrogen or a π electron from the CN bond. In any case the above considerations do not help to distinguish between the electronic structures I and II.

The stronger uv absorption band of HgX peaking around 250 nm is attributed to a transition of an electron which is more or less exclusively located at the mercury atom since its position does not seem to depend on the nature of X. Furthermore, the naked Hg^+ radical ion has been found to absorb at the same wavelength and with about the same extinction coefficient.[5] The existence of the 250-nm band therefore favors structure II for HgCl, HgBr, HgI, and HgSCN. The complete lack of this absorption band for HgCN on the other hand strongly suggests structure I for this species, i.e., a three electron bond between the mercury and the CN group. (Other low wavelength absorption bands, i.e., $\lambda_{max} < 240$ nm, observed for Hg^+,[5] HgCN,[30] and also indicated for $X_2^{\cdot-}$ are not taken into consideration since strong ground state absorptions of HgX_2 did not permit corresponding optical measurements for all HgX.)

Both structures seem to be able to transfer their unpaired electron to suitable electron acceptors such as tetranitromethane or *p*-benzoquinone. They behave differently, however, toward oxygen. The "hybrid" structure II seems to add oxygen whereas the "σ^*" structure I rather transfers its electron to O_2. It may be interesting to note that carbon centered radicals with sp^3 hybrid electron functions (i.e., where the electronic situation is more similar to structure II) also primarily add oxygen.

The difference in electronic structure between HgCN and the other HgX might also help to explain the different probabilities to form stable Hg_2X_2 molecules. Structure II is expected to facilitate radical–radical combination the result of which is Hg_2Cl_2, Hg_2Br_2, Hg_2I_2, and $Hg_2(SCN)_2$ formation. The HgCN may rather undergo an electron transfer process, i.e., immediate disproportionation or alternatively, as has been suggested very recently by Fujita et al.,[30] form a very short lived dimer complex before disproportionation into the mercury +2 and zero oxidation states.

At this point it finally also seems worthwhile to briefly discuss the results on the HgOH radical molecule published by Fujita et al.[28] in view of our present findings. They observed a strong absorption at 233 nm and a shoulder at about 265 nm. On the whole the spectrum resembles more the one we found for HgCl etc. It may therefore be expected that two HgOH also primarily combine to $Hg_2(OH)_2$ or its dehydrated form, Hg_2O. This reaction should then be followed by disproportionation since $Hg_2(OH)_2/Hg_2O$ do not exist as stable compounds in aqueous solution.[1] This mechanism is indeed demonstrated in the work of Fujita et al. who report a considerable lifetime of several minutes for the dimer complex. Only a minor fraction of HgOH if any is left for direct disproportionation. Taking this into account and considering that the long wavelength absorption band of HgOH is not as distinct as that of HgCl etc. it is suggested that the overall electronic structure of HgOH is mainly given by the hybrid model II with possibly some contribution of the three electron bond model I.

References and Notes

(1) see textbooks on "Inorganic Chemistry", e.g., F. A. Cotton and G. Wilkinson, Verlag Chemie, Interscience, Weinheim, 1970.
(2) N. B. Nazhat and K.-D. Asmus, *J. Phys. Chem.*, **77**, 614 (1973).
(3) D. Maeder, *Helv. Phys. Acta*, **16**, 503, 520 (1943).
(4) W. O'Deen and R. A. Osteryoung, *Anal. Chem.*, **43**, 1879 (1971).
(5) S. Fujita, H. Horii, and S. Taniguchi, *J. Phys. Chem.*, **77**, 2868 (1973).
(6) A. Henglein, *Allg. Prakt. Chem.*, **17**, 296 (1966).
(7) G. Beck, *Int. J. Radiat. Phys. Chem.*, **1**, 361 (1969).
(8) K.-D. Asmus, *Int. J. Radiat. Phys. Chem.*, **4**, 417 (1972).
(9) K.-D. Asmus in "Fast Processes in Radiation Chemistry and Biology", G. E. Adams, E. M. Fielden, and B. D. Michael, Ed., The Institute of Physics, Wiley, New York, N.Y., 1973, pp 40–59.
(10) K.-D. Asmus, H. Mockel, and A. Henglein, *J. Phys. Chem.*, **77**, 1218 (1973).
(11) G. E. Adams, B. D. Michael, and E. J. Land, *Nature (London)*, **211**, 293 (1966).
(12) K. B. Patel and R. L. Willson, *J. Chem. Soc., Faraday Trans. 1*, **69**, 814 (1973).
(13) M. S. Matheson and L. M. Dorfman in "Pulse Radiolysis", The M.I.T. Press, Cambridge, Mass., 1969, and references cited therein.
(14) (a) J. Rabani and S. O. Nielsen, *J. Phys. Chem.*, **73**, 3736 (1969); (b) D. Behar, G. Czapski, L. M. Dorfman, J. Rabani, and H. A. Schwarz, *ibid.*, **74**, 3209 (1970).
(15) See, for example, (a) K. Stockhausen, A. Henglein, and G. Beck, *Ber. Bunsenges. Phys. Chem.*, **73**, 567 (1969); (b) K. Stockhausen, A. Fojtik, and A. Henglein, *ibid.*, **74**, 34 (1970); (c) J. Rabani, M. Pick, and M. Simic, *J. Phys. Chem.*, **78**, 1050 (1974); (d) J. Rabani, D. Klug-Roth, and A. Henglein, *ibid.*, **78**, 2089 (1974).
(16) M. Anbar and J. K. Thomas, *J. Phys. Chem.*, **68**, 3829 (1964).
(17) (a) M. S. Matheson, W. A. Mulac, J. L. Weeks, and J. Rabani, *J. Phys. Chem.*, **70**, 2092 (1966); (b) B. Cercek, M. Ebert, L. W. Gilbert, and A. J. Swallow in "Pulse Radiolysis", M. Ebert, J. P. Keene, A. J. Swallow, and J. H. Baxendale, Ed., Academic Press, London, 1965, p 83.
(18) J. K. Thomas, *Trans. Faraday Soc.*, **61**, 702 (1965).
(19) J. H. Baxendale, P. L. T. Bevan, and D. A. Stott, *Trans. Faraday Soc.*, **64**, 2389 (1968).
(20) G. E. Adams, J. W. Boag, J. Currant, and B. D. Michael in ref 17b, p 131.
(21) I. G. Draganić, Z. D. Draganić, and R. A. Holroyd, *J. Phys. Chem.*, **75**, 608 (1971).
(22) (a) P. W. Atkins and M. C. R. Symons in "The Structure of Inorganic Radicals", Elsevier, Amsterdam, 1967, pp 114–116; (b) I. Marov and M. C. R. Symons, *J. Chem. Soc. A*, 201 (1971).
(23) M. Schöneshöfer and A. Henglein, *Ber. Bunsenges. Phys. Chem.*, **73**, 289 (1969).
(24) (a) B. C. Gilbert, D. K. C. Hodgeman, and R. O. C. Norman, *J. Chem. Soc., Perkin Trans. 2*, 1748 (1973); (b) B. C. Gilbert, J. P. Larkin, and R. O. C. Norman, *ibid.*, 272 (1973).
(25) (a) M. Bonifačić, H. Möckel, D. Bahnemann, and K.-D. Asmus, *J. Chem. Soc., Perkin Trans. 2*, 675 (1975); (b) D. Bahnemann and K.-D. Asmus, *J. Chem. Soc., Chem. Commun.*, **7**, 238 (1975).
(26) K. Nishikida and F. Williams, *Chem. Phys. Lett.*, **34**, 302 (1975).
(27) R. W. Fessenden and R. H. Schuler, *Adv. Radiat. Chem.*, **2** 1–176 (1970).
(28) S. Fujita, H. Horii, T. Mori, and S. Taniguchi, *J. Phys. Chem.*, **79**, 960 (1975).
(29) B. W. Fullam and M. C. R. Symons, *J. Chem. Soc., Dalton Trans.*, 1086 (1974).
(30) S. Fujita, H. Horii, T. Mori, and S. Taniguchi, *Bull. Chem. Soc. Jpn.*, **48**, 3067 (1975).

Dry Electron Yields and Localization in Pulse-Irradiated Water and Heavy Water

Cz. Stradowski[1] and William H. Hamill*

Department of Chemistry and the Radiation Laboratory,[2] University of Notre Dame, Notre Dame, Indiana 46556
(Received October 8, 1975)

Publication costs assisted by the United States Energy Research and Development Administration

The rate constants for scavenging hydrated electrons by Cd^{2+} in H_2O and D_2O are the same. In solutions containing 0.025 to 0.4 *m* $CdSO_4$ and 4 M $HClO_4$ or 4 M $DClO_4$ (to remove e_{aq}^-) the efficiency of scavenging dry electrons e^- in D_2O is 47% greater than in H_2O. In terms of simple competition with dry electron scavenging by Cd^{2+} and localization, the isotope effect is attributed principally to the latter process which is due to formation of H_2O^-. The yields of dry electrons accessible to scavenging by Cd^{2+} (per 100 eV of absorbed energy) are 5.2 in H_2O and 4.9 in D_2O. The difference between $G(Cd^+)$ and $-\Delta G(e_{aq}^-)$ at 30 ps is attributed to prompt recombination of e^- and H_2O^+ for small initial charge separations. After relaxation the distribution of e_{aq}^- may approximate a spherical annulus, causing a delay in e_{aq}^- decay.

Introduction

On the basis of first principles the vertical ionization of water by high energy irradiation produces the dry (nonhydrated) charge pair, H_2O^+ and e^-.[3] The formation of these species can be inferred from early results of ^{60}Co-irradiated aqueous systems.[4] Recent work by Hunt and his associates in the picosecond time range provides compelling evidence that substantially all hydrated electrons e_{aq}^- are produced from precursor e^-.[5]

According to simple theoretical arguments it appears that H_2O^+ migrates electronically prior to localization by formation of dry H_3O^+.[6] Consequently, hole trapping at impurity sites by charge exchange should compete with formation of H_3O^+ by H-atom transfer. This proposal was supported by an isotope effect for oxidation of Cl^- in H_2O and D_2O at neutral pH.[7]

There has been no theoretical work reported on the mechanism for localizing the dry electron in polar liquids. (The primary localized transient is distinguished from the fully solvated state.) Experimental evidence bearing on this problem is therefore particularly desirable and the possibility of an isotope effect is indicated. For example, if the rate-determining process of localization is translation, or vibration, or rotation alone, the isotope effects in H_2O and D_2O would be quite different.

An experimental procedure can be based on the negligible reactivity of e^- with acid and the high reactivity with Cd^{2+}.[4,5] At large ratios of $[H^+]/[Cd^{2+}]$ it is possible to describe trapping of e^- in terms of the semiempirical equation

$$G(Cd^+) = G^0 f\left(\frac{\nu_1[Cd^{2+}]}{\nu_1[Cd^{2+}] + \nu_2}\right) \quad (1)$$

by minimizing contributions from e_{aq}^-.[5] G^0 is the primary yield of dry electrons, f is a correction for contact pairs of e_{aq}^- with Cd^{2+} tentatively taken as unity, ν_1 is the effective encounter frequency of e^- and Cd^{2+}, ν_2 is the solvent-trapping frequency. Localization is considered to terminate reaction of e^- and Cd^{2+} for the condition specified. Actually, correction for some scavenging of e_{aq}^- by Cd^{2+} is also required.

It will be assumed that an isotope effect in ν_1/ν_2 for H_2O and D_2O is due entirely to the mechanism of localization or solvent trapping of e^- which initiates hydration. Whatever the nature of this site, the binding energy must be disposed of by phonon emission. In contrast, Cd^{2+} provides a large number of vacant orbitals below $\sim kT$ for electron capture while aquation provides strong coupling with vibration and trapping is expected to be efficient and substantially free of isotope effects.

Experimental Section

Irradiations were performed with an ARCO LP-7 linear accelerator providing ~8 MeV electrons and 10-ns pulses of ~5 krads. Dosimetry was based on the optical density (OD) of e_{aq}^- at 600 nm using $\epsilon = 1.17 \times 10^4\ M^{-1}\ cm^{-1}$[8] and $G(e_{aq}^-) = 3.3$ at 10 ns.[5] Ordinary corrections for electron density have been applied.

Water was triply distilled and D_2O was used as received from Merck Sharp and Dohme. $DClO_4$ was prepared by vacuum evaporation of $HClO_4$ and D_2O. All irradiated solutions were purged with nitrogen.

Results

The spectra of Cd^+ for 0.1 M $CdSO_4$ in H_2O and D_2O appear in Figure 1. There is a small isotope effect which may be due to vibrational broadening of the aquated ion states. Subsequent measurements of $OD(Cd^+)$ were made at 300 nm in H_2O and 290 nm in D_2O.

The rate of formation of Cd^+ in 10^{-4} M Cd^{2+} was measured in H_2O and in D_2O. For the results in Figure 2 the first-order rate constants $k(Cd^{2+} + e_{aq}^-)$ were $5.1 \times 10^{10}\ M^{-1}\ s^{-1}$ in H_2O and $5.3 \times 10^{10}\ M^{-1}\ s^{-1}$ in D_2O. The expected value in H_2O is $5.3 \times 10^{10}\ M^{-1}\ s^{-1}$.[9]

For 10^{-4} M Cd^{2+} the yields of scavengable hydrated electrons expected in H_2O and D_2O are 3.0[8] and 3.4,[10] respectively. The corresponding extinction coefficients of Cd^+ at λ_{max} are $9.8 \times 10^3\ M^{-1}\ cm^{-1}$ in H_2O and $10.5 \times 10^3\ M^{-1}\ cm^{-1}$ in D_2O. The former value is in adequate agreement with results of Baxendale et al.[11] and of Buxton and Sellers,[12] but lower than the result $\epsilon = 1.1 \times 10^4\ M^{-1}\ cm^{-1}$ of Wolff et al.[5]

For the purpose of comparing yields in H_2O and D_2O with each other, as well as with Figure 9 of Wolff et al.,[5] the dependence of $G(Cd^+)$ on $t = 1/k[Cd^{2+}]$, for $k = 3.5 \times 10^{10}\ M^{-1}\ s^{-1}$, is presented in Figure 3. The k from Figure 2 for D_2O was adjusted proportionately. Figure 3 also includes $G(e_{aq}^-)$ vs. t, given by the continuous curve for the spur model.[13] For the two highest concentrations of Cd^{2+} the calculated time de-

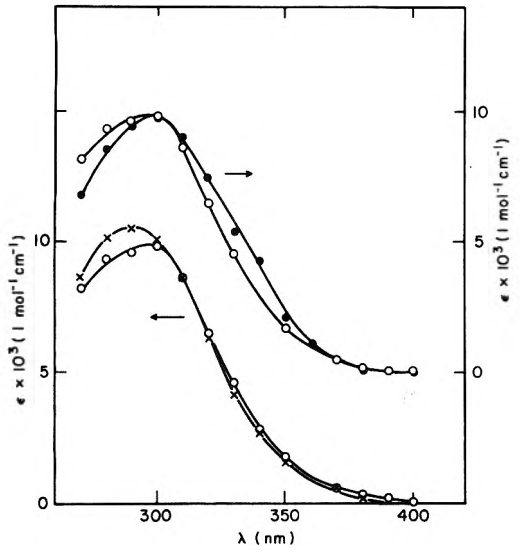

Figure 1. The spectra of Cd^+ in H_2O (●, 0.1 M $CdSO_4$, O, 1 M $CdSO_4$) and D_2O (×, 1 M $CdSO_4$).

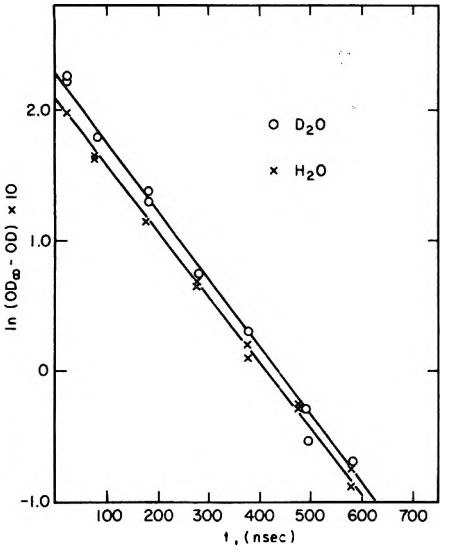

Figure 2. The rates of reaction for Cd^{2+} and e_{aq}^- in H_2O and D_2O.

pendence is not significant since there was appreciable dry-electron scavenging.

Dry-electron scavenging by Cd^{2+} in H_2O and in D_2O was partially resolved from reaction with e_{aq}^- by adding 4 M $HClO_4$ and 4 M $DClO_4$, respectively. Contributions to the observed $G(Cd^+)$ arising from reaction with hydrated electrons were determined using the rate constants measured in this work. Concentrations of Cd^{2+} ranged from 0.025 to 0.4 M. The corrected results are presented in Figure 4 in terms of eq 1 as a simple competition between trapping by solvent and by Cd^{2+} of dry electrons. They are described by eq 2 for H_2O and by eq 3 for D_2O. The relative scavenging efficiency is 47% greater in D_2O than in H_2O.

$$G(Cd^+) = 5.24(1 + 0.348[Cd^{2+}]^{-1})^{-1} \quad (2)$$

$$G(Cd^+) = 4.94(1 + 0.235[Cd^{2+}]^{-1})^{-1} \quad (3)$$

Discussion

The dependence of $G(Cd^+)$ vs. $1/k[Cd^{2+}]$ in Figure 3 correlates fairly well with $G(e_{aq}^-)$ vs. t from calculated results

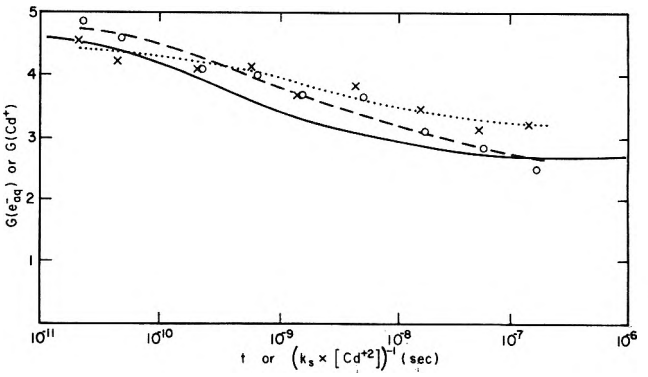

Figure 3. The dependence of $G(Cd^+)$ on $k[Cd^{2+}]$ at various concentrations of $CdSO_4$ (O, H_2O; ×, D_2O) with $k = 3.5 \times 10^{10}\ M^{-1}\ s^{-1}$. The continuous curve corresponds to $G(e_{aq}^-)$ vs. t from the spur model.

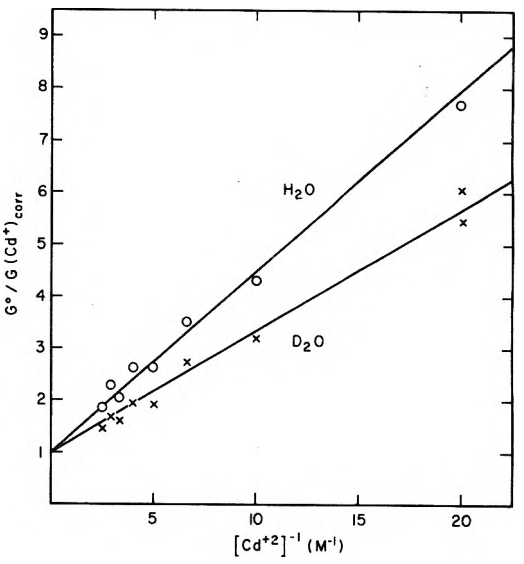

Figure 4. Dry-electron scavenging by Cd^{2+} in H_2O + 4 M $HClO_4$ and D_2O + 4 M $DClO_4$ in terms of eq 2 and 3.

for the spur model,[13] except for a shift of ~7% in G over most of the range. It should be noted that $G(Cd^+)$ and $G(e_{aq}^-)$ are being compared, which is responsible for the systematic difference at $t < 10^{-7}$ s. The present data are also in fairly good agreement with results of Wolff et al.[5] for $G(Cd^+)$ vs. $[Cd^{2+}]$ at 2×10^{-11} s.

They found that the prompt decrease in $G(e_{aq}^-)$ due to Cd^{2+} was always appreciably less than $G(Cd^+)$, demonstrating spur reactions of dry electrons which amount to ~20% of the initial yield. This prompt loss occurs prior to hydration and dipole relaxation while the high-frequency dielectric constant applies. Large Coulombic effects ensure that upon relaxation (i) $G(e_{aq}^-)$ is rather less than that postulated for the spur-diffusion model and (2) that the average separation of (e_{aq}^-)–(H_3O^+, OH) is considerably greater. This perturbed distribution of e^-, resembling a spherical annulus centered on H_3O^+, gives rise to a time-dependent rate constant for e_{aq}^- removal immediately after dipole relaxation. Very little reaction of e_{aq}^- with H_3O^+, OH, and H can occur at short times across the depleted region. According to the results of Hunt's group, the initial rate of decay of e_{aq}^- (350 ps) is about zero and $G(e_{aq}^-)$ is smaller than predicted. No strongly correlated pairs e^-–H_2O^+ survived the subpicosecond regime.

After the reactants randomize by conventional diffusion, reaction of hydrated species begins. Data from Argonne show

a delay of ~8 ns with $G(e_{aq}^-)$ now as much as ~0.6 larger than predicted. Observed and predicted yields converge at ~20 ns.[13] The values of $G(Cd^{2+})$ in H_2O of Figure 3, transposed to a time scale, correlate rather well with data for $G(e_{aq}^-)$ vs. t from Argonne in the range 10^{-10} to 2×10^{-8} s.[13] In this range Cd^{2+} reacts mainly with e_{aq}^- rather than e^-.

The dry electron regime introduces a large perturbation into the spur-diffusion model for $G(e_{aq}^-)$ at $t < 10^{-8}$ s or $[S] \gtrsim 10^{-2}$ M. Measurements at small [S] provide no information concerning very early events, no matter what their mechanism.

The difference between the results in Figure 3 for H_2O and D_2O may be interpreted as supporting a larger initial yield of dry electrons in H_2O than in D_2O. The relatively large $G(Cd^+)$ at ~10^{-7} s in D_2O can then be attributed to isotope effects in the spur reactions which consume e_{aq}^-.

Since the curves of Figure 4 are described by eq 2 and 3 it appears that corrections for contact pairs[14] are not very important. The correction factor, f, is given by

$$f = 1 + \frac{\nu_2}{\nu_1[Cd^{2+}]}\{1 - \exp(-(4\pi r^3/3)[Cd^{2+}])\} \qquad (4)$$

Choosing $r(e_{aq}^-) = r(Cd^{2+}) = 2.2$ Å, then r is 4.4 Å. The exponent is small and it follows that $f \simeq 1 + 0.21(\nu_2/\nu_1)$ or ~1.07 for H_2O and ~1.05 for D_2O, independent of $[Cd^{2+}]$. Because the correction is small and partially cancels for the isotope effect, it has been ignored for this comparison. The effect of contact pairs of $e_{aq}^- + H^+$ and $e_{aq}^- + D^+$ was also ignored because it is even smaller.

The intercepts 5.24 and 4.94 from Figure 4 and eq 2 and 3 can now be corrected using eq 1 and 4 to $G^0 = 4.9$ in H_2O and 4.7 in D_2O. In 1 M $CdSO_4$ at neutral pH the observed yields in this work were 4.9 and 4.6, respectively, at 10 ns. (In terms of $G\epsilon$ the yields are 4.8×10^4 and 5.0×10^4 $Cd^+/100$ eV M^{-1} cm^{-1} at 10 ns and 30 ps, respectively.) For 1 M $Cd(ClO_4)_2$ the yield of Cd^+ was 4.6 ± 0.2 at 30 ps.[5] At this concentration almost all e^- and e_{aq}^- are scavenged, ~90% as e^-, but some Cd^+ is lost by spur reactions with OH or OD. Addition of 1 M t-C_4H_9OH to H_2O increased $G(Cd^+)$ by 10%, in approximate agreement with expectation.[12] The preceding facts indicate that there is no considerable loss of Cd^+ by reactions in the spur and this may account for the possibility of fitting eq 1 to the data. In fact, the results of Wolff et al.[5] for $G(Cd^+)$ vs. $[Cd^{2+}]$ at 30 ps, which are uncomplicated by spur reactions, are fit quite well by eq 1 with $G^0 = 5.7$ and $\nu_1/\nu_2 = 0.33$.

The present results do not supply evidence concerning a contribution to fast electron scavenging in terms of the time-dependent rate constant, k_t, of

$$k_t = k_\infty[1 + r(\Pi D t)^{-1/2}] \qquad (5)$$

for Cd^{2+} and e_{aq}^-, where D is the sum of the diffusion coefficients. The results of Figure 2 show, however, that there is no isotope effect in k_∞. Lam and Hunt[5] have considered the effect of such kinetic transients at high concentrations of electron scavengers. The decrease in $G(e_{aq}^-)$ at the end of the pulse is much greater than that expected by eq 5. Consequently, no appreciable isotope effect can arise in this manner.

It is very improbable that the yields of Cd^+ contain contributions from long-range electron tunneling. Pulse radiolysis of 8 M $NaClO_4$ in H_2O and D_2O with 0.025–0.15 M $Cd(ClO_4)_2$ at 77 K showed no change in $OD(e_s^-)$ at 535 nm from 10^{-8} to 10^{-5} s. Other experiments with ^{60}Co-irradiated glasses showed that both $OD(e_s^-)$ and $OD(Cd^+)$ were constant to ~50 min.[15] In the range 10^{-3} to >1 s for Cd^{2+} in 6 M $NaClO_4$–methanol glass at 77 K, Miller found no change in $OD(e_s^-)$ and $OD(Cd^{2+})$.[16] Consequently, over a wide range of experimental conditions there is no evidence for electron tunneling from e_s^- to Cd^{2+}.

The efficiency of dry-electron trapping by Cd^{2+} for 8 M $NaClO_4$ in D_2O at 77 K was 30% greater than in H_2O.[15]

Rentzepis, Jones, and Jortner[17] noted that there is a rather limited understanding of the dynamics of initial localization of an excess electron in polar solvents. They considered the two extreme situations: one, interaction with collective long-range polarization modes of the liquid; the other, preexisting traps due to fluctuation potentials. Both were considered to contribute, but only the latter mechanism will be considered here since it is not evident how the former entails an appreciable isotope effect. Neither is dipole rotation possible in aqueous solids at 77 K except in proximity to trapped charges.

It will be assumed that primary localization of dry electrons near the bottom of the conduction band (to be distinguished from terminal solvation) requires intrinsic preexisting defects which arise from statistical fluctuations. To be trapped, rather than scattered, an electron must transfer its binding energy E_b to the lattice, approximated by a molecule of H_2O or D_2O. An efficient mechanism must be fast, indicating vibrational excitation. This, in turn, establishes minimal trap depths, or values of E_b. Both requirements entail isotope effects. The transit time of e^- in the region of a defect is roughly estimated at $\Delta t = 10^{-7}$ cm/10^8 cm s^{-1} for a zero-point kinetic energy of ~1 eV, arising from the inner potential of the medium. Binding is relatively slow, since the energy of an electron during Δt is uncertain by ΔE_b and it follows that $\Delta t = h/\Delta E_b = \omega^{-1}$, in terms of the lowest vibration frequency, or ~3×10^{-14} s for H_2O.

The preceding considerations are rather rough, but they indicate a requirement for strong coupling of the electron with lattice vibrations. There is no evidence that a cavity meets this requirement.

Trapping at an L defect, proposed by Naleway and Schwartz,[18] is not directly applicable in 8 M $HClO_4$ or 8 M $NaClO_4$ aqueous solids at 77 K. Nevertheless, the large binding of permanent dipoles to solute ions is quite capable of sustaining small regions which resemble L defects at positive potential and may serve as electron trapping sites. Since hydration energies amount to several electron volts per ion, the defect concentration may not be strongly temperature dependent.

Comparable isotope effects for solid and liquid aqueous systems suggest the involvement of a common molecular process. These isotope effects and the requirement for energy transfer from the electron to the lattice are not incompatible with compound negative ion states, H_2O^- and D_2O^-. These provide the only known efficient mechanism for exciting molecular vibrations by low-energy electron impact. Sanche and Schulz[19] were unable to detect evidence for H_2O^- in the low-pressure vapor, which they attributed to a total width of >1 eV for $H_2O^- \rightarrow H_2O + e^-$. In solid H_2O at 77 K (probably amorphous), Hiraoka and Hamill[20] observed a resonance with considerable cross section attributed to $H_2O + e^- \rightarrow H_2O^-$ at 0.55 eV above the bottom of the conduction band. In the absence of theoretical treatment of the problem of electron localization, or other suitable experimental evidence, the mechanism of compound negative ion formation provides an established mechanism for efficient energy transfer from the electron to the lattice.

It should be noted that negative ion states can be populated by "thermalized" electrons only at defect sites which provide at least 0.55 eV of binding energy prior to the relaxation of the lattice.

The half-width of the resonance for H_2O^- in solid H_2O was $\sim 0.5 \pm 0.1$ eV, indistinguishable from that of the incident electron beam. This requires the lifetime to be somewhat longer than that of H_2O^- in the low-pressure vapor. For $\Delta E = 0.1$ eV, $\Delta t = 10^{-14}$ s. Consequently, competition between ionization and an isotope-dependent vibrational excitation may be possible. If the latter occurs, it is assumed that $H_2O + H_2O^{*-} \rightarrow H_2O^* + H_2O^- \rightarrow e_{aq}^-$.

There remains a possibility that the observed isotope effect depends directly upon energy, rather than frequency. In the context of the preceding considerations, the resonance energy at maximum cross section for D_2O^- may differ from that for H_2O^- because of Frank–Condon effects and different trap depths would be required. There are no theoretical or experimental results for testing this possibility.

References and Notes

(1) On leave of absence from the Institute of Applied Radiation Chemistry, Technical University, Lodz, Wroblewskiege, 15 Poland.
(2) The Radiation Laboratory of the University of Notre Dame is operated under contract with the U.S. Energy Research and Development Administration. This is ERDA Document No. COO-38-1019.
(3) A. H. Samuel and J. L. Magee, *J. Chem. Phys.*, **21**, 1080 (1953).
(4) W. H. Hamill, *J. Phys. Chem.*, **73**, 1341 (1969).
(5) K. Y. Lam and J. W. Hunt, *Int. J. Radiat. Phys. Chem.*, **7**, 317 (1975); R. K. Wolff, J. E. Aldrich, T. L. Penner, and J. W. Hunt, *J. Phys. Chem.*, **79**, 210 (1975).
(6) S. Kalarical, Ph.D. Dissertation, University of Notre Dame, 1956.
(7) H. Ogura and W. H. Hamill, *J. Phys. Chem.*, **77**, 2952 (1973).
(8) E. M. Fielden and E. J. Hart, *Radiat. Res.*, **32**, 568 (1967).
(9) J. H. Baxendale and A. S. Dixon, *Z. Phys. Chem. (Frankfurt am Main)*, **43**, 161 (1964).
(10) E. M. Fielden and E. J. Hart, *Radiat. Res.*, **33**, 426 (1968).
(11) J. H. Baxendale, E. M. Fielden, and J. P. Keen, *Proc. R. Soc. London, Ser. A*, **286**, 320 (1965).
(12) G. V. Buxton and R. M. Sellers, *J. Chem. Soc., Faraday Trans. 1*, **71**, 558 (1975).
(13) M. Matheson, private communication.
(14) G. Czapski and E. Peled, *J. Phys. Chem.*, **77**, 893 (1973).
(15) Work in progress.
(16) J. R. Miller, private communication.
(17) P. M. Rentzepis, R. P. Jones, and J. Jortner, *J. Chem. Phys.*, **59**, 766 (1973).
(18) C. A. Naleway and M. E. Schwartz, *J. Phys. Chem.*, **76**, 3905 (1972).
(19) L. Sanche and G. J. Schultz, *J. Chem. Phys.*, **58**, 479 (1972).
(20) K. Hiraoka and W. H. Hamill, *J. Chem. Phys.*, **57**, 3870 (1972).

Monomer Mobility and Solid State Polymerization of Alkali Metal Acrylates

Pier Paolo Saviotti[1] and D. F. R. Gilson*

Department of Chemistry, McGill University, Montreal H3C 3G1, Quebec, Canada

(Received November 5, 1975)

Publication costs assisted by the National Research Council of Canada

The presence of phase transitions in potassium and rubidium acrylates has been shown by wide-line nuclear magnetic resonance and differential scanning calorimetry. Transitions were not observed for the lithium and sodium salts. The differences in post-irradiation polymerization behavior of the alkali metal acrylates can be better explained by changes in monomer mobility than by control of the polymerization by the lattice geometry.

Introduction

The existence of some minimum degree of molecular mobility appears to be a prerequisite for solid state polymerization of crystalline monomers at temperatures well below the melting points, i.e., in the absence of enhanced molecular motions associated with premelting phenomena. The role of the crystal lattice is of less direct importance except in determining the nature of lattice defects where polymerization can occur. Few examples have been reported which directly correlate an increased rate of polymerization with the onset of molecular motion. Trioxane polymerizes above 293 K with a rapid increase in rate above 313 K and wide-line nuclear magnetic resonance studies indicated the presence of two transitions at these temperatures respectively.[2a] The polymerization of acrylonitrile[2b] has been associated with phase transitions which were subsequently shown to involve reorientation of the acrylonitrile molecule.[3]

An interesting example of significant differences in polymerization behavior by otherwise similar materials is found in the solid state polymerization of irradiated alkali metal acrylate salts studied by Morawetz and Rubin.[4] Potassium acrylate polymerized at 273 K at a higher rate than lithium acrylate at 374 K or sodium acrylate at 393 K. The rubidium salt polymerized only slightly slower than potassium acrylate. X-ray powder diffraction studies[4] showed that lithium, sodium, and potassium acrylates are not isomorphous and that the lithium and sodium salts did not undergo any phase transitions up to 413 K. Potassium acrylate is orthorhombic[5] but no other crystal structural information appears to have been reported for this series of compounds. Since it appeared unlikely that the alkali metal cation should play a significant role these wide differences in polymerization rates were attributed by Morawetz and Rubin to differences in the geometrical arrangement of the acrylate ion in the lattice. We have undertaken a wide-line NMR study of lithium, sodium, potassium, and rubidium acrylates to investigate whether monomer mobility differences could provide an alternative explanation.

Experimental Section

Lithium, sodium, and potassium acrylates were prepared by addition of acrylic acid to solutions of the alkali metal hydroxide in methanol. The salts were precipitated by addition of diethyl ether, washed with ether, redissolved in methanol,

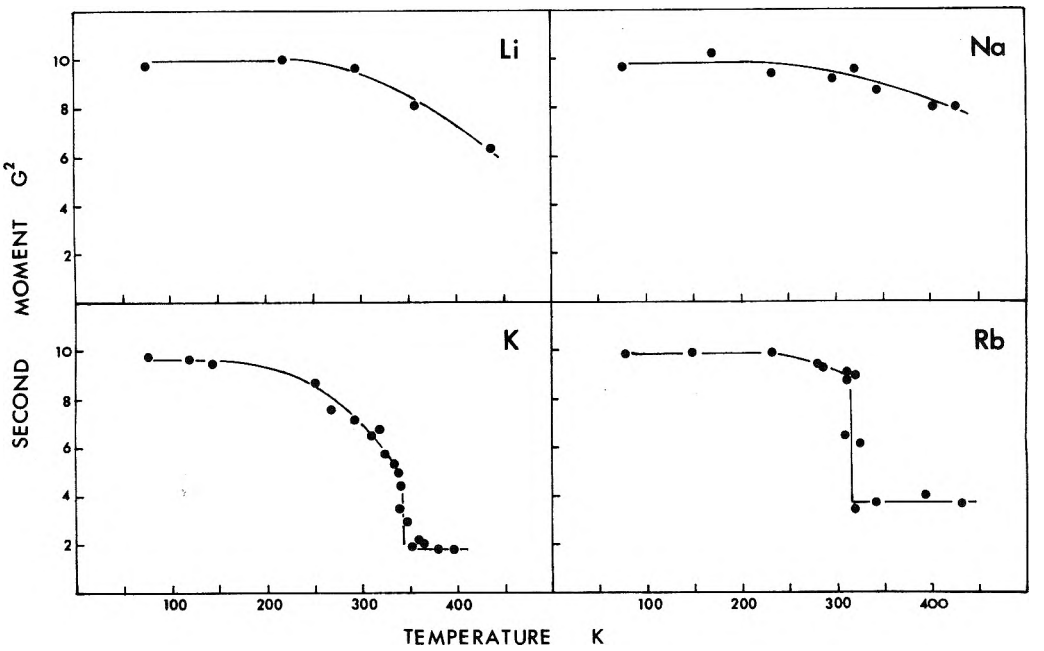

Figure 1. Temperature dependence of second moments of alkali metal acrylates.

and reprecipitated by slow (over 12 h) addition of ether. Rubidium acrylate was prepared by addition of the carbonate to a solution of acrylic acid in methanol followed by the procedure outlined above.

Wide-line NMR spectra were obtained using a 60-MHz spectrometer constructed essentially from Varian components. Sample temperatures were controlled by passing a heated or cooled stream of nitrogen gas around the sample and temperatures measured with copper–constantan thermocouples placed upstream and downstream from the sample.

Differential scanning calorimetric measurements were performed with a Perkin-Elmer DSC-1B calorimeter.

Results and Discussion

The temperature dependences of the second moments of the acrylate salts are shown in Figure 1. Potassium and rubidium acrylates undergo sharp transitions, at 334 and 320 K, respectively, which usually indicates a cooperative effect involving a change in crystal structure. The existence of these changes is confirmed by the observation of differential scanning calorimetric transitions at 339 K (potassium acrylate) and 333 K (rubidium acrylate). Attempts to obtain x-ray powder diffraction photographs for potassium acrylate above and below the transition were unsuccessful due to polymerization of the sample in the x-ray beam. The transition in the potassium salt is preceded by a gradual decrease in second moment starting at about 200 K.

Lithium and sodium acrylates show only gradual decreases in second moment with increasing temperature and no DSC transitions over the range 273–473 K were observed.

In order to determine the types of molecular motion responsible for the changes in second moments it is necessary to calculate the theoretical values and compare these with experiment. The intramolecular contribution to the total second moment can be easily computed from reasonable bond lengths and angles but the intermolecular second moment for an unknown structure can only be estimated by comparison with similar molecules. Acrylic acid,[6] acrylamide,[7] and acrylonitrile[3] have been investigated by wide-line NMR methods. The x-ray crystal structures of these compounds have been

TABLE I: Experimental Second Moments for Alkali Metal Acrylates

	Second moment, G^2	Temp, K
Lithium acrylate	9.7 ± 0.1	77
	6.5 ± 0.2	440
Sodium acrylate	9.8 ± 0.1	77
	8.2 ± 0.2	430
Potassium acrylate	9.7 ± 0.2	77
	2.0 ± 0.4	350–400
Rubidium acrylate	9.9 ± 0.5	77
	3.7 ± 0.4	350–450

reported[8–10] and these permit the calculation of the intermolecular second moment contributions in each case. Taking account of the different number of protons in acrylic acid and acrylamide, the intermolecular second moment contribution for the acrylates is estimated to be 2.79 ± 0.25 G^2. The intramolecular contribution was calculated from the structure given in Figure 2 to be 6.90 G^2 to give a total of 9.69 G^2 which is in good agreement with the experimental values at 77 K and therefore the acrylate ions are rigid at this temperature. This calculation assumes that the acrylate ion retains the same structure and that the intermolecular second moment is the same in each case even though the crystal structures are different. Contributions from alkali metal isotopes with nonzero spin are small and have been neglected.

The acrylate ion has no symmetry axis and thus there is no obvious choice of a preferred axis of reorientation. The following possible axes can be considered, Figure 3: (i) an internal rotation about the C_1–C_2 bond, (ii) and (iii) whole molecule rotation about a C–O bond direction, (iv) whole molecule rotation about the C_2=C_3 bond direction, (v) rotation about the axis of minimum moment of inertia, (vi) the axis perpendicular to the plane of the acrylate ion through the centre of gravity, and (vii) isotropic rotation. The calculated second moment contributions for these reorientational motions are given in Table II. The intermolecular values are estimated by applying the reduction factors calculated from Ban and

TABLE II: Calculated Second Moment Contributions (G^2)

		Intramolecular contribution	Intermolecular contribution	Total
	Rigid	6.68	2.79	9.47 ± 1.4
(i)	C_1–C_2 rotation	2.13	1.40	3.53 ± 0.7
(ii)	C_1–O_1 rotation	2.52	1.40	3.92 ± 0.7
(iii)	C_1–O_2 rotation	2.24	1.40	3.64 ± 0.7
(iv)	C_2=C_3 rotation	2.52	1.98	4.50 ± 1.0
(v)	Inertial axis rotation	3.31	1.41	4.72 ± 0.7
(vi)	Perpendicular axis rotation	1.67	1.41	3.08 ± 0.7
(vii)	Isotropic rotation	0	<1.0	<1.0

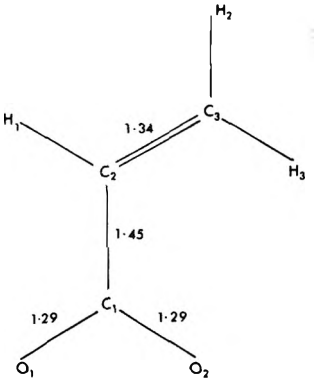

Figure 2. Bond lengths in the acrylate ion. All angles assumed to be 120°.

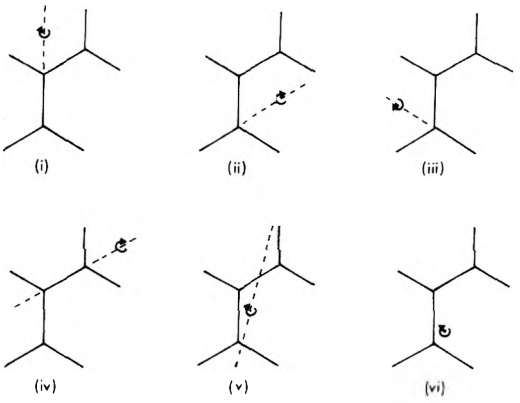

Figure 3. Possible reorientational motions of the acrylate ion.

Chachaty's results for acrylonitrile[3] and the error limits quoted are an arbitrary 50% of this contribution. Comparison of the theoretical second moments of Table II with the experimental values shows that no one particular motion can be unequivocally assigned as responsible for the line narrowing transitions in potassium and rubidium acrylates. The decrease in second moment in lithium and sodium acrylates, and in potassium acrylate prior to the transition, is due to increased torsional oscillation about some axis.

Isotropic rotation of an acrylate ion is unlikely and can be eliminated since the experimental second moments are too high. The second moment value above the transition in potassium acrylate is lower than any calculated value and this may be due to a combination of different motions. Ban and Chachaty[3] favored the rotation about the axis of least moment of inertia for acrylonitrile. The same motion could occur for the acrylate ions although the calculated second moment is high. The Coulombic forces between the carboxylic acid groups and the alkali metal ions would be stronger than the dipole forces in acrylonitrile and this would favor motions in which the carboxyl groups remain fixed in the lattice. Oscillations of 20 to 25° would account for the observed decreases in second moments for the lithium and sodium salts at 373 and 393 K, respectively.

In their studies of the post-polymerization of γ-irradiated acrylate salts Morawetz and Rubin[4] observed that the chain length of poly(potassium acrylate) produced under comparable dose rates and conversions, but at different temperatures, decreased by a factor of 3 from 273 to 333 K and then increased again at 374 K. An Arrhenius plot of the rates of polymerization for 19% conversion showed a straight line except for the point at 333 K. These specific effects observed in the polymerization of potassium acrylate can be attributed to the presence of the phase transition.

The degree of monomer mobility of the acrylate ion in this series of compounds, as indicated by the second moment values, parallels the rates of polymerization; Na < Li ≪ K < Rb. The hindrance to motion is determined by the interatomic forces in the crystal lattice and as such represents an indirect control by the lattice rather than a direct effect through the geometrical arrangement of the monomer units. Furthermore, polymerization in this type of compound occurs at defects and the extent of molecular motion in the bulk lattice is itself only an indirect measure of the influence of monomer mobility upon the polymerization reaction step.

Acknowledgment. The work was supported by grants from the National Research Council of Canada.

References and Notes

(1) NRCC Studentship 1971–1974.
(2) (a) A. Komaki and T. Matsumoto, *J. Polym. Sci. B1*, 671 (1963); (b) R. Bensasson, A. Dworkin, and R. Marx, *J. Polym. Sci. C*, **4**, 881 (1963).
(3) B. Ban and C. Chachaty, *Can. J. Chem.*, **51**, 3889 (1973).
(4) H. Morawetz and I. D. Rubin, *J. Polym. Sci.*, **57**, 669 (1962).
(5) I. Fankuchen, quoted in ref 4.
(6) B. Arnold and G. C. Eastmond, *Trans. Faraday Soc.*, **67**, 772 (1971).
(7) C. Chachaty and A. Forchioni, *J. Polym. Sci. A*, **10**, 1905 (1972).
(8) Y. Chatani, Y. Sakata, and I. Nitta, *J. Polym. Sci. B*, **1**, 419 (1963).
(9) I. V. Isakov, *Zh. Strukt. Khim.*, **7**, 808 (1966).
(10) R. H. Reddy, J. H. Goldstein, and L. Mandell, *J. Am. Chem. Soc.*, **83**, 1300 (1961).

Solubility Product Variability at Constant Pressure and Temperature

Robert I. Stearns and Alan F. Berndt*

Department of Chemistry, University of Missouri—St. Louis, St. Louis, Missouri 63121 *(Received November 14, 1975)*

Basic thermodynamic principles are applied to the concept of the solubility product and are used to demonstrate that the activity solubility product is not a constant at constant pressure and temperature but will vary with the composition of the aqueous phase. Experimental data are presented to verify this prediction.

Introduction

The classical theory of solubility products describes the equilibrium between an ionic solid and an aqueous solution containing its ions. In so doing the classical theory implicitly assumes the solid to be a perfect crystal of invariant composition, i.e., one possessing ideal stoichiometry. Modern solid-state theory teaches that the concept of the perfect crystal is an idealization tenable only at absolute zero.[1] As proven by Albers,[2] at temperatures above absolute zero, every ionic compound has an existence region extending to nonstoichiometric compositions. These deviations from stoichiometry arise from the presence of point defects in the solid.[2-4] While these deviations are usually quite small and undetectable by normal chemical analyses, they are nevertheless present at all temperatures above absolute zero.

Since ionic solids in equilibrium with aqueous solutions containing their ions do not have invariant compositions and may be nonstoichiometric, the fundamental requirements of the classical theory of solubility products are not met. It is the purpose of this paper to examine the concept of the solubility product in this context.

Theory

The classical theory considers an idealized solid salt, MA, to be in equilibrium with an aqueous solution containing the ions M^+ and A^- as well as possibly other ions at constant temperature and pressure (usually atmospheric). When two phases are in equilibrium then the chemical potentials of each and every chemical species are the same in both phases.[5] Thus we may write

$$\mu_{M^+,s} = \mu_{M^+,l} \quad (1)$$

$$\mu_{A^-,s} = \mu_{A^-,l} \quad (2)$$

From this it follows that

$$\mu^0_{M^+,s} + RT \ln a_{M^+,s} = \mu^0_{M^+,l} + RT \ln a_{M^+,l} \quad (3)$$

$$\mu^0_{A^-,s} + RT \ln a_{A^-,s} = \mu^0_{A^-,l} + RT \ln a_{A^-,l} \quad (4)$$

For the chemical potential of the solid, μ_s, we may make the usual approximation in which the contributions of point defects in the solid such as vacancies, interstitial, and misplaced atoms (antistructure), etc.,[3,4] are neglected. We may write

$$\mu_s = \mu_{M^+,s} + \mu_{A^-,s} = \mu_{M^+,l} + \mu_{A^-,l} \quad (5)$$

Therefore

$$\mu^0_s + RT \ln a_s = \mu^0_{M^+,l} + RT \ln a_{M^+,l} + \mu^0_{A^-,l} + RT \ln a_{A^-,l} \quad (6)$$

Equation 6 gives

$$a_{M^+,l} a_{A^-,l} / a_s = K \quad (7)$$

where

$$RT \ln K = \mu^0_s - \mu^0_{M^+,l} - \mu^0_{A^-,l} \quad (8)$$

When the classical theory is applied the pure solid is chosen as the standard state. The activity of the solid, a_s, is assigned a value of one. The solid is implicitly assumed to be the idealized perfect crystal of exact stoichiometric composition and point defects are ignored. With these stipulations eq 7 reduces to

$$a_{M^+,l} a_{A^-,l} = K_{sp} \quad (9)$$

Equation 9 is the classical equation for the solubility product expressed in terms of activities. However, as we have seen above, ionic solids in equilibria with aqueous solutions do not possess invariant compositions and need not be, and usually are not, of perfect stoichiometry. Moreover point defects are present. Therefore, eq 9 is at best an approximation.

The precise way to describe these equilibria can be obtained from the combination of eq 7 and 8 to give

$$a_{M^+,l} a_{A^-,l} = a_s \exp\{(\mu^0_s - \mu^0_{M^+,l} - \mu^0_{A^-,l})/RT\} \quad (10)$$

In eq 10 the chemical potentials and activities of the ionic species in the aqueous phase have their usual meanings.[5] If the hypothetical perfect crystal of ideal stoichiometry having fixed, however, unknown, concentrations of point defects, is chosen as the standard state for the solid then μ^0_s is invariant (a function of temperature and pressure only). In this case a_s varies as the stoichiometry and concentrations of the point defects vary. From eq 3 and 4 which neglect the point defects, it can be seen that the activities of M^+ and A^- in the aqueous phase need not be equal. Their numerical values may vary over many orders of magnitude. It is evident from eq 3 and 4 that as their activities in the aqueous phase vary, so must the activities of M^+ and A^- in the solid phase vary, thus causing a variation in the activity of the solid, a_s.

Another way of looking at this is to assign $a_s = 1$ for any stoichiometry, i.e., to choose as the standard state the particular solid which exists under the particular set of equilibrium conditions. In this case as the stoichiometry varies so must μ^0_s vary.

Whichever approach is taken to the assignment of a standard state results in the conclusion that the right-hand side of eq 10 is not a constant, i.e., the solubility product

$$a_{M^+,l} a_{A^-,l}$$

will vary as the activities of the species in solution vary. The classical assumption is equivalent to assigning $a_s = 1$ and simultaneously assuming μ^0_s to be constant.

For convenience and simplicity in writing eq 1–10 the salt was taken to have 1:1 stoichiometry with unit charges on the ions. The arguments which are presented are equally valid for salts of other compositions and for ions with other charges and thus the conclusion that variations in the activities of the ions

TABLE I: Experimental and Calculated Data for Solubility of Calcium Fluoride

$[Ca^{2+}]_i$	$[NaC_2H_3O_2]_i$	$[HC_2H_3O_2]_i$	$[F^-]_{eq}$	$[Ca^{2+}]_{tot}$,[a] eq	$[Ca^{2+}]_{eq}$	μ	$\gamma_{Ca^{2+}}$	γ_{F^-}	$-\log (a_{Ca^{2+}})$	$-\log (a_{F^-})$	$10^{12}(a_{Ca^{2+}})(a_{F^-})^2$
1×10^{-1}	0.587	2.958×10^{-2}	4.65×10^{-5}	1.000×10^{-1}	2.507×10^{-2}	0.734	0.218	0.597	2.262	4.557	4.22
5×10^{-2}	0.588	2.970×10^{-2}	7.1×10^{-5}	5.004×10^{-2}	1.190×10^{-2}	0.658	0.225	0.605	2.572	4.367	4.94
2×10^{-2}	0.590	2.974×10^{-2}	1.21×10^{-4}	2.006×10^{-2}	4.628×10^{-3}	0.615	0.229	0.610	2.975	4.132	5.77
1×10^{-2}	0.590	2.976×10^{-2}	1.8×10^{-4}	1.009×10^{-2}	2.306×10^{-3}	0.600	0.231	0.612	3.274	3.958	6.46
5×10^{-3}	0.590	2.976×10^{-2}	2.5×10^{-4}	5.125×10^{-3}	1.165×10^{-3}	0.592	0.232	0.613	3.568	3.815	6.35
2×10^{-3}	0.590	2.976×10^{-2}	3.8×10^{-4}	2.190×10^{-3}	4.961×10^{-4}	0.588	0.232	0.614	3.939	3.632	6.26
1×10^{-3}	0.590	2.976×10^{-2}	4.6×10^{-4}	1.230×10^{-3}	2.787×10^{-4}	0.587	0.232	0.614	4.189	3.549	5.16
5×10^{-4}	0.590	2.976×10^{-2}	5.5×10^{-4}	7.756×10^{-4}	1.758×10^{-4}	0.586	0.232	0.614	4.389	3.471	4.66
0	0.590	2.976×10^{-2}	7.0×10^{-4}	3.507×10^{-4}	7.932×10^{-5}	0.585	0.232	0.614	4.735	3.367	3.40

[a] $[Ca^{2+}]_{tot} = [Ca^{2+}]_i + (1.002/2)[F^-]_{eq} = [Ca^{2+}]_{eq} + [CaC_2H_3O_2^+]_{eq}$.

in solution lead to variations in the solubility product is true for salts of any composition.

It should be noted that nonstoichiometry due to the presence of impurities is not a factor here. The effect on solubility of the substitution of an impurity such as B^- which gives rise to a solid solution with MA, i.e., $MA_xB_{(1-x)}$, has been previously discussed.[6]

Although the above discussion demonstrates that the solubility product will vary with ionic composition at constant temperature and pressure it might be argued that the possible variations are too small to be measured experimentally and therefore are of no consequence. In the next section data are presented to show that in at least one case, CaF_2, an effect consistent with the theoretical prediction can be observed experimentally.

Experimental Section

The solubility product of CaF_2 was measured experimentally, at 20 °C, in this laboratory. A series of solutions was prepared with various concentrations of Ca^{2+}, added as $Ca(NO_3)_2 \cdot 4H_2O$, in a pH 5.9 acetate buffer (prepared by adding glacial acetic acid to a sodium acetate solution until a pH of 5.9 was obtained). Excess solid CaF_2 was added to approximately 50 ml of each solution and the fluoride ion concentration was measured with a specific fluoride ion electrode.[7] The buffer was used primarily to fix pH but also to provide a medium of relatively constant ionic strength. Equilibrium was assumed to be reached when the measured fluoride ion concentration no longer changed with time. This occurred within 24 h but the values reported in Table I were measured 2 days after the solutions were prepared. Each reported value was measured twice on each of two separate portions of the sample. In each case the measured potential was precisely the same for both portions.

The initial calcium ion, sodium acetate, and acetic acid concentrations, and the measured equilibrium fluoride concentrations are given in Table I for each of nine solutions. The pH of each of these solutions was measured initially and at equilibrium and was found to be 5.9 in every case. Dissolved calcium is present as two species, the simple hydrated calcium ion and the complex ion, $CaC_2H_3O_2^+$. The total calcium concentration, $[Ca^{2+}]_{tot}$, is taken to be equal to the initial calcium concentration plus one-half of the total fluoride concentration due to dissolved CaF_2. This latter value is equal to $[F^-]$ at equilibrium plus [HF] at equilibrium. At pH 5.9 and taking the ionization constant of hydrofluoric acid to be 6.7×10^{-4} [8] the total dissolved fluoride concentration is equal to $1.002[F^-]$.

The equilibrium calcium ion concentration, $[Ca^{2+}]_{eq}$, was calculated using the following quadratic equation:

$$5.9[Ca^{2+}]_{eq}^2 + \{1.07 + 5.9([C_2H_3O_2^-]_{tot} - [Ca^{2+}]_{tot})\}[Ca^{2+}]_{eq} - 1.07[Ca^{2+}]_{tot} = 0$$

Here $[Ca^{2+}]_{tot}$ is the total calcium concentration as defined above and $[C_2H_3O_2^-]_{tot}$ is given by the initial concentration of sodium acetate plus acetic acid, Table I. This quadratic equation was derived from the following four equations:

$$[C_2H_3O_2^-]_{eq} = [C_2H_3O_2^-]_{tot} - [CaC_2H_3O_2^+]_{eq} - [HC_2H_3O_2]_{eq}$$

$$[Ca^{2+}]_{tot} = [Ca^{2+}]_{eq} + [CaC_2H_3O_2^+]_{eq}$$

$$\frac{[CaC_2H_3O_2^+]_{eq}}{[Ca^{2+}]_{eq}[C_2H_3O_2^-]_{eq}} = 1/0.17 = 5.9 \text{ [9]}$$

$$\frac{[H^+][C_2H_3O_2^-]_{eq}}{[HC_2H_3O_2]_{eq}} = 1.8 \times 10^{-5} \text{ [10]}$$

Activities were calculated by the Debye–Huckel approximation[11] after correcting the constants for temperature.[12] At 20 °C the Debye–Huckel formula for the ionic activity coefficient becomes $\log \gamma_i = -0.5216Z_i^2 \sqrt{\mu}/(1 + 0.3309\alpha_i \sqrt{\mu})$ where Z_i is the charge on the ion and α_i is the hydrated ionic diameter (3.5 Å for F^- and 6 Å for Ca^{2+}).[13] The ionic strength is given by[9] $\mu = \frac{1}{2}\Sigma Z_i^2[i]$.

In Table I are presented calculated values of $[Ca^{2+}]$ at equilibrium, μ, $\gamma_{Ca^{2+}}$, and γ_{F^-}. Also tabulated is the apparent activity solubility product, $(a_{Ca^{2+}})(a_{F^-})^2$, and values of $-\log (a_{Ca^{2+}})$ and $-\log (a_{F^-})$. From these last three sets of calculated results it is seen that indeed the apparent activity solubility product is not constant but does vary with calcium and fluoride ion activities. The relationship between the apparent activity solubility product and the activity of solubility product and the activity of Ca^{2+} in the aqueous phase is shown graphically in Figure 1.

If the error in measuring the $[F^-]$ by the specific fluoride ion electrode were to be about 1 mV, and actually the difference between equivalent readings was much less than this, then the error in $[F^-]$ would be about 4%. This translates to about a maximum 8% error in the calculated apparent activity solubility product. The variations in ionic strength between some of our solutions and those solutions used to calibrate the specific fluoride ion electrode ($\mu \approx 0.59$) translate to a maximum possible error of about 5% in the measured $[F^-]$ in those solutions of higher initial $[Ca^{2+}]$. This results from the variation in γ_{F^-} (Table I) and the fact that the electrode actually measures activities and not concentrations. This error is of the same order of magnitude as the possible error from reading the potential. Thus experimental error cannot account for the observed variation.

Nearly half a century ago the solubility of CaF_2 was inves-

TABLE II: Experimental Data of Auméras and Calculated Results for Solubility of Calcium Fluoride

[HF]	[$CaCl_2$]	[HCl]	μ	$\gamma_{Ca^{2+}}$	γ_{H^+}	γ_{F^-}	$[F^-]10^4$	$-\log (a_{F^-})$	$-\log (a_{Ca^{2+}})$	$10^{10}(a_{Ca^{2+}})\cdot(a_{F^-})^2$
0.01	0.005	0.017	0.032	0.538	0.872	0.841	5.08	3.369	2.570	4.92
0.02	0.010	0.045	0.075	0.435	0.838	0.784	4.42	3.460	2.362	5.22
0.03	0.015	0.080	0.125	0.377	0.817	0.745	4.06	3.519	2.248	5.18
0.04	0.020	0.132	0.192	0.332	0.800	0.711	3.53	3.600	2.178	4.19
0.05	0.025	0.195	0.270	0.300	0.787	0.683	3.17	3.665	2.125	3.51
0.02	0.005	0.034	0.049	0.486	0.855	0.813	5.49	3.350	2.614	4.85
0.03	0.005	0.050	0.065	0.452	0.843	0.794	5.86	3.332	2.646	4.90
0.04	0.005	0.069	0.084	0.421	0.833	0.775	5.90	3.340	2.677	4.40
0.05	0.005	0.086	0.101	0.400	0.825	0.761	6.10	3.333	2.699	4.32
0.06	0.005	0.102	0.117	0.384	0.819	0.750	6.32	3.324	2.717	4.32
0.01	0.010	0.024	0.054	0.474	0.851	0.807	3.90	3.502	2.324	4.70
0.01	0.015	0.029	0.074	0.436	0.838	0.785	3.38	3.576	2.184	4.61
0.01	0.020	0.035	0.095	0.407	0.828	0.766	2.92	3.650	2.089	4.08
0.01	0.025	0.038	0.113	0.388	0.821	0.753	2.77	3.681	2.013	4.22
0.01	0.030	0.042	0.132	0.371	0.814	0.741	2.57	3.720	1.954	4.04

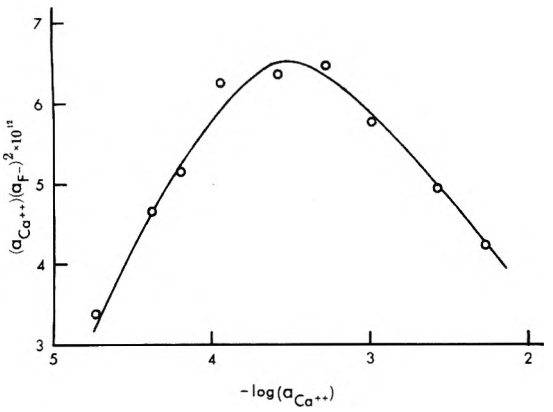

Figure 1. Variation of apparent activity solubility product of calcium fluoride with calcium ion activity in the aqueous phase.

tigated as a function of calcium and fluoride ion concentrations by Auméras.[14] He prepared a series of solutions by mixing, at 25 °C, known amounts of standard aqueous solutions of HF and $CaCl_2$. In each case a precipitate of CaF_2 was formed. The resulting mixtures were titrated with a standard HCl solution, with agitation, until the precipitate was observed just to disappear. In each case the volume was adjusted by the addition of water to be exactly 100 ml at the end point.

The molar concentrations of HF, $CaCl_2$, and HCl were reported for the final solutions for 15 different experiments. His data are reproduced in Table II. Auméras assumed, properly so, that these final solutions were essentially in equilibrium with solid CaF_2 and thus the data may be used to calculate the solubility of CaF_2.

We have reexamined his data, applying the Debye–Huckel approximation for the estimation of ionic activity coefficients, and have calculated the apparent solubility product of CaF_2 as a function of the ionic activities in the aqueous phase. The Debye–Huckel formula at 25 °C,[11] $\log \gamma_i = -0.5085Z_i^2\sqrt{\mu}/(1 + 0.3281\alpha_i\sqrt{\mu})$, was used to calculate the activity coefficients for Ca^{2+}, H^+, and F^-. The ionic strengths were calculated in the usual way, assuming that $CaCl_2$ and HCl were completely ionized and neglecting the contribution of the fluoride ion. The value of α_{H^+} was taken as 9 Å.[13]

The value of [HF] reported by Auméras and presented in Table II represents the total fluoride in solution which may exist as molecular HF, the complex species HF_2^-, or the ionic species F^-. Thus one may write

$$[HF]_{tot} = [HF] + 2[HF_2^-] + [F^-]$$

Also

$$\frac{(a_{H^+})(a_{F^-})}{a_{HF}} = 6.7 \times 10^{-4} = \frac{\gamma_{H^+}[H^+]\gamma_{F^-}[F^-]}{\gamma_{HF}[HF]}$$

and for the dissociation of HF_2^- [15]

$$\frac{(a_{F^-})(a_{HF})}{a_{HF_2^-}} = 0.26 = \frac{\gamma_{F^-}[F^-]\gamma_{HF}[HF]}{\gamma_{HF_2^-}[HF_2^-]}$$

The value of $[H^+]$ was taken to be equal to the concentration of added HCl and γ_{HF} was taken to be unity for the molecular species HF. To calculate $\gamma_{HF_2^-}$ the value of $\alpha_{HF_2^-}$ is necessary but unavailable. The value of $\gamma_{HF_2^-}$ was approximated to be equal to γ_{F^-} since charge is more important in the Debye–Huckel formula than the hydrated ion diameter. (The existence of HF_2^- was neglected in the calculations made with our set of data because the fact that these solutions were buffered to pH 5.9 made $[HF_2^-]$ negligible.)

The above three equations were combined to give

$$\frac{2\gamma_{H^+}\gamma_{F^-}[H^+]}{(0.26)(6.7 \times 10^{-4})}[F^-]^2 + \left\{1 + \frac{\gamma_{H^+}\gamma_{F^-}[H^+]}{6.7 \times 10^{-4}}\right\}[F^-] - [HF]_{tot} = 0$$

This equation was solved for $[F^-]$ for each of the 15 sets of data. The calculated values of $[F^-]$ are presented in Table II along with values for $-\log (a_{Ca^{2+}})$, $-\log (a_{F^-})$, and $(a_{Ca^{2+}})(a_{F^-})^2$.

The calculated results presented in Table II indicate that the apparent activity solubility product of CaF_2 varies as the activities of Ca^{2+} and F^- vary in the aqueous phase. The relationship between the apparent solubility product and the activity of Ca^{2+} in the aqueous phase, as calculated from the data of Auméras, is shown graphically in Figure 2.

Discussion

Our data, Table I and Figure 1, cover a range of $\log (a_{Ca^{2+}})$ from −4.74 to −2.26 and show that the apparent activity solubility product of CaF_2 passes through a maximum at approximately $\log (a_{Ca^{2+}}) = -3.5$. Auméras' data, Table II and Figure 2, covering a much smaller range ($\log (a_{Ca^{2+}})$ varies from −2.72 to −1.95) show a maximum at about $\log (a_{Ca^{2+}}) = -2.45$ in pleasing agreement with the results calculated from our data.

The textbook value for the classical solubility product of CaF_2 at 25 °C is 4×10^{-11}.[16] The solubility product may be

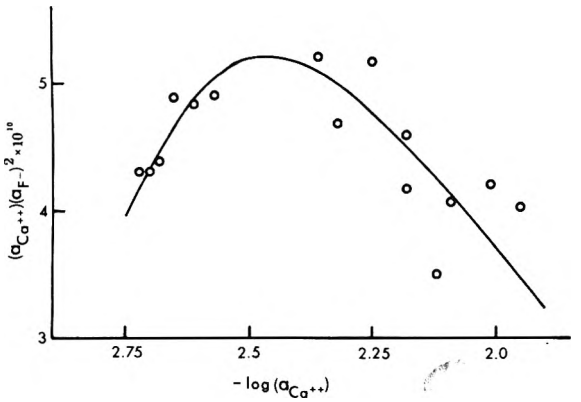

Figure 2. Variation of apparent activity solubility product of calcium fluoride with calcium ion activity in the aqueous phase (from data of Auméras).

calculated from available standard free energy of formation data by the equation

$$\Delta G^\circ_{\text{ionization}} = -RT \ln K_{sp}$$

If one takes $\Delta G^\circ_{f,CaF_2(s)} = -277.7$ kcal/mol, $\Delta G^\circ_{f,Ca^{2+}(aq)} = -132.18$ kcal/mol and $\Delta G^\circ_{f,F^-(aq)} = -66.08$ kcal/mol[17] the calculated solubility product is 1.6×10^{-10} at 25 °C. Our data give an average value of 5.2×10^{-12} at 20 °C while Auméras' data yield an average of 4.5×10^{-10} at 25 °C. The latter value is quite sensitive to the value chosen for the ionization constant of HF while the effect of the number chosen for this constant on our calculated results is negligible. Our value is sensitive to the value of the equilibrium constant for the complex ion formation.

The differences between the value from Auméras' data and our value and between these values and others, both reported (experimental) and calculated, are not important. What is important is that each set of data, Tables I and II, is internally consistent and each shows a variation of the apparent activity solubility product with variations in the ionic activities in the aqueous phase.

It might be argued that the observed variation in the apparent activity solubility product might be the result of inaccuracies in the Debye–Huckel theory or its application. Errors introduced from inherent imprecision in the Debye–Huckel theory, or from its improper application (such as errors in the values of the hydrated ion diameters used, which are merely averages for many systems), should be expected to increase with ionic strength. If the observed effect were due to these errors then a plot of the apparent activity solubility product vs. ionic strength would be expected to be a smooth curve (within experimental error) which would extrapolate to the true solubility product at $\mu = 0$. Such plots made with the data of Tables I and II show a random distribution of points. It is therefore concluded that the observed variation is real and is not caused by an artifact in the Debye–Huckel theory. Inaccuracies in the Debye–Huckel approximation may well effect the absolute values of the calculated apparent activity solubility products. However, the variation in these numbers with $a_{Ca^{2+}}$ cannot be so explained.

In our experiments all reagents used came from the same stock bottles for all experiments. Thus any impurities present in one experiment must have been present in all. It is unlikely that the possible presence of impurities could account for the observed results. We cannot, however, vouch for Auméras' techniques.

We can offer no clear explanation or hypothesis as to why the apparent activity solubility product goes through a maximum as $a_{Ca^{2+}}$ increases. The theory we have presented merely states that there should be a variation but does not predict the nature of this variation. The system is much more complicated than might be intuitively assumed. This becomes evident when it is realized that a complete description of the solid requires consideration of all kinds of point defects.[3,4]

Conclusion

A theoretical discussion is presented which demonstrates that the classical activity solubility product of an ionic solid is not truly a constant, at constant temperature and pressure, but varies with the ionic composition of the aqueous phase in equilibrium with it. This variation results from the fact that any ionic solid in equilibrium with an aqueous phase does not have an invariant composition and will in general be nonstoichiometric. These deviations from stoichiometry may be too small to measure by ordinary chemical analysis but, nevertheless, they are present and are the result of the existence of point defects in the solid. The theoretical conclusion is verified experimentally in the case of CaF_2.

References and Notes

(1) W. Albers, "Physical Chemistry of Defects", in "Physics and Chemistry of II-VI Compounds", M. Aven and J. S. Prener, Ed., Wiley, New York, N.Y., 1967, p 170.
(2) Reference 1, p 171.
(3) F. A. Kroger, "The Chemistry of Imperfect Crystals", Wiley, New York, N.Y., 1964.
(4) W. Van Gool, "Principles of Defect Chemistry of Crystalline Solids", Academic Press, New York, N.Y., 1966.
(5) See any standard text on Physical Chemistry.
(6) A. F. Berndt and R. I. Stearns, *J. Chem. Educ.*, **50**, 415 (1973).
(7) Orion Model 94-09.
(8) R. B. Fischer and D. G. Peters, "Quantitative Chemical Analysis", W. B. Saunders, Philadelphia, Pa., 1968, p 833.
(9) C. A. Colman-Porter and C. B. Monk, *J. Chem. Soc.*, 4363 (1952).
(10) W. J. Blaedel and V. W. Meloche, "Elementary Quantitative Analysis", Harper and Row, New York, N.Y., 1963, p 925.
(11) Reference 10, p 702.
(12) W. J. Moore, "Physical Chemistry", 3d ed, Prentice-Hall, Englewood Cliffs, N.J., 1962, pp 354–356.
(13) Reference 10, p 921.
(14) M. Auméras, *J. Chim. Phys. Physicochim. Biol.*, **24**, 548 (1927).
(15) Reference 10, p 923.
(16) Reference 8, p 829.
(17) R. C. Weast, Ed., "Handbook of Chemistry and Physics", 52nd ed, Chemical Rubber Company Press, Cleveland, Ohio, 1971, pp D-63, D-65.

The Deuterium Isotope Separation Factor between Hydrogen and Liquid Water†

J. H. Rolston,* J. den Hartog, and J. P. Butler

Atomic Energy of Canada Limited, Chalk River Nuclear Laboratories, Chalk River, Ontario, Canada K0J 1J0 *(Received July 28, 1975)*

Publication costs assisted by Atomic Energy of Canada Limited

The overall deuterium isotope separation factor between hydrogen and liquid water, α, has been measured directly for the first time between 280 and 370 K. The data are in good agreement with values of α calculated from literature data on the equilibrium constant for isotopic exchange between hydrogen and water vapor, K_1, and the liquid–vapor separation factor, α_V. The temperature dependence of α over the range 273–473 K based upon these new experimental results and existing literature data is given by the equation $\ln \alpha = -0.2143 + (368.9/T) + (27\,870/T^2)$. Measurements on α_V given in the literature have been surveyed and the results are summarized over the same temperature range by the equation $\ln \alpha_V = 0.0592 - (80.3/T) + (25\,490/T^2)$.

Introduction

A precise knowledge of the equilibrium distribution of deuterium between hydrogen and liquid water is required for the economic evaluation of heavy water production processes involving exchange of isotopes between hydrogen and liquid water. This distribution has not previously been measured directly but has been calculated from gas phase exchange data and the isotopic fractionation between vapor and liquid water. At low deuterium levels the isotope distribution in the gas phase is given by the equilibrium constant, K_1, for the exchange reaction

$$H_2O(v) + HD \rightleftharpoons HDO(v) + H_2 \qquad (1)$$

Early determinations of K_1, involving equilibration over a variety of noble and base metal catalysts, show considerable scatter but in general support the values calculated from statistical mechanics.[1]

Examination of the data on K_1 reported by Kirshenbaum[1] together with those of Cerrai et al.[2] and Suess[3] shows there are very few data available below 323 K; a fact which has been noted by Weston[4] and by Wolfsberg.[5] Furthermore, below 373 K, the agreement with theory is rather poor and both authors have suggested that refined measurements of K_1 should be attempted in the low temperature range.

Such a study would appear opportune in view of the recent advances in the theoretical calculation of isotope exchange equilibrium constants which have followed from the rediscovery[6] of G_0, an isotope and quantum number-dependent term in the expression for the vibrational energy of a molecule in its rotational ground state. With this modification, most of the controversy concerning corrections for anharmonicity effects appears to have been resolved.[7] Previously Bottinga[8] reported an anharmonicity correction to K_1 as large as −16.1% at 298 K while Wolfsberg[5] has shown that the corrections are only −10.8% of the value calculated under the usual harmonic approximation. Furthermore, Wolfsberg has demonstrated that these corrections are partially off-set by the incorporation of G_0 into the partition functions and lead to revised theoretical values of K_1 numerically identical with those calculated 32 years ago and reported by Kirshenbaum et al.[1]

More recently, isotope partition function ratios for selected simple molecules have been evaluated from molecular potential functions.[9] These functions are independent of the isotopic mass within the Born–Oppenheimer (BO) approximation and together with equilibrium geometries evaluated from spectroscopic studies provide an alternative approach to the evaluation of isotopic equilibrium constants. This method is gaining general acceptance as it does not rely directly on the measured values of vibrational frequencies in the determination of the partition functions. In the next paper Bardo and Wolfsberg[10] have calculated values of K_1 by this procedure and have compared their results with the experimental data presented here. The theoretical curve of the equilibrium constant as a function of temperature agrees with the experimental curve within 0.5% in the temperature range 273–473 K.

The general paucity of low temperature data on K_1 and the less than satisfactory agreement between theory and experiment reduced our confidence in being able to predict the value of the equilibrium constant, K_2, for the gas–liquid exchange reaction

$$H_2O(l) + HD \rightleftharpoons HDO(l) + H_2 \qquad (2)$$

over an extended range of temperature. At low deuterium levels K_2 can be calculated by multiplying K_1 by the separation factor for isotopic distillation, α_V. The more straightforward approach, reported below, is to measure K_2 directly and to avoid the additional work and uncertainties in measuring K_1 and α_V separately.

Experimental Section

(1) *Apparatus.* The equilibration cell used was fabricated from a 50-ml round-bottom flask as shown in Figure 1. The solid glass barrel of the Young valve (J. Young Co. Ltd., Acton, England) was lengthened by a 4 cm length of glass rod which served to compress a silicone rubber tip against a 13-μm diameter hole in the wall of the reaction flask. The "pinhole" leak was created by sealing a 13-μm diameter tungsten wire in the glass wall, grinding the outside surface flat and removing the metal by applying a discharge from a Tesla coil through the wire to a ground. The length of the leak was kept to the thickness of the wall and thus minimized the dead space available during sampling.

A stainless steel bellows was used to connect the Young valve to a series of spirally wound vapor traps which were kept partially immersed in liquid N_2.

(2) *Procedure.* A novel catalyst suitable for equilibrating hydrogen with liquid water was prepared by impregnating a

† A.E.C.L.-5412.

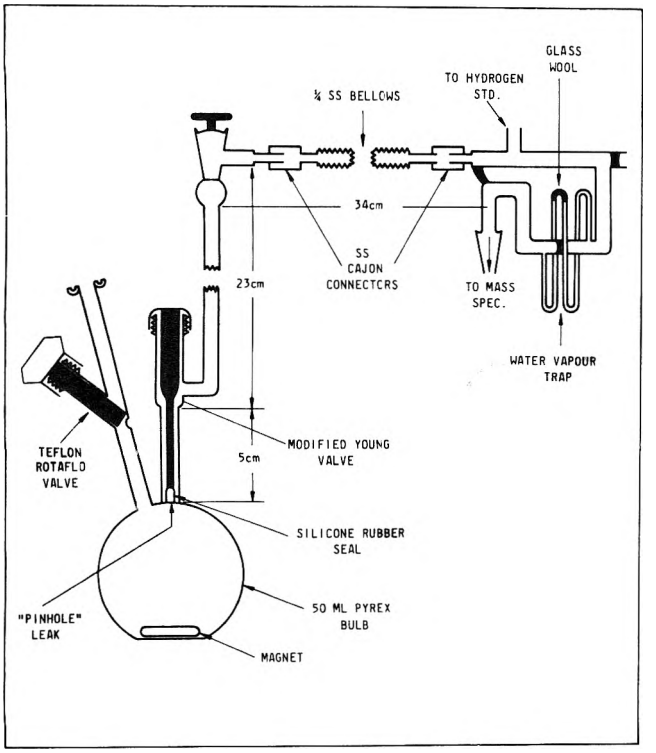

Figure 1. Schematic drawing of hydrogen–liquid water isotope equilibration cell.

3-mm thick porous Teflon sheet[11] with an acetone solution of chloroplatinic acid, evaporating the solvent, and reducing the acidic deposits at 473 K under hydrogen.[12] The impregnated sheet was cut into 3-mm cubes, weighed, and loaded into the equilibration flask. The flask and catalyst were rinsed with a stock solution of deuterium enriched water (atom ratio, D/H = 19 564 × 10^{-6}) and evacuated to dryness. A fresh 5-ml sample of deuterium enriched water was transferred to the flask and degassed by three freeze–pump–thaw cycles, using liquid nitrogen. The degassed water and catalyst were frozen and the flask was pressurized with 0.1450 MPa of purified hydrogen (D/H = 9681 × 10^{-6}). The flask was placed in a thermostatted bath controlled to ±0.005 K and cell temperatures were measured with a calibrated thermometer to ±0.01 K. The solution and floating catalyst cubes were continuously agitated by a magnetic stirrer mounted below the cell. After allowing time for temperature equilibration, gas samples for mass spectrometric analysis were taken from the exchange cell at intervals of 30 min.

(3) *Mass Spectrometry.* The hydrogen samples were analyzed on a Consolidated Electronics Corp. spectrometer Model CEC 21-614. To ensure reliable and reproducible results the inlet gas pressure was carefully controlled and provision was made for analysis of standard samples under conditions nearly identical with those prevailing at the time of the equilibration experiments. The spectrometer was operated with high input sensitivity (low input pressures). During each analysis masses 2 and 3 were scanned consecutively and both peak heights were measured 2.0 min after introduction of the sample, by linear extrapolation of the peak heights.

A correction curve for H_3^+ was constructed by measuring a hydrogen sample with a low deuterium concentration (D/H = 10 × 10^{-6}) over an extended range of inlet pressures and filament currents. These data were fitted to an equation of the form

$$\Delta_3 = A\cdot\mathrm{Pht}(2) + B\cdot\mathrm{Pht}(2)^2 \qquad (3)$$

so that given the mass 2 peak height, Pht(2), the H_3^+ correction to the mass 3 peak, Δ_3, could be accurately calculated. For inlet pressures of 0.6 Pa the hydrogen background and H_3^+ correction were less than 0.5 and 1% of the mass 2 and mass 3 peak heights, respectively, when measured against a hydrogen sample with an atom ratio D/H = 5000 × 10^{-6}.

(4) *Standards.* Hydrogen standards of varying deuterium contents were prepared by total decomposition of deuterium enriched water over uranium metal at 873 K. These were used to establish the sensitivity factor, f, of the spectrometer for the H_2 and HD species and to show that this ratio was independent of the deuterium concentration over the range expected for samples from the reaction cell. Analysis of each hydrogen sample taken from the exchange cell was followed by an analysis of a hydrogen standard attached above the spiral trap so as to avert errors due to drifting of the spectrometer sensitivity with time.

(5) *Calculations.* The determination of the separation factor between two chemical species such as hydrogen and water generally requires simultaneous analysis of both components under conditions which do not disturb the isotopic equilibrium. This procedure can be simplified when there is a large molar excess of one component relative to the other so that the deuterium content of the major component is not substantially altered.[13] In the present instance the use of an excess of liquid water ensures this condition.

Liquid water was transferred from a reservoir of known isotopic content and frozen in the cell before hydrogen was added. Thus initially the reactor cell contained no water vapor or dissolved hydrogen. Provided the quantities of hydrogen and water vapor removed from the cell in the course of the experiments are negligible, a deuterium balance between the phases can be applied. Hence the deuterium atom fraction of the liquid at equilibrium, F_L^e, can be evaluated from

$$F_L^e N_L^e = F_L^i N_L^i + F_H^i N_H^i - F_H^e N_H^e - F_V^e N_V^e - F_D^e N_D^e \qquad (4)$$

in which F denotes the deuterium atom fraction and N the number of moles of each component. The superscripts i and e refer respectively to the initial charges to the cell and to the values at equilibrium and the subscripts L, V, H, and D refer to liquid water, water vapor, gaseous hydrogen, and dissolved hydrogen, respectively. Application of mass balances over the chemical species simplifies eq 4 to

$$F_L^e = F_L^i(1 + S) + R(F_H^i - F_H^e) - SF_V^e + QF_H^e(1 - \alpha_D) \qquad (5)$$

where R denotes the mole ratio of the initially added hydrogen to liquid water at equilibrium and S is the mole ratio of vapor to liquid water at equilibrium. The deuterium separation factor between dissolved and gaseous hydrogen, α_D, is given, at low concentrations, by the ratio F_D^e/F_H^e and Q is the equilibrium mole ratio of dissolved hydrogen to liquid at each temperature. Typically, Q is 1.5 × 10^{-5} and α_D is not expected to exceed 1.1 at any temperature above 273 K,[25] hence the last term in eq 5 is 10^{-4}% of the first term in the expression and can therefore be neglected. If it is further assumed that F_V^e/F_L^e can be equated to α_V^{-1} where

$$\alpha_V = \frac{F_L^e(1 - F_V^e)}{F_V^e(1 - F_L^e)} \qquad (6)$$

then the equilibrium atom fraction of the liquid can be calculated from

$$F_L^e = \frac{F_L^i(1 + S) + R(F_H^i - F_H^e)}{1 + S\alpha_V^{-1}} \qquad (7)$$

It should be noted that F_L^e is essentially equal to F_L^i plus a small correction. The correction is about 0.2% because the molar ratios of hydrogen and water vapor to liquid water are small (typically 0.008 and 0.005, respectively) and the initial deuterium concentration of the hydrogen was not too different from the equilibrium values at each temperature. Thus an error in the fractionation factor between liquid water and water vapor or in the relative amounts of gas to liquid will have little effect on the calculated value of F_L^e.

Results and Discussion

At low deuterium concentrations the isotopic separation factor, α, between hydrogen and liquid water is defined in terms of the atom fractions of deuterium to protium in the liquid water, F_L^e, and in the hydrogen gas, F_H^e, at equilibrium, by the equation

$$\alpha = \frac{F_L^e(1 - F_H^e)}{(1 - F_L^e)F_H^e} \tag{8}$$

The atom fraction of deuterium present in the liquid at equilibrium at each temperature was calculated from eq 7. The results from two runs with initial deuterium contents of $F_L^i = 19\,964 \times 10^{-6}$ and $34\,626 \times 10^{-6}$ are listed in Table I. These data are compared in Figure 2 with the product of vapor phase measurements of K_1 made by Cerrai et al.[2] and Suess[3] and the vapor liquid separation factor, α_V (eq 10). With the exception of the two data points of Cerrai et al. at 332 and 337 K the agreement between the two independent methods of determining the overall separation factor α is excellent. On the strength of the more numerous data collected in the present study the two points mentioned above were excluded and the remaining data points were fitted by a weighted linear least-squares regression for one dependent variable[14] to

$$\ln \alpha = -0.2143 + \frac{368.9}{T} + \frac{27\,870}{T^2} \tag{9}$$

in which T is the absolute temperature. Weights for the individual dependent variables, $\ln \alpha_i$, were set equal to α_i^2 divided by the variance of α_i. The standard deviations of the α_i were assumed to be constant at 0.04 through the range of temperatures studied.

Our measurements of the separation factor, α, depend primarily on the initial deuterium content of the liquid water, F_L^i, and the deuterium content of the hydorgen gas at equilibrium, F_H^e. The liquid was prepared by gravimetric dilutions of 99.80% D_2O and its deuterium concentration has an estimated error of ±0.1%. The deuterium atom fraction of the hydrogen gas depends primarily on the peak height ratio of mass 2 and 3, the sensitivity factor, f, and the accuracy of the hydrogen standards. An error of ±0.5% is estimated for each of these determinations. Assuming all these errors to be random, the overall accuracy of α is estimated as ±1.0%. This estimate of the error is reasonable since this is approximately equal to the standard deviation of ±1.2% of the five values given in Table I at 333.9 K. The standard deviation in ln α obtained from the residual variance in the weighted least-squares fitting of eq 9 is 0.013 units which corresponds to a ±1.3% error in α.

As mentioned in the Introduction, it is possible to extract values of K_1 from measurements of the overall separation factor, α, between hydrogen and liquid water if allowance is made for the vapor–liquid fractionation. The necessary fractionation factors, α_V, for temperatures up to 473 K were obtained from the data of Van Hook et al.[15] below 373 K and by the application of the relation, $\alpha = (P_{H_2O}/P_{D_2O})^{0.524}$, sug-

TABLE I: Temperature Dependence of Isotope Separation Factor, α

Temp, K	Deuterium atom fractions $10^6F_H^e$	$10^6F_L^e$	Separation factor (α)
280.03	4 672	20 005	4.349
295.40	5 213	20 000	3.894
295.40	5 173	20 000	3.925
313.14	5 648	19 997	3.592
333.92	6 399	19 992	3.168
333.92	6 389	19 992	3.173
333.92	6 475	19 992	3.130
354.62	7 130	19 988	2.840
305.35	5 563	19 999	3.648
305.35	5 503	19 999	3.688
313.99	5 810	19 997	3.492
330.17	6 251	19 993	3.243
291.25	5 132	20 002	3.916
286.00	4 900	20 003	4.145
323.47	6 084	19 995	3.333
367.91	7 504	19 985	2.697
279.70	8 290	34 64[illegible]	4.293
279.70	8 364	34 64[illegible]	4.251
292.39	8 891	34 633	3.999
292.39	9 069	34 633	3.920
292.39	8 999	34 633	3.951
296.95	9 379	34 630	3.789
296.95	9 619	34 630	3.693
304.02	9 734	34 626	3.649
304.02	9 674	34 626	3.672
313.37	10 073	34 620	3.524
313.37	10 094	34 620	3.517
324.46	10 899	34 614	3.255
324.46	10 894	34 614	3.255
333.88	11 453	34 609	3.094
333.88	11 448	34 609	3.094
344.45	11 938	34 604	2.967
344.45	11 788	34 604	3.005
355.28	12 498	34 598	2.832
364.23	13 116	34 59[illegible]	2.696
364.23	12 763	34 59[illegible]	2.772
288.00	8 639	34 637	4.117
288.00	8 834	34 637	4.026

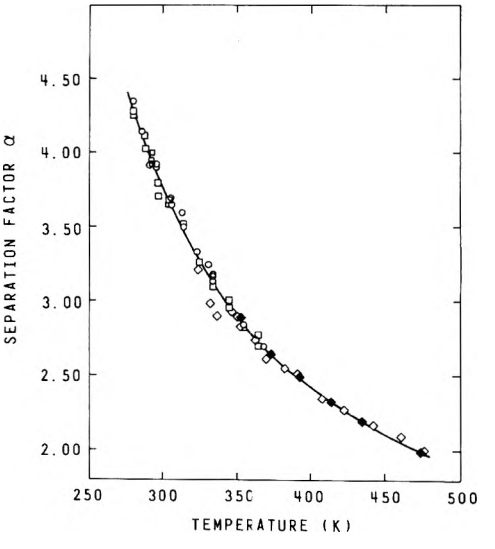

Figure 2. Dependence of hydrogen–liquid water separation factor α upon temperature: (O) data from run A; (□) data from run B; data of Cerrai et al. (◊) and of Suess (♦) multiplied by α_V from eq 10.

gested by Van Hook,[16] to the vapor pressure data above 373 K summarized by Whalley.[17] The exponent is larger than 0.500 predicted on the assumption of the rule of the geometric mean[18] formulated from the suggestion of Lewis and Cornish[19] that the vapor pressure of a mixed isotope molecule such as HDO could be calculated as the square root of the product of the vapor pressures of the isotopically pure species. However, it is necessary to use the higher power dependence of the vapor pressure ratio to bring consistency between the data on vapor pressure isotope effects (VPIE) reported by Van Hook et al.[15] and the direct measurements of Majoube[20] and Merlivat et al.[21] Similar deviations from the law of the mean are noted[22] in the equilibrium constant for isotopic self-exchange in water.

The combined data were fitted by a weighted least-squares regression to

$$\ln \alpha_V = 0.0592 - \frac{80.3}{T} + \frac{25\,490}{T^2} \qquad (10)$$

The standard deviation in $\ln \alpha_V$ as estimated from the residual variance is 0.0003 units corresponding to 0.03% in α_V. However, the uncertainty in the magnitude of the exponent 0.524 required to bring consistency between the VPIE data of Van Hook et al. and the direct measurements of Majoube and Merlivat et al. raises the error in α_V to ±0.1%. Values of the vapor–liquid separation factor α_V calculated from this equation over the temperature range 273–473 K differ by less than +0.1% from those calculated from the three appropriate equations recently published by Van Hook.[23]

The hydrogen–water vapor equilibrium constant, K_1, is equal to α/α_V, so that by combining eq 9 and 10, K_1 as a function of temperature is given by

$$\ln K_1 = -0.2735 + \frac{449.2}{T} + \frac{2380}{T^2} \qquad (11)$$

Values of K_1 at three temperatures calculated from eq 11 are listed in Table II. Also tabulated are theoretical values calculated by Wolfsberg[5] and Bottinga[8] under the harmonic approximation together with those calculated with the inclusion of G_0.[5] The value of K_1 calculated by Bottinga at 298 K is 18% larger than the experimental value obtained in this study. As discussed by Bardo and Wolfsberg[10] in the accompanying paper this large discrepancy arises through the neglect of G_0 and to the direct use of spectroscopic data in the evaluation of the partition function ratios. Better agreement (1.9–2.5%) is shown between the experimental values and those calculated[5] with the G_0 correction. This can be compared with agreement of better than 1% claimed[22] for the NH_3–HD exchange.

Values of K_1 calculated by Bardo and Wolfsberg[10] in the next paper within the framework of the BO approximation likewise show a positive deviation from our experimental values. However, refinements of their theoretical procedures to account for the inexactness of the BO approximation give theoretical values of the equilibrium constant as a function of temperature which are in excellent agreement with our experimental least-squares curve obtained between 273 and 473 K. Over the entire temperature range the experimental values are only 0.5% lower than the theoretical values. Such agreement between experiment and theory for values of K_1 in the low temperature range reported here supports the validity of our expression for calculating α to a nominal accuracy of 1%.

TABLE II: Comparison of Values of K_1 with Theory

	Values of K_1			
		Harmonic		
Temp, K	This work	Ref 8	Ref 5	G_0 corr ref 5
298	3.53	4.17	3.86	3.62
348	2.82		3.04	2.88
373	2.58		2.77	2.63

Acknowledgment. We wish to thank the following CRNL staff for assistance in this study: M. Hammerli and W. J. Olmstead for the preparation of hydrogen standards of known isotopic abundance and J. G. Wesanko for fabrication of the exchange cell. In addition we wish to express our thanks to Professor Wolfsberg for communicating to us his interest in this study prior to publication.

References and Notes

(1) I. Kirshenbaum, H. C. Urey, and G. M. Murphy, Ed., "Physical Properties and Analysis of Heavy Water", McGraw-Hill, New York, N.Y., 1951 p 46.
(2) E. Cerrai, C. Marchetti, R. Renzoni, L. Roseo, M. Silvestri, and S. Villani, *Chem. Eng. Prog. Ser.*, **50**, No. 11, 271 (1954).
(3) H. E. Suess, *Z. Naturforsch. A*, **4**, 328 (1949).
(4) R. E. Weston, Jr., *J. Chem. Phys.*, **42**, 2635 (1965).
(5) M. Wolfsberg, *J. Chem. Phys.*, **50**, 1484 (1969).
(6) M. Wolfsberg, *Adv. Chem. Ser.*, **No. 89**, 185 (1969).
(7) J. Bigeleisen, M. W. Lee, and F. Mandel, *Ann. Rev. Phys. Chem.*, **24**, 407 (1973).
(8) Y. Bottinga, *J. Phys. Chem.*, **72**, 4338 (1968).
(9) J. Bron, C. F. Chang, and M. Wolfsberg, *Z. Naturforsch. A*, **28**, 129 (1973).
(10) R. D. Bardo and M. Wolfsberg, *J. Phys. Chem.*, following paper in this issue.
(11) Original sample obtained from Cadillac Plastics, similar material is presently available from Fluoro Plastics Inc., Philadelphia, Pa.
(12) J. H. Rolston, W. H. Stevens, J. P. Butler, and J. den Hartog, Canadian Patent No. 941 134 (1974).
(13) J. Ravoire, P. Grandcollot, and G. Dirian, *J. Chim. Phys.*, **60**, 130 (1963).
(14) D. M. Himmelblau, "Process Analysis by Statistical Methods", Wiley, New York, N.Y., 1970, p 114.
(15) J. Pupezin, G. Jakli, G. Jansco, and W. A. Van Hook, *J. Phys. Chem.*, **76**, 743 (1972).
(16) W. A. Van Hook, *J. Phys. Chem.*, **76**, 3040 (1972).
(17) E. Whalley, *Proc. Jt. Conf. Thermodyn. Transp. Prop. Fluids, 1957*, 15, (1958).
(18) J. Bigelseisen, *J. Chem. Phys.*, **23**, 2264 (1955).
(19) G. N. Lewis and R. E. Cornish, *J. Am. Chem. Soc.*, **55**, 2616 (1933).
(20) M. Majoube, *J. Chim. Phys., Physiochim. Biol.*, **68**, 1423 (1971).
(21) L. Merlivat, R. Botter, and G. Nief, *J. Chim. Phys.*, **60**, 56 (1963).
(22) J. W. Pyper and L. D. Christensen, *J. Chem. Phys.*, **62**, 2596 (1975).
(23) G. Jansco and W. A. Van Hook, *Chem. Rev.*, **74**, 689 (1974).
(24) E. A. Symons and E. Buncel, *Can. J. Chem.*, **51**, 1673 (1973).
(25) A value of $\alpha_D = 1.02$ can be calculated by applying the mean law to the solubility of H_2 and D_2 in water at 298 K.[24]

A Theoretical Calculation of the Equilibrium Constant for the Isotopic Exchange Reaction between H_2O and HD

Richard D. Bardo and Max Wolfsberg*

Department of Chemistry, University of California, Irvine, California 92717 *(Received September 22, 1975)*

Publication costs assisted by the U.S. Energy Research and Development Agency

A theoretical calculation is presented for the equilibrium constant of the isotopic exchange reaction H_2O + HD = HDO + H_2 between 220 and 600 K and compared with experimental data in the temperature range 280–600 K. A correction for the Born–Oppenheimer approximation is included in the calculation. The theoretical curve of the equilibrium constant as a function of temperature differs from the experimental least-squares curve obtained between 280 and 475 K by at most 0.7%.

Introduction

Experimental values of the equilibrium constant K_1 for the isotopic exchange reaction

$$H_2O(g) + HD(g) = HDO(g) + H_2(g) \quad (1)$$

have been reported in the literature by three groups of workers.[1-3] The interest in this equilibrium arises, at least in part, from the possibility of economically producing heavy water from the exchange between water and hydrogen. The latest data are described in the preceding paper[3] and were obtained by combining measured data for an equilibrium such as that in eq 1, for liquid water, with values of the vapor pressure ratio H_2O/HDO deduced from experiment. The experimental values of K_1 will be compared here with those obtained theoretically by statistical and quantum mechanics. It should be noted that effects of gas phase nonideality were reasonably considered negligible in the experimental evaluations of K_1.

Theoretical Calculation

Bron, Chang, and Wolfsberg[4] (BCW) obtained ideal gas phase partition function ratios Q_{HDO}/Q_{H_2O} and Q_{HD}/Q_{H_2} a few years ago within the framework of the Born–Oppenheimer (BO) approximation and expressed the logarithms of these ratios in a power series of $1/T$ (where T is the absolute temperature). The series reproduced the partition function ratios with a maximum error of 0.1% over the temperature range 220–600 K.

Within the framework of the BO approximation, the equilibrium constant can be expressed in terms of the partition function ratios as

$$K_1 = (Q_{HDO}/Q_{H_2O})/(Q_{HD}/Q_{H_2}) \quad (2)$$

With use of the above series expansions, the following expression is then obtained for K_1

$$\ln K_1(\mathrm{BCW}) = -0.17739 + 1.12486\left(\frac{300}{T}\right) + 0.61704\left(\frac{300}{T}\right)^2 - 0.36997\left(\frac{300}{T}\right)^3 + 0.07978\left(\frac{300}{T}\right)^4 \quad (3)$$

Equation 3 can be used between 220 and 600 K. Since it forms the basis of the values theoretically calculated here within the framework of the BO approximation, comparison is only made with those experimental data below 600 K (Cerrai et al.[2] also reported data at seven temperatures between 600 and 1015 K).

Recently, Kleinman, Wolfsberg, and Bardo[5,6] have considered that calculations such as K_1(BCW) must be corrected for the BO approximation. Within the BO approximation, the molecular quantum mechanics problem can be divided into one of electronic motion (with nuclei fixed) and one of nuclear motion. The potential function for nuclear motion is the electronic energy as a function of internuclear coordinates. The minimum of this potential function will be designated here as the zero of vibrational–rotational–translational energy (ZVRTE) of the molecule. Since the electronic energy of a molecule is independent of the nuclear masses of the substituent atoms, the ZVRTE of a molecule is independent of isotopic substitution. Thus, for an exchange reaction such as eq 1, the energy change between the ZVRTE of reactants and the corresponding ZVRTE of products vanishes. When first-order corrections to the BO approximation are considered, this energy change is no longer equal to zero, but is given by

$$\Delta E = -\Delta_{\mathrm{BOELE}} = C(H_2) - C(\mathrm{HD}) - C(H_2O) + C(\mathrm{HDO}) \quad (4)$$

where C is the isotope dependent adiabatic correction evaluated at the equilibrium BO internuclear configuration of the respective molecule. ΔE leads to a multiplicative correction factor K(BOELE) to the equilibrium constant calculated within the BO approximation

$$K(\mathrm{BOELE}) = \exp(\Delta_{\mathrm{BOELE}}/kT) \quad (5)$$

Kleinman and Wolfsberg[5] have shown that K(BOELE) is expected to be the main correction to the BO approximation for theoretically calculated isotope exchange equilibrium constants among diatomic molecules. They have also shown that one expects correction factors of the order of a few percent in the case of H/D exchange equilibria involving diatomic molecules.

The assumption is now made that K(BOELE) represents the main correction factor to K_1 from failure of the BO approximation. C values for H_2 and HD have been previously reported.[5] Evaluations of C for H_2O and HDO have just been completed.[7] Both sets of C values were evaluated with electronic wave functions which may be described as being close to the Hartree–Fock limit. It is found that (appropriately rounded-off)

TABLE I: Comparison of K_1 Calculated with the BO Approximation K_1(BCW) (Eq 3), K_1 Calculated with Inclusion of the Adiabatic Correction K_1(BW) (Eq 8), Experimental Values K_1(expt), and the Values from the Least-Squares Fit Experimental Curve K_1(ls expt) (Eq 9)[a]

	T, K	K_1(BCW)	K_1(BW)	K_1(expt)[b]	K_1(ls expt)
A	279.7	4.01	3.93	3.87 ± 0.02[c]	3.91
	280.0	4.00	3.92	3.94	3.90
	286.0	3.86	3.79	3.79	3.77
	288.0	3.82	3.75	3.73 ± 0.04	3.72
	291.2	3.75	3.68	3.60	3.66
	292.4	3.73	3.66	3.64 ± 0.04	3.63
	295.4	3.66	3.60	3.61 ± 0.01	3.58
	297.0	3.63	3.57	3.46 ± 0.04	3.55
	304.0	3.50	3.44	3.41 ± 0.01	3.42
	305.4	3.48	3.42	3.42 ± 0.02	3.40
	313.1	3.35	3.29	3.37	3.27
	313.4	3.34	3.29	3.31 ± 0.00	3.27
	314.0	3.33	3.28	3.28	3.26
	323.5	3.19	3.14	3.16	3.12
	324.5	3.18	3.12	3.08 ± 0.00	3.11
	330.2	3.10	3.05	3.09	3.03
	333.9	3.05	3.00	2.99 ± 0.04	2.98
	344.4	2.92	2.88	2.87 ± 0.02	2.86
	354.6	2.81	2.77	2.74	2.75
	355.3	2.80	2.76	2.73	2.74
	364.2	2.71	2.67	2.65 ± 0.04	2.66
	367.9	2.68	2.64	2.62	2.62
B	324.2	3.18	3.13	3.04 ± 0.06	3.11
	332.2	3.07	3.02	2.84 ± 0.06	3.00
	337.2	3.01	2.96	2.77 ± 0.06	2.94
	347.2	2.87	2.84	2.81 ± 0.05	2.83
	350.7	2.85	2.81	2.79 ± 0.05	2.79
	352.6	2.83	2.79	2.72 ± 0.05	2.77
	362.7	2.73	2.69	2.65 ± 0.05	2.67
	370.2	2.66	2.62	2.54 ± 0.05	2.60
	382.2	2.55	2.52	2.48 ± 0.05	2.50
	391.7	2.48	2.44	2.46 ± 0.05	2.43
	407.2	2.37	2.34	2.30 ± 0.05	2.33
	421.6	2.28	2.25	2.24 ± 0.05	2.24
	441.2	2.17	2.14	2.15 ± 0.04	2.14
	459.7	2.08	2.05	2.08 ± 0.04	2.05
	475.2	2.01	1.99	1.99 ± 0.04	1.98
	492.2	1.95	1.92	1.95 ± 0.04	1.92
	524.2	1.84	1.82	1.85 ± 0.04	1.82
	553.2	1.75	1.74	1.73 ± 0.04	1.74
	588.2	1.67	1.66	1.60 ± 0.04	1.66
C	353.2	2.82	2.78	2.79	2.76
	373.2	2.63	2.59	2.57	2.58
	393.2	2.47	2.43	2.42	2.42
	413.2	2.33	2.30	2.29	2.29
	433.2	2.21	2.18	2.17	2.18
	473.2	2.02	2.00	1.98	1.99

[a] The temperatures T were chosen to be those of the experimental values. A refers to experimental values from ref 3, B from ref 2, C from ref 1. [b] K_1(expt) values for ref 3 are obtained by combining the measured values of the equilibrium constant for reaction 10 with the vapor pressure ratio H_2O/HDO given by eq 10 of ref 3. [c] Whenever error limits are given for K_1(expt) from ref 3 under A, more than one experiment was performed at this temperature and the error limits show the range of the results. For K_1(expt) under B, the error limits are those given by the authors of ref 2.

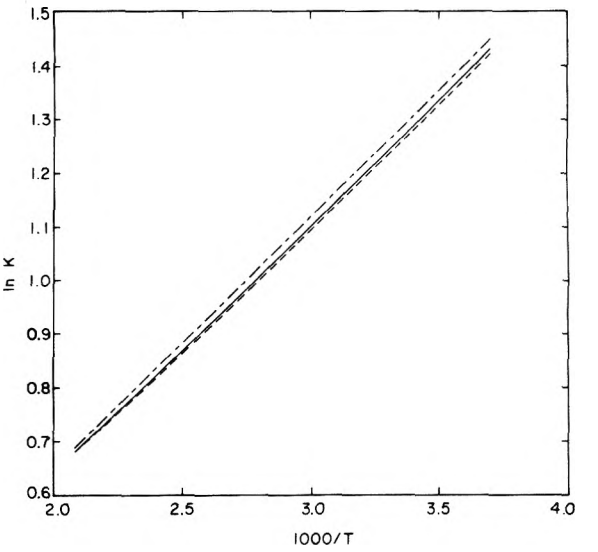

Figure 1. Plot of ln K_1 vs. 1000/T: (- - -) K_1 calculated within BO approximation K_1(BCW) eq (3); (—) K_1 calculated with inclusion of adiabatic correction K_1(BW) (eq 8); (– –) least-squares fit to experimental values K_1(ls expt) (eq 9) in the temperature range T = 280–475 K.

$$\Delta_{\mathrm{BOELE}} = -3.8\ \mathrm{cm}^{-1} \tag{6}$$

and

$$K(\mathrm{BOELE}) = \exp(-5.5/T) \tag{7}$$

When the correction factor K(BOELE) is applied to K_1 evaluated within the BO approximation [K_1 = K_1(BCW)K(BOELE)], the following expression is now obtained for K_1:

$$\ln K_1(\mathrm{BW}) = -0.17739 + 1.10658\left(\frac{300}{T}\right) + 0.61704\left(\frac{300}{T}\right)^2 - 0.36997\left(\frac{300}{T}\right)^3 + 0.07978\left(\frac{300}{T}\right)^4 \tag{8}$$

In Table I, K_1(BCW) corresponding to the BO approximation, and K_1(BW) corresponding to inclusion of the adiabatic correction are compared with the experimental data, K_1(expt), below 600 K. Comparison is also made with K_1(ls expt) which corresponds to the least-squares curve obtained by Rolston et al.[3] to fit their own data and that of the other two series of measurements between 280 and 475 K

$$\ln K_1(\text{ls expt}) = -0.2735 + \frac{449.2}{T} + \frac{2380}{T^2} \tag{9}$$

In Figure 1, comparison is made between K_1(BCW), K_1(BW), and K_1(ls expt) over the temperature range 270–480 K. Such agreement between theoretical calculations and experimental results, obtained independently, must be termed as excellent.

Discussion

The numerical values of K_1(BCW), K_1(BW), K_1(expt), and K_1(ls expt) in Table I demonstrate the good agreement between theory and experiment and the fact that K_1(BW) leads to better overall agreement with experiment than does K_1(BCW). The numerical values show that the correction factor K(BOELE) = K_1(BW)/K_1(BCW) is about 0.98 in the room temperature region and decreases with increasing temperature. If the numerical values are not rounded off as

in Table I, it follows that K_1(BW)/K_1(ls expt) is about 1.003 at 273 K, reaches a maximum of 1.007 around 330 K, and then decreases to 1.001 at 480 K. While K_1(ls expt) really only applies to the temperature range below 475 K, K_1(ls expt) and K_1(BW) are in almost perfect agreement at the relevant temperatures above 475 K.

The comparison in Figure 1 clearly confirms the good agreement between the theoretical curves K_1(BCW) and K_1(BW) and the experimental curve K_1(ls expt). Moreover, the inclusion of the adiabatic correction in K_1(BW) leads to better agreement with the experimental curve.

As already noted by Rolston et al.,[3] the measurements in ref 2 at 332 and 337 K appear spurious. For most of the other measured values in ref 2, there is agreement with K_1(BW) when the stated error limits of the experiments are considered. The measured values of ref 1 are in excellent agreement with the K_1(BW) values.

As noted above, Rolston et al.[3] combined data for the equilibrium constant

$$H_2O(l) + HD(g) = HDO(l) + H_2(g) \qquad (10)$$

with the vapor pressure ratio H_2O/HDO. The analytic expression which they employed for the vapor pressure ratio reproduces the experimental data of Majoube[8] mostly to better than 0.1%. Since Majoube's measurements of the vapor pressure ratio and the measurements of Rolston et al. of the equilibrium constant of eq 10 were both carried out with a very low D/H ratio, any effects due to liquid nonideality in H_2O–D_2O should cancel in the evaluation of K_1 from these data. The main error in values of K_1 deduced experimentally by Rolston et al. most probably arises from the uncertainty in their measured equilibrium constants for reaction 10. Rolston et al. estimate the overall accuracy of their measurements to be ±1%. They also state that this error estimate is reasonable since it approximately equals the standard deviation (±1.2%) of their five measurements at 333.9 K. One might regard this estimate of accuracy somewhat optimistic when one looks at their experimental values centered around 293.5 K, but, as Rolston[9] has pointed out, the situation does not look so bad if one experimental point at 297.0 K is omitted. K_1(ls expt) of Rolston et al. is obtained by combining a least-squares fit expression to equilibrium constant data for reaction 10 with the above mentioned analytic expression for the vapor pressure ratio H_2O/HDO. It is to be noted that the equilibrium constant data for reaction 10 included not only their own data but also that of ref 1 and 2 appropriately converted to the liquid phase. Rolston et al. estimate the error in the least-squares fit expression for the equilibrium constant of reaction 10 to be ±1.3%.

BCW[4] evaluated isotopic partition function ratios within the BO approximation on the basis of isotope independent force fields and equilibrium geometries. The philosophy underlying theoretical isotope effect calculations carried out in this laboratory and by most other workers in this field is that such a procedure is superior to using available spectroscopic data on isotopic molecules directly in the evaluation of isotopic partition function ratios, since small errors in isotope effects on spectroscopic measurements can lead to large errors in the calculations.[10] It must also be noted that some of the factors which enter into partition function calculations such as G_0[11] cannot usually be directly deduced from spectroscopic data. In the BCW calculations, the partition function ratio was calculated in the so-called harmonic approximation[4] and then various correction factors were applied on the basis of perturbation theory. It was shown that the only major correction factor is the anharmonicity correction ANHC except in the case of the molecular hydrogen molecules where the correction for quantum rotation QMRC is also important.

It was pointed out by BCW that the choice of molecular potential functions could introduce uncertainties into the partition function ratios. The potential functions are based on spectroscopic data (interpreted within the BO approximation[5]). It is not felt that there is much problem with the partition function ratios of molecular hydrogen. For the water partition function ratios, a potential function deduced by Kuchitsu and Morino[12] (KM) was employed. This potential function is based on an evaluation of spectroscopic data by Benedict, Gailar, and Plyler[13] (BGP). The partition function ratio Q_{HDO}/Q_{H_2O} has also been evaluated from the MUBFF force field of Papoušek and Plíva.[14] This force field was also chosen to yield agreement with the BGP data. Q_{HDO}/Q_{H_2O} calculated in the harmonic approximation with the MUBFF force field differs from that calculated with the KM force field by less than 0.1% over the temperature range considered here. If the anharmonicity correction is also considered, a maximum deviation of 0.2% occurs at the lowest temperatures of the experiments here and the deviation decreases with increasing temperature.[15]

In view of the above, the K_1(BCW) values are expected to be quite precise values of the equilibrium constants within the framework of the BO approximation. It is suspected that the main uncertainty in the K(BOELE) correction factor, which takes into account the deviation from the BO approximation, is in the use of Hartree–Fock limiting wave functions rather than configuration interaction wave functions; at this time no uncertainty estimate can be given.

Overall, considering the accuracy of both the theoretical calculations and the experiments, the agreement of K_1(BW) and K_1(ls expt) should not be really surprising. Nevertheless, the agreement is very gratifying. K(BOELE) has been calculated for very few equilibria.[5,6] The present instance represents the first time where a theoretical calculation of an isotopic exchange equilibrium constant, including a nonnegligible[16] adiabatic correction, has been compared with experiment.

Acknowledgment. It is a pleasure to acknowledge discussions with Dr. R. A. Rolston, and also the technical help of L. A. Laing in the preparation of this manuscript.

This research was supported by the U.S. Energy Research and Development Agency under Contract No. AT(04-3)-34, Project Agreement No. 188.

References and Notes

(1) H. Suess, *Z. Naturforsch.*, **42**, 328 (1949).
(2) E. Cerrai, C. Marchetti, R. Renzoni, L. Roseo, M. Silvestri, and S. Villari, *Chem. Eng. Prog. Symp. Ser.*, **50**, No. 11, 271 (1954).
(3) J. H. Rolston, J. den Hartog, and J. P. Butler, *J. Phys. Chem.*, preceding paper in this issue.
(4) J. Bron, C. F. Chang, and M. Wolfsberg, *Z. Naturforsch. A*, **28**, 129 (1973). It may be noted that atomic masses, rather than nuclear masses, were used in evaluating the partition function ratios. This choice will be the subject of a future discussion (see also ref 5).
(5) L. Kleinman and M. Wolfsberg, *J. Chem. Phys.*, **58**, 2043 (1973); **60**, 4740, 4749 (1974); M. Wolfsberg and L. Kleinman, *Am. Chem. Soc., Symp. Ser.*, **11**, 64 (1975).
(6) R. D. Bardo and M. Wolfsberg, *J. Chem. Phys.*, **62**, 4555 (1975).
(7) R. D. Bardo and M. Wolfsberg, to be submitted for publication.
(8) M. Majoube, *J. Chim. Phys., Physiochim., Biol.*, **68**, 1423 (1971).
(9) J. H. Rolston, private communication.
(10) Such a procedure was employed, however, by Y. Bottinga, *J. Phys. Chem.*, **72**, 4338 (1968), in his calculation of K_1.
(11) M. Wolfsberg, A. A. Massa, and J. W. Pyper, *J. Chem. Phys.*, 53, 3138 (1970).

(12) K. Kuchitsu and Y. Morino, *Bull. Chem. Soc. Jpn.*, **38**, 814 (1965).
(13) W. S. Benedict, N. Gailar, and E. K. Plyler, *J. Chem. Phys.*, **24**, 1139 (1956).
(14) D. Papoušek and J. Pliva, *Collec. Czech. Chem. Commun.*, **29**, 1973 (1964).
(15) M. Wolfsberg, *J. Chem. Phys.*, **50**, 1484 (1969), has previously calculated K_1 within the BO approximation with use of the MUBFF force field for water. This calculation differed slightly from the BCW calculation since in the BCW calculation all constants were calculated directly from the force field while in the earlier calculation the values calculated by Papousek and Pliva[14] from their force field were used (see ref 11).
(16) Bardo and Wolfsberg[6] have shown that, for self-exchange equilibria such as $H_2O + D_2O = 2HDO$, the adiabatic correction makes no contribution to the equilibrium constant.

Analysis of Sedimentation Equilibrium Results Obtained with Indefinitely Self-Associating Systems Using a Procedure Based on Laplace Transformation

L. W. Nichol,* P. D. Jeffrey, and B. K. Milthorpe

Department of Physical Biochemistry, John Curtin School of Medical Research, Australian National University, Canberra, A.C.T. 2601, Australia *(Received December 22, 1975)*

Equations are developed in closed form which permit the simulation of the distribution of total concentration vs. radial distance obtainable in the sedimentation equilibrium of a system of specified initial concentration undergoing indefinite self-association. Simulated distributions obtained with a variety of systems involving one or more equilibrium constants are used to test an analysis procedure which fits the distribution to a function capable of inverse Laplace transformation and leads to a specification of the relative amounts of the species in the cell as a function of their molecular weights. It is shown that such results may be related to the equilibrium concentrations of oligomeric forms at each radial distance, thereby permitting successive equilibrium constants appropriate to the indefinite self-association to be estimated.

Several systems have been shown by analysis of sedimentation equilibrium results to be indefinitely self-associating.[1-6] In general these may be specified by $A_{j-1} + A_1 \rightleftharpoons A_j$, one or more equilibrium constants governing the successive addition of monomer to higher polymeric forms. Major emphasis has been placed on cases (isodesmic) where only one equilibrium constant pertains.[1-5] The interpretation of more complicated systems is undeniably more difficult, since attempts to define successive equilibrium constants on the basis of the weight fraction of monomer as a function of total concentration[7] are known[8] to be subject to considerable uncertainty when the number of oligomeric states is large.

Concurrent with the interest in self-associating systems has been the development of an analysis procedure based on the use of Laplace transformation to define the composition of a solution containing several noninteracting solutes.[9-11] It is the aim of the present work to explore the possibility that the latter method may be applied to chemically interacting systems undergoing indefinite self-association of monomer. Such an approach has the potential of not only elucidating isodesmic self-associations, but also of providing estimates of the successive equilibrium constants appropriate to more complicated systems.

Basic Theory

The sedimentation equilibrium distribution of each species i ($i = 1, 2, \ldots, \infty$) in a thermodynamically ideal system comprising monomer ($i = 1$) in chemical equilibrium with a series of polymeric states ($A_{j-1} + A_1 \rightleftharpoons A_j$) is described by

$$c_i(r) = c_i(r_m)e^{\phi_i M_i(r^2 - r_m^2)} \quad (1a)$$

$$\phi_i = (1 - \bar{v}_i\rho)\omega^2/2RT \quad (1b)$$

where $c_i(r)$ is the weight concentration at radial distance r of species i whose molecular weight and partial specific volume are M_i and $\bar{v}_i$, respectively; r_m is the radial distance of the meniscus, ω the angular velocity, ρ the solution density, and T the temperature. It will be assumed that all $\phi_i = \phi$, implying through the equality of all $\bar{v}_i$ that no volume changes are inherent in the formation of successive polymers: in turn, this means that successive equilibrium constants are independent of pressure and hence of radial distance. The amount of species i in the cell does not equal the corresponding amount in the original solution,[12] but is given by[13]

$$(Q_i)_{cell} = \theta h \int_{r_m}^{r_b} r c_i(r)\, dr = \frac{c_i(r_m)\theta h(e^{\phi M_i b} - 1)}{2\phi M_i} \quad (2)$$

where θ and h are the cell sector angle and thickness and $b = (r_b^2 - r_m^2)$, r_b being the radial distance of the base. Combination of eq 1a and 2 yields

$$c_i(\xi) = \frac{2t_i(Q_i)_{cell}e^{t_i(1-\xi)}}{b\theta h(e^{t_i} - 1)} \quad (3a)$$

$$t_i = \phi M_i b \quad \text{and} \quad \xi = (r_b^2 - r^2)/b \quad (3b)$$

Equation 3 may be divided by the total amount of solute in the cell, which according to mass conservation is given by

$$Q_T = \bar{c}^0\theta h(b/2) = \sum_i (Q_i)_{cell} \quad (4)$$

where $\bar{c}^0$ is the original loading concentration. Thus

$$c_i(\xi) = \bar{c}^0 t_i f_i e^{t_i(1-\xi)}/(e^{t_i} - 1) \quad (5)$$

where $f_i = (Q_i)_{cell}/Q_T$. It follows that the total concentration at each radial distance is

$$\bar{c}(\xi) = \bar{c}^0 \sum_{i=1}^{i=\infty} \{t_i f_i e^{-\xi t_i}/(1 - e^{-t_i})\} \quad (6a)$$

Equation 6a may be written in terms of the Laplace transform of a continuous function[9-11], $g(t_i)$, replacing f_i

$$\bar{c}(\xi) = \bar{c}^0 \int_0^\infty \{t_i\, g(t_i)\, e^{-\xi t_i}/(1 - e^{-t_i})\}\, dt_i \quad (6b)$$

$$\bar{c}(\xi) = \bar{c}^0 \mathcal{L}\{t_i\, g(t_i)/(1 - e^{-t_i})\} \quad (6c)$$

where $\mathcal{L}$ denotes the Laplace transform operator. Inversion of eq 6c leads to

$$g(t_i) = \frac{(1 - e^{-t_i})\mathcal{L}^{-1}\{\bar{c}(\xi)\}}{\bar{c}^0 t_i} \quad (7)$$

Analysis of the sedimentation equilibrium distribution obtainable experimentally as a plot of $\bar{c}(\xi)$ vs. ξ is, therefore, possible in terms of the distribution function $g(t_i)$, provided the experimental plot may be fitted to a function whose inverse Laplace transform is available. In selecting a suitable function three basic requirements must be met, which will be discussed in terms of the function derived earlier[11] on the basis of the treatment presented by Donnelly.[9,10] This function, which offers advantage in that it describes integrated[11] rather than differentiated[9,10] sedimentation equilibrium results, is expressed by

$$\bar{c}(\xi) = \bar{c}(r_m) e^{\alpha_2(\xi-1)}(1 - \alpha_3)^{\alpha_4}/(\xi - \alpha_3)^{\alpha_4} \quad (8)$$

where α_2, α_3, and α_4 are constants. The first requirement is evidently met in that eq 8 describes the point $(\bar{c}(r_m), r_m)$ when $r = r_m(\xi = 1)$. The fulfilment of the second requirement is ensured by the inclusion in eq 8 of the coefficient $\exp(\alpha_2(\xi - 1))$, for this permits use of the second translational property of Laplace inversion to introduce a step function in $\mathcal{L}^{-1}\{\bar{c}(\xi)\}$ and hence by eq 7 in $g(t_i)$: this is required physically since no material possesses a value of t_i less than that of the monomer. Thus,

$$\mathcal{L}^{-1}\{\bar{c}(\xi)\} = \begin{cases} \bar{c}(r_m)(1 - \alpha_3)^{\alpha_4} e^{-\alpha_2}(t_i + \alpha_2)^{(\alpha_4-1)} e^{\alpha_3(t_i+\alpha_2)}/\Gamma(\alpha_4) \\ \quad ; t_i > -\alpha_2 \\ 0; t_i < -\alpha_2 \end{cases} \quad (9)$$

where $\Gamma(\alpha_4)$ is the gamma function of α_4. Combination of eq 7 and 9 together with the requirement that the continuous function $f(M_i) = g(t_i)\, dt_i/dM_i = \phi b\, g(t_i)$ gives for $t_i > -\alpha_2$

$$f(M_i) = \frac{\phi b(1 - e^{-t_i})\bar{c}(r_m)(1 - \alpha_3)^{\alpha_4} e^{-\alpha_2}(t_i + \alpha_2)^{(\alpha_4-1)} e^{\alpha_3(t_i+\alpha_2)}}{\bar{c}^0 t_i \Gamma(\alpha_4)} \quad (10)$$

It is noted that a plot of $f(M_i)$ vs. M_i (which from eq 3b equals $t_i/\phi b$) exhibits a step function at $t_i = -\alpha_2$ and is thereafter continuous for $t_i > -\alpha_2$. This feature, inherent in the choice of the function defined in eq 8, is of considerable advantage in handling indefinite self-associations since it permits explicit definition of α_2 in terms of the molecular weight of the monomer: $\alpha_2 = -\phi M_1 b$. This in turn means that the fitting of eq 8 to the experimental plot of $\bar{c}(\xi)$ vs. ξ to find α_3 and α_4 may be performed explicitly in terms of any two values $(\psi(\xi_1), \xi_1)$ and $(\psi(\xi_2), \xi_2)$, where

$$\psi(\xi) = \bar{c}(\xi)/\bar{c}(r_m) e^{\alpha_2(\xi-1)} = (1 - \alpha_3)^{\alpha_4}/(\xi - \alpha_3)^{\alpha_4} \quad (11)$$

It remains to be shown with the aid of numerical examples that the third and final requirement of eq 8 (or its equivalent, eq 11) is met: thus, the function must be capable of fitting $\bar{c}(r)$ vs. r plots in terms of definable values of α_3 and α_4.

Application of Theory to Experimental Results

For the sake of clarity, the use of the above theory will be outlined in a series of steps which an experimenter might take.

Step 1. It is first required to determine $(1 - \bar{v}\rho)$, and hence ϕ, by standard density measurements and the value of M_1 (if unknown) by extrapolation to infinite dilution of apparent weight-average molecular weights available from the sedimentation equilibrium results. The values of α_2, α_3, and α_4 may now be found using the experimental $\bar{c}(\xi)$ vs. ξ plot and the experimental parameters. In this connection, it will be demonstrated later that use of two $(\psi(\xi), \xi)$ points near the cell base, where the curvature of the plot is greatest, leads to sufficiently precise estimates of α_3 and α_4 when the following relations based on eq 8 and 11 are solved numerically.

$$\frac{\ln \psi(\xi_1)}{\ln \psi(\xi_2)} = \ln\left\{\frac{1 - \alpha_3}{\xi_1 - \alpha_3}\right\} \Big/ \ln\left\{\frac{1 - \alpha_3}{\xi_2 - \alpha_3}\right\} \quad (12a)$$

$$\alpha_4 = \ln \psi(\xi)/\ln\left|\frac{1 - \alpha_3}{\xi - \alpha_3}\right| \quad (12b)$$

Certainly the values thus obtained may be checked and if necessary refined by employing eq 8 to construct a plot of $\bar{c}(\xi)$ vs. ξ which may be compared with the experimental result.

Step 2. Equations 10 and 3b may now be used to compute corresponding values of $f(M_i)$ and M_i $(i = 2, 3, \ldots)$. The product $M_1 f(M_i)$ gives an estimate of the area enclosed by the $f(M_i)$ curve and lines situated at $M_i \pm (M_1/2)$ which corresponds to the relative amount in the cell, $f_i = (Q_i)_{cell}/Q_T$, of the species with molecular weight M_i. This integration procedure serves to reverse the introduction of the continuous distribution function $g(t_i)$, and hence of $f(M_i)$, in place of f_i (eq 6 and 7) and evidently may be refined, if required, by a more elaborate method of trapezoidal integration. The values of f_i, thus obtained, may be used in conjunction with eq 2 and 4 to calculate the molar concentration $m_i(r_m)$ from

$$m_i(r_m) = \phi b \bar{c}^0 f_i/(e^{\phi M_i b} - 1) \qquad i = 2, 3, \ldots \quad (13)$$

Step 3. The above procedure is not recommended for the determination of $m_1(r_m)$ because of the existence of a step function in the $f(M_i)$ distribution at M_1: nor is it likely that a sufficiently precise value of f_1 and hence $m_1(r_m)$ could be found using the relation

$$f_1 = 1 - \sum_{i=2}^{\infty} f_i$$

because this introduces additive error inherent in all f_i. Fortunately an alternative procedure is available for the evaluation of this basic quantity. It involves extrapolation of $\Omega_1(r)$ values to infinite dilution, where[14]

$$\Omega_1(r) = \bar{c}(r) e^{\phi M_1(r_F^2 - r^2)}/\bar{c}(r_F) \quad (14a)$$

and the reference point $(\bar{c}(r_F), r_F)$ is selected as any point in the experimental plot of $\bar{c}(r)$ vs. r. It has been shown[14] that

$$\lim_{c(r)\to 0} \Omega_1(r) = c_1(r_F)/\bar{c}(r_F) \quad (14b)$$

Thus, $c_1(r_F)$ is available from eq 14b, $c_1(r_m)$ from eq 1 and $m_1(r_m) = c_1(r_m)/M_1$. Since all $m_i(r_m)$ $(i = 1, 2, \ldots)$ are now available, it is a simple matter to calculate the successive apparent equilibrium constants from

$$K_i = m_i(r_m)/m_{i-1}(r_m) m_1(r_m) \quad (15)$$

TABLE I: Evaluation of the Equilibrium Constant for Isodesmically Associating Systems from Simulated Sedimentation Equilibrium Distributions[a]

M_1	K, M^{-1}	ω, rpm	$\bar{c}(r_m)$, g/l.	$m_1(r_m)$	f_1	α_2	α_3	α_4	Std dev, μ	K_{calcd}, M^{-1}	Std dev, M^{-1}
500	3×10^2	60 000	1.353	1.156×10^{-3}	0.294	−0.4624	−0.8254	0.9419	±8	3×10^2	±40
	3×10^3	36 000	1.317	2.340×10^{-4}	0.051	−0.1665	−0.9674	1.5673	±4	3×10^3	±100
5 000	3×10^3	20 000	1.265	1.118×10^{-4}	0.292	−0.5138	−0.7140	0.9447	±11	3×10^3	±400
	3×10^4	12 000	1.230	2.312×10^{-5}	0.051	−0.1850	−0.8391	1.5687	±5	3×10^4	±200
50 000	3×10^4	6 400	1.244	1.108×10^{-5}	0.292	−0.5261	−0.6901	0.9448	±11	3×10^4	±3 500
	3×10^5	4 000	1.140	2.280×10^{-6}	0.051	−0.2055	−0.7249	1.5697	±6	3×10^5	±15 000

[a] The following parameters were common to all simulations: $\bar{c}^0$ = 2.5 g/l.; $\bar{v}$ = 0.73 ml/g; ρ = 1.000 g/ml; T = 293.2°A; r_m = 6.9 cm, r_b = 7.2 cm.

where K_i is on the molar scale, suitable for the examination of the isodesmic nature or otherwise of the indefinite self-association.

In a more general vein, it should be stressed that several sedimentation equilibrium experiments must be performed with the system of interest. In the first place, results from several experiments would assist in the evaluation of M_1 and of $m_1(r_m)$ appropriate to each experiment, the latter being available from overlapping $\Omega_1(r)$ vs. $\bar{c}(r)$ plots.[14] Secondly, it would be unwise to attempt to apply the above procedure to those experiments where the total concentration range spanned was such that the relative amount of monomer in the cell dominated that of other species: this may immediately be assessed by calculating f_1 for each experiment using $m_1(r_m)$ and eq 13. Thirdly, the distributions chosen for analysis should be such that they can be fitted with reasonable precision to eq 8; this point receives further attention in the next section. Finally, while the present method of analysis may only be applied to individual sedimentation equilibrium distributions, a model and associated apparent equilibrium constants indicated by the analysis of a single sedimentation equilibrium distribution can and should be checked and, if necessary, refined in relation to other experiments covering a wide range of total concentration. This would be aided if expressions were available to simulate $\bar{c}(r)$ vs. r plots for a defined system. It is thus timely to discuss the numerical simulation of sedimentation equilibrium distributions for indefinitely self-associating systems and to use such simulated examples in the further discussion of the analysis procedure.

Numerical Illustrations

It has been shown that the total concentration of an indefinitely self-associating system, $A_{j-1} + A_1 \rightleftharpoons A_j$, may be written in terms of $m_1(r)$ in closed form since the basic expressions involve the sums of infinite converging geometric series. For example, the appropriate expression for an indefinite self-association governed by a single equilibrium constant (isodesmic) is[2]

$$\bar{c}(r) = M_1 m_1(r)/(1 - Km_1(r))^2 \qquad Km_1(r) < 1 \quad (16a)$$

For a system in which dimer formation is governed by $K_2 = m_2/m_1^2$ and the addition of monomer to dimer and to higher polymers by a different equilibrium constant, K_3, the analogous expression is[6]

$$\bar{c}(r) = \frac{M_1 m_1(r)\{1 + 2m_1(r)[K_2 - K_3] + K_3 m_1^2(r)[K_3 - K_2]\}}{(1 - K_3 m_1(r))^2}$$
$$K_3 m_1(r) < 1 \quad (16b)$$

Analogous closed solutions may readily be formulated when three or more equilibrium constants are involved. It follows that if $m_1(r_m)$ could be found from a conservation of mass condition, eq 1 and 16 could be used to simulate $\bar{c}(r)$ vs. r curves. Combination of eq 2 and 4 gives on rearrangement

$$\bar{c}^0 b\phi = \sum_{i=1}^{i=\infty} m_i(r_m)[e^{i\phi M_1 b} - 1] \quad (17a)$$

For a system involving two equilibrium constants (corresponding to eq 16b), eq 17a becomes on separation of the series and summing

$$\bar{c}^0 b\phi = m_1(r_m)\{e^{\phi M_1 b} - 1\} + K_2 m_1^2(r_m) \times \left\{\frac{e^{2\phi M_1 b}}{(1 - K_3 m_1(r_m)e^{\phi M_1 b})} - \frac{1}{(1 - K_3 m_1(r_m))}\right\} \quad (17b)$$

The corresponding expression for the isodesmic case (eq 16a) is obtained by placing $K_2 = K_3 = K$ in eq 17b and rearranging to give

$$\bar{c}^0 b\phi = \frac{m_1(r_m)e^{\phi M_1 b}}{(1 - Km_1(r_m)e^{\phi M_1 b})} - \frac{m_1(r_m)}{(1 - Km_1(r_m))} \quad (17c)$$

Equations 17b and 17c contain the single unknown $m_1(r_m)$ and thus complete the set required to simulate sedimentation equilibrium distributions for defined systems based on the initial loading concentration.

It was decided first to explore the applicability of the analysis procedure in relation to a set of isodesmic indefinite self-associations, the results of which are summarized in Table I. The range of monomer molecular weights shown in column 1 was selected to emphasize that relatively small molecules as well as macromolecules could be studied by the method. The equilibrium constants in column 2 were selected arbitrarily except that for each M_1 the first cited value corresponds to a dimerization constant of 1.2 l./g and the second to 12 l./g. The angular velocities in column 3 were chosen to give a $\bar{c}(r_b)/\bar{c}(r_m)$ ratio of approximately 4 with a measurable fringe density at the base (<200 fringes/cm). Column 5 reports values of $m_1(r_m)$ available to the experimenter by use of eq 1 and 14, from which were calculated f_1 values shown in column 6; evidently, for each simulation, the relative amount of monomer in the cell is not unduly large. Column 7 tabulates α_2 values calculated from $\alpha_2 = -\phi M_1 b$ and, in this connection, it is noted that α_2 must necessarily be negative if $(1 - \bar{v}_i\rho)$ is positive. Column 8 gives the values of α_3 obtained using eq 12a with $(\psi(\xi), \xi)$ points near the base. From eq 12a, it follows that $(1 - \alpha_3)/(\xi - \alpha_3) > 0$ for all $0 \leq \xi \leq 1$, which means that $\alpha_3 < 0$ or $\alpha_3 > 1$; the latter domain did not satisfy the required convergence of eq 12a, indicating that negative values of α_3 were appropriate. Column 9 reports the corresponding values of α_4 calculated from eq 12b. These values of α were used in eq 8 to construct plots of $\bar{c}(\xi)$ vs. ξ which were compared with the original simulation (11 comparisons over the whole range

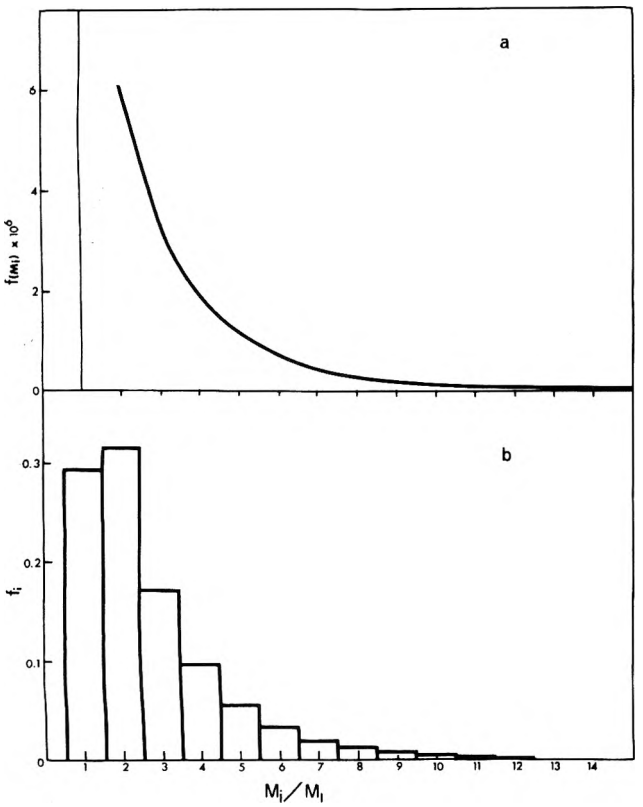

Figure 1. Distributions referring to the sedimentation equilibrium of an isodesmically indefinitely self-associating system with monomer molecular weight 5×10^4 and equilibrium constant 3×10^4: other parameters are given in Table I: (a) a continuous distribution of $f(M_i)$ described by eq 10; (b) a corresponding histogram showing the relative amount, $f_i = (Q_i)_{cell}/Q_T$, of species i with molecular weight M_i in the cell at sedimentation equilibrium.

of ξ) to give the standard deviations shown in column 10. Evidently the fit is within experimental ability to measure interferograms and thus the applicability of eq 8 is confirmed. Equation 10 was then applied to yield $(f(M_i), M_i)$ values and hence, as described in step 2, corresponding values of f_i. A typical result is shown in Figure 1, where both the continuous distribution in Figure 1a and the corresponding histogram in Figure 1b, which incorporates the value of f_1 (Table I), show that a reasonable number of species are reflected. Values of f_i, for all simulations, were used to calculate corresponding values of $m_i(r_m)$ (eq 13) and of K_i (eq 15). Ten successive values of K_i were used to obtain the arithmetic average values and their standard deviations shown in the last two columns of Table I. Clearly, the maximum percentage error is only 11% and, of greater relevance, the analysis procedure has led in each case to a value of the equilibrium constant in close agreement with that originally postulated.

The second type of system considered was that described by eq 16b and 17c involving two equilibrium constants in the indefinite self-association. A sedimentation equilibrium distribution was simulated with the parameters reported in Table I for the system $M_1 = 5000$, $K_2 = 3 \times 10^4$, K_3 (isodesmic) $= 3 \times 10^3\ M^{-1}$, and $\omega = 20\,000$ rpm. The value of f_1 was 0.139, with $\alpha_2 = -0.5138$, $\alpha_3 = -2.8570$, $\alpha_4 = 2.0669$, and $\bar{c}(r_m) = 1.366$ g/l.; these values led to a plot of $\bar{c}(\xi)$ vs. ξ with standard deviation (11 comparisons) of less than $\pm 1\ \mu$ when compared with the original simulation. This provides yet another illustration of the applicability of eq 8 in describing diverse distributions with $\bar{c}(r_b)/\bar{c}(r_m) \sim 4$. Application of step 2 and eq 15 led to the following values of K_i (M^{-1}): $K_2 = 2.7 \times 10^4$ and $K_j = 2.8 \pm 0.3 \times 10^3$ ($j = 3, 4, \ldots, 11$). The analysis procedure has therefore reproduced both values of the equilibrium constant (each within 10%) and correctly reflected their tenfold difference in magnitude. Several additional numerical examples led to similar findings, but with a further observation which is exemplified in the final illustration. This was performed with parameters identical with those of the preceding example except that three equilibrium constants were introduced, $K_2 = 3 \times 10^4$, $K_3 = 5 \times 10^3$, and K_4 (isodesmic) $= 1 \times 10^3\ M^{-1}$. The value of f_1 was 0.134 and the standard deviation of fit to the $\bar{c}(\xi)$ vs. ξ curve was $\pm 3\ \mu$. The analysis procedure led to the following apparent values of K_i (M^{-1}): $K_2 = 3.4 \times 10^4$, $K_3 = 3.2 \times 10^3$, and $K_j = 1.6 \pm 0.2 \times 10^3$ ($j = 4, 5, \ldots, 11$). Again the correct magnitude for each equilibrium constant is predicted, but there is evidently greater error in each numerical value than that predicted for the simpler systems.

Discussion

Two features of the use of the Laplace transform analysis as applied to a chemically interacting system, as distinct from a noninteracting mixture,[9-11] merit comment. First, the difficulty of fitting eq 8 to experimental results in terms of three parameters α_2, α_3, and α_4 has been discussed in detail previously,[11] in relation to a polydisperse lipoprotein system where α_2 was not available. In contrast, for polymerizing systems, it is always possible to evaluate $M_1(1 - \bar{v}\rho)$ and hence α_2, defining the step function, which renders tractable the determination of α_3 and α_4. Moreover, the possibility is not excluded that functions alternative to eq 8 may exist which meet the requirements of fitting experimental distributions and of inverting to yield a step function in the plot of $f(M_i)$ vs. M_i; at present, the demonstrated applicability of the simple function in eq 8 renders unwarranted a search for alternatives. Secondly, it is important to stress that for both types of system, derived f_i values refer to relative amounts in the cell. For noninteracting mixtures these may be correctly identified with relative amounts in the original mixture,[9-11] whereas for chemically interacting mixtures this identification cannot be made[12] and it is only by use of eq 13 and 15 that K_i values may be determined. These in turn could be used to calculate amounts of oligomeric forms in the original solution, if required.

For all systems examined, the analysis procedure has indicated that several species are present in significant amount and has correctly predicted the number and magnitudes of the relevant equilibrium constants describing the indefinite self-association of monomer. It is not claimed that the *numerical* values of the predicted K_i are exact, the error increasing with increasing values of f_1 (Table I) and with the number of equilibrium constants involved. On the other hand, comparison of all pairs of original and predicted K_i values reveals that they differ by no more than a factor of 2, which corresponds to a $\Delta(\Delta G°)$ of only 0.4 kcal/mol ($-RT$ ln 2). Certainly, in practice, where experimental error in $\bar{c}(r)$ values is encountered, the errors in predicted K_i values may be greater. It is accordingly recommended that K_i values derived from the analysis procedure be treated as first estimates and used to simulate plots of $\bar{c}(r)$ vs. r (in the manner used herein to calculate numerical examples) for direct comparison with experimental distributions. The potential is thereby offered of refining the values (and of considering nonideality effects[15]) in relation to a series of experiments encompassing a wide range of total solute concentration.

References and Notes

(1) K. E. Van Holde and G. P. Rossetti, *Biochemistry*, **6**, 2189 (1967).
(2) E. T. Adams and M. S. Lewis, *Biochemistry*, **7**, 1044 (1968).
(3) T. N. Solie and J. A. Schellman, *J. Mol. Biol.*, **33**, 61 (1968).
(4) K. E. Van Holde, G. P. Rossetti, and R. D. Dyson, *Ann. N.Y. Acad. Sci.*, **164**, 279 (1969).
(5) P. W. Chun, S. J. Kim, J. D. Williams, W. T. Cope, L. H. Tang, and E. T. Adams, *Biopolymers*, **11**, 197 (1972).
(6) G. J. Howlett, L. W. Nichol, and P. R. Andrews, *J. Phys. Chem.*, **77**, 2907 (1973).
(7) R. F. Steiner, *Arch. Biochem. Biophys.*, **39**, 333 (1952).
(8) P. D. Jeffrey and J. H. Coates, *Biochemistry*, **5**, 489 (1966).
(9) T. H. Donnelly, *J. Phys. Chem.*, **70**, 1862 (1966).
(10) T. H. Donnelly, *Ann. N.Y. Acad. Sci.*, **164**, 147 (1969).
(11) P. D. Jeffrey, L. W. Nichol, and G. D. Smith, *J. Biol. Chem.*, **250**, 533 (1975).
(12) E. T. Adams, *Proc. Nat. Acad. Sci. U.S.A.*, **51**, 509 (1964).
(13) G. J. Howlett, P. D. Jeffrey, and L. W. Nichol, *J. Phys. Chem.*, **74**, 3607 (1970).
(14) B. K. Milthorpe, L. W. Nichol, and P. D. Jeffrey, *Biophys. Chem.*, **3**, 169 (1975).
(15) A. G. Ogston and D. J. Winzor, *J. Phys. Chem.*, **79**, 2496 (1975).

An Investigation of the Micellar Phase of Sodium Dodecyl Sulfate in Aqueous Sodium Chloride Solutions Using Quasielastic Light Scattering Spectroscopy

Norman A. Mazer,* George B. Benedek,

Department of Physics, Center for Materials Science and Engineering, and Harvard–M.I.T. Program in Health Sciences and Technology, Massachusetts Institute of Technology, Cambridge, Massachusetts 02139

and Martin C. Carey[1]

Department of Medicine, Peter Bent Brigham Hospital, and Harvard Medical School, Boston, Massachusetts 02115

(Received December 10, 1975)

Publication costs assisted by the National Science Foundation and National Institutes of Health

Measurements of the autocorrelation function and average intensity of light quasielastically scattered from aqueous solutions of sodium dodecyl sulfate (SDS) in the presence of added NaCl were carried out over a wide region of the micellar phase and in the supercooled state below the critical micellar temperature (cmt). The mean size, shape, aggregation number, and polydispersity of SDS micelles have been deduced as a function of temperature (10–85 °C) and NaCl concentration (0.15–0.6 M) for detergent concentrations (1.7×10^{-2}, 3.5×10^{-2}, and 6.9×10^{-2} M) which appreciably exceed the critical micellar concentration (cmc). At these SDS concentrations the size and shape of the micelles show a marked dependence on the temperature and NaCl concentration. A minimum micellar size corresponding to a sphere with a hydrated radius of about 25 Å is asymptotically approached at high temperature in all NaCl concentrations. In NaCl concentrations greater than 0.3 M significant micellar growth occurs as the temperature is lowered, and the enlarged SDS micelle can be approximated by a prolate ellipsoid with a semiminor axis of 25 Å and a semimajor axis that approaches 675 Å in 0.6 M NaCl. The mean aggregation numbers of these rodlike micelles were found to vary approximately with the square root of the SDS concentration, and the width of the distribution of aggregation numbers was estimated at ±70% of the mean value. In supercooled solutions, micellar size and shape have the same dependence on detergent concentration, NaCl concentration, and temperature as occurs above the cmt. It is demonstrated that the cmt, its dependence on NaCl concentration, and the metastability of supercooled micellar solutions can be qualitatively understood by an extension of the Murray–Hartley theory of detergent solubility which accounts for the cmt phenomenon on the basis of the coupling between the monomer–hydrated solid equilibrium and the monomer–micelle equilibrium.

Introduction

Over the years a considerable experimental literature on sodium dodecyl sulfate (SDS) in aqueous NaCl solutions has been compiled, yet many important aspects of this system remain unexplored. In studies of the micellar phase boundaries, for example, particular attention has been given to the effect of NaCl concentration on the critical micellar concentration (cmc),[2] whereas the equally important boundary between the hydrated solid phase and the micellar phase (the critical micellar temperature, cmt)[3] has received little attention. In addition, previous studies of the size, shape, and aggregation numbers of SDS micelles have been confined to a rather small region of the micellar phase located at detergent concentrations in the vicinity of the cmc and at temperatures near 25 °C. This confinement to concentrations near the cmc is a result of the fact that the experimental techniques employed (i.e., conventional light scattering,[4] tracer diffusion,[5] and ultracentrifugation[6]) require extrapolation to zero micellar concentration (the cmc) in order to eliminate the effects of micellar interactions. With the exception of low-angle x-ray scattering studies of concentrated SDS solutions in water,[7] remarkably few efforts have been made to ascertain the size

and shape of SDS micelles at high detergent concentrations, particularly as a function of NaCl concentration and temperature.

We have undertaken an investigation of the micellar phase of SDS solutions at concentrations extending well above the cmc, in various NaCl concentrations, and over a wide range of temperatures, including the supercooled region below the cmt phase boundary for several reasons: (1) there is a distinct lack of experimental information in these regions of the micellar phase; (2) our experimental methods are ideally suited to the study of micellar solutions under these conditions, especially at detergent concentrations much greater than the cmc; and (3) data obtained in this region are vital to a theoretical understanding of micelle formation by ionic detergents in general.

We employed the technique of quasielastic light scattering spectroscopy[8] (QLS) which allows one to measure the diffusion coefficients of macromolecules rapidly and noninvasively, and yet has only recently been applied to the study of micellar solutions.[9-11] In addition, QLS offers a quantitative characterization of colloidal polydispersity,[12,13] an important micellar property that is difficult to assess with most other physical-chemical techniques. Since it has been shown that the diffusion coefficient measured by QLS is only weakly affected by the macromolecular interactions that occur in concentrated solutions,[14,15] the Stokes–Einstein relation[16] can therefore be used to relate the diffusion coefficient to the hydrodynamic radius of the macromolecules even in relatively concentrated solutions. Thus QLS provides a measure of the hydrodynamic radius and hence the size of SDS micelles applicable to a significant portion of the micellar phase, as well as the supercooled region below the cmt. Moreover, by employing measurements of the average scattered light intensity in conjunction with the hydrodynamic radii, we have deduced the corresponding shape and aggregation numbers of SDS micelles as functions of temperature, NaCl concentration, and detergent concentration. Accordingly, we believe that these observations on SDS micelles may have a substantial application in resolving the current controversies with regard to the shape and size of typical ionic detergent micelles.

Materials and Methods

A. *Reagents and Solutions.* Gel electrophoresis grade SDS (BioRad Laboratories, San Diego, Calif.) was employed, and its purity (~99.7%) was verified by thin layer chromatography, potentiometric titration, and surface tension (Wilhelmy blade method). Titration of a 1 g/dl solution of SDS with 1 M HCl gave a correct titration curve, and the surface tension measured as a function of SDS concentration indicated that dodecanol was not a contaminant. Sodium chloride (ACS grade, Fisher Scientific, Boston, Mass.) was roasted in air for 3 h at 600 °C in order to oxidize and remove organic impurities. Water was deionized and twice distilled. The final distillation was from a seasoned all-Pyrex laboratory distillation assembly. The surface tension of the water was 73.5 dyn/cm (22 °C), and did not change after sweeping and removal of the surface, which was marked with a few grains of pure talc, indicating the absence of surface active impurities. The water was filtered through a thoroughly washed medium-grain glass filter to exclude dust before use.

The required concentrations (w/v) of SDS were dissolved in aqueous NaCl solutions in acid-washed volumetric flasks which were periodically warmed above their cmt's to achieve complete dissolution. Solutions were stored at 30 °C in stoppered flasks for about 24 h in order to allow surface and suspended bubbles to separate before the final aliquots of solvent were added. The SDS solutions were then introduced into the Teflon and glass light scattering cells through a double layer of two 0.1-μ Nuclepore filters (A. H. Thomas Co., Philadelphia, Pa.) that were part of a closed cell filling system.

B. *Critical Micellar Temperatures.* Prior to the cmt measurements, the temperatures of the SDS solutions were lowered from 30 to 4 °C for about 1 h to enable the hydrated solid phase to form. The cmt values were then determined as the midpoint of a narrow temperature range over which the hydrated solid phase of SDS clarified on slow warming (at a rate of 0.3 °C/min) and with continuous vigorous shaking.

C. *QLS Measurements.* (1) *Theory.* It is well known that if a solution of macromolecules is illuminated, the mean intensity of the scattered light contains information on the molecular weight of the macromolecules.[17] In actual fact, however, the intensity of the scattered light continuously fluctuates around this mean value due to the Brownian movement of the macromolecules. The method of QLS makes use of the fact that the time dependence of these fluctuations can be related to the translational diffusion coefficient of the macromolecules. In order to quantitate this time dependence, one can measure the autocorrelation function of the scattered light intensity,[18] and from its time decay the correlation time (or times) of the intensity fluctuations is obtained. For a monodisperse solution of macromolecules a single correlation time, τ_c, is obtained, which is related to the translational diffusion coefficient, D, by the equation[18]

$$\tau_c = 1/D\mathbf{K}^2 \tag{1}$$

The magnitude of the scattering vector, $\mathbf{K}$, is given by[18]

$$\mathbf{K} = \frac{4\pi \sin \frac{1}{2}\theta}{\lambda/n} \tag{2}$$

where θ is the scattering angle, λ is the wavelength of the incident light in vacuo, and n is the index of refraction of the scattering medium. By combining the measurement of τ_c with the appropriate value of $\mathbf{K}$, one obtains, using eq 1, the diffusion coefficient of the macromolecules.

(2) *Apparatus and Methods.* A Spectra-Physics argon-ion laser (λ 5145 Å), operating at 150 mW, was used in conjunction with a 19-channel doubly scaled digital autocorrelator for measuring the autocorrelation function of the scattered light intensity. The scattering angle was varied by relocation of the photomultiplier tube which was mounted on a rotatable platform, and the temperature of the scattering cell was controlled to within 0.1 °C by means of a Peltier thermoelectric heating and cooling device. Equilibration times at each temperature were generally of the order of 15 min. Computer analysis[13] of the time decay of the autocorrelation function using the method of cumulants[12] provides a characterization of the distribution of correlation times associated with the polydispersity of the solution. In the present experiments the observed autocorrelation functions could be fit by two cumulants with a precision of better than 5 parts in 10^3 in each of the 19 channels. This precision could not be improved upon with the addition of further cumulants. From these two cumulants and the appropriate value of $\mathbf{K}$, the mean diffusion coefficient ($\bar{D}$) of the micelles and the variance (V), a quantitative measure of solution polydispersity, were obtained. The exact relationship of $\bar{D}$ and V to the distribution of micellar sizes is given in Appendix A. The index of refraction of the medium (n) needed for the calculation of $\mathbf{K}$ (eq 2) was determined by using the known refractive increments due to SDS and NaCl,[4] and the temperature dependence of n for pure

water.[19] Further details of the theory and methods of QLS can be found in ref 20 and 21.

D. *Calculation of the Mean Hydrodynamic Radii.* The mean hydrodynamic radius, $\bar{R}$, was calculated from $\bar{D}$ using a formula analogous to the Stokes–Einstein relation for spherical particles[16]

$$\bar{D} = kT/6\pi\eta\bar{R} \tag{3}$$

where k is Boltzmann's constant, T is the absolute temperature, and η is the coefficient of viscosity of the solvent. In these calculations the temperature dependence of η for aqueous NaCl solutions (i.e., $\eta(T)/\eta(20\ °C)$) was taken to be the same as that for pure water.[19] The value of $\bar{R}$ as defined in eq 3 represents a "mean" radius in two ways. First, $\bar{R}$ corresponds to the average hydrodynamic radius of all micellar species present in solution due to the fact that $\bar{D}$ is an average over this distribution. (See Appendix A.) Secondly, even for a monodisperse solution of micelles, the definition of $\bar{R}$ implies an average of the hydrodynamic frictional factors over all possible orientations of the micelles with respect to their translational motion. For spherical micelles $\bar{R}$ is the hydrated radius of the sphere, whereas for nonspherical micelles $\bar{R}$ depends in a complicated way on the hydrated volume and shape of the micelles through the orientational averaging.

E. *Mean Intensity Measurements.* A measure of the mean scattered light intensity was obtained from the time-averaged rate at which photopulses entered the autocorrelator as detected by a digital frequency meter. The system was calibrated by using a series of neutral density light filters to vary the scattered intensity from an arbitrary standard solution in a known way. This calibration provided a relative measure of the scattered intensity from the photopulse rate, expressible as the ratio I'/I_0, where I' is the absolute scattered intensity from a SDS solution, and I_0 is the intensity of the arbitrary standard. Since reflections from cell windows and sources other than the detergent molecules contribute to the scattered intensity, the value I' contains, in general, a small background component. The relative background intensity, I_B/I_0, was assumed to be equal to the relative scattered intensity obtained from a cell filled with solvent. The relative intensity scattered by the detergent alone, I/I_0, is therefore given by

$$\frac{I}{I_0} = \frac{I'}{I_0} - \frac{I_B}{I_0} \tag{4}$$

Results

A. *Critical Micellar Temperatures.* The cmt values of solutions containing 6.9×10^{-2} M (2 g/dl) SDS are plotted as a function of NaCl concentration (0–0.6 M) in Figure 1. The characteristic temperature range over which each solution clarified is of the order of 1 °C. The cmt values for SDS in 0–0.05 M NaCl taken from the solubility data of Nakayama and Shinoda[22] are also shown for comparison. The cmt increases by nearly 10° as the NaCl concentration is raised from 0 to 0.6 M; however, about half of this increase takes place between 0 and 0.1 M NaCl. Additional cmt measurements made on solutions containing 3.5×10^{-2} M (1 g/dl) and 1.7×10^{-2} M (0.5 g/dl) SDS in 0.6 M NaCl showed that the cmt is independent of detergent concentration within this range.

B. *Mean Diffusion Coefficients and Variances.* (1) *Dependence on NaCl Concentration and Temperature.* The values for $\bar{D}$ and V (90° scattering angle) as functions of temperature for 6.9×10^{-2} M SDS and NaCl concentrations of 0.15, 0.3, 0.45, 0.55, and 0.6 M are listed in Table I. The lowest temperatures for which values are listed correspond to the temperatures at which the precipitation of SDS occurred within the scattering cell. In general $\bar{D}$ and V values were obtained for supercooled micellar solutions over a 7–10 °C range below the corresponding cmt values. The reproducibilities of $\bar{D}$ and V were within ±1 and ±5% for the same sample, and within ±5 and ±10% of the values given in Table I for different samples under identical conditions. Both $\bar{D}$ and V were completely reversible functions of temperature within experimental error. $\bar{D}$ (Table I) increases as a function of temperature at fixed NaCl concentration and decreases with increasing NaCl concentration at fixed temperatures. In contrast to the dramatic variation of $\bar{D}$ with temperature and NaCl concentration, the V values, which were typically of the order of 35%, showed no appreciable dependence on either variable.

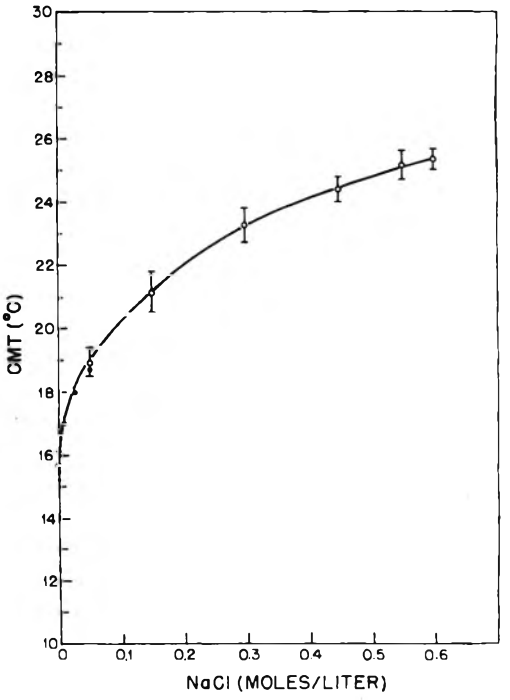

Figure 1. The critical micellar temperature (cmt) of 6.9×10^{-2} M SDS as a function of NaCl concentration: O, this study; ●, from the solubility data of Nakayama and Shinoda.[22] Brackets indicate temperature range over which solutions clarified.

(2) *Dependence on SDS Concentration.* The temperature dependence of $\bar{D}$ and V (90° scattering angle) for SDS solutions of 1.7×10^{-2} and 3.5×10^{-2} M in 0.6 M NaCl are listed in Table II. When compared with the corresponding values for 6.9×10^{-2} M in 0.6 M NaCl (Table I), the $\bar{D}$ values decrease with SDS concentration at all temperatures, whereas the V values are not significantly affected.

(3) *Dependence on Scattering Angle.* The angular dependence of the autocorrelation function was studied for 6.9×10^{-2} M SDS in 0.6 M NaCl at 30 °C. By varying the scattering angle from 30 to 150°, the value of $\mathbf{K}^2$ was increased by a factor of 13.9. Over this range of scattering angles the deduced values of $\bar{D}$ and V were found to be independent of scattering angle within the experimental error.

C. *Mean Hydrodynamic Radii.* (1) *Dependence on NaCl Concentration and Temperature.* The temperature dependence of $\bar{R}$, calculated from the data in Table I, is plotted for 6.9×10^{-2} M SDS in various NaCl concentrations in Figure 2. It is apparent that $\bar{R}$ is significantly dependent on both temperature and NaCl concentration. At high NaCl concentrations a dramatic increase in $\bar{R}$ occurs as the temperature

TABLE I: Mean Diffusion Coefficients and Variances in 6.9×10^{-2} M SDS as a Function of NaCl Concentration and Temperature

NaCl, M	Temp, °C	Mean diffusion coeff $\bar{D}$, 10^{-7} cm^2/s	Variance V, %
0.15	11	5.59	28
	13	6.06	21
	15	6.67	33
	17	7.17	28
	20	8.32	33
	25	9.69	28
	35	13.3	41
0.3	15	5.44	45
	17	5.92	37
	18	6.23	34
	20	6.78	30
	25	8.23	30
	30	9.92	35
	40	13.3	35
	50	16.4	32
0.45	17	2.84	33
	18	3.12	34
	20	3.65	30
	25	5.69	35
	30	8.00	32
	35	9.98	27
	40	12.1	36
	50	16.1	36
	60	21.0	41
	70	25.6	42
0.55	17	1.56	37
	18	1.67	38
	20	1.90	35
	25	2.77	39
	35	5.75	41
	45	10.8	36
	55	15.6	37
0.6	18	1.13	32
	19	1.22	35
	20	1.34	34
	21	1.43	31
	22	1.53	31
	23	1.76	34
	25	2.03	36
	30	2.92	37
	35	3.96	40
	40	5.92	38
	45	8.01	46
	50	11.2	42
	55	14.3	39
	60	17.2	45
	65	19.0	38
	75	24.0	35
	85	29.8	42

TABLE II: Mean Diffusion Coefficients and Variances in 0.6 M NaCl as a Function of SDS Concentration and Temperature

SDS, M	Temp, °C	Mean diffusion coeff $\bar{D}$, 10^{-7} cm^2/s	Variance V, %
1.7×10^{-2}	16	1.77	39
	18	2.03	38
	20	2.36	39
	25	3.42	38
	35	7.13	38
	45	11.7	40
	55	15.5	42
3.5×10^{-2}	17	1.40	30
	18	1.54	36
	20	1.78	37
	25	2.63	38
	35	5.77	38
	45	10.3	31
	55	14.9	41
	65	19.2	49

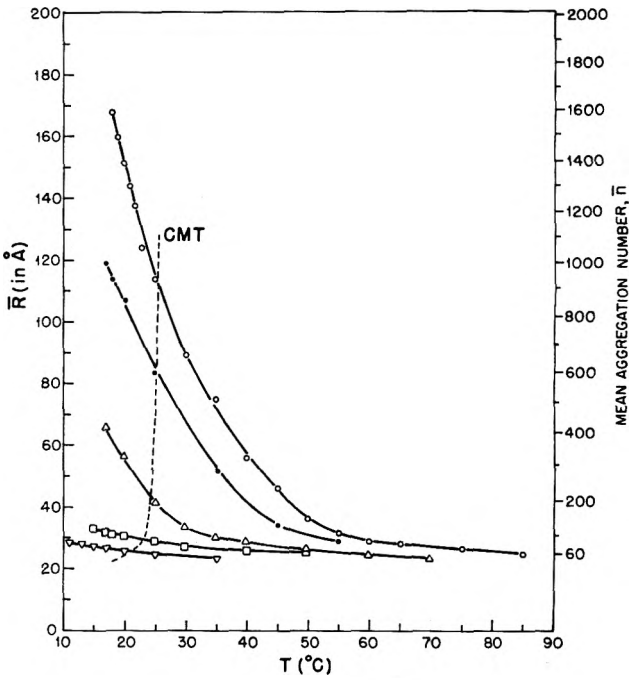

Figure 2. The mean hydrodynamic radius ($\bar{R}$) of 6.9×10^{-2} M SDS as a function of temperature: O, in 0.6 M NaCl; ●, in 0.55 M NaCl; △, in 0.45 M NaCl; □, in 0.3 M NaCl; ▽, in 0.15 M NaCl. Dashed line intersects solid curves at the respective cmt values. Points to the left of cmt represent supercooled sulutions. Vertical axis on right provides a nonlinear scale of mean aggregation numbers ($\bar{n}$) corresponding to the $\bar{R}$ axis for a micellar shape represented by a prolate ellipsoid whose semiminor axis is fixed at 25 Å.

approaches and then passes below the cmt. However, at low NaCl concentrations only a small increase in $\bar{R}$ occurs as the temperature is lowered. Conversely, at high temperatures $\bar{R}$ decreases asymptotically to values that are nearly independent of NaCl concentration. The asymptotic minimum is about 25 Å in 0.6 M NaCl and appears to be 1 to 2 Å less for the lower NaCl concentrations. The continuity of all curves as they pass below the cmt (Figure 2) indicates that the micellar size in supercooled solutions has the same dependence on NaCl concentration and temperature as above the cmt. The hydrodynamic radius attained the largest value (167 Å) in 0.6 M NaCl at 18 °C.

The vertical axes on the right-hand sides of Figures 2 and 3 provide a scale of mean aggregation numbers ($\bar{n}$) that correspond to the respective $\bar{R}$ values assuming that the micellar shape of SDS is represented by a prolate ellipsoid whose semiminor axis is fixed at 25 Å. The rationale for the prolate shape is given later.

(2) *Dependence on SDS Concentration.* The influence of three concentrations of SDS (1.7×10^{-2}, 3.5×10^{-2}, and 6.9×10^{-2} M) in 0.6 M NaCl on $\bar{R}$ is plotted as a function of temperature in Figure 3. At each temperature $\bar{R}$ becomes

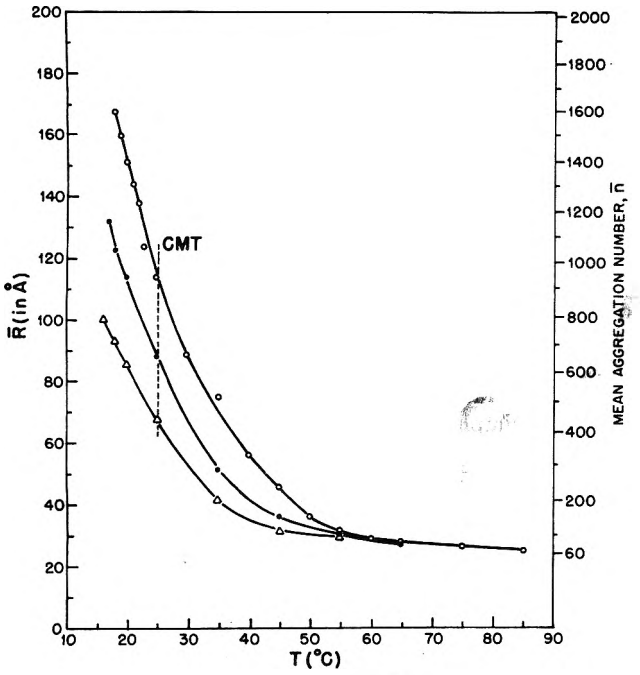

Figure 3. The mean hydrodynamic radius ($\bar{R}$) of SDS in 0.6 M NaCl as a function of temperature: O, in 6.9×10^{-2} M SDS; ●, in 3.5×10^{-2} M SDS; △, in 1.7×10^{-2} M SDS. Dashed line intersects solid curves at the respective cmt values. Vertical axis on right provides a nonlinear scale of mean aggregation numbers ($\bar{n}$) corresponding to the $\bar{R}$ axis for a micellar shape represented by a prolate ellipsoid whose semiminor axis is fixed at 25 Å.

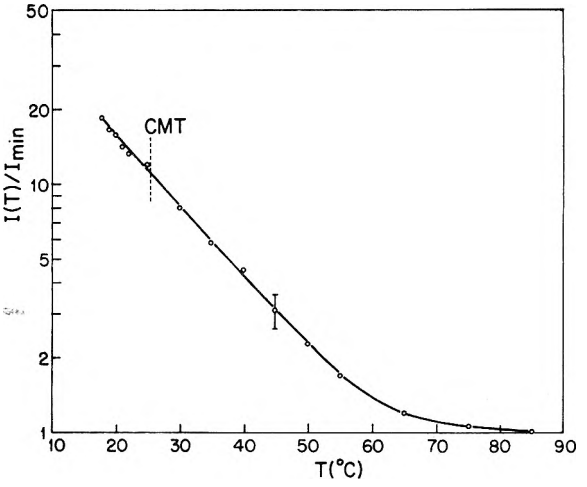

Figure 4. The temperature dependence of the intensity ratio ($I(T)/I_{min}$) for the solution containing 6.9×10^{-2} M SDS in 0.6 M NaCl. Bracket indicates the maximum uncertainty of ±15% in all points.

larger with increases in the SDS concentration; however, as the temperature approaches 55 °C, $\bar{R}$ becomes independent of the SDS concentration and asymptotically approaches a value of 25 Å.

D. *Scattered Intensity Measurements.* The temperature dependence of the relative scattered light intensity (90° scattering angle) was measured for the 6.9×10^{-2} M SDS solution in 0.6 M NaCl. By dividing the relative intensity measured at each temperature, $I(T)/I_0$, by the minimum relative intensity measured at 85 °C, I_{min}/I_0, we obtain an intensity ratio, $I(T)/I_{min}$, which is plotted in Figure 4. $I(T)/I_{min}$ dramatically increases from an asymptotic value of 1 at 85 °C to about 19 at 18 °C. From eq 4, $I(T)/I_{min}$ is equal to $(I'(T) - I_B)/(I_{min}' - I_B)$, where the primes indicate that the intensities have not been corrected for the background scattering, I_B. If the uncertainties in I_{min}' and I_B are not small compared to the difference $I_{min}' - I_B$, then these uncertainties contribute significantly to the uncertainty in the intensity ratio. Our analysis of this contribution leads to a maximum uncertainty of about 15% for all data points, as indicated by the bracket on the curve in Figure 4.

Interpretation of the Autocorrelation Functions, $\bar{R}$ Values, and Scattered Intensity Ratios

A. *Relationship of the Autocorrelation Function to the Translational Diffusion Coefficients of Micelles.* The autocorrelation function of the scattered light intensity primarily contains information on the Brownian movement of the micelles. In addition, however, there may be contributions from: (1) the Brownian movement of small molecules in the solution (detergent monomers, Na^+ and Cl^- ions), (2) the rotational motion of the micelles, and (3) the fluctuations associated with the dynamic equilibrium between micelles and monomers. These three effects make no measurable contribution to the autocorrelation function for the following reasons. First, the intensity of the light scattered by any species is proportional to the product of its concentration (w/v) and its molecular weight.[17] One can estimate therefore that the intensity of the light scattered by micelles is at least 1000 times greater than the intensity of light scattered by the small solute molecules. In addition, the short correlation times associated with the small molecules renders their contribution to the autocorrelation function completely negligible on the time scales being examined (typically 2–50 μs). Secondly, the fact that the deduced value of $\bar{D}$ is the same at every scattering angle provides strong evidence that the effects of rotation and monomer–micelle equilibria are negligible. Such effects, if sizeable, should introduce an apparent angular dependence on the deduced value of $\bar{D}$.[9,20] In particular, our conclusion that the monomer–micelle equilibrium makes no measurable contribution to the autocorrelation function is in agreement with previous QLS studies of micellar systems.[9,10] We therefore conclude that the quantity $\bar{D}$ obtained from the cumulants analysis of the autocorrelation function gives a precise measurement of the mean translational diffusion coefficient of the micelles. It should be noted that the values of $\bar{D}$ reported here are in substantial agreement with a limited number of apparent diffusion coefficients measured over a small region of the micellar phase using conventional methods.[5,6] McQueen and Hermans[9] who used QLS to study SDS solutions at a single NaCl concentration (0.1 M) and temperature (22 °C) have obtained values for the micellar diffusion coefficient comparable to ours.

B. *Relationship between $\bar{D}$ and $\bar{R}$.* We have deduced $\bar{R}$ from $\bar{D}$ using eq 3 on the assumption that $\bar{D}$ is not substantially affected by micellar interactions. In effect, we are assuming that the value of $\bar{D}$ measured at the moderately high SDS concentrations employed should be nearly the same as the value that would be found at very low SDS concentrations, if it were possible to dilute the system without altering the distribution of micellar sizes. This assumption is consistent with a variety of experimental[14,23] and theoretical[14,15] results concerning the concentration dependence of $\bar{D}$ measured in other macromolecular systems using QLS. It has been shown[14,15] that when nonaggregating macromolecules interact as hard spheres (i.e., excluded volume interactions) that the value of $\bar{D}$ is only weakly dependent on particle concentration. For the largest detergent concentration (w/v) used in the

present study (2 g/dl), the hard sphere interactions are predicted[14] to change $\bar{D}$ by only 2%, a negligible amount. However, since the SDS micelle carries a significant charge,[4] the possible effects of electrostatic interactions on $\bar{D}$ must be considered. In this regard the interactions between charged particles have been experimentally shown to approach the hard sphere limit as the ionic strength of the solution becomes sufficiently large so as to screen out the electrostatic effects. In a study of charged R17 virus particles by Pusey et al.[14] the hard sphere limit is attained in NaCl concentrations between 0.15 and 1 M. Before this limit is reached, however, the diffusion coefficient of the R17 particles is found to increase significantly with particle concentration. Thus the electrostatic interactions between micelles can be expected to raise the value of $\bar{D}$ obtained at low NaCl concentrations, and thereby cause the apparent value of $\bar{R}$ to be less than the actual $\bar{R}$. By extrapolating the concentration dependence of $\bar{D}$ obtained by Pusey et al.[14] in 0.15 M NaCl when electrostatic screening is incomplete, we may expect the values of $\bar{R}$ deduced for 6.9×10^{-2} M SDS to be about 12% smaller than the actual value of $\bar{R}$.

The above considerations of hard sphere and electrostatic interactions permit us to conclude that for the SDS concentrations employed in this study, the effect of micellar interactions should be negligible for solutions containing greater than 0.45 M NaCl (an estimate of the NaCl concentration needed for the hard sphere limit). Under these conditions, the values of $\bar{D}$ should approximately equal the values which would obtain for the same distribution of micellar sizes at very low concentration. It is therefore valid to deduce $\bar{R}$ from $\bar{D}$ using eq 3 by employing a viscosity value equal to that of the solvent alone. In this way we have found, for example, that in 0.6 M NaCl the $\bar{R}$ values asymptotically approach the same value of 25 Å at high temperature, regardless of SDS concentration (Figure 3). For SDS solutions containing lower concentrations of NaCl (<0.45 M), the apparent $\bar{R}$ values may underestimate the actual $\bar{R}$ values by at most 12%. This suggests that the small effect of NaCl concentration on the apparent asymptotic values of $\bar{R}$ (Figure 2) could result solely from the effect of NaCl on the electrostatic interactions between micelles.

Finally our observation that the smallest SDS micelles have $\bar{R}$ values of about 25 Å is in satisfactory agreement with values of 23 and 24 Å for the apparent radii of spherical SDS micelles from small-angle x-ray scattering studies.[7] Hydration of the micelle would account for the slightly larger micellar radius obtained from the QLS measurement. Furthermore, as the length of the extended SDS anion as measured from a Stuart–Briegleb molecular model is 23 Å, our data are consistent with the classical view[24] that the minimum size of a detergent micelle corresponds to a spherical aggregate whose radius is approximately the length of the extended detergent chain.

C. *Relationship between Intensity Ratio and Micellar Mass and Form Factor.* The temperature dependence of the intensity ratio $I(T)/I_{min}$ can readily be related to the temperature dependence of the micellar mass. If the micelles are treated as monodisperse and noninteracting, and the scattering by small molecules neglected, then the turbidity of the solution, τ, is given by[17]

$$\tau = HCMP \tag{5}$$

where H is related to the index of refraction of the solution and its derivative with respect to detergent concentration, C is the concentration of micelles (w/v), M is the micellar mass, and P is the form factor of the scattered light.[17] The latter depends on the size and shape of the micelles and the magnitude of the wave vector, **K**. Since the relative scattered intensity is proportional to τ, the intensity ratio will be given by

$$\frac{I(T)}{I_{min}} = \frac{H(T)C(T)M(T)P(T)}{H_{min}C_{min}M_{min}P_{min}} \tag{6}$$

where H_{min}, C_{min}, M_{min}, and P_{min} correspond to the minimum spherical micelle formed at 85 °C. For the SDS concentration employed in the intensity measurements (2 g/dl), the concentration of micelles (w/v) is greater than 100 times the concentration of monomers (w/v), the value of which is equivalent to the cmc in 0.6 M NaCl.[25] Thus to a high degree of accuracy both $C(T)$ and C_{min} are equal to the total detergent concentration, and therefore cancel in eq 6. Equation 6 is further simplified by neglecting the dependence of H on temperature which is estimated[26] to vary by less than 3% between 15 and 85 °C, and by noting that P_{min} is unity for the minimum spherical micelle. The intensity ratio then reduces to

$$\frac{I(T)}{I_{min}} = \frac{M(T)P(T)}{M_{min}} \tag{7}$$

Thus $I(T)/I_{min}$ will be less than or equal to the ratio of the micellar masses depending on the magnitude of $P(T)$ which beomes smaller than unity at temperatures where the micellar size becomes comparable to $\mathbf{K}^{-1}$.

A meaningful interpretation of the intensity ratio is provided by eq 7, even when the complications of polydispersity, micellar interactions, and charge effects are taken into account. To account for polydispersity, one uses the values of $M(T)P(T)$ and M_{min} that correspond to averages over the distribution of micelles, where each species is weighted by its concentration (w/v).[4] Secondly, since we have taken the ratio of scattered intensities, we expect that the effect of micellar interactions on the absolute intensities should approximately cancel between $I(T)$ and I_{min}. This is based on the reasonable assumption that in 0.6 M NaCl the predominant interactions are due to the excluded volumes (hard sphere interactions). The excluded volume is a function of the volume fraction ϕ[15] of the micelles in solution which is about 0.02 in the present case and does not vary with temperature. If we ignore the effect of micellar shape on the excluded volume interaction, then the effect of this interaction on the scattered intensities can be expected to cancel between numerator and denominator of the intensity ratio. It is also known that the micellar charge can affect the absolute intensity of the scattered light even in solutions of high ionic strength.[27] The magnitude of the so-called charge effect depends primarily on the micellar charge-to-mass ratio. However, since we measure the ratio of intensities at two different temperatures, this effect of charge will also cancel in the intensity ratio, assuming that the micellar charge-to-mass ratio has no significant dependence on either temperature or micellar size. Experimental estimates of the charge-to-mass ratio of SDS and other ionic micelles support this assumption.[4,28] Thus, in spite of the effects of micellar interactions and micellar charge on the absolute scattered intensities, the relationship between intensity ratio, micellar mass ratio, and form factor, given in eq 7, should be a good approximation even when the detergent concentration greatly exceeds the cmc.

Discussion

A. *Micellar Phase Boundaries.* As a preliminary in this study, it was necessary to establish the location of the cmt phase boundary as a function of NaCl concentration (Figure

1). The prevailing theory of this phase boundary, based on the work of Krafft,[29] suggests that a conformational change in the hydrocarbon chain of the detergent molecule occurs at the cmt and thereby causes the transformation from hydrated solid to micelles and vice versa.[3,30] The Krafft theory, however, does not readily explain how the cmt can depend on the NaCl concentration of the solution. On the other hand, a theory first proposed by Murray and Hartley[31] provides a natural means to understand the observed dependence of the cmt on NaCl concentration. In addition, the Murray–Hartley theory of the cmt can provide insight into the behavior of supercooled micellar solutions. In a future paper we shall quantitatively apply the Murray–Hartley theory to the present SDS data; however, it is useful at the present time to describe the physical content of this theory.

Let us first assume that the solubility (in aqueous NaCl) of a detergent molecule in its monomeric form is a weakly increasing function of temperature denoted by $S_1(T)$. Since the detergent molecules can exist in solution, both as monomers and micelles, the total solubility of the detergent, $S(T)$, may differ from $S_1(T)$. However, at temperatures where $S_1(T)$ is less than or equal to the cmc of the detergent, $S(T)$ will be equal to $S_1(T)$. This is a result of the fact that the formation of micelles does not occur until the dissolved monomer concentration reaches the cmc. The temperature at which $S_1(T)$ = cmc is commonly defined as the Krafft temperature,[3,30] T_k. Below T_k, $S(T)$ increases weakly with temperature in exactly the same manner as $S_1(T)$, whereas above T_k the behavior of $S(T)$ deviates dramatically from $S_1(T)$. These temperature dependences are illustrated by hypothetical curves of $S_1(T)$ and $S(T)$ which are plotted in Figure 5. To understand the abrupt increase in $S(T)$ shown in the figure, let us consider a solution at temperature T_k which has a detergent concentration, C_D, much greater than $S_1(T_k)$. Under these conditions the solution contains dissolved monomers, whose concentration $S_1(T_k)$ is equal to cmc, in equilibrium with a hydrated solid precipitate whose concentration is C_D − cmc (Figure 5). Suppose the temperature of the solution is increased to the slightly greater value $T_k + \Delta T$, then the monomeric solubility, $S_1(T_k + \Delta T)$, becomes equal to cmc + ΔC, where ΔC is a small concentration increment dependent on the slope of $S_1(T)$ (Figure 5). To reestablish equilibrium between hydrated solid and monomer at $T_k + \Delta T$, the monomer concentration must increase by the amount ΔC. However, the formation of micelles prevents this increase in monomer concentration from occurring. A classical mass action analysis of the equilibrium between micelles and monomers[31,32] shows that any effort to increase the monomer concentration to values greater than the cmc results, at equilibrium, in the formation of micelles, while the monomer concentration remains essentially fixed at the cmc. Though the hydrated solid releases monomer in order to achieve the solid–monomer equilibrium, this equilibrium can never be reached because of the sequestration of monomer within micelles. Continued release of monomer thus takes place until the hydrated solid dissolves completely. Hence above T_k the total detergent solubility $S(T)$ increases dramatically with temperature. Alternatively, we can say that solutions containing detergent concentrations well above the cmc will clarify at about the same temperature independent of concentration. This clarification temperature is called the critical micellar temperature. One can appreciate from Figure 5 that the cmt correlates closely with T_k, being generally a few degrees higher.

The Murray–Hartley theory thus relates the abrupt increase in the detergent solubility (i.e., the existence of a critical

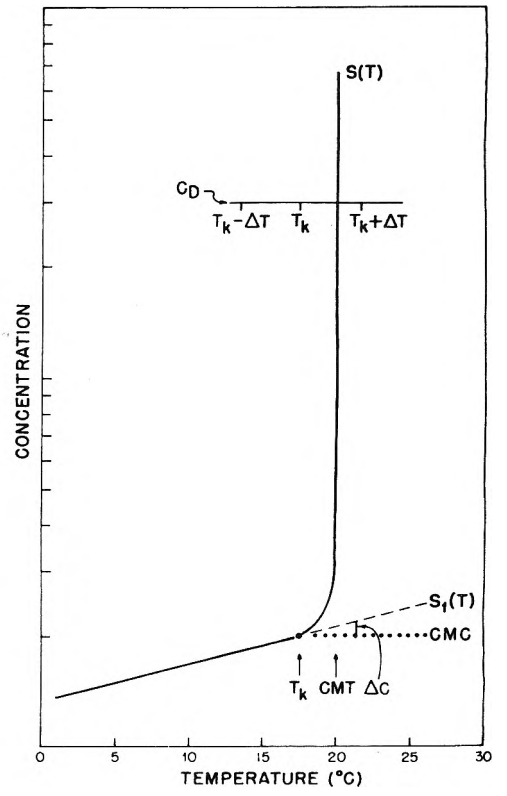

Figure 5. Hypothetical curve of detergent solubility as a function of temperature (concentration scale is arbitrary). Continuous curve indicates total solubility, $S(T)$. Dashed curve indicates the extrapolation of the monomeric solubility, $S_1(T)$, above T_k. Dotted line indicates the cmc, whose weak variation with temperature is neglected. Vertical arrows indicate the temperature values corresponding to T_k and cmt. Horizontal line indicates a detergent concentration C_D much greater than the cmc. ΔC is the difference in monomer concentration between $S_1(T_k + \Delta T)$ and cmc.

micellar temperature) to the saturation of the monomer concentration associated with the formation of micelles (i.e., the phenomenon of the cmc). From the Murray–Hartley theory we can see phenomenologically how the cmt, or more simply T_k, may depend on the NaCl concentration. The value of T_k is defined as the intersection between the curve of $S_1(T)$ and the cmc. Since both $S_1(T)$ and cmc vary with NaCl concentration, their intersection, i.e., T_k, also changes with NaCl concentration. Using this idea, and employing the experimental variation of cmc[2] and $S_1(T)$[22] with NaCl concentration, it is in fact possible to obtain a prediction of the NaCl dependence of the cmt. This prediction is in satisfactory agreement with the experimental data for SDS and will be presented in a future paper.

Lastly, the Murray–Hartley model for the dissolution of the hydrated solid can also be used to gain insight into the reverse process, i.e., the formation of hydrated solid from the micellar phase. Referring back to Figure 5, let us consider a solution at temperature $T_k + \Delta T$ with detergent concentration C_D. In this state only micelles and monomers are present. If the temperature is now lowered to $T_k - \Delta T$, the equilibrium state will be one consisting of monomers and solid. In order for this state to be achieved the monomers must start to precipitate from solution, thereby temporarily reducing the monomer concentration below the cmc. The monomer concentration, however, is quickly restored to the cmc by dissolution of some micelles, in order to maintain the monomer–micelle equilibrium. This process yields more monomer for further produc-

tion of the hydrated solid. In effect, then, the detergent molecules now flow from the micellar form through the monomer form into the hydrated solid form, the precise reverse of the dissolution transformation. The phenomenon of metastability is associated with the initiation of precipitation of the monomers, which are present in the low concentration corresponding to the cmc. The small number of dissolved monomers reduces the likelihood of the nucleation process and thereby favors metastability. These considerations are consistent with our observations of the continued growth of the micelles at temperatures below the cmt, since in the absence of monomer precipitation, micelle formation will occur in exactly the same manner as above the cmt.

B. *Micellar Shape and Aggregation Numbers.* By plotting the intensity ratio $I(T)/I_{min}$ vs. $\bar{R}$ measured at the corresponding temperature for 6.9×10^{-2} M SDS in 0.6 M NaCl, we obtain a curve (Figure 6) which is capable of providing a sensitive experimental test of micellar shape. Model calculations of the dependence of I/I_{min} on $\bar{R}$ were carried out for three possible shapes: the prolate ellipsoid (I), the oblate ellipsoid (II), and the sphere (III). In the case of the ellipsoids it is assumed that the semiminor axis (b) is always 25 Å, i.e., the radius of the minimum spherical micelle. This constraint is consistent with a micellar structure in which the hydrocarbon chains of the SDS molecules form a continuous hydrophobic core within the micelle.[33] The spherical shape is chosen to represent a spherical "grapelike" aggregate of minimum spherical micelles. By comparing the calculated dependences of I/I_{min} on $\bar{R}$ with the experimental results (Figure 6), we can identify which of these shapes best describes the data. Furthermore, the deduction of micellar shape enables us to estimate the mean aggregation number, $\bar{n}$, from the corresponding value of $\bar{R}$.

(1) *Model Calculations.* In order to calculate the dependence of I/I_{min} on $\bar{R}$, eq 7 is employed with the simplifying assumption of monodispersity. It is thus necessary to determine the dependence of the micellar mass ratio and form factor, P, on $\bar{R}$. Since the partial specific volume of SDS micelles varies by less than 10% with micellar size[34,35] and solution temperature,[7] the micellar mass ratio is essentially equal to the micellar volume ratio. The dependence of micellar volume on $\bar{R}$ is obtained for the ellipsoidal shapes by first deducing the semimajor axis, a, from the hydrodynamic radius $\bar{R}$ with the aid of Perrin's equations for prolate and oblate ellipsoids.[21] These equations relate the hydrodynamic radii to the ellipsoidal axes, a and b, and are represented by the functions $\bar{R}_I(a,b)$ and $\bar{R}_{II}(a,b)$, respectively. After setting b equal to 25 Å, we can invert the above functions and thus obtain two different relations between a and $\bar{R}$ denoted by $a_I(\bar{R})$ and $a_{II}(\bar{R})$. The micellar volume ratios V/V_{min} for shapes I, II, and III are related to $a_I(\bar{R})$, $a_{II}(\bar{R})$, and $\bar{R}$, respectively, by:

$$\frac{V_I(\bar{R})}{V_{min}} = \left(\frac{a_I(\bar{R})}{25}\right) \quad \text{prolate shape (I)} \qquad (8i)$$

$$\frac{V_{II}(\bar{R})}{V_{min}} = \left(\frac{a_{II}(\bar{R})}{25}\right)^2 \quad \text{oblate shape (II)} \qquad (8ii)$$

$$\frac{V_{III}(\bar{R})}{V_{min}} = \left(\frac{\bar{R}}{25}\right)^3 \quad \text{spherical shape (III)} \qquad (8iii)$$

The dependence of P on $\bar{R}$ for each of the three models can be calculated, using the equations of Debye and Anacker.[36] These equations show that P remains very close to unity for both the spherical and oblate shapes in the size range being considered.

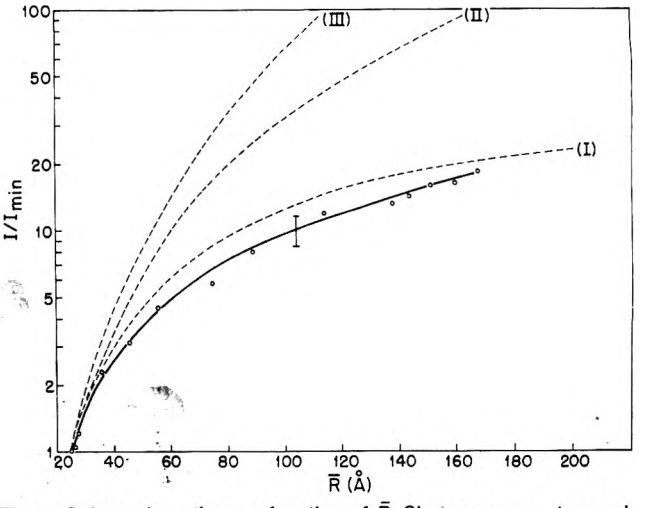

Figure 6. Intensity ratio as a function of $\bar{R}$. Circles represent experimental dependence obtained from $\bar{R}$ values and intensity ratios plotted in Figures 3 and 4. Bracket indicates the maximum uncertainty (±15%) in all data points. Dashed curves represent model calculations for the following shapes: I, prolate ellipsoid; II, oblate ellipsoid, III, sphere.

However, for the prolate shape, P depends on $\bar{R}$ through $a_I(\bar{R})$ and becomes substantially less than unity as $\bar{R}$ approaches 100 Å. Combining eq 8i, 8ii, and 8iii with the respective P values, we obtain, through eq 7, the dependence of I/I_{min} on the hydrodynamic radius $\bar{R}$ for each model. The three theoretical curves are plotted along with the experimentally derived curve in Figure 6.

(2) *Deduction of Shape.* The experimental intensity ratios clearly increase with $\bar{R}$ in a manner close to that predicted by the prolate model (Figure 6). The agreement between theory and experiment is not exact, but in view of the simplifying assumptions made in the model calculations, the result provides compelling evidence that SDS micelles become elongated (rodlike) structures under the conditions of low temperature, high detergent, and high NaCl concentration. The x-ray scattering studies of Reiss-Husson and Luzzati[7] support this deduction in that SDS micelles were shown to undergo a sphere–rod transition at very high concentrations (~20 g/dl) in pure water. Rodlike micelles were first proposed by Debye and Anacker[36] who showed that the angular dependence of light scattered by n-hexadecyltrimethylammonium bromide micelles in the presence of high KBr concentration was consistent with the presence of long cylindrical micelles. These authors deduced axial ratios of about 18 in 0.178 M KBr and 27 in 0.233 M KBr for these cationic micelles. Stigter[37] has also suggested, on the basis of viscosity studies, that n-dodecylammonium chloride micelles are rod-shaped but flexible. Tanford,[33] however, has proposed that nonspherical micelles of ionic detergents should have oblate ellipsoidal shapes and has also suggested that the rodlike micelles seen in high salt solutions may constitute a linear aggregation of small micelles. This latter possibility cannot be excluded from our results, although it would seem more likely that small spherical micelles would polymerize as globular aggregates rather than linear chains, a hypothesis which is not supported by the present data.

(3) *Aggregation Numbers.* It becomes possible with the deduction of micellar shape to estimate the mean aggregation number, $\bar{n}$, corresponding to different values of $\bar{R}$. Since $\bar{n}$ is proportional to micellar volume, it follows immediately from eq 8i that for the prolate shape $\bar{n}$ is proportional to the axial ratio of the micelle and is therefore related to $\bar{R}$ by

$$\bar{n} = n_{\min} \frac{a_1(\bar{R})}{25} \quad (9)$$

where $n_{\min}$ is the aggregation number of the minimum spherical micelle, and $a_1(\bar{R})$ is the semimajor axis (in Å) of a prolate micelle with hydrodynamic radius $\bar{R}$ and a semiminor axis of 25 Å. We estimate the value of $n_{\min}$ to be 60 which corresponds closely to both the aggregation number of 62 measured for SDS micelles in water at the cmc,[4] and the theoretical estimate of 56 given by Tanford[38] for the maximum number of monomers in a spherical SDS micelle. Using eq 9, we have constructed vertical axes on the right sides of Figures 2 and 3, which provide a scale of $\bar{n}$ values appropriate to the $\bar{R}$ values plotted in these figures. These axes permit one to observe the temperature dependence of $\bar{n}$ at the various NaCl and SDS concentrations studied. For 6.9×10^{-2} M SDS in 0.6 M NaCl, $\bar{n}$ undergoes an extraordinary increase from 60 to about 1600 as the temperature decreases from 85 to 18 °C. The axial ratio corresponding to $\bar{n} = 1600$ is about 27, indicating a highly elongated shape ($a \sim 675$ Å) which is quite similar to the rodlike micelles formed by the cationic detergents studied by Debye and Anacker.[36] In order to compare the $\bar{n}$ values deduced from eq 9 to the previous literature on SDS, it must be appreciated that the published values have been obtained for various NaCl concentrations but only at temperatures near 25 °C. For this reason we have plotted $\bar{n}$ as a function of NaCl concentration for 6.9×10^{-2} M SDS at 25 °C in Figure 7 (continuous curve). The $\bar{n}$ values corresponding to low NaCl concentrations (<0.45 M) incorporate a small correction for the residual electrostatic effects on $\bar{R}$. The aggregation numbers obtained by Mysels and Princen[4] using conventional light scattering are also shown in Figure 7 (dashed curve). These values represent extrapolations to the cmc which decreases from $\sim 8.2 \times 10^{-3}$ to $\sim 4.4 \times 10^{-4}$ M as the NaCl concentration increases from 0 to 0.6 M.[2] The figure shows that in 6.9×10^{-2} M SDS $\bar{n}$ undergoes an increase with NaCl concentration that is far more dramatic than the increase in $\bar{n}$ that is seen at the respective cmc values. This finding indicates that the mean size of the micelles is a function of both the NaCl concentration and the SDS concentration, the latter variable becoming particularly important for NaCl concentrations greater than ~0.4 M. In this regard the data of Figure 3 explicitly show that the aggregation numbers of large rodlike micelles grow substantially with increasing SDS concentration at fixed temperature and NaCl concentration. With successive doubling of the SDS concentrations the $\bar{n}$ values increase by factors of about 1.5, in approximate agreement with the square root dependence of mean aggregation number on detergent concentration predicted in Mukerjee's[39] theory of micelle formation.

C. *Polydispersity.* The polydispersity of micellar solutions can be assessed from the V values (Tables I and II) obtained from computer analysis of the autocorrelation functions using the method of cumulants. The typical value of V is about 35% and implies a significant degree of micellar polydispersity. This is demonstrated by utilizing a result,[14] derived for random coil polymers, to relate the variance V to the ratio of the z-average aggregation number, $\bar{n}_z$,[40] to the weight-average aggregation number, $\bar{n}_w$, a more familiar index of micellar polydispersity. It can be shown that the ratio $\bar{n}_z/\bar{n}_w$ is approximately given by

$$\bar{n}_z/\bar{n}_w \approx 1 + 4V^2 \quad (10)$$

provided that the distribution of sizes is not too wide. Thus the 35% variance corresponds to a value of 1.49 for $\bar{n}_z/\bar{n}_w$.

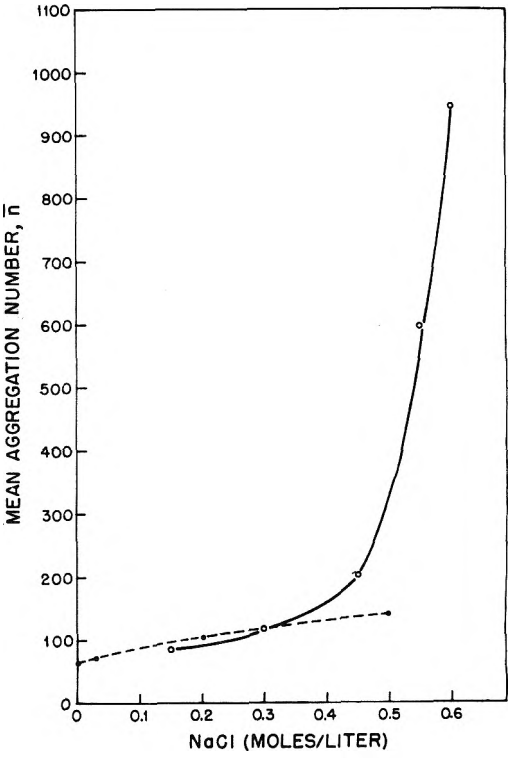

Figure 7. The mean aggregation number ($\bar{n}$) as a function of NaCl concentration at 25 °C. Continuous curve represents our results for a fixed SDS concentration (6.9×10^{-2} M). Dashed curve represents extrapolations to the cmc corresponding to each NaCl concentration from the data of Mysels and Princen.[4]

From the definition of $\bar{n}_z$ and $\bar{n}_w$,[40] it can be shown, using eq 10, that the "variance" of the distribution of aggregation numbers, whose mean is $\bar{n}_w$ is approximately $2V$, i.e., $(\overline{n_w^2} - \bar{n}_w^2)^{1/2}/\bar{n}_w \approx 2V$.[41] Thus the distribution of aggregation numbers extends 70% above and below its mean value indicating substantial polydispersity. This result is consistent with the degree of polydispersity predicted by Mukerjee.[39] It must be added, however, that eq 10 is only valid for estimates of polydispersity when the micellar shapes can be approximated by random coil polymers. This approximation is reasonable for the rodlike micelles, but is inappropriate when the micelles approach the minimum spherical shape. In addition the V values corresponding to the latter situation may sometimes reflect the presence of a few microscopic dust particles in the scattering solution, and therefore tend to overestimate the actual degree of micellar polydispersity. The sporadic scattering by dust (one or two large intensity fluctuations per 3-min run) is occasionally seen as the light scattered by micelles becomes weak, i.e., as the micelles approach the minimum size. In unpublished observations made on dilute polystyrene sphere solutions in our laboratory, we found that the presence of a few small dust particles has a negligible effect on $\bar{D}$ but may add about 10% in absolute amount to the V values.

Conclusions

We have deduced the size, shape, and degree of polydispersity of SDS micelles as a function of temperature (10–85 °C) for a wide range of NaCl concentrations (0.15–0.6 M) and at SDS concentrations (1.7×10^{-2}, 3.5×10^{-2}, 6.9×10^{-2} M) which significantly exceed the cmc. In addition we have measured the dependence of the cmt on NaCl concentration (0–0.6 M) and have obtained a characterization of supercooled

micellar solutions. These deductions have been made from our measurements of both the mean intensity and the temporal fluctuations in the intensity of light scattered from SDS solutions. These temporal fluctuations are produced by the Brownian movement of the micelles and were detected and analyzed using the techniques of quasielastic light scattering spectroscopy.[8,20,21] The QLS method has provided a sensitive and noninvasive means for determining the mean translational diffusion coefficient ($\bar{D}$) of the micelles and has also given a quantitative measure of micellar polydispersity. The mean hydrodynamic radius ($\bar{R}$) of SDS micelles has been deduced from $\bar{D}$ under the assumption that micellar interactions do not appreciably affect $\bar{D}$. We have examined in detail the validity of this assumption at the SDS and NaCl concentrations employed. The mean intensity of the scattered light has provided information on the temperature dependence of the micellar mass for 6.9×10^{-2} M SDS in 0.6 M NaCl. Using this information in conjunction with the corresponding temperature dependence of $\bar{R}$, we have performed a quantitative test of the validity of three plausible models of micellar growth (prolate ellipsoid, oblate ellipsoid, and sphere). Having identified the most appropriate model, we have deduced from it the shapes and mean aggregation numbers ($\bar{n}$) of SDS micelles for those regions of the micellar phase that we have investigated.

In summary, we have found that with increasing temperature the SDS micelle asymptotically approaches a minimum spherical shape with a hydrated radius of about 25 Å that is nearly independent of NaCl and SDS concentration. As the temperature is lowered in NaCl concentrations greater than 0.3 M, the micelles develop a shape consistent with a prolate ellipsoid having a semiminor axis of 25 Å and a semimajor axis that increases markedly with decreases in temperature and with increases in the NaCl concentration. For 6.9×10^{-2} M SDS in 0.6 M NaCl, $\bar{n}$ increases from ~60 (corresponding to the minimum spherical micelle at 85 °C) to ~1600 (corresponding to a semimajor axis of 675 Å at 18 °C). Alternatively, for the same SDS concentration at fixed temperature (25 °C), $\bar{n}$ is found to increase from ~80 (in 0.15 M NaCl) to ~1000 (in 0.6 M NaCl). We also find that for temperatures and NaCl concentrations at which the micelles are markedly elongated that the $\bar{n}$ values vary approximately with the square root of the SDS concentration, and also that the distribution of the micellar aggregation numbers is quite broad (±70% of the mean value). In supercooled solutions we have observed the same dependence of micellar size on temperature, NaCl concentration, and SDS concentration as seen above the cmt. Finally, the Murray–Hartley theory of detergent solubility has been shown to provide a natural framework for an understanding of both the metastability of detergent solutions, and also the NaCl dependence of the cmt which was found to increase by 10 °C over the NaCl concentration range examined.

We believe that the data reported here provides important new insights into the aggregative behavior of SDS molecules, and also demonstrates the utility of the QLS method for studying micellar systems.

Acknowledgments. This research was supported by the National Science Foundation under Grant No. DMR 72-03027A05 to the Center for Materials Science and Engineering, M.I.T.; by the National Institutes of Health Interdisciplinary Program in Biomaterials Science under Grant No. 1 P01-HL-14322-04; and by Public Health Service Grant No. AM 18559 from the NIAMDD Division of the U.S. Public Health Service.

Appendix A. The Relationship of $\bar{D}$ and V to the Distribution of Micellar Sizes

A polydisperse system is considered where each micellar component i is specified by its molecular weight M_i, diffusion coefficient D_i, form factor for light scattering P_i, and concentration (w/v) C_i. It follows from eq 5 that if the refractive increment of all micellar components is the same, then the fraction G_i of the total light intensity scattered by component i is given by:

$$G_i = \frac{C_i M_i P_i}{\Sigma C_i M_i P_i} \tag{A1}$$

The cumulants analysis of the autocorrelation function of the scattered light intensity provides statistical measures of the distribution of diffusion coefficients, D_i, where each component is weighted by G_i. The mean value $\bar{D}$ is given by

$$\bar{D} = \Sigma G_i D_i \tag{A2}$$

The variance V is related to the second moment of the distribution, $\overline{D^2}$, defined as:

$$\overline{D^2} = \Sigma G_i D_i^2 \tag{A3}$$

V is given by:

$$V = 100\,(\overline{D^2} - \bar{D}^2)^{1/2}/\bar{D}\ \% \tag{A4}$$

References and Notes

(1) J. S. Guggenheim Memorial Fellow (1974–1975)
(2) R. J. Williams, J. N. Phillips, and K. J. Mysels, *Trans. Faraday Soc.*, **51**, 728 (1955).
(3) M. C. Carey and D. M. Small, *Am. J. Med.*, **49**, 590 (1970).
(4) K. J. Mysels and L. H. Princen, *J. Phys. Chem.*, **63**, 1696 (1959).
(5) D. Stigter, R. J. Williams, and K. J. Mysels, *J. Phys. Chem.*, **59**, 330 (1955).
(6) K. Granath, *Acta Chem. Scand.*, **7**, 297 (1953).
(7) F. Reiss-Husson and V. Luzzati, *J. Phys. Chem.*, **68**, 3504 (1964).
(8) G. B. Benedek, "Optical Mixing Spectroscopy with Applications to Problems in Physics, Chemistry, Biology and Engineering" in the Jubilee volume in honor of Alfred Kastler entitled "Polarization, Matter and Radiation", Presses Universitaire de France, Paris, 1969.
(9) D. McQueen and J. Hermans, *J. Colloid Interface Sci.*, **39**, 389 (1972).
(10) M. Corti and V. Degiorgio, *Opt. Commun.*, **14**, 358 (1975).
(11) V. Cooper, S. Yedgar, and Y. Barenholz, *Biochim. Biophys. Acta*, **363**, 86 (1974).
(12) D. E. Koppel, *J. Chem. Phys.*, **57**, 4814 (1972).
(13) N. A. Mazer, S.B. Thesis, M.I.T., 1973, unpublished.
(14) P. N. Pusey in "Photon Correlation and Light Beating Spectroscopy", H. Z. Cummins and E. R. Pike, Ed., Plenum Press, New York, N.Y., 1974.
(15) G. D. J. Phillies, *J. Chem. Phys.*, **60**, 976 (1974).
(16) A. Einstein, "Investigation on the Theory of the Brownian Movement", Dover Publications, New York, N.Y., 1956, p 58.
(17) D. McIntyre and F. Gornick, Ed., "Light Scattering from Dilute Polymer Solutions", Gordon and Breach, New York, N.Y., 1964.
(18) N. A. Clark, J. H. Lunacek, and G. B. Benedek, *Am. J. Phys.*, **38**, 575 (1970).
(19) "Handbook of Chemistry and Physics", 55th ed, Chemical Rubber Company Press, Cleveland, Ohio, 1974.
(20) H. Z. Cummins and E. R. Pike, Ed., "Photon Correlation and Light Beating Spectroscopy", Plenum Press, New York, N.Y., 1974.
(21) B. Chu, "Laser Light Scattering", Academic Press, New York, N.Y., 1974.
(22) H. Nakayama and K. Shinoda, *Bull. Chem. Soc. Jpn.*, **40**, 1797 (1967).
(23) G. D. J. Phillies, Sc.D. Thesis, M.I.T., 1973, unpublished.
(24) G. S. Hartley, "Aqueous Solutions of Paraffin-Chain Salts", Hermann et Cie., Paris, 1936.
(25) The cmc in 0.6 M NaCl is estimated to be 1.26×10^{-2} g/dl from the formula given in ref 2.
(26) This estimate is based on the temperature dependence of n for water (ref 19) and assumes a constant refractive increment due to SDS.
(27) K. J. Mysels, *J. Colloid Interface Sci.*, **10**, 507 (1955).
(28) M. C. Carey and D. M. Small, *J. Colloid Interface Sci.*, **31**, 382 (1969).
(29) F. Krafft and H. Wiglow, *Berichte*, **28**, 2543, 2566 (1895).
(30) K. Shinoda and E. Hutchinson, *J. Phys. Chem.*, **66**, 577 (1962).
(31) R. C. Murray and G. S. Hartley, *Trans. Faraday Soc.*, **31**, 183 (1935).
(32) P. Debye, *Ann. N.Y. Acad. Sci.*, **51**, 575 (1949).
(33) C. Tanford, *J. Phys. Chem.*, **78**, 2469 (1974).

(34) M. Kodama and M. Miura, *Bull. Chem. Soc. Jpn.*, **45**, 2265 (1972).
(35) M. Kodama, Y. Kubota, and M. Miura, *Bull. Chem. Soc. Jpn.*, **45**, 2953 (1972).
(36) P. Debye and E. W. Anacker, *J. Phys. Colloid Chem.*, **55**, 644 (1951).
(37) D. Stigter, *J. Phys. Chem.*, **70**, 1323 (1966).
(38) C. Tanford, *J. Phys. Chem.*, **76**, 3020 (1972).
(39) P. Mukerjee, *J. Phys. Chem.*, **76**, 565 (1972).
(40) If c_i and n_i are respectively the concentration (w/v) and aggregation number of species i, then $\bar{n}_w$ and $\bar{n}_z$ are given by:

$$\bar{n}_w = \Sigma c_i n_i / \Sigma c_i$$

$$\bar{n}_z = \Sigma c_i n_i^2 / \Sigma c_i n_i$$

(41) This result follows from the fact that $\overline{n_w^2} = \bar{n}_w \bar{n}_z$

The Structure of Carbanion Aggregates. 1. Absorption and Emission Spectra of Bis(fluorenyl)barium and Its Crown Ether Complex in Tetrahydrofuran and Tetrahydropyran

T. E. Hogen-Esch and M. J. Plodinec*[1]

Department of Chemistry, University of Florida, Gainesville, Florida 32611 *(Received June 24, 1975)*

Electronic absorption fluorescence and excitation spectra of bis(fluorenyl)barium ($BaFl_2$) have been determined in tetrahydrofuran (THF) and tetrahydropyran (THP). Excitation at 373 nm in THF produced emission at 528 nm while excitation at 347 nm gave a broad emission at 568 nm. Lowering the concentration increases the relative intensity of the 528-nm emission. These phenomena were shown to be due to the presence of free fluorenyl anions absorbing and emitting at 373 and 528 nm, respectively, while the emission at 568 nm is due to the $BaFl_2$ ion triple. In THP the emission is concentration independent and only occurs at 568 nm due to a much lower dissociation constant in this solvent. On complexation of about 20% crown ether, emission occurs at 533 and 568 nm. Subtraction of the separated ion pair component from this spectrum yields an emission spectrum at 540 nm attributable to the [CE, BaFl] ion pair. Relative emission intensity was found to be 100:30:1.3 respectively for $\|Fl^-$, [CE BaFl], and $BaFl_2$. The absorption band at 372 nm was shown to be most likely due to an exciton exchange mechanism. This mechanism predicts twofold splitting of excited state energy levels, the separation of which depends on the dimer geometry. Through such an analysis the two fluorenyl moieties were shown to be significantly tilted with respect to one another making possible external coordination of Ba^{2+} ion by solvent. As expected this tilting was less pronounced in THP since THP is a less strongly cation coordinating solvent than THP. Exciton exchange was also shown to be most likely the cause for the pronounced emission red shift of 40 nm in comparing free anion with $BaFl_2$ emission. In the ion triple emission occurs from the lower excited state exciton levels.

Introduction

It is well known that aggregation of molecules in solution can significantly alter their physical properties, for example, their electronic spectra, as well as their chemical reactivity. The influence of aggregation on the spectroscopic properties of molecules is well-documented experimentally,[2-6] and, at least semiquantitatively, well-understood theoretically.[2,7-9] Unfortunately, the best understood aggregated systems are dyes in protic solvents, whose reactions are relatively unimportant. (An exception is the sensitization of silver halide crystals in photographic emulsions by adsorbed dye aggregates.)[10-13]

While many reactions in solution involve one or all of the reactants in an aggregated state, the effect of this aggregation on the reaction mechanism has usually been ignored, due to a lack of information about the properties of molecular aggregates, in particular their structure.

This paper will be concerned with the effect of aggregate structure on absorption and emission spectra[14] of bis(fluorenyl)barium[15] in two low dielectric constant aprotic media tetrahydrofuran (THF) and tetrahydropyran (THP). The system was chosen because of its sandwich dimer structure in low dielectric constant media such as THF. The ion triple is therefore of potential use as a model for aggregation of other fluorenyl and similar carbanion salts thought to be aggregated on the basis of uv–visible and kinetic studies. Moreover, this model system has several advantages for studies of this type. First the effect of ion pairing on absorption[16] and fluorescent emission[14,17] of fluorenyl and similar salts is well understood in terms of cation size, cation solvation or complexation,[17] and ion pair dissociation.[18]

Second the bis(fluorenyl)barium ion triple is well characterized in solution. Its dissociation into $BaFl^+$ and Fl^- ions in THF is less extensive than fluorenyl alkali salts ($K_d = 5.3 \times 10^{-9}$ at 20°C) so that at concentrations above 10^{-5} *M* the ion triple is essentially undissociated. Moreover, its complex with dibenzo-18-crown-6 has been shown by NMR to possess a sandwich type structure in which the Ba^{2+} ion is located between the cyclopentadienyl rings.[15] Uv–visible studies on this complex suggest an asymmetric position of Ba^{2+} being close to one fluorenyl unit and separated from the other by crown ether.[15,19]

Experimental Section

The preparation of the salts and the purification of the solvents were all done under vacuum ($\sim 10^{-6}$ Torr), as described elsewhere.[15,16,20] Absorption spectra were measured on a Beckman Acta V, and excitation and fluorescence spectra were measured on a Perkin-Elmer MPF-2A in the ratio record mode. The same 1-cm square quartz cells were used to obtain all spectra.

Absorption spectra were obtained with optical density as a function of wavelength. These were converted manually to plots of extinction coefficient (ϵ) vs. wavenumber (cm^{-1}), and integrated using a planimeter. Each value is the average of ten readings.

To calculate the ratio of lower and higher wavelength band oscillator strengths, f_L and f_H, respectively, it was necessary to separate the two absorption bands rather arbitrarily. This was done by assuming that the smaller peak was symmetric around its maximum, and subtracting its area from that of the larger band. As a check, the assumed smaller band was manually subtracted from the larger band for $BaFl_2$ in THF, and it was found that the resultant band was smooth. This procedure is probably not optimally accurate but should indicate trends.

Results and Discussion

Absorption Spectra. Certain anomalies of the Ba salt must be borne in mind in applying results from this study to the other alkali fluorenyl aggregates. First the size of the Ba cation is roughly that of potassium (1.35 Å for Ba^{2+}, 1.33 Å for K^+) but the charge/radius ratio is nearly that of lithium (1.48 for Ba^{2+}, 1.67 for Li^+). Thus certain peculiarities of lithium fluorenyl that have been ascribed to the small size of the Li ion may not be elucidated by the barium system.[21] Further the presence of the second fluorenyl moiety is expected to influence alkaline earth cation solvation in these systems. For instance the absorption spectrum of $BaFl_2$ in THF shows a distinct shoulder at about 372 nm. One might expect that this band would correspond to the existence of a small fraction of asymmetrically solvated separated ion pairs generated by the solvation process

$$BaFl_2 + n\text{THF} \rightleftharpoons Fl^-Ba^{2+}\|Fl^- \qquad (1)$$

that was previously demonstrated for the Sr salt.[22] However, a number of observations cast doubt on this conclusion. First, a distinct shoulder is also observed in THP even though the solvating power of this solvent is substantially less than that of THF. Thus while the fraction of separated ion pairs of fluoradenyl sodium in THF is about 50%, in THP no separated ion pairs are observed.[23] Furthermore, a clearly visible shoulder at about 370 nm is observed even in a very poorly cation solvating solvent such as dioxane while in a solvent of superior solvating power such as DME a spectrum is observed that is very similar to that in THF. Second, on lowering the temperature of a $BaFl_2$–THF solution from +25 to −75°C the ratio of the absorption bands at 347 and 372 nm remains essentially constant within experimental error. Such behavior seems unusual given the fact that in bis(fluorenyl)strontium there is a pronounced increase in the ratio of separated/contact ion pairs with temperature leading to a ΔH of about −12 kcal/mol for reaction 1.[22] Such very large differences in enthalpy seem unusual for cations that are not greatly different in electrostatic field strength suggesting that the absorption at 372 nm may be due to some other effect (see below). It should be noted, incidentally, that the extinction coefficient of the main peak has been found to be lower than for the alkali salts (7300 vs. 11000–14000).[20]

Emission and Excitation Spectra. The fluorescence and excitation spectra of the salt in THF and THP are very instructive (see Figures 1–4 and Table I). In THF, excitation at 373 nm produces emission at 528 and 568 nm, identical with the separated ion pair observed on addition of crown ether to fluorenyl sodium in THF or THP or free ion.[17] However, if excited at 347 nm, the intensity of the peak at 568 nm is increased relative to the 528 peak, indicating that the species excited at 373 nm is different from that excited at 347 nm.

Emission at 528 nm may be produced by two species,[17] the free fluorenyl anion or a separated pair. Such a separated ion pair may be present in the ground state or may be generated from excited state contact ion pairs through cation–solvent relaxation processes.[17] However, excitation of contact ion pairs at 347 nm decreases the emission at 528 nm indicating that no such excited state relaxation process is of primary importance. The presence of an appreciable fraction of separated ion pairs in the ground state seems somewhat doubtful on the basis of observations made in the preceding section. This conclusion is further supported by the intensity of the $BaFl_2$–THF emission at 528 nm (excitation at 372 nm) that is much lower than that expected if the 372-nm band represented separated ion pairs. The latter species emit much more intensely than ion pairs or ion triples (see below).

However, a pronounced concentration dependence of the emission signal (excitation at 347 nm) was obvious indicating a ground state dissociation process into free ions. To test for this the emission of fluorenylsodium in THF was compared to the $BaFl_2$ at the same anion concentration (3×10^{-6} *M*) and excited at the free anion absorption maximum. Under these conditions, using the reported dissociation constants[19] at 20°C in THF, one calculates 4.1 and 32.5% as the fractions of free anions for fluorenylbarium and -sodium, respectively. The relative intensities at 528 nm were determined as 1:11 for barium and sodium salt, respectively, in good agreement with expectations.

Further if the salt concentration is varied over a range (10^{-4} to 10^{-6} *M*) in which the fluorescence intensity is proportional to ion pair concentration in the absence of dissociation (checked for several fluorenyl salts in THP) deviations from proportionality can be used to obtain an equilibrium constant of dissociation defined by

$$BaFl_2 \rightleftharpoons BaFl^+ + Fl^- \qquad (2)$$

By this method one obtains a K_d of about 4×10^{-9} (lit. 5.3×10^{-9})[19] which is a satisfactory confirmation that the free anion is being excited at 373 nm.

However what is the nature of the second species, the one excited at 347 nm? This can best be seen in Figure 4, $BaFl_2$ in THP. Here, emission occurs only in a broad band centered at 570 nm which is of very low intensity; about 30 times lower than that of the free ion at 570 nm, and 75 times lower than the intensity of the free ion at its maximum (528 nm).

In this solvent, where the dissociation constant should be substantially less than in THF,[24] the undissociated molecule would be essentially the only species present so that the emission spectrum would not depend on the wavelength of excitation. This is confirmed. In THF, however, the ion triple and a small fraction of free ions are present. Because of its much greater quantum yield, the free ion

TABLE I: Fluorescence of $BaFl_2$ in THF and THP[a]

Solvent	Absorption max, nm	Excitation wavelength, nm	Emission max, nm	Type ion pair emitting
THP	347, 731	All wavelengths	570	Ion triple
THF	348, 372	373	528, 568	Free anion
		347	530/570	Free anion/ion triple
THF, 20% CE[b]	349, 373	347	533, 568	Crown separated/ crown complexed ion pair
		373	528, 568	Crown separated ion pair

[a] $[BaFl_2] \sim 10^{-5}$ *M* emission, $\sim 10^{-4}$ *M* (absorption). [b] Dicyclohexyl-18-crown-6.

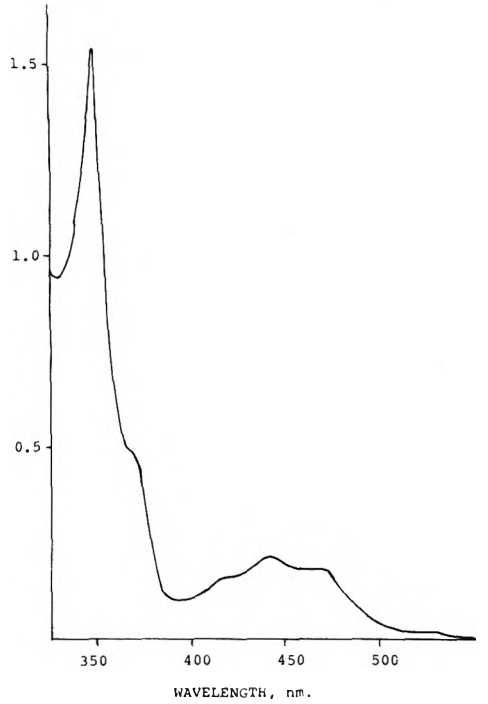

Figure 1. Absorption spectrum of bis(fluorenyl)barium in THF.

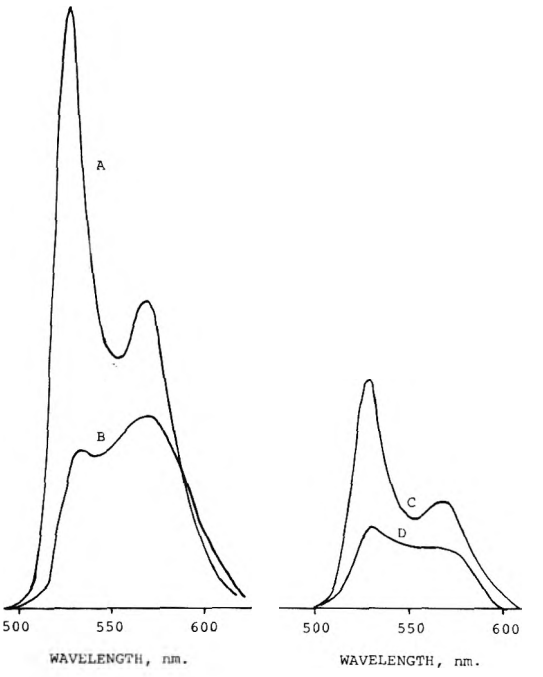

Figure 2. Emission spectra of bis(fluorenyl)barium in THF as a function of exciting wavelength: A,B $[Fl^-] = 1 \times 10^{-5}$ *M*; C,D $[Fl^-] = 3 \times 10^{-6}$ *M*; A,C excited at 373 nm; B,D excited at 347 nm.

masks the ion triple fluorescence when excited at wavelengths where the free ion absorbs strongly (373 nm) and distorts it even when the excitation wavelength corresponds to the ion triple absorption maximum. Thus, the second species emitting at 570 nm is most likely the ion triple.

Not discussed so far is the "ion pair", (BaFl).[15,19] For reasons that will be dealt with in a subsequent publication, this species emits too weakly to be seen. However, if one adds a small amount of a crown ether (dicyclohexyl-18-crown-6 was used at a concentration of ~20% that of $BaFl_2$) to a 10^{-5} *M* solution of $BaFl_2$ in THF, interesting effects are seen. Excitation at 347 nm now leads to emission at 533 and 568 nm. This is surprising since one would expect emission to occur at 528 nm because of the relatively high emission intensity of the separated Fl^- unit (see above). Since the separated Fl^- unit, regardless of counterion, and the free Fl^- have about the same quantum yield[25] the contribution of these two species to the spectrum is easily evaluated using the reported[19] dissociation constants of $BaFl_2$ and FlCEBaFl in THF. Subtracting these contributions from the spectrum one obtains an emission spectrum with maxima at 540 and 580 nm tentatively attributed to the CEBaFl ion pair with an emission intensity about 30% of that of the separated Fl^- unit. Whether we deal here with the ion $CEBaFl^+$ or the contact "half" of the ion triple FlCEBaFl is not clear since at a concentration of 10^{-5} *M* both would be present at comparable concentrations.

As a final experimental finding, it should be noted that, while the monomeric fluorenyl–alkali metal ion pairs have virtually identical absorption and excitation spectra,[17] this is not the case for $BaFl_2$, especially in THP. The reasons for this are unclear, but it has been checked at several concentrations below 4×10^{-5} *M*.

Thus, the effects of aggregation on the molecular spectra of the fluorenyl anion system are: (1) a pronounced red shift of the emission band, for $BaFl_2$, this shift is about 30 nm; (2) a precipitous decrease in the emission intensity of the ion triple compared to the free anion or separated ion pair; and (3) splitting and/or anomalous shifts in the absorption–excitation spectrum.

Discussion

The Structure of Bis(fluorenyl)barium. Theory and Model. All of the above are what would be predicted by ap-

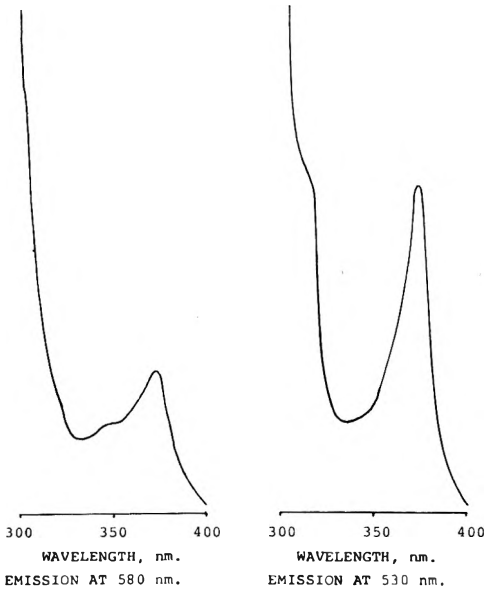

Figure 3. Excitation spectrum of bis(fluorenyl)barium in THF as a function of emitting wavelength; total fluorenyl concentration = 3×10^{-6} *M*.

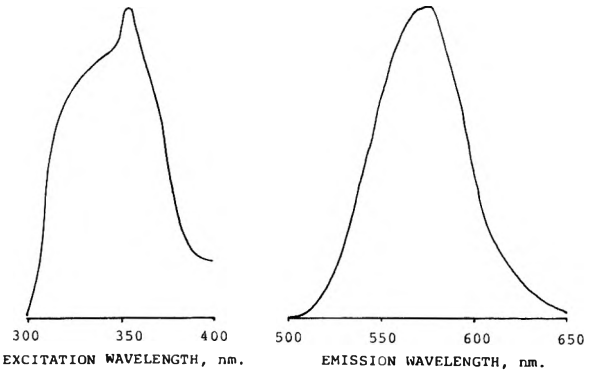

Figure 4. Excitation and emission spectrum of bis(fluorenyl)barium in THP; total fluorenyl concentration = 1×10^{-4} *M*.

plication of a simple exciton coupling scheme, such as that Simpson et al.[2] and Kasha[7-9] et al. applied to dye systems.

In the following discussion, the basic relations of the theory of molecular excitons will be set down as they apply specifically to the ion triple case, in the manner of Kasha.[9] It is assumed that the overlap between the two fluorenyl units in the ion triple is small, but finite, so that the fluorenyl units preserve their individuality and the aggregate wave functions and energies may be obtained by applying perturbation theory to the monomer. Denoting the two fluorenyl units in the ion triple by A and B, the splitting of the fluorenyl absorption band due to exchange of excitation energy between A and B, ΔE, is given by

$$\Delta E = \frac{2\vec{M}_A \cdot \vec{M}_B}{R^3} - \frac{6(\vec{M}_A \cdot \vec{R})(\vec{M}_B \cdot \vec{R})}{R^5}$$

where $\vec{M}_A$ and $\vec{M}_B$ are the vector transition dipoles (such that $|\vec{M}_A|^2 = |\vec{M}_B|^2 = |\vec{M}|^2$, $\vec{M}$ the transition moment for the anion), and $\vec{R}$ is a position vector from the center of $\vec{M}_A$ to the center of $\vec{M}_B$, i.e., R is the distance between the transition moment vectors of the two anion units. This simplifies to $\Delta E = (2|\vec{M}|^2/R^3)G$, where G is a factor depending on

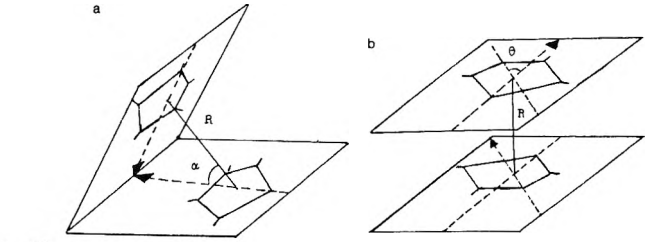

Figure 5.

the angular geometry of the aggregate. Further, the intensity of the transition from the ground state to the exciton states is proportional to the vector sum of $\vec{M}_A$ and $\vec{M}_B$. Thus, while the exciton splitting will always occur, only one transition need be seen because the vector summation constitutes a sort of selection rule.

It was previously[15] concluded that the structure of bis(fluorenyl)barium was essentially that of two planar anions stacked one above the other with the cation between. If one accepts this gross picture but allows the two planar anions to incline one to the other, then the simple exciton model predicts two bands will appear, such that the oscillator strength of the lower wavelength band, f_L, divided by that of the higher wavelength band, f_H, will be equal to the square of the tangent of the angle (α) between $\vec{M}_A$ (or $\vec{M}_B$) and the position vector, $\vec{R}$, i.e., $f_L/f_H = \tan^2 \alpha$ (see I).

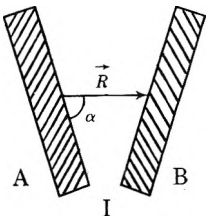

Two bands would also be predicted if, instead of the above model, the two planar anions were allowed to remain coplanar, but twisted about R. This model does not agree with recent x-ray diffraction data on crystalline fluorenyl salts,[26,27] nor does it lend itself to explaining the dependence of structure of the ion triple on solvent. For these reasons, this model will not be considered further, and that pictured above will be assumed.

As a check on the applicability of the theory, the distance R was determined by transforming the fluorenyl anion spectrum (assuming fluorenylsodium with a slight excess of crown ether to be a very good approximation of the unperturbed anion) as above, and the anion transition moment was evaluated by

$$|M|^2 = \frac{3he^2}{8\pi^2 mc} \frac{f}{\langle \tilde{\nu} \rangle} = 2.126 \times 10^{-30} \frac{f}{\langle \tilde{\nu} \rangle}$$

where f is the monomer oscillator strength, and $\langle \tilde{\nu} \rangle$ is the average wavenumber of the absorption band, determined by

$$f = 4.319 \times 10^{-9} n \int \epsilon(\tilde{\nu})\, d\tilde{\nu}$$

$$\langle \tilde{\nu} \rangle = \frac{\int \tilde{\nu} \epsilon(\tilde{\nu})\, d\tilde{\nu}}{\int \epsilon(\tilde{\nu})\, d\tilde{\nu}}$$

where the term involving n, the refractive index, is a correction for medium effects.[28] Thus, $|\vec{M}|^2$ was finally evaluated by

$$|\vec{M}|^2 = 1.304 \times 10^{-38} \frac{(\int \epsilon(\tilde{\nu})\, d\tilde{\nu})^2}{\int \tilde{\nu}\epsilon(\tilde{\nu})\, d\tilde{\nu}} \text{ esu}$$

This value for the anion, 15.95×10^{-36} esu, was then used to evaluate R^3 according to eq 2, which, for the assumed geometry, is equal to

$$R^3 = \frac{2(1 + \cos^2 \alpha)|\vec{M}|^2}{\Delta E\ (1.9863 \times 10^{-16})} \quad (3)$$

where ΔE is in cm^{-1}, the numerical factor converts cm^{-1} to ergs, and R is in cm.

The data used in the theoretical model and the results are listed in Table II, as well as R (distance between anionic centers). In THF, the two anions are further apart and slightly more inclined to each other than in THP. This is exactly what one would expect, considering the greater cation solvation. To make room for the Ba^{2+} coordinated THF, the anion sandwich opens up a bit. Thus, this simple exciton coupling scheme gives surprisingly good numerical results for the absorption spectral data of this system.

It should be pointed out that the results have been obtained using rather arbitrary procedures to evaluate the ratios of low and high wavelength oscillator strengths. For the same reason ΔE cannot be very accurately determined. Thus in THP and THF the same value was used since the small shoulders occurred at approximately the same wavelength. However α does not strongly depend on the oscillator strength ratio particularly at higher ratios (>5) while R in turn does not strongly depend on α particularly for larger values of α (>45°). In any event the significance of reported α and R values lies in their trends from THP to THF rather than in their absolute values.

The exciton coupling model may also be used to explain the rather pronounced emission red shift observed for the $BaFl_2$-THP system. Splitting of the excited state into two levels above and below the monomer level would give rise to a fluorescence red shift due to emission from a lower level (Figure 6). The emission maximum of a monomeric contact ion pair for an ion with a charge/radius ratio similar to that of Ba^{2+} can be estimated as 542 nm from an extrapolation of a plot of reciprocal cationic radius vs. emission wavenumber.[17] The actual shift from the unsplit level is thus about 28 nm or 907 cm^{-1} leading to a energy difference between the exciton levels of about 1800 cm^{-1} [29] (Table II).

TABLE II: Structure of $BaFl_2$ in THF and THP

Solvent	$\tan^2 \alpha (= f_L/f_H)^a$	ΔE, cm^{-1}	α, deg	R,[b] Å
THP	25.8	1860	79	4.5
THF	5.5	1860	67	4.7

[a] f_L, f_H are the oscillator strengths of the low and high wavelength bands, respectively. [b] Calculated using $|\vec{M}|$ for the monomer equal to that of fluorenylsodium crown ether in THP, 15.95×10^{-36} esu.

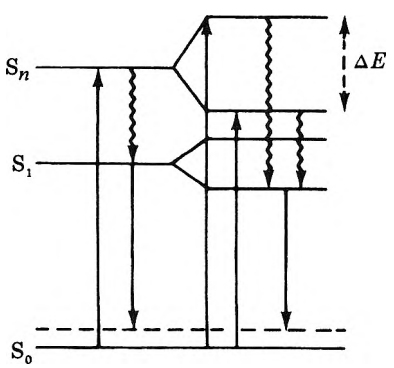

Figure 6.

Conclusion

It has been shown that aggregation of fluorenyl anions in a model compound bis(fluorenyl)barium has the following effects on absorption and emission. (i) Absorption spectra are split due to exciton coupling. This coupling is most reasonably explained by two mutually tilted fluorenyl units containing the peripherally solvated Ba^{2+} ion. (ii) Fluorescence is red shifted presumably due to emission from the lower of the two split exciton levels. (iii) Emission is generally considerably decreased probably due to effective quenching within the ion triple while the shape of the dimer emission band is generally quite different from that of monomer.

Acknowledgments. We wish to thank Professor S. G. Schulman for the use of his spectrofluorimeter. We also thank Drs. N. H. Velthorst and H. W. Vos as well as one of the referees for their helpful comments.

References and Notes

(1) E. I. Du Pont de Nemours, Savannah River Laboratory, Aiken, S.C. 29801. To whom correspondence should be addressed.
(2) G. S. Levinson, W. T. Simpson, and W. Curtis, *J. Am. Chem. Soc.*, **79**, 4314 (1957).
(3) K. K. Rohatgi, *J. Mol. Spectrosc.*, **27**, 545 (1968); K. K. Rohatgi and A. K. Mukhopadhyay, *J. Phys. Chem.*, **76**, 3970 (1972).
(4) M. K. Pal and M. Schubert, *J. Phys. Chem.*, **67**, 1821 (1963).
(5) R. W. Chambers, T. Kajiwara, and D. R. Kearns, *J. Phys. Chem.*, **78**, 380 (1974).
(6) J. T. Knudtson and E. M. Eyring, *J. Phys. Chem.*, **78**, 2355 (1974).
(7) E. G. McRae and M. Kasha, *J. Chem. Phys.*, **28**, 721 (1958).
(8) M. Kasha, *Rev. Mod. Phys.*, **31**, 162 (1959).
(9) M. Kasha, H. R. Rawls, and M. Ashraf El-Bayoumi, *Pure Appl. Chem.*, **11**, 371 (1965).
(10) G. E. Ficken in "Photographic Sensitivity", R. J. Cox, Ed., Academic Press, London, 1973, pp 205–220.
(11) R. Steiger, R. Kitzing, and P. Junoc, ref 10, pp 221–240.
(12) W. West, B. H. Carroll, and D. H. Whitcomb, *J. Phys. Chem.*, **56**, 1054 (1952).
(13) R. Steiger, R. Kitzing, R. Hagen, and H. Stoeckli-Evans, *J. Photg. Sci.*, **22**, 151 (1954).
(14) Emission spectra of carbanions have been reported by others: (a) E. vander Donckt, J. Nasielski, and P. Thiry, *Chem. Commun.*, 1249 (1969); (b) J. W. Burley and R. N. Young, *ibid.*, 1649 (1970); (c) H. W. Vos, H. H. Blom, N. H. Velthorst, and C. McLean, *J. Chem. Soc., Perkin Trans. 2*, 635 (1972); H. W. Vos, C. McLean, and N. H. Velthorst, *J. Chem. Soc., Faraday Trans. 2*, **72**, 63 (1976).
(15) T. E. Hogen-Esch and J. Smid, *J. Am. Chem. Soc.*, **91**, 4580 (1969).
(16) T. E. Hogen-Esch and J. Smid, *J. Am. Chem. Soc.*, **88**, 307 (1966).
(17) M. J. Plodinec and T. E. Hogen-Esch, *J. Am. Chem. Soc.*, **96**, 5262 (1974).
(18) T. E. Hogen-Esch and J. Smid, *J. Am. Chem. Soc.*, **88**, 318 (1966).
(19) T. E. Hogen-Esch and J. Smid, *J. Phys. Chem.*, **79**, 233 (1975).
(20) U. Takaki and J. Smid, *J. Am. Chem. Soc.*, **96**, 2588 (1974).
(21) It has been postulated that the Li^+ fluorenyl carbanion interaction may resemble that between Li^+ and allyl anion while the larger cations interact in a purely electrostatic manner (see ref 26).
(22) T. E. Hogen-Esch and J. Smid, *J. Am. Chem. Soc.*, **94**, 9240 (1972).
(23) T. E. Hogen-Esch, *J. Am. Chem. Soc.*, **95**, 639 (1973).
(24) M. Szwarc in "Carbanions", "Living Polymers and Electron Transfer Processes", Wiley-Interscience, New York, N.Y., 1968, and references therein.
(25) M. J. Plodinec and T. E. Hogen-Esch, to be submitted for publication.
(26) J. J. Brooks, W. Rhine, and G. D. Stucky, *J. Am. Chem. Soc.*, **94**, 7339 (1972).
(27) R. Zerger, W. Rhine, and G. D. Stucky, *J. Am. Chem. Soc.*, **96**, 5441 (1974).
(28) N. Nataga and T. Kubota, "Molecular Interactions and Electronic Spectra", Marcel Dekker, New York, N.Y., 1970, pp 113–114.
(29) The spacing between exciton levels in absorption and emission have been drawn the same in Figure 5. Due to excited state cation/solvent relaxation[17] the values of α and R may also be changed resulting in different ΔE values for absorption and emission involving the same excited state. We thank Drs. N. H. Velthorst and H. W. Vos for this suggestion.

Carbanion Aggregates. 2. Absorption and Fluorescence Spectra of Fluorenylsodium in Dioxane and Fluorenyllithium in Dioxane and Toluene

T. E. Hogen-Esch*[1] and M. J. Plodinec

Department of Chemistry, University of Florida, Gainesville, Florida 32611 *(Received August 15, 1975)*

Fluorenyllithium, -sodium, and -cesium have been studied by absorption and emission spectrometry in THF, tetrahydropyran (THP), dioxane, and toluene. In dioxane and toluene the Li and Na salts give small absorption blue shifts (3–6 nm) but larger emission red shifts (5–13 nm) compared to the spectra in THP. In addition emission intensities and lifetimes are much lower compared to the same salts in THF and THP. Moreover, the bandshapes are distinctly different and for fluorenyllithium in dioxane the emission and excitation spectra are concentration dependent. However, the Cs salts do not show this anomalous behavior in any of the solvent. Intensities and lifetimes are unaffected by solvent and the emission bandshape resembles that of the Li and Na salts in THP and THF. The results are described in terms of ion pair aggregation of the Li and Na salts in toluene and dioxane using an exciton exchange model. This model predicts a twofold splitting of energy levels leading to two exciton bands, the relative intensity of which depends on aggregate geometry while the energy separation between the bands depends on the reciprocal cube of the distance between the two chromophores. The model is also applied to other similar systems.

Introduction

The aggregation of ion pairs to quadrupoles or higher aggregates in low dielectric constant solvents is well known,[2] and has been under study for some time to determine its mechanistic role; for example, in stereospecific anionic polymerization reactions of carbanion salts. Thus, the aggregation of allyl lithium type ion pairs has been extensively studied in hydrocarbon solvents by viscometry, light scattering, NMR, and other techniques,[3–5] and much progress has been made. On the other hand, aggregation of fluorenyl type ion pairs has been studied mainly in low dielectric constant ethereal solvents by uv–visible spectroscopy,[6] ebulliometry,[6] and the kinetics of proton transfer reactions.[7]

In many of these cases there is little agreement on the extent and type of aggregation and essentially no information on the actual geometry of the aggregate in solution. Thus, the existence of such aggregates at concentrations as low as 10^{-5} M in solvents such as THF and DME has recently been questioned.[8]

In part 1 of this series, we examined the absorption and emission spectra of bis(fluorenyl)barium in THF and THP and concluded that aggregation could have one or all of the following effects on the spectra of the fluorenyl anion: (1) A pronounced red shift of the emission band; (2) A precipitous decrease in the emission intensity of the ion triple compared to the free ion or separated ion pair; (3) Splitting and/or anomalous shifts in the absorption/excitation spectrum. We further showed how application of a simple exciton coupling scheme could lead to a qualitative, and perhaps semiquantitative, understanding of the above phenomena in terms of the structure of the aggregate.

In this part, we will examine the uv–visible absorption and fluorescence spectra of fluorenyllithium, -sodium, and -cesium in the low dielectric constant media toluene and dioxane, and find that aggregation of these salts is again indicated, in agreement with earlier kinetic and spectrophotometric results.[6,7]

Again, the alkali fluorenyl salts will be used as probes, for several reasons. Obviously, they are the closest systems possible to the model, bis(fluorenyl)barium. Further, their absorption[9] and emission[10] spectra are well understood in higher dielectric constant solvents in terms of ion pair structure and dissociation so that these parameters can be taken into account.[11] For instance absorption and emission spectral shifts with cation and solvent in aprotic polar media have been shown to be largely due to specific cation solvation often resulting in the formation of solvent-separated ion pairs while the carbanion is not specifically solvated. Moreover, no direct correlation has been found between dielectric constant and the carbanion spectrum.[9]

Experimental Section

The preparation of the salts and purification of solvents were done in vacuo ($\sim 10^{-6}$ Torr) as described elsewhere in detail.[9] Fluorenyl alkali salts were prepared by allowing the corresponding salts of 1,1,4,4-tetraphenylbutane dianion to react with a slight excess (~10%) of fluorene in THF. The excess fluorene did not have a measurable effect on the absorption or emission spectra. Solutions in other solvents were obtained by evaporating a particular salt in THF to dryness on the vacuum line and distilling in the desired solvent. This procedure was repeated at least once. Absorption spectra were obtained on a Beckmann Acta V spectrophotometer in the double beam mode. Uncorrected excitation and fluorescence spectra were obtained from a Perkin-Elmer MPF-2A in the ratio record mode. It was ascertained, however, that in the emission wavelength range employed (530–370 nm) the effect of correction on bandshapes and maxima is negligible. The same 1-cm square optical grade quartz cells (Pyrocell) were used to obtain all spectra.

Results

The results on absorption and fluorescence spectra of fluorenylsodium and -cesium in dioxane and fluorenyllithium in dioxane and toluene are shown in Table I and Figures 1–3.[14] The absorption maxima of the Li and Na salts are blue shifted relative to the contact ion pairs in THF and tetrahydropyran (THP) while the Cs salts are not affected by solvent in agreement with earlier results.[9] The emission maxima of the Li and Na salts are generally red shifted compared to the

TABLE I: Electronic Spectra of Fluorenyllithium, -Sodium, and -Cesium in Low Polarity Media[a]

Cation	Solvent	Absorption max	Emission max[b]	Rel. intensity	Lifetime, ns
Li^+	THF	349, 372	528, 568[c]	1.0	85
	THP	349, 372	(542, 582)[d]	0.24[e]	
	Dioxane	346	547[f]	0.11	24
	Toluene	343	555	0.04	
Na^+	THP	356	538, 578	0.47	40
	Dioxane	353	540, 580[g]	0.16	
Cs^+	THF	364	533, 574	0.20	15
	THP	364	533, 574	0.20	15
	Dioxane	363	534, 574	0.20	15

[a] In nanometers. [b] The higher wavelength refers to a second less intense emission due to transition to the vibrationally excited ground state (see ref 10). [c] Solvent separated ion pairs (see ref 10). [d] Calculated for the Li contact ion pair by extrapolation of a plot of wave number vs. reciprocal cationic radius of contact ion pairs of Cs, Rb, K, and Na fluorenyl salts in THP. [e] Calculated for the contact ion pair from the excitation spectrum. [f] Concentration dependent, see text. [g] Shoulder at 580 nm (see text).

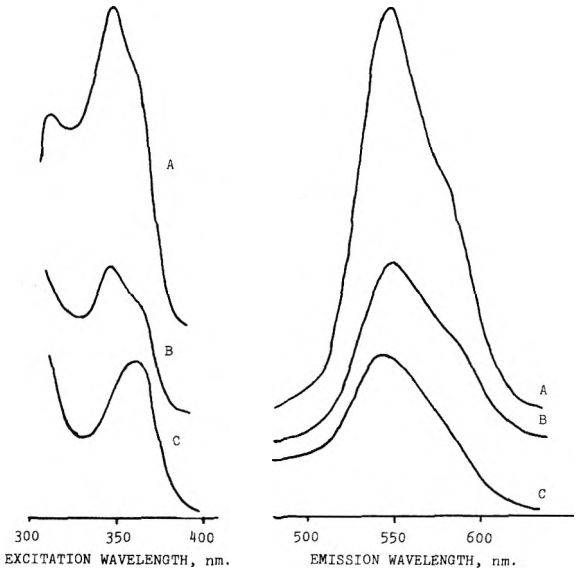

Figure 2. Excitation and emission of fluorenyllithium in dioxane: (A) 2 × 10^{-4} M; (B) 2.3 × 10^{-5} M; (C) 1 × 10^{-6} M.

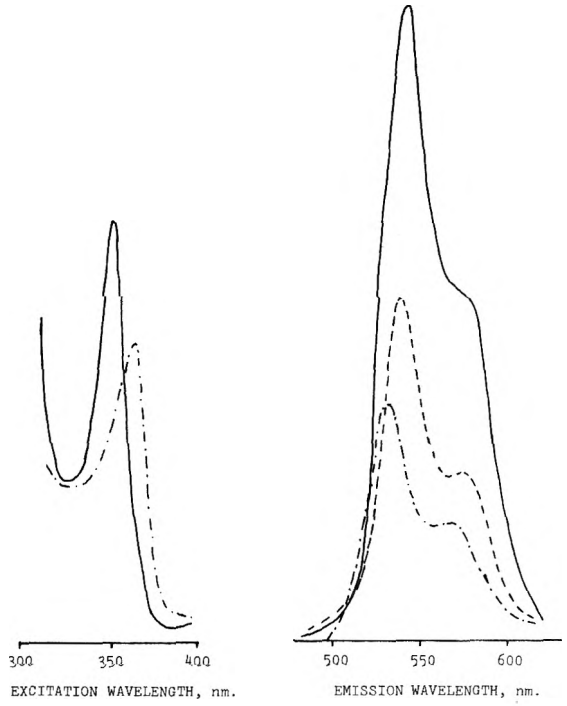

Figure 1. Excitation and emission spectra of (—) fluorenylsodium in dioxane, (- - -) fluorenylsodium in THP, (- · -) fluorenylcesium in THF. Concentrations ~10^{-4} M. Relative emittivities in Table I.

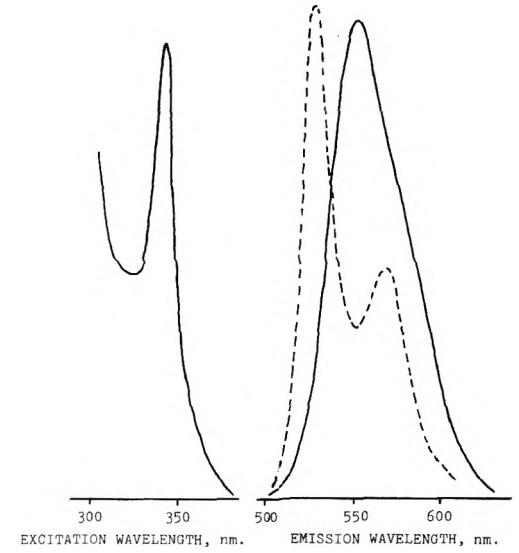

Figure 3. Excitation and emission spectrum of fluorenyllithium in toluene; (LiFl) = 1 × 10^{-5} M. Dotted line represents the salt in THF at 10^{-4} M. Relative emittivities of the two systems are shown in Table I.

contact ion pair spectra in THF and THP. For the Li salts at 10^{-4} M these red shifts are 5 and 13 nm in dioxane and toluene, respectively, the emission maximum of the Li salt in dioxane being concentration dependent (Figure 2) (see below). For the Na salt in dioxane this red shift is about 2 nm, while the Cs salt emission is identical in the three solvents. Generally the shifts in emission maximum for the Li and Na salts are comparable or larger than the corresponding shifts in absorption maxima. This is unusual since emission shifts due to ion pairing have been found to be smaller than the corresponding absorption shifts[10] (see Discussion). Differences in the emission and excitation bands shapes are also readily apparent (Figures 1–3). Generally the emission bands of the Li and Na salts in dioxane and toluene are broader than the spectra in THF and THP (Figures 2 and 3) and show only a small high wavelength shoulder. Of interest is the pronounced concentration dependence of the emission and particularly the excitation spectrum of LiFl in dioxane.[4] In the 10^{-4} to 10^{-6} M range, the emission maximum shifts from 547 to 542 nm at about 10^{-6} M. The excitation spectrum is clearly concentration dependent and changes from a maximum at 345 nm with a shoulder at 360 nm to a single maximum around 360 nm at 10^{-6} M. This behavior resembles that shown by the bis(fluorenyl)barium THP system which possesses an excitation spectrum different from the absorption spectrum.[11] The concentration dependent spectra of LiFl in dioxane were not due to dissociation of ion pairs into free anions since in such a case emission at 528 nm due to the free anion should have been visible.[10] Also the dielectric constant of this solvent (ϵ

= 2.2[25°C]) is much too low to observe any appreciable dissociation above 10^{-6} M.

The bandshape of the Cs salt is identical in all three solvents. Moreover none of the Cs salts show concentration dependent spectra in the 10^{-4} to 10^{-6} M concentration range. Finally Table I indicates differences in relative intensities with cation and solvent. For instance the Cs salt lifetimes and relative intensities are the same in all three solvents while for the Li and Na salts in dioxane and toluene, the relative intensities are lower compared to their contact ion pairs in THP.

Since the Cs salts have been shown by kinetic measurements to probably exist in these media as monomeric ion pairs[7] it appears that the changes observed for the Li and Na salts in dioxane and toluene are most probably due to changes in ionic association. Since in dioxane and toluene essentially no dissociation occurs into free ions or ion pair solvation leading to separated ion pairs, these processes most likely involve association of contact ion pairs to ion pair aggregates. Such a process is supported by the concentration dependent emission and excitation spectra of LiFl in dioxane and by the lower emission intensities and lifetimes observed for the Li and Na salts in dioxane and toluene compared to THF and THP. Such an effect might be expected to result from more efficient quenching within an ionic aggregate. The sizable emission red shift observed for the Li salt in toluene provides further support for ionic aggregation (see Discussion).

Discussion

The effect of ion pairing on absorption and emission spectra has been described previously.[9,10,16] Briefly, increasing cation size in a series of contact ion pairs red shifts the absorption but blue shifts the emission maximum (Table II). The absorption results have been explained as due to a greater perturbation of the ground state by the cation compared to the relevant excited state mainly because of the Franck–Condon destablization. The same effect might have the opposite shift in emission. However, the resultant red shift is expected (and found) to be smaller than in absorption shifts since the perturbation of the first excited state is probably relatively small since the charge distribution is more diffuse than in the ground state. These effects are shown schematically in Figure 4.

The effect of cation solvation leading to greater charge separation, i.e., the formation of solvent-separated ion pairs, is essentially the same as increasing the cationic radius. Thus on adding crown ethers (CE) or glymes to Li and Na salts absorption red shifts[9] and emission blue shifts[10] are observed consistent with the formation of separated ion pairs. However, again the emission shifts are less than the corresponding shifts in absorption maximum (Table II).

The absorption and emission results of the Li and Na salts in dioxane and toluene (Table I) however are quite different and seem to be consistent with association of ion pairs into dimers or higher aggregates. The similarity of emission intensity as well as emission and excitation spectra of CsFl in dioxane on one hand, and in THP or THF on the other precludes carbanion–solvent interactions as a cause for the anomalous spectra of the Li and Na salts in toluene and dioxane. The aggregation of ion pairs explains the low intensity of the three systems through effective quenching within the ion pair aggregate and is consistent with the concentration dependence of the emission and excitation spectra of the LiFl/dioxane system. Certainly such aggregation is expected to be more extensive in toluene and it is therefore not surprising that concentration dependent emission in this solvent

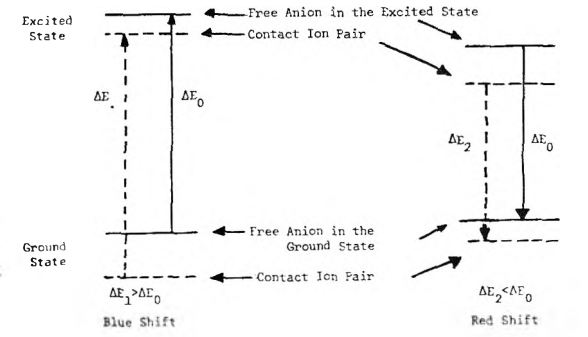

Figure 4.

TABLE II: Effect of Cation on Emission of Alkali Fluorenyl Salts in Tetrahydropyran at 25 °C

M+	Solvent	Ion pair[a]	Emission λ_{max}, nm	Absorption λ_{max}, nm
Li	THP	C	542[b]	349
Na	THP	C	538	355
K	THP	C	535	362
Rb	THP	C	534	363
Cs	THP	C	534	364
Na, CE[e]	THP	S	528	373
Free anion[c]	THP		528	373[d]

[a] C = contact ion pair, S = separated ion pair. [b] Calculated value, see Table I. [c] Observed in THP solutions below 10^{-7} M. [d] Extrapolated value (see ref 9). [e] Dicyclohexyl-18-crown-6.

is not observed in the 10^{-4} to 10^{-6} M range. However, the emission of LiFl in toluene is strongly red shifted to 555 nm. This behavior is readily understood on the basis of the exciton coupling[12,13] invoked in the preceding paper[11] to describe absorption and emission of bis(fluorenyl)barium.

In this scheme exciton exchange between two chromophores in close proximity causes a twofold splitting of excited state energy levels leading to a doubling of transitions, the relative intensity of which depends on the mutual orientation of the chromophores. It can be shown[12,13] that if the two chromophores are lined up in a parallel head-to-head fashion only the high energy transition is observed whereas for instance a parallel head-to-tail orientation allows only the low energy transition.[11] Alternative parallel or nonparallel orientations are also possible resulting in the appearance of two bands, the relative intensity of which depends on dimer geometry. (Figures 5a and 5b of the preceding paper). The energy difference ΔE between the two exciton levels equals $2|\vec{M}|^2G/R^3$ where $|\vec{M}|$ is the transition moment vector, R is the distance between the chromophores, the G is a factor depending on dimer geometry.[11]

The above spectra lack the details to fully evaluate the geometry of the aggregate structure. No exciton splitting into two bands is observed as is the case with bis(fluorenyl)barium.[11] However, the gross features of the aggregate may be evaluated with the exciton model. First the pronounced absorption blue shifts and emission red shifts of the Li salt in dioxane and toluene indicate a head-to-head parallel alignment of the fluorenyl moieties. Thus absorption is blue shifted due to a transition to a higher exciton state while emission occurs from the lower exciton level following nonradiative transition from the higher to the lower exciton levels (Figure 5). The greater energy difference between the exciton states

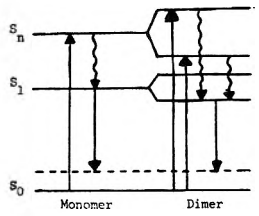

Figure 5.

in toluene is reasonable since here the aggregate ought to be tighter (R is smaller) due to the absence of Li coordination by ether.

Since the transition moment vector will vary in orientation and magnitude from transition to transition the ΔE values of the various exciton levels will in general be different. Also exciton splitting for a particular transition will be dependent on the geometry factor G which may be cation dependent. As a result emission and absorption shifts may differ for one cation while for another cation they may be similar, consistent with our observations. Also the greater emission shift compared to absorption for the Li salt in dioxane and toluene, contrary to the general trend observed in ion pairing induced shifts,[10] can be accomodated by the exciton interaction scheme.

It seemed of interest to us whether an exciton exchange description might be apt for the description of similar systems. One such system, 1-(2-hexyl)fluorenyllithium has been the subject of a thorough study by Exner and Waack.[6] Using a wide range of experimental techniques such as uv–visible, NMR, and ebulliometry, they found evidence for aggregation of the ion pairs in such solvents as THF, diethyl ether (DEE), cyclohexane, and benzene. The solvent separated ion pair absorbed at 387 nm in agreement with earlier results[17] and the contact ion pairs, observed in diethyl ether, absorbed at 358 nm. However, in the hydrocarbon solvents such as cyclohexane the absorption occurred at 367–370 nm, surprisingly red shifted relative to the unperturbed contact ion pair. Equally interesting, addition of small quantities of DEE to the cyclohexane solution gave an absorption maximum at 348 nm with occurrence of an isosbestic point while addition of small quantities of THF gave an absorption at 357 nm.

The above observations are of interest and seem highly anomalous in terms of ion pairing as indeed the authors pointed out. The spectral shifts, however, may be consistent with exciton coupling. For instance, the "tight" dimer likely to exist in the nonpolar cyclohexane might exist in an antiparallel geometry due to steric repulsion by the 2-hexyl groups in the parallel orientation. This would lead to absorption corresponding to the lower energy exciton band. Addition of the bulky diethyl ether would lead to peripheral cation solvation possibly causing a parallel or equivalent[11] orientation and giving rise to the higher energy exciton band. Addition of THF would result in strong cation solvation and ion pair separation so that quite possibly the distance R between the chromophores becomes too large for exciton interaction.

Since, for these type carbanions in more polar media, chromophore interaction in a possible aggregate is most likely too weak to be observable; absorption spectrometry would be of little value in detecting such aggregation. Emission spectroscopy might be useful here since aggregation could give rise to lower intensity and lifetime because of effective quenching within the aggregate (see above). However, in such systems as fluorenyllithium in THF and dimethoxyethane thought to be aggregated on kinetic grounds no decreased lifetime or intensity was apparent when compared with monomeric ion pairs such as fluorenylsodium in THF or with free anions observed with fluorenyllithium salts in acetonitrile at low concentration.

Summary

It has been shown that exciton coupling in aggregates of alkali salts of fluorenyl type carbanions in low dielectric constant media may result in significant red or blue shifts in absorption maximum depending on the mutual alignment of the chromophores. The same exciton splitting may cause a pronounced emission red shift comparable to or larger than the absorption shift.

Aggregate formation of the above systems is also indicated by much lower emission intensities of NaFl in dioxane and especially of LiFl in dioxane and toluene and by the concentration dependent emission and excitation spectra of LiFl in dioxane.

It was also shown that exciton coupling may be applicable to other similar systems and could be helpful in elucidating the alignment of chromophores in such carbanion aggregates.

Acknowledgment. We wish to thank Professor S. G. Schulman for the use of his spectrofluorimeter.

References and Notes

(1) To whom correspondence should be addressed.
(2) R. M. Fuoss and C. A. Kraus, *J. Am. Chem. Soc.*, **55**, 3614 (1933); C. A. Kraus, *J. Phys. Chem.*, **58**, 673 (1954); **60**, 129 (1956).
(3) For a review of NMR studies of aggregation of Li carbanions see D. McKeever in "Ion and Ion Pairs in Organic Reactions", Vol. I, M. Szwarc, Ed., Interscience, New York, N.Y., Chapter 6, and references therein.
(4) (a) L. J. Fetters and M. Morton, *Macromolecules*, **7**, 552 (1974); (b) D. J. Worsfold and S. Bywater, *ibid.*, **5**, 393 (1972).
(5) A. Guyot and J. Vialle, *J. Makromol. Sci., Chem.*, **4**, 107 (1970); H. Hsieh, *J. Polym. Sci., A3*, 173 (1965); D. Margerison, D. M. Bishop, G. C. East, and P. MacBride, *Trans. Faraday Soc.*, **64**, 1872 (1968); W. Gerbert, J. Hinz, and H. Sinn, *Makromol. Chem.*, **144**, 97 (1971).
(6) M. M. Exner, R. Waack, and E. C. Steiner, *J. Am. Chem. Soc.*, **95**, 7009 (1973).
(7) T. E. Hogen-Esch and J. Smid, *J. Am. Chem. Soc.*, **89**, 2764 (1967).
(8) M. Szwarc, Ed., "Ions and Ion Pairs in Organic Reactions", Wiley, New York, N.Y., 1974, p 204.
(9) T. E. Hogen-Esch and J. Smid, *J. Am. Chem. Soc.*, **88**, 307 (1966).
(10) M. J. Plodinec and T. E. Hogen-Esch, *J. Am. Chem. Soc.*, **96**, 5262 (1974).
(11) M. J. Plodinec and T. E. Hogen-Esch, *J. Phys. Chem.*, preceding paper in this issue.
(12) G. S. Levinson, W. T. Simpson, and W. Curtis, *J. Am. Chem. Soc.*, **79**, 4314 (1957).
(13) E. G. McRae and M. Kasha, *J. Chem. Phys.*, **28**, 721 (1958); M. Kasha, *Rev. Mod. Phys.*, **31**, 162 (1959).
(14) The solubility of fluorenylsodium and -cesium in toluene ($<10^{-7}$ M) is too low for study.
(15) M. J. Plodinec and T. E. Hogen-Esch, to be submitted for publication.
(16) H. W. Vos, H. H. Blom, N. H. Velthorst, and C. McLean, *J. Chem. Soc., Perkin Trans. 2*, 635 (1972); H. W. Vos C. McLean, and N. H. Velthorst, *J. Chem. Soc., Faraday Trans. 2*, **72**, 63 (1976).
(17) L. L. Chan and J. Smid, *J. Am. Chem. Soc.*, **90**, 4654 (1968).

Molecular Orbital Calculations on *N*-Phenylnaphthylamines, Fluorescence and Circular Dichroism Probes

Jerry C. Smith and Robert W. Woody*

Department of Chemistry, Arizona State University, Tempe, Arizona 85281 *(Received January 8, 1976)*

Publication costs assisted by the National Institutes of Health

Molecular orbital calculations on the π-electron structure of N-phenyl-α-naphthylamine and N-phenyl-β-naphthylamine have been performed. These diarylamines are models of the widely used fluorescent probes 1,8-anilinonaphthalenesulfonate (1,8-ANS) and 2,6-toluidinonaphthalenesulfonate (2,6-TNS). The results support the conclusions of Seliskar and Brand that (1) the lowest singlet → singlet transition has appreciable charge transfer (amino nitrogen and phenyl group → naphthalene) character; (2) the first excited singlet state has a much larger dipole moment than the ground state (about 6 D vs. 1 D); (3) the lowest triplet state has a dipole moment intermediate between that of S_0 and S_1. The relative insensitivity of the absorption spectrum to solvent polarity is explained by the fact that the dipole moment in S_1 is nearly orthogonal to that of S_0, especially in the β isomer. Calculations of rotational strength as a function of conformation were carried out to explore the possibilities of using the inherently dissymmetric ANS chromophore as a CD probe in complexes with proteins. However, the contributions of inherent dissymmetry to the rotational strengths of the long-wavelength bands are small. Coupled oscillator interactions with protein groups may therefore be dominant and one cannot infer the conformation or absolute configuration from the sign of these bands. This does not preclude other applications of ANS as a CD probe, however.

Naphthylamine derivatives, especially 1,8-anilinonaphthalenesulfonate (1,8-ANS) and 2,6-toluidinonaphthalenesulfonate (2,6-TNS) have been widely used in recent years as probes of macromolecular conformation and related phenomena. Their usefulness was first recognized by Weber and Laurence.[1] Subsequent applications of these fluorescence probes have been recently reviewed by Brand and Gohlke,[2] by Radda,[3] and by Radda and Vanderkooi.[4]

The usefulness of these probes results from the marked environmental sensitivity of their fluorescence parameters. For example, the quantum yield of 1,7-ANS increases from 0.009 in aqueous solution to 0.56 in ethanol, while the emission maximum shifts from 516 nm in water to 443 nm in ethanol.[5] The spectacular increase in fluorescence intensity and the blue shift in the emission which occurs on going from an aqueous medium to a less polar environment has been observed upon the binding of ANS or TNS to a number of proteins, such as bovine serum albumin,[1,6] apomyoglobin and apohemoglobin,[7] chymotrypsinogen and chymotrypsin,[8] liver alcohol dehydrogenase,[9] glyceraldehyde-3-phosphate dehydrogenase,[10] and tryptophanyl-tRNA synthetase.[11] In most of the enzymes studied (except for chymotrypsin[8]) ANS or TNS binding is competitive with substrates, indicating that the probe binds in the active site region, despite the fact that the naphthylamine derivatives have no obvious structural analogy to the substrates. Glazer[12] has commented on the marked tendency of dyelike molecules to seek out functionally important sites of enzymes.

The sensitivity of the emission characteristics of ANS and TNS to environment have also been utilized in the study of much more complex systems, particularly biological membranes.[3,4] Changes in the fluorescence of ANS bound to mitochondrial membranes have been observed[13] upon addition of ATP or of substrates such as succinate and NADH, while uncouplers of oxidative phosphorylation abolish the effect of substrate addition. ANS bound to the membrane of a nerve axon exhibits a transient increase in fluorescence intensity upon passage of a nerve impulse.[14] The interpretation of these types of experiments is still controversial.[2,4] However, the use of fluorescence probes in the study of membrane processes has great promise. ANS and related molecules may also be useful as circular dichroism (CD) probes. Induced CD bands have been reported for 1,8-ANS bound to bovine serum albumin[15,16] and to apohemoglobin,[17] and for 2,6-TNS bound to chymotrypsin.[18] CD studies of 1,8-ANS and 2,6-TNS binding to liver and yeast alcohol dehydrogenase are underway in our laboratory (C. Vanek and R. W. Woody, work in progress).

Although there have been several MO treatments of α- and β-naphthylamine,[19-22] there have been no theoretical studies of the N-phenylnaphthylamines which constitute the chromophores of ANS and TNS. We have performed such calculations for a number of possible conformations in order to examine theoretically (a) Seliskar and Brand's interpretation[23,24] (see Discussion) of solvent effects on ANS fluorescence and (b) the circular dichroism of ANS resulting from nonplanarity of the chromophore.

Methods

The calculations described in this paper are based upon the Pariser–Parr–Pople approximations to π-electron systems.[25,26] The computer program SCFCIO used was originally written by J. E. Bloor and B. R. Gilson and was obtained through the Quantum Chemistry Program Exchange.[27] This program was adapted for calculating rotational strengths by the addition of subroutines to calculate dipole velocity and angular momentum matrix elements. These matrix elements were then used to calculate the oscillator strength in the dipole velocity approximation and the rotational strength of the transition between the ground state and the ith excited states, using the relationships;[28]

$$f_{0\rightarrow i} = \frac{\hbar}{3\pi m\nu}(\psi_0|\nabla|\psi_i)^2$$

* Address correspondence to this author at the Department of Biochemistry, Colorado State University, Fort Collins, Colo. 80523.

$$R_{0\to i} = \frac{-e^2\hbar^3}{2m^2cE}(\psi_0|\nabla|\psi_i)\cdot(\psi_i|\mathbf{r}\times\nabla|\psi_0)$$

Here $f_{0\to i}$ and $R_{0\to i}$ are, respectively, the oscillator and rotational strengths, ν is the frequency in s^{-1}, and E is the energy of the transition. The symbols e, $\hbar$, m, and c have their usual meaning.

Atomic coordinates were generated from either experimental or assumed bond lengths and angles using the program COORD[29] developed by M. J. S. Dewar and N. C. Baird, also obtained through the Quantum Chemistry Program Exchange. In the case of β-ANS,[30] the bond lengths and angles given by Camerman and Jensen[31] from an x-ray crystal study were used, with certain approximations described below. All the C–C bond lengths and angles of the benzene ring were taken to be equal, as these vary only slightly. Essentially the same naphthalene ring geometry was assumed for α-ANS. The C–N bond lengths were also taken to be the same for α- and β-ANS.

We have neglected the effect of the sulfonate group which occurs in all of these systems and of the methyl group which occurs on the phenyl ring of TNS. The methyl group generally has only a small effect on transition energies and polarizations. The neglect of the sulfonate might be more serious. However, Seliskar and Brand[23] found only small differences in band position and oscillator strength between *N*-phenyl-2-naphthylamine and 2,6-ANS. The sulfonate group appears to act as a weakly perturbing substituent.

In any semiempirical MO calculation, the choice of parameters is critical. Several schemes were tested by performing calculations on α- and β-ANS. Two sets of parameters were used in more extensive calculations: the variable β approximation of Nishimoto and Forster,[20,32] and the parameterization of Bailey.[33,34] These approximations differ primarily in the choice of resonance integrals. The Nishimoto–Forster method assumes the resonance integral, β, to be a linear function of bond order, p: $\beta_{rs} = a + bp_{rs}$. The constants a and b depend on the nature of the atoms r and s, and upon the size of the ring system. The Bailey method takes β_{rs} to be proportional to dS_{rs}/dr where S_{rs} is the overlap integral between centers r and s, and r is the bond length. The choice of Coulomb integrals and one-center repulsion integrals is nearly identical, and both methods approximate two-center repulsion integrals by the Mataga–Nishimoto[35,36] formula.

Configuration interaction was considered, using the 16 singly excited configurations resulting from transitions from the four highest filled orbitals to the four lowest empty orbitals.

In addition to the calculations using the experimental dihedral angles for β-ANS (or TNS) and the same angles for α-ANS, calculations were also carried out for the following isomers:

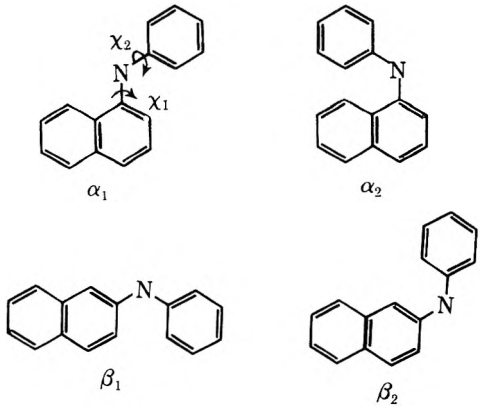

The geometries considered for each of these isomers included those with symmetrical dihedral angles, χ_1 and χ_2 of 0, −10, −20, −30, and −40°, and unsymmetrical combinations of $\chi_1 = 0°$, $\chi_2 = -40°$ or $\chi_1 = -40°$, $\chi_2 = 0°$. The negative angles denote a left-handed sense of torsion.

Results

The results of the calculations using the Nishimoto–Forster (NF) and Bailey (B) parameters for α- and β-ANS with $\chi_1 = -25.4°$, $\chi_2 = -27.7°$, the experimental angles for β-TNS,[31] are given in Table I. For comparison, some experimental data are included. The most complete experimental data for direct comparison with these calculations are those of Seliskar and Brand[23] for *N*-phenyl-2-naphthylamine. These data are most appropriate for comparison with the calculations on β-ANS, since we have neglected the sulfonate group of ANS. We have also included data for 1,7-ANS[5] and 2,6-TNS[8] for comparison with α- and β-ANS, respectively.

With respect to predicted band positions, both sets of parameters give comparable results, and both sets are in reasonable agreement with experiment. The long wavelength bands are uniformly predicted at somewhat shorter wavelengths than observed. However, each predicted band of significant intensity can be correlated with an observed band. The presence of a second weak transition in the long-wavelength region of 1,7-ANS is not apparent from the absorption spectrum in ethanol.[5] However, there is abundant evidence[5,7,15,16] that α-ANS derivatives, like other α-naphthylamines, have a second weak band which is obscured by the more intense long-wavelength band. The calculations using the Nishimoto–Forster parameters are consistent with the much stronger overlap of the two low-energy transitions for the α isomer (10 nm difference) than for the β isomer (~30 nm difference). The Bailey parameters yield energy differences which in fact predict a slightly larger splitting for α-ANS than for β-ANS. Both sets of parameters predict a small red shift in the long wavelength maximum on going from α-ANS to β-ANS, in agreement with experiment. The Nishimoto–Forster parameters also give a substantially better prediction of the energy of the first-excited triplet state in β-ANS.

Comparing intensities, we again find general agreement between theory and experiment. The Nishimoto–Forster parameters appear to do somewhat better in predicting intensities. For example, the Bailey parameters predict that the longest-wavelength band is substantially more intense than the band at ca. 250 nm in α-ANS and at ca. 270 nm in β-ANS, contrary to observation. The Bailey parameters also lead to the prediction that the two long-wavelength bands in β-ANS differ by less than a factor of 2 in intensity, whereas experimentally there is nearly a fourfold difference in intensity. The Nishimoto–Forster parameters lead to much more satisfactory results on both counts.

These comparisons have led us to favor the Nishimoto–Forster procedure for choosing π-MO parameters. Throughout the remainder of this paper, we will confine our attention to results obtained from these parameters.

In Table II, excited state properties of α- and β-ANS in the same conformation as described above are characterized further. The transition dipole moment, polarization direction, rotational strength, and excited state dipole moment is given for each of the first eight $S_0 \to S_i$ transitions.

The polarization of the two longest wavelength transitions is quite different in the case of α-ANS, but very similar for β-ANS. This is consistent with fluorescence polarization measurements, which show a large change across the long-

TABLE I: Comparison of Experimental and Theoretical Wavelengths and Intensities[a]

Excited state	α-ANS			β-ANS			
	1,7-ANS[b]	NF[c]	B[d]	2,6-TNS[e]	NPAN[f]	NF	B
S_1	352[9.2]	327(0.30)	333(0.37)	357(0.07)	347(0.05)	329(0.06)	324(0.22)
S_2		317(0.01)	305(0.02)	317(0.25)	308(0.20)	298(0.33)	302(0.39)
S_3		276(0.01)	295(0.01)			277(0.01)	296(0.01)
S_4		254(0.16)	263(0.08)	274[27]	270[24]	264(0.50)	259(0.13)
S_5	253[17]	238(0.41)	240(0.23)			236(0.06)	235(0.08)
S_6		237(0.01)	233(0.01)			221(0.16)	228(0.21)
S_7		209(0.10)	212(0.12)	224[55]	225[49]	213(0.47)	211(0.23)
S_8	223[63]	208(0.41)	205(0.64)			204(0.11)	206(0.46)
T_1		533	482	513	541	508	457

[a] Wavelengths in nm; oscillator strengths in parentheses, ϵ_{max} ($\times 10^{-3}$) in brackets. [b] D. C. Turner and L. Brand, ref 5. Solvent is ethanol. [c] Nishimoto–Forster parameters. [d] Bailey parameters. [e] Data for two long-wavelength bands from C. J. Seliskar and L. Brand, ref 37. Data for shorter-wavelength bands from W. O. McClure and G. M. Edelman, ref. 38. Solvent is ethanol in both cases. [f] *N*-Phenyl-2-aminonaphthalene in ethanol. Data from C. J. Seliskar and L. Brand, ref 37.

TABLE II: Polarization, Rotational Strength, and Excited-State Dipole Moments

Excited state	λ	μ_{oa}[a]	γ_x[b]	γ_y[b]	γ_z[b]	R_{oa}[c]	μ_{aa}[d]
				α-ANS			
S_1	327	4.57	64	27	81	−0.083	5.73
S_2	317	0.92	16	106	93	−0.036	2.60
S_3	276	0.74	88	43	133	−0.111	7.42
S_4	254	2.98	42	52	74	0.286	3.90
S_5	238	4.57	3	91	92	−0.649	8.00
S_6	237	0.55	71	20	82	−0.009	6.88
S_7	209	2.12	50	59	124	−2.010	1.88
S_8	208	4.23	167	80	97	1.909	5.47
				β-ANS			
S_1	329	2.10	22	111	85	0.078	5.93
S_2	298	4.56	10	96	82	0.163	3.70
S_3	277	0.76	57	56	128	0.002	6.17
S_4	264	5.30	22	70	82	−0.620	2.01
S_5	236	1.68	38	127	97	−0.225	13.57
S_6	221	2.76	44	47	96	0.061	3.09
S_7	213	4.61	19	108	95	−1.033	4.44
S_8	204	2.15	82	44	133	0.660	7.96

[a] Transition moment magnitude (Debye). [b] γ_x, γ_y, and γ_z are angles of transition moment with respect to *x*, *y*, and *z* axes. The naphthalene ring lies in *xy* plane with its long axis being the *x* axis, its short axis being the *y* axis. [c] Rotational strength in Debye Bohr magnetons (1 DBM = 0.9273 $\times 10^{-38}$ cgs units). [d] Permanent dipole moment of excited state (Debye).

wavelength band containing both low-energy transitions in 1,7-ANS,[5] but little change over the two long-wavelength bands of 2,6-TNS.[37] It is also consistent with experimental data and theoretical calculations[20,22,39] on α- and β-naphthylamines and naphthols.

Most of the transitions are polarized primarily in the *xy* plane (naphthalene ring plane), with $\gamma_z = 90 \pm 10°$. This reflects the dominance of the naphthalene ring system in the low-energy transitions. The largest deviations are shown by the bands near 275 and 205–210 nm in both α- and β-ANS. These are primarily transitions involving the phenyl group.

The rotational strengths of the longest-wavelength transitions are small for both α- and β-ANS. The 238-nm transition in α-ANS and the 264-nm band in β-ANS have substantial rotational strengths, and both α- and β-ANS display two strong and closely spaced CD bands of opposite sign in the 210-nm region.

The ground state dipole moments are small for both α-ANS and β-TNS, being 1.07 and 0.89 D, respectively. As Table II shows, nearly all of the excited states have much larger dipole moments than the ground state, and the first excited state in both systems has a dipole moment about a factor of 6 larger than the ground state moment. These results for the α isomer agree quite well with the experimental work of Kawski and Pasztor[40] who obtained dipole moments of 1.5 and 5.2 D for the ground and first excited states, respectively, of *N*-phenyl-1-naphthylamine. The results for the β isomer are in qualitative agreement with the work of Seliskar and Brand,[24] who studied solvent shifts in absorption and fluorescence maxima. Their estimate of $(\mu_e - \mu_g)$ for *N*-phenyl-2-naphthylamine is 20 D which is much larger than our calculated value. Because of approximations in the calculations (e.g., neglect of the sulfonate group) and in the analysis[41,42] of the experimental data (e.g., estimation of the size of the Onsager cavity), one can only expect qualitative agreement.

The dipole moment of the lowest triplet state is 2.03 D in α-ANS and 2.49 D in β-ANS. Thus, these values fall between the value for S_0 and S_1. This was suggested by Seliskar and Brand[24] based upon measurements of p*K* values in S_0, S_1, and T_1 by Jackson and Porter.[43]

Figures 1–3 gives the π-electron densities and bond orders for α- and β-ANS in the S_0, S_1, and T_1 states. It is clear from these molecular diagrams that a substantial amount of charge (~0.2 e) is transferred from the nitrogen into the naphthalene ring on going from $S_0 \rightarrow S_1$. To a lesser extent, the ortho and para positions of the phenyl group also lose electron density to the naphthalene ring. Both of these types of charge transfer occur also in the $S_0 \rightarrow T_1$ transition, but to a lesser extent.

Table III gives data on the four longest-wavelength bands as a function of dihedral angle. In general, the transition energy is rather insensitive to the dihedral angle, at least in the range considered here. As the dihedral angles increase, there are small blue shifts of the various bands due to decreasing conjugation with the amino group.

The oscillator strength is somewhat more sensitive to dihedral angle than the transition energy is. The general tendency is for the oscillator strength to decrease with increasing angle, again reflecting the decreasing degree of conjugation between the aromatic rings and the amino nitrogen. An exception is the 260-nm band of β-ANS, which shows an increase in oscillator strength with dihedral angle. This band involves charge transfer from the amino nitrogen into both the naphthalene and the phenyl groups, primarily the latter. The extent of this charge transfer increases with dihedral angle, at least up to 40°.

The most sensitive parameter is naturally the rotational strength. This must necessarily vanish for the planar conformation. The magnitude of the rotational strength goes

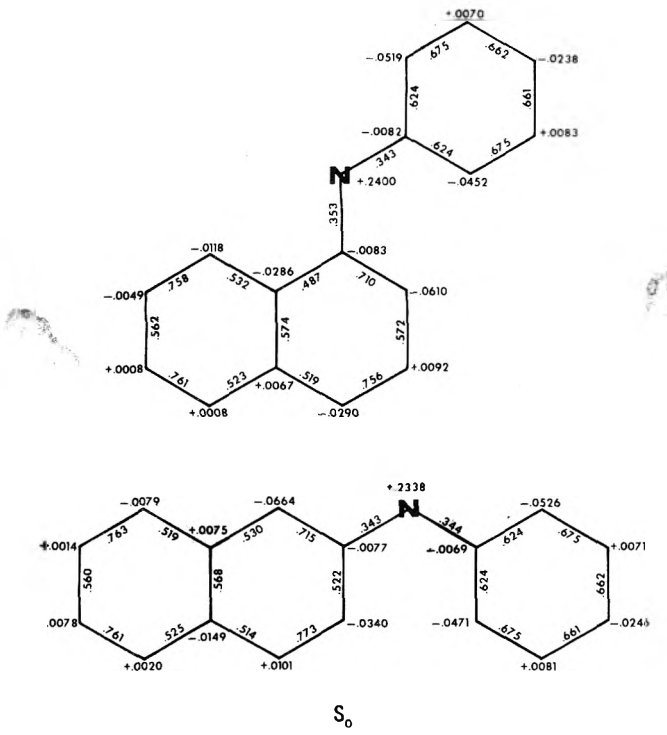

Figure 1. Molecular diagrams for α-ANS (upper) and β-ANS (lower) in the ground state (S_0). The numbers at the atomic positions give the theoretical charge densities associated with the π-electron system, while the numbers along the bonds give the π-electron bond orders.

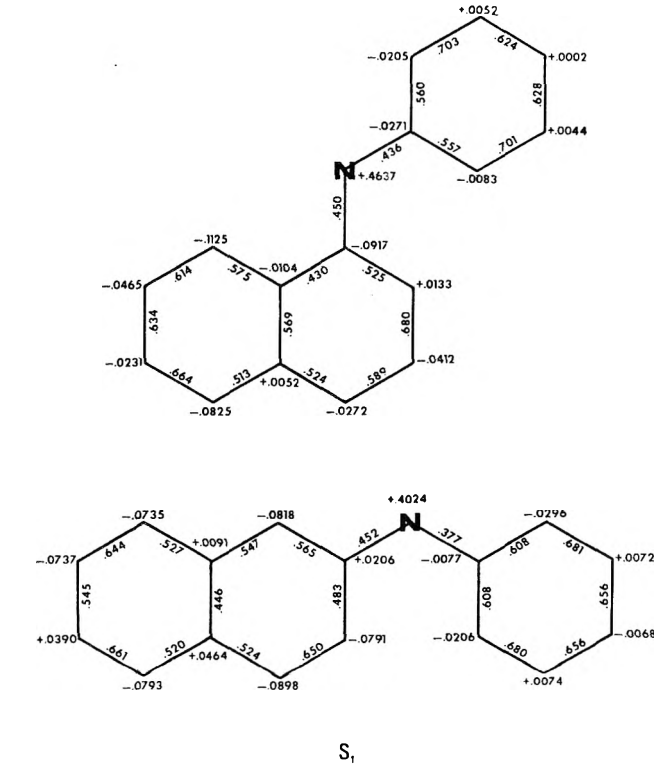

Figure 2. Molecular diagrams for α-ANS (upper) and β-ANS (lower) in the first excited singlet state (S_1). (See caption to Figure 1.)

through a maximum for some bands at dihedral angles of 20° or 30°. For others, the increase continues to at least 40°. In two cases (band 3 for α_2 and β_1) the rotational strength changes sign between 30 and 40°. Comparison of conformations with symmetrical dihedral angles with those having two very different dihedral angles indicates that in many cases, though the magnitudes of the rotational strengths are changed significantly, the signs are unchanged. However, there are exceptions to this, e.g., band 4 in α_1 and bands 1 and 2 in β_1.

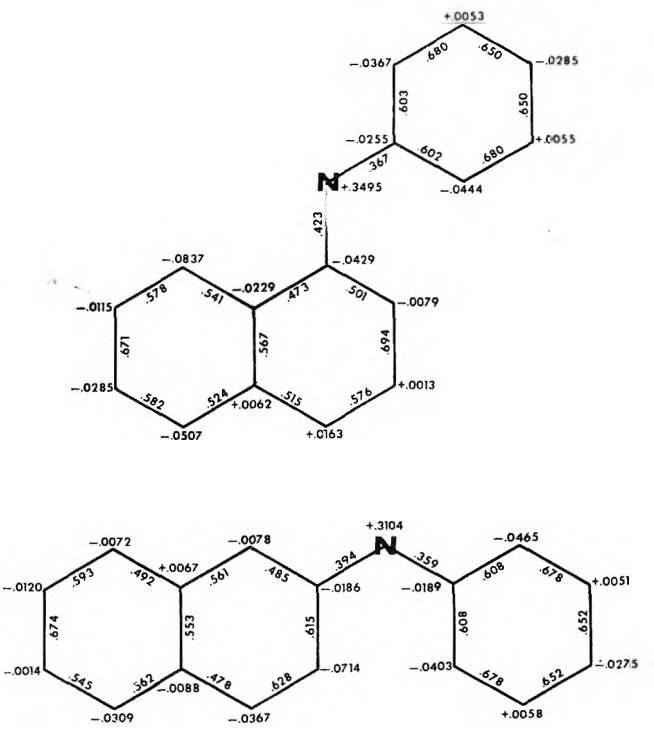

Figure 3. Molecular diagrams for α-ANS (upper) and β-ANS (lower) in the first excited triplet state (T_1). (See caption to Figure 1.)

We have not been able to discern any rules for predicting the signs of the long-wavelength bands. No sector rule or chirality rule appears to govern the sign of the long-wavelength bands. The two generalizations that we can make are: (1) the two lowest energy CD bands have the same sign for all conformations considered; and (2) the most favorable conformations of α- and β-ANS (α_1 and β_1) have opposite signs for the two long-wavelength bands.

Discussion

The origin of the strong solvent dependence of ANS, TNS, and related molecules has been discussed extensively. There seems to be a consensus[2] that the wavelength shift results from solvent relaxation during the excited state lifetime. However, the solvent effects on quantum yield have been attributed to several different causes. (1) Weber and Laurence[1] and, more recently, Penzer[46] have suggested that in aqueous solution, the conformation of ANS shows marked nonplanarity and hence fluoresces weakly, while in less polar solvents, the conformation is more nearly planar and exhibits strong fluorescence. (2) McClure and Edelman[37] and Ainsworth and Flanagan[47] noted that intramolecular rotations of the fluorophore during the excited state lifetime should reduce the quantum yield by promoting radiationless transitions to the ground state. Hence more viscous solvents lead to a more intense fluorescence. (3) Seliskar and Brand[29] postulated that relaxation of the solvent cage during the excited-state lifetime decreases the energy of the first excited singlet (^{1}S) more than that of the first excited triplet (^{1}T) because the ^{1}S state has a larger dipole moment than does ^{1}T.[2,19,20] The narrowing of

TABLE III: Conformational Dependence of Parameters for Long-Wavelength Bands in α-ANS (α_1), α-ANS (α_2), β-ANS (β_1), and β-ANS (β_2)

	Band 1			Band 2			Band 3			Band 4		
(χ_1, χ_2)	λ	f	R	λ	f	R	λ	f	R	λ	f	R
					α-ANS (α_1)							
(0, 0)	333	0.303	0	318	0.015	0	279	0.013	0	257	0.143	0
(−10, −10)	333	0.302	−0.039	318	0.014	−0.026	279	0.013	−0.089	257	0.144	0.098
(−20, −20)	330	0.292	−0.072	317	0.013	−0.036	278	0.012	−0.129	256	0.147	0.213
(−30, −30)	327	0.275	−0.096	316	0.012	−0.029	276	0.010	−0.106	254	0.145	0.341
(−40, −40)	322	0.249	−0.114	315	0.009	−0.007	274	0.007	−0.047	253	0.132	0.464
(0, −40)	328	0.276	−0.102	318	0.016	−0.051	277	0.004	−0.043	260	0.114	−0.089
(−40, 0)	329	0.257	−0.038	315	0.010	−0.087	275	0.022	−0.251	256	0.065	0.423
					α-ANS (α_2)							
(0, 0)	336	0.274	0	320	0.018	0	279	0.013	0	261	0.014	0
(−10, −10)	335	0.259	−0.323	319	0.017	−0.016	279	0.012	−0.101	260	0.018	−0.321
(−20, −20)	333	0.216	−0.249	318	0.015	−0.025	277	0.011	−0.118	258	0.032	−0.756
(−30, −30)	329	0.211	−0.313	317	0.012	−0.015	276	0.009	−0.053	256	0.039	−0.982
(−40, −40)	324	0.201	−0.320	315	0.009	−0.009	274	0.005	0.014	254	0.021	−1.008
(0, −40)	329	0.199	−0.064	313	0.025	−0.034	276	0.002	−0.050	263	0.025	−0.121
(−40, 0)	332	0.202	−0.290	315	0.007	−0.038	275	0.023	−0.197	259	0.009	−0.522
					β-ANS (β_1)							
(0, 0)	332	0.081	0	301	0.359	0	279	0.013	0	266	0.419	0
(−10, −10)	332	0.080	0.037	301	0.356	0.063	279	0.013	−0.021	266	0.418	−0.293
(−20, −20)	330	0.072	0.075	300	0.332	0.142	278	0.012	−0.022	265	0.434	−0.555
(−30, −30)	328	0.061	0.107	297	0.299	0.240	277	0.010	−0.003	264	0.453	−0.758
(−40, −40)	325	0.047	0.126	295	0.254	0.350	275	0.007	0.019	263	0.469	−0.876
(0, −40)	331	0.055	−0.034	298	0.324	−0.087	276	0.004	−0.007	265	0.405	−0.129
(−40, 0)	327	0.078	0.182	299	0.272	0.353	277	0.022	−0.051	266	0.382	−0.793
					β-ANS (β_2)							
(0, 0)	334	0.034	0	305	0.204	0	282	0.029	0	264	0.482	0
(−10, −10)	333	0.034	−0.144	305	0.205	−0.251	282	0.027	0.009	264	0.479	0.101
(−20, −20)	331	0.034	−0.227	303	0.197	−0.464	280	0.022	0.016	264	0.486	0.197
(−30, −30)	329	0.031	−0.239	300	0.185	−0.617	279	0.014	0.022	264	0.491	0.278
(−40, −40)	326	0.027	−0.202	297	0.163	−0.679	277	0.008	0.022	263	0.492	0.343
(0, −40)	332	0.024	−0.095	302	0.192	−0.200	279	0.009	0.038	264	0.441	−0.098
(−40, 0)	329	0.044	−0.327	301	0.165	−0.609	279	0.035	−0.070	265	0.414	0.488

the singlet–triplet gap should enhance the intersystem crossing rate and thus contribute to fluorescence quenching. (4) Kosower and co-workers argue that there are[44,45] two emitting excited singlet species: $S_{1,np}$, a species having a distinctly nonplanar structure whose emission is not markedly sensitive to solvent and substituents; and $S_{1,ct}$, a species whose emission is markedly solvent and substituent dependent, formed from $S_{1,np}$ by an intramolecular charge transfer. Polar solvents favor the conversion $S_{1,np}$ to $S_{1,ct}$, and also promote the radiationless deactivation of $S_{1,ct}$ to the ground state by a reverse intramolecular charge transfer. In viscous solvents, both of these transformations are hindered. (5) Li et al.[50] have suggested that the large effect of polar solvents on the fluorescence yield in α-ANS may be due to a solvent-induced inversion of the ^1L_a and ^1L_b states, with ^1L_b lying lowest in nonpolar solvents and ^1L_a in polar solvents. This hypothesis is based upon studies of dimethylaminonaphthalenesulfonate analogues of ANS. However, this mechanism could at best account for the effect in α-ANS, leaving similar effects in β-ANS unexplained.

Our calculations provide support for several of Seliskar and Brand's[23,24] key arguments. The changes in charge density upon excitation (Figures 1–3) are those expected for an intramolecular charge transfer (in the notation of Kasha and Rawls,[48] an $l \rightarrow a_\pi$ transition), as suggested by Seliskar and Brand.[23]

Seliskar and Brand[24] also derived from solvent effects on the Stokes shift very large values of ($\mu_e - \mu_g$) ranging from 20 to 50 D for various β-ANS derivatives. These values seem unusually large and as Seliskar and Brand point out are subject to rather large errors. Nonetheless they indicate a highly polar excited state, a conclusion which our calculations support.

Kosower and co-workers[45,49] have pointed out that the absorption maximum of 2,6-ANS and several of its derivatives is rather insensitive to solvent, with only small shifts on going from water to ethanol. Further, the direction of this shift is to lower energies. From this observation, they argue that the Franck–Condon state produced upon excitation into the S_1 state is not highly polar. Our calculations indicate that not only does the dipole moment of these diarylamines increase sharply in magnitude upon excitation, but there is also a large change in direction. In fact for the β isomer, the dipole moment in S_1 is almost exactly perpendicular to the ground state dipole moment. (For the α isomer, the change in the angle upon excitation is 57°.) If the sulfonate group does not change this picture entirely, the near orthogonality of ground- and excited-state dipole moments would lead to little or no stabilization of the excited state by the solvent sheath in the Franck–Condon state. The small observed blue shift between ethanol and water could then be attributed to the greater polarizability of ethanol.

Another major point in Seliskar and Brand's[24] explanation of solvent quenching of ANS fluorescence is that the dipole moment of the T_1 state is intermediate between that of S_0 and S_1. This assumption is verified by our calculations for both the α and β isomers.

Our calculations do not bear as directly upon the quenching

mechanism proposed by Kosower et al.[45] One relevant feature is that we do not predict any qualitative difference in the degree of charge transfer in the first excited state for the completely planar form and the nonplanar form of either α- or β-ANS. For the planar β isomer, the dipole moment of S_1 is 6.38 D and the charge on the amino nitrogen is +0.427 e as compared to 5.93 D and 0.402 e in the nonplanar ($\chi_1 = -25°$, $\chi_2 = -28°$) form observed in the ground state in the crystal. However, we cannot rule out the possibility that the presence of the sulfonate and/or interactions with polar solvents might stabilize a nearly planar form with a substantially greater degree of charge transfer.

The laser pulse experiments of Kosower et al.[45] have pointed up a possible difficulty with Seliskar and Brand's[24] hypothesis. The increase in yield of T_1 in polar solvents anticipated by Seliskar and Brand's hypothesis are not evident. Whether this is a fatal flaw or whether the transient species populations can be reconciled with the solvent relaxation picture remains to be determined. However, Weber[51] has pointed out that systems such as 2-diethylaminonaphthalene-5-sulfonate and 1,8-naphthosultam show solvent-dependent quenching of fluorescence similar to ANS derivatives. In these systems, particularly the latter, a nonplanar → planar conversion with attendant intramolecular charge transfer is highly improbable.

The interpretation of CD bands induced upon binding chromophoric molecules to proteins is still in its infancy. However, three general mechanisms can be postulated: (1) inherent dissymmetry[52] in the chromophore, i.e., the bound chromophore has no elements of reflection symmetry; (2) coupled oscillator interactions[53] between the bound chromophore and groups on the protein; (3) mixing of excited states of differing symmetry within the chromophore under the influence of the electrostatic field produced by the protein binding site (the one-electron mechanism[54]). The latter two mechanisms are impossible to predict a priori because of their dependence on the protein geometry. However, mechanism 1 is susceptible to analysis through molecular orbital calculations or, in cases where the chromophore has a C_2 axis, through application of the rule of Hug and Wagniére.[55] If the inherent dissymmetry dominates one or more CD bands, the absolute configuration of the bound chromophore can be determined. This has been done in the case of auramine O bound to liver alcohol dehydrogenase[56] and of bilirubin and biliverdin bound to serum albumin.[57]

ANS, TNS, and related molecules are inherently dissymmetric chromophores. Examination of molecular models indicates that steric hindrance precludes an all-planar conformation, and this is confirmed by the x-ray diffraction study by Camerman and Jensen[31] of 2,6-TNS. One of the objectives of this work was to determine whether the chiral ANS chromophore would generate sufficiently strong rotational strengths that its CD bands might be diagnostic of its conformation and absolute configuration when bound to the enzyme. Unfortunately, we can see from Tables II and III that the rotational strengths of the long-wavelength bands are small for both α and β isomers. Only the far ultraviolet bands have rotational strengths (ca. 1 DBM) which would be likely to exceed contributions of coupling with protein groups and thus be diagnostic of ligand conformation. However, these bands fall in the region where the peptide groups of the protein will dominate the CD of protein and ligand.

Complexes of 1,8-ANS with bovine serum albumin have been studied by Anderson[15] and by Daniel and Yang.[16] Bovine serum albumin binds 5 molecules of 1,8-ANS tightly and about 15 more molecules much less tightly. There are some unresolved discrepancies between these two studies concerning the dependence of the CD upon the number of ligands bound. However, we shall only consider the data for an average of one dye bound per molecule, in which case there is fair agreement between the two studies. Daniel and Yang report rotational strengths of +0.031, −0.027, +0.028, and −0.209 DBM for bands centered at 380, 340, 300, and 272 nm, respectively. This pattern of signs does not agree with the calculated rotational strengths, since the rotational strength of the two long-wavelength bands is predicted to be the same in all cases. This presumably is a reflection of the effect of coupling with protein chromophores.

Hsu and Woody[17] observed an induced CD band in the complex of 1,8-ANS with apohemoglobin. Stryer,[7] using fluorescence techniques, had shown that ANS binds in the heme-binding pocket of apohemoglobin. The CD spectrum of the complex showed a negative band at 370 nm, corresponding to the $S_0 \rightarrow S_1$ transition in α-ANS derivatives. No separate band was resolved corresponding to the near-by $S_0 \rightarrow S_2$ transition but the shape of the CD curve suggests that the $S_0 \rightarrow S_2$ transition has a weaker negative rotational strength. The rotational strength of the 370-nm band was estimated to be −0.08 DBM. These results agree remarkably well with the predictions of Tables II and IIIa. However, because the band is weak and coupling with protein transitions is unlikely to be negligible, the agreement is probably fortuitous.

Schlessinger and Steinberg[18] reported the CD of the complex of chymotrypsin with 2,6-TNS. Their data cover only the longest-wavelength band, revealing a negative CD band centered at 365 nm with a rotational strength of ca. −0.12 DBM (our estimate). From the shape of the curve, it appears that the second band is also negative but weaker. Theoretically, the second band should be stronger.

The major emphasis of Schlessinger and Steinberg's paper was not on ordinary CD spectra but on circularly polarized luminescence, which measures the circular dichroism associated with the transition $S_1 \rightarrow S_0$. The quantity actually measured is the anisotropy factor $g_e = 2(f_l - f_r)/f$ where f_l = intensity of emitted left-circularly polarized light, f_r = intensity of right-circularly polarized light emitted, and f = total intensity of emission. This anisotropy factor[10] should be the same as the anisotropy factor for absorption, $g_a = (\epsilon_l - \epsilon_r)/\epsilon = 4R_{0i}/D_{0i}$ (where $D_{0i} = \mu_{0i}^2$ is the dipole strength of the transition) if the conformation and environment of the emitting species does not change during the excited-state lifetime. However, Schlessinger and Steinberg found that g_e is nearly an order of magnitude smaller than g_a for 2,6-TNS–chymotrypsin. This implies that the location or orientation of the excited species is different from that of the ground state, or that the conformation of the fluorophore has changed. The marked reduction may reflect a greater flexibility in position and conformation, leading to an averaging process with contributions of opposing sign.

Ivanov and Nagradova[58] reported CD data for the 2,6-TNS complex with yeast glyceraldehyde-3-phosphate dehydrogenase. Their published CD curve does not extend into the long-wavelength region, but shows a small negative contribution in the 270-nm region.

The present calculations and the limited available experimental data indicate that the induced CD of ANS and related molecules is not likely to be dominated by inherent dissymmetry, but rather by coupling to protein chromophores, at least in the wavelength range above 250 nm. Thus we cannot

infer absolute configurations from the CD of bound ANS. However, the induced CD of ANS is still a potentially useful probe of the protein conformation at the binding site, and can be used to monitor conformational changes produced by a variety of physical and chemical agents.

Acknowledgments. This work was supported by a grant from the U.S. Public Health Service, GM17850.

References and Notes

(1) G. Weber and D. J. R. Laurence, *Biochem. J.*, **56**, 31P (1954).
(2) L. Brand and J. R. Gohlke, *Ann. Rev. Biochem.*, **41**, 843 (1972).
(3) G. K. Radda, *Curr. Top. Bioenerg.*, **4**, 81 (1971).
(4) G. K. Radda and J. Vanderkooi, *Biochim. Biophys. Acta.*, **265**, 509 (1972).
(5) D. C. Turner and L. Brand, *Biochemistry*, **7**, 3381 (1968).
(6) E. Daniel and G. Weber, *Biochemistry*, **5**, 1893 (1966).
(7) L. Stryer, *J. Mol. Biol.*, **13**, 482 (1965).
(8) W. O. McClure and G. M. Edelman, *Biochemistry*, **6**, 559 (1967).
(9) L. Brand, J. R. Gohlke, and D. S. Rao, *Biochemistry*, **6**, 3510 (1967).
(10) N. K. Nagradova, R. A. Asryants, and M. V. Ivanov, *Experientia*, **27**, 1169 (1971).
(11) N. Cittanova and A. Alfsen, *Eur. J. Biochem.*, **13**, 539 (1970).
(12) A. N. Glazer, *Proc. Natl. Acad. Sci. U.S.A.*, **65**, 1057 (1970).
(13) A. Azzi, B. Chance, G. K. Radda, and C. P. Lee, *Proc. Natl. Acad. Sci. U.S.A.*, **62**, 612 (1969).
(14) I. Tasaki, A. Watanabe, A. Sandlin, and L. Carnay, *Proc. Natl. Acad. Sci. U.S.A.*, **61**, 883 (1968).
(15) S. R. Anderson, *Biochemistry*, **8**, 4838 (1969).
(16) E. Daniel and J. T. Yang, *Biochemistry*, **12**, 508 (1973).
(17) M-C. Hsu and R. W. Woody, *Biopolymers*, **10**, 1421 (1971).
(18) J. Schlessinger and I. Z. Steinberg, *Proc. Natl. Acad. Sci. U.S.A.*, **69**, 769 (1972).
(19) H. Baba and S. Suzuki, *Bull. Chem. Soc. Jpn.*, **34**, 82 (1961).
(20) K. Nishimoto and L. S. Forster, *Theor. Chim. Acta*, **4**, 155 (1966).
(21) K. Nishimoto, *Theor. Chim. Acta*, **7**, 207 (1967).
(22) S. Suzuki, T. Fujii, and H. Baba, *J. Mol. Spectrosc.*, **47**, 243 (1973).
(23) C. J. Seliskar and L. Brand, *J. Am. Chem. Soc.*, **93**, 5405 (1971).
(24) C. J. Seliskar and L. Brand, *J. Am. Chem. Soc.*, **93**, 5414 (1971).
(25) R. G. Parr, "Quantum Theory of Molecular Electronic Structure", W. A. Benjamin, New York, N.Y., 1963.
(26) J. N. Murrell and A. J. Harget, "Semi-Empirical Self-Consistent-Field Molecular Orbital Theory of Molecules", Wiley-Interscience, London, 1972, Chapter 2, p 11.
(27) Quantum Chemistry Program Exchange. Bloomington, Ind., Program 71.2.
(28) A. Moscowitz, Ph.D. Thesis, Harvard University, 1956.
(29) Quantum Chemistry Program Exchange, Bloomington, Ind., Program 136. In using this program for optical activity calculations, it is important to note that apparently Dewar and Baird used a left-handed coordinate system. That is, if one follows the instructions in the program and interprets the results as referring to right-handed coordinates, the sense of rotation is incorrect. We therefore reversed the sign of all input data for dihedral angles and interpreted the output as right-handed coordinates.
(30) We shall use the designation α-ANS for any *N*-phenyl-1-naphthylaminesulfonate and β-ANS for *N*-phenyl-2-naphthylaminesulfonates. Thus the commonly used fluorescent probe **2**,6-TNS will be referred to as β-ANS for the remainder of this paper. In our approximation, the position of the sulfonate group is irrelevant, as is the presence or absence of a methyl group.
(31) A. Camerman and L. H. Jensen, *J. Am. Chem. Soc.*, **92**, 4200 (1970).
(32) K. Nishimoto and L. S. Forster, *Theor. Chim. Acta*, **3**, 407 (1965).
(33) M. L. Bailey, *Theor. Chim. Acta*, **13**, 56 (1969).
(34) M. L. Bailey, *Theor. Chim. Acta*, **16**, 309 (1970).
(35) N. Mataga and K. Nishimoto, *Z. Phys. Chem. (Frankfurt am Main)*, **12**, 335 (1957).
(36) N. Mataga and K. Nishimoto, *Z. Phys. Chem. (Frankfurt am Main)*, **13**, 140 (1957).
(37) W. O. McClure and G. M. Edelman, *Biochemistry*, **5**, 1908 (1966).
(38) Y. Tanizaki and S.-I. Kubodera, *J. Mol. Spectrosc.*, **24**, 1 (1967).
(39) K. Nishimoto and R. Fujishiro, *Bull. Chem. Soc. Jpn.*, **37**, 1660 (1964).
(40) A. Kawski and B. Pasztor, *Acta. Phys. Polon.*, **29**, 187 (1966).
(41) N. Mataga, Y. Keifu, and M. Koizumi, *Bull. Chem. Soc. Jpn.*, **29**, 465 (1956).
(42) E. Lippert, *Z. Naturforsch. A*, **10**, 541 (1955).
(43) G. Jackson and G. Porter, *Proc. R. Soc. London, Ser. A*, **260**, 13 (1961).
(44) E. M. Kosower and H. Dodiuk, *Chem. Phys. Lett.*, **26**, 545 (1974).
(45) E. M. Kosower, H. Dodiuk, K. Tanizawa, M. Ottolenghi, and N. Orbach, *J. Am. Chem. Soc.*, **97**, 2167 (1975).
(46) G. R. Penzer, *Eur. J. Biochem.*, **25**, 218 (1972).
(47) A. Ainsworth and M. T. Flanagan, *Biochim. Biophys. Acta*, **194**, 213 (1969).
(48) M. Kasha and H. R. Rawls, *Photochem. Photobiol.*, **7**, 561 (1968).
(49) E. M. Kosower and K. Tanizawa, *Chem. Phys. Lett.*, **16**, 419 (1972).
(50) Y.-H. Li, L.-M. Chan, L. Tyer, R. T. Moody, C. M. Himel, and D. M. Hercules, *J. Am. Chem. Soc.*, **97**, 3118 (1975).
(51) G. Weber in "Protein-Ligand Interactions", H. Sund and G. Blauer, Ed., W. de Gruyter, Berlin, 1975, p 15.
(52) A. Moscowitz in "Optical Rotatory Dispersion", C. Djerassi, Ed., McGraw-Hill, New York, N.Y., 1960, p 150.
(53) J. G. Kirkwood, *J. Chem. Phys.*, **5**, 479 (1937).
(54) E. U. Condon, W. Altar, and H. Eyring, *J. Chem. Phys.*, **5**, 753 (1937).
(55) W. Hug and G. Wagnière, *Tetrahedron*, **28**, 1241 (1972).
(56) J. S. Wicken and R. W. Woody, *Biochemistry*, **12**, 3459 (1973).
(57) G. Wagnière and G. Blauer, *J. Am. Chem. Soc.*, **97**, 1949 (1975).
(58) M. V. Ivanov and N. K. Nagradova, *Int. J. Biochem.*, **5**, 569 (1974).

Spectrophotometric Studies of the Radiolysis of Liquid Ammonia

M. O. Delcourt, J. Belloni,*

Laboratoire de Physico-chimie des Rayonnements, Associé au CNRS, 91405 Orsay, France

and E. Saito

DRA, SRIRMA, CEN Saclay, 91190 Gif-sur-Yvette, France *(Received December 1, 1975)*

Publication costs assisted by DRA, SRIRMA, Centre d'Etudes Nucléaires de Saclay

The optical absorption spectra of liquid ammonia with or without solutes have been investigated at different doses of γ irradiation and different temperatures. The absorption spectrum recorded in initially pure ammonia, at room temperature and doses $\geq 3 \times 10^{19}$ eV ml^{-1}, corresponds to the azide ion N_3^- (ϵ_{247nm} 1380 ± 30 M^{-1} cm^{-1}) with a yield $G(N_3^-) = 0.05$ which completes the material balance of the other products N_2, H_2, and N_2H_4. At low temperature, the yields are $G(H_2) = 0.61 \pm 0.02$, $G(N_2) = 0.11 \pm 0.01$, and $G(N_2H_4) = 0.305 \pm 0.01$ within (2–150) $\times 10^{19}$ eV ml^{-1}; and $G(H_2) = 0.74 \pm 0.03$, $G(N_2) = 0.18 \pm 0.01$, and $G(N_2H_4) = 0.26 \pm 0.03$ in the range (150–500) $\times 10^{19}$ eV ml^{-1}. The spectrum recorded corresponds to the weak absorption of hydrazine (ϵ_{247nm} 2.5 ± 0.5 M^{-1} cm^{-1}) and the azide formation is then negligible, a conclusion which is also expected from the material balance. Solutions of N_2H_4 in liquid ammonia irradiated at room temperature give absorption bands in the uv. These are the sums of the optical densities of N_2H_4 which still remains after partial decomposition and the optical densities of a band which increases and is attributed to the azide ion N_3^- ($G(N_3^-) = 0.17 \pm 0.02$ at low doses). The conclusion is that N_3^- is formed from a secondary decomposition of N_2H_4 by the primary radical ^TNH. This mechanism holds in the radiolysis of initially pure ammonia. The azide yields provided by the spectrophotometric method in complement to those of other products are used to deduce some primary radical yields.

Introduction

It is not necessary to insist on interest for the understanding of fundamental processes of the interaction of radiation with liquids, to be able to compare various solvents. In the case of ammonia, certain important aspects of mechanisms had to be clarified.

Although several studies[1-4] seem to have confirmed that ammonium azide is one of the radiolytic products of liquid ammonia, there is not much agreement on the conditions of the formation of this compound. In particular, Sutherland and Kramer[2] found, at low doses and at 20 °C, molecules with -N=N- bonds such as N_4H_4 (or N_3H_3 or N_2H_2) while we found that NH_4N_3 appears only above a dose of 3×10^{19} eV ml^{-1}.[1] The results of radiolysis at low temperatures are even more scarce apart from those of the recent study by Blum and Broszkiewicz[3,4] who also conclude that over a wide pH range the formation of NH_4N_3 starts at low doses. Depending on the results which are accepted even the type of the very initial reactions may be quite different and the primary yields would be consequently affected. In one case, molecules with three or more atoms of nitrogen would result from reactions between the primary species before the diffusion of the spurs,[2] whereas in the other case, NH_4N_3 would be formed by secondary reactions of the radicals with stable products which have been accumulated.[1] We have therefore undertaken this study again by a more direct method rendered possible by the use of pressure resistant quartz optical cells to record the absorption spectra of liquid ammonia irradiated progressively.

For the study at low temperature, where data are scant,[3,5] we have added the usual determinations of radiolytic products in order to obtain the yields of the transient species before diffusion. Using pulse radiolysis,[6] we have already measured the yield $G_{e_{am}^-}$ at −50 °C, but with the results presently available it is difficult to obtain the yields of the oxidizing species NH_2 or ^TNH as well. Nevertheless, the conclusions deriving from the results of stationary radiolysis, as in the case of room temperature studies, enable us to write relations between the radical yields and hence calculate their values.

In the case of pulse radiolysis we see bands which could belong to stable products such as N_2H_4, NH_2^-, and N_3^- for which the yields are not well known. Therefore we are interested in determining if the observed bands are due to these products or due to some other intermediate species.

Experimental Section

Methods of purifying ammonia are described in ref 7. The pure ammonia is then condensed in the side arm of quartz cells with thick (10 mm) optical windows[8] which withstand internal pressures up to 20 atm. Solutions were prepared by placing a known amount of solute in the side arm, then condensing the ammonia and sealing off the cell. Some of these cells had another side arm with a tapered joint ending in a thin capillary tube, which allowed us to extract the gases for analysis and seal the cell again.

Sodium azide (Merck 99%) was used as supplied. Hydrazine hydrate (Prolabo 95%) was refluxed on potassium hydroxide under argon before distillation into the cell.

A double beam Beckman DK-1A spectrophotometer was used to record the spectra. The reference cell contained liquid ammonia. Both cells were enclosed in a box in which cold nitrogen gas could reduce the temperature to −80 °C. A 600 Ci source of ^{60}Co was used for the irradiations. The dose rate determined using a Fricke dosimeter and accounting for the electron density of liquid ammonia relative to water was found to be of the order of 10^{19} eV h^{-1} ml^{-1} of NH_3.

The Suprasil optical windows became slightly colored after long irradiation. The windows were annealed thermally to remove the color while the solution was kept frozen in the side

arm. The cell was then slowly warmed to the appropriate temperature for the spectrophotometric measurement.

Chemical analysis or gas chromotography were used[7] to analyze the irradiation products. The determination of N_2H_4 was checked on blanks containing azide ions. It was found that the presence of azide ions does not affect the chemical determination of N_2H_4.

Results and Discussion

A. *Radiolysis of Pure Ammonia.* (a) *Irradiation at Room Temperature.* We first followed the appearance of an absorption spectrum from 360 to 230 nm in an initially pure sample of liquid ammonia irradiated at 20 °C. The lower limit of the wavelength measured was 230 nm due to the strong absorption of NH_3 at this wavelength. It was verified that in this range there was no absorption before irradiation. As long as this dose is lower than 2×10^{19} eV ml^{-1} no new absorption was observed but above this value a uv band appears of which the maximum is masked by the absorption of the solvent (Figure 1). The intensity of this absorption increases with the time of irradiation and, in Figure 2, we have plotted the variation of the optical density measured at 247 nm vs. dose. Following an induction period the optical density increases rapidly, then more slowly from $\sim 5 \times 10^{20}$ eV ml^{-1}.

Chemical analysis at each dose gives us the concentration of radiolytic products. We can determine the contribution of hydrazine to the spectrum after recording spectra with known amounts of hydrazine in liquid ammonia. The absorption spectra of a 7.5×10^{-2} M solution of N_2H_4 at −50 and 20 °C are given in Figure 3. They show that the extinction coefficients are quite low, i.e., $\epsilon_{N_2H_4,247nm}$ 2.5 ± 0.5 M^{-1} cm^{-1} at −50 °C and 15.7 ± 0.6 M^{-1} cm^{-1} at 20 °C, nearly equal to the value found for N_2H_4 in the gas phase.[9] These extinction coefficients are too low to allow the assignment of the absorption curve of Figure 1 to hydrazine, since even with doses above 3×10^{19} eV ml^{-1} the concentration formed is limited to 5×10^{-5} M.[5] Several authors[1,2] have postulated the formation of NH_4N_3. Therefore we studied the spectrum of the N_3^- anion in liquid NH_3.

Figure 4 shows the spectra of a 2.4×10^{-3} M NaN_3 solution at several temperatures. The characteristic band adjoins that belonging to the solvent. The azide ion dissolved in liquid ammonia absorbs in the same spectral region as its aqueous solution for which the spectrum is attributed partly to charge transfer to solvent (CTTS) process.[10] The shift which we observed as a function of temperature suggests that the same process occurs in liquid ammonia. The spectrum has the same appearance as that of the irradiated sample, but the extinction coefficient is much higher than that of N_2H_4: $\epsilon_{N_3^-,247nm}$ 1380 ± 30 m^{-1} cm^{-1} at 20 °C and 430 ± 50 M^{-1} cm^{-1} at −47 °C.

Assuming that the spectrum observed is entirely due to the radiolytic formation of NH_4N_3, then the calculated amount formed satisfactorily completes the material balance of the products. At doses below 3×10^{19} eV ml^{-1} for which the quantities of H_2, N_2, and N_2H_4 correspond to a complete material balance (insert Figure 2) the concentration of N_3^- will be in fact negligible; between 3×10^{19} and 5×10^{20} eV ml^{-1}, $[N_3^-]$ would increase quickly and $G(N_3^-) = 0.05$ according to

$$G(H_2) = G(N_2H_4) + 3G(N_2) + 4G(NH_4N_3) \quad (1)$$

For doses above 5×10^{20} eV ml^{-1} the yield decreases notably, but we do not have sufficient data of $G(H_2)$ and $G(N_2)$ to be able to calculate a precise material balance. We therefore assign the observed absorption to N_3^-. The accumulation of the associated cation NH_4^+ implies an increasing acidity of the medium. Thus, our direct spectrophotometric measurements on the liquid samples at low dose contradict the results of Sutherland and Kramer[2] who found molecules with –N=N– bonds from 3.6×10^{17} eV ml^{-1}.

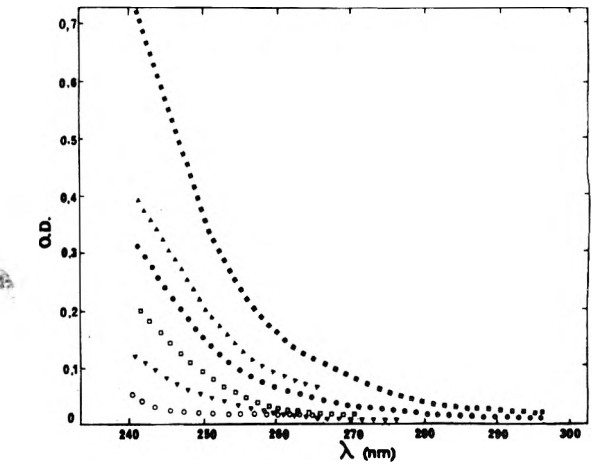

Figure 1. Absorption spectra of liquid ammonia irradiated at different doses (T_{irr} = 20 °C, optical path 2.5 cm): O, 4×10^{19} eV ml^{-1}; ▼, 7×10^{19}; □, 1.2×10^{20}; ● 1.6×10^{20}; △, 2.6×10^{20}; ■, 7.3×10^{20}.

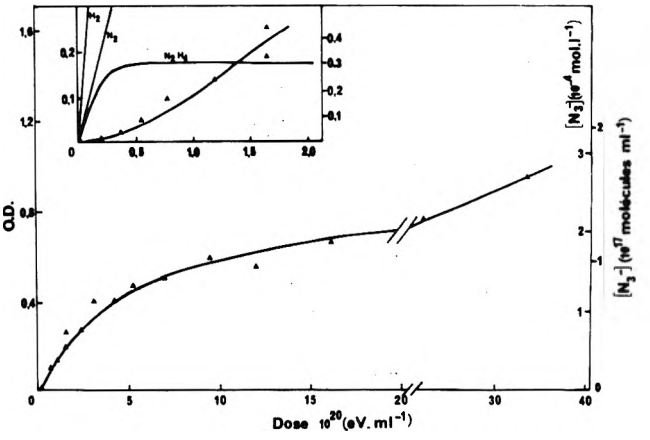

Figure 2. Variation of absorption measured at λ 247 nm with dose; T = 20 °C, optical path 2.5 cm. Insert shows comparison at low doses of spectrophotometric results with analyses of H_2, N_2, and N_2H_4.[1]

(b) *Irradiation at Low Temperature.* Figures 5 and 6a show the formation of the products H_2, N_2, and N_2H_4 in liquid ammonia irradiated at −55 °C. Table I presents the yields as well as those published by other authors.

Measurements of the spectra in the same wavelength range, taken at room temperature after irradiation at low temperature, show that the absorption is negligible up to doses as high as 5×10^{20} eV ml^{-1}. Even at higher doses where the absorption increases linearly, this increase is much less pronounced than for irradiation at 20 °C. The spectra resemble those found for calibration either of N_2H_4 or N_3^-. Figure 6b shows the variation of the optical density at 247 nm determined at 20 °C after warming the sample. We have also recorded spectra of irradiated samples at an irradiation temperature of −55 °C in order to detect unstable radiolytic products which could be decomposed during warming but we found no difference between these spectra and those recorded after warming.

If we calculate the absorption corresponding to the hydrazine formed by radiolysis (from Figure 6a), allowing for the uncertainties in $G(N_2H_4)$ and $\epsilon_{N_2H_4}$ we obtain the shaded zone

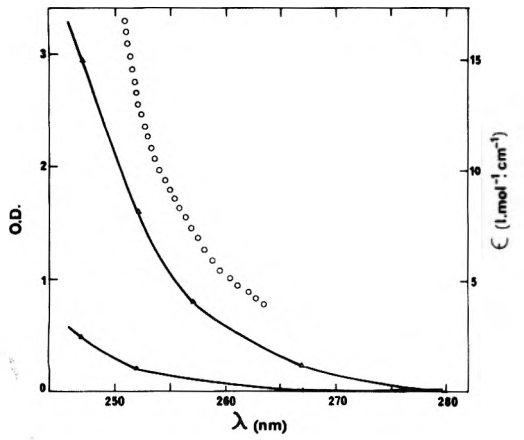

Figure 3. Calibration spectra of hydrazine in liquid ammonia solutions (7.5×10^{-2} M, optical path 2.5 cm): △, 20 °C; ▲, −50 °C (corrected for density variation); O, N_2H_4 in gas phase.[9]

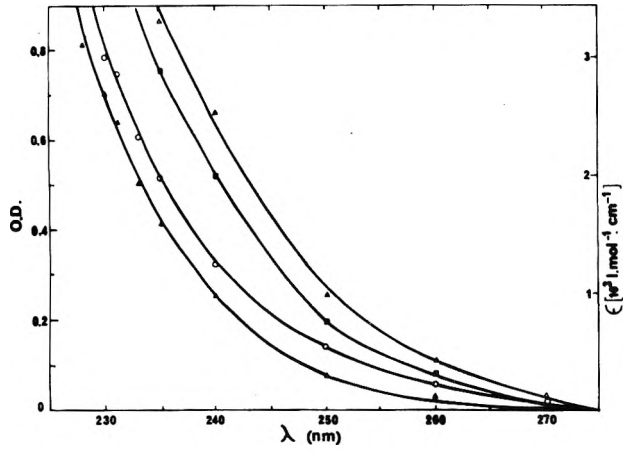

Figure 4. Calibration spectra of N_3^- in liquid ammonia solution (2.4×10^{-3} M, optical path 2.5 cm): △, 20 °C; □, 2 °C; O, −32 °C, ▲, −47 °C (corrected for density variation).

of Figure 6. If the absorption in Figure 6b were due solely to the azide ion then its yield would be at least a factor of 10 less than that found by Blum and Broszkiewicz[3,4] and would thus be entirely negligible in the material balance. Considering the form, the intensity, and the shift of the spectrum with temperature, we conclude that the absorption is due only to hydrazine. Let us point out that Blum and Broszkiewicz found, by polarographic measurements, $G(N_3^-)$ values giving a complete material balance with the other products. Unless the difference in temperature of radiolysis is responsible we cannot at present propose any explanation for the apparent disagreement between the results of Blum and Broszkiewicz and ours in view of the fact that both series give good material balance. We cannot discard the catalytic action of some impurity but our direct, nondestructive, method of observation of the azide ion avoids any ambiguity arising from chemical analysis.

B. *Hydrazine–Ammonia Solutions Irradiated at Room Temperature.* During the radiolysis of pure ammonia at 20 °C, we have seen that the appearance of the azide ion occurs above 3×10^{19} eV ml^{-1} and is concomitant with the decrease in the formation rate of hydrazine. This suggests that the azide ion is a radiolytic decomposition product of hydrazine and we have already given a hypothesis[1] based on the defect of the material balance observed for doses above 3×10^{19} eV ml^{-1}. Therefore it was interesting to study again the radiolysis of

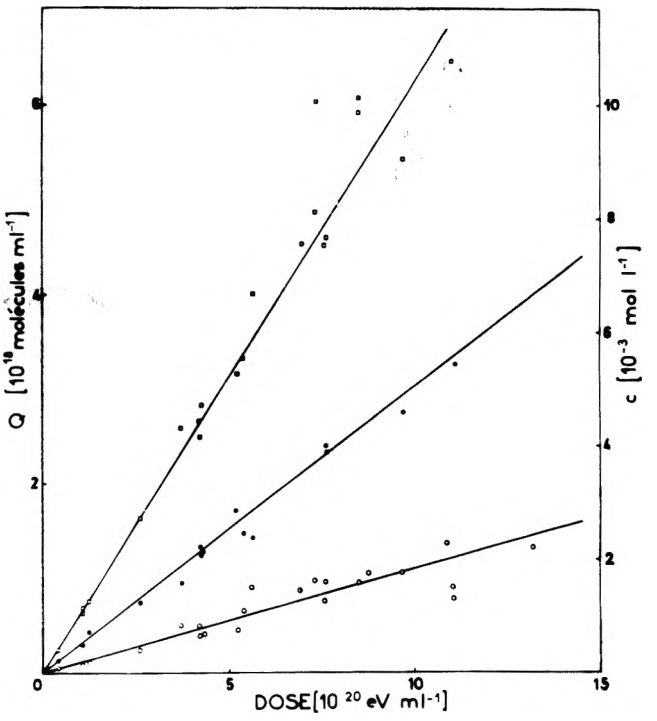

Figure 5. Products of the radiolysis of liquid ammonia as a function of dose ($T_{irr} = -55$ °C): O, N_2; ●, N_2H_4; □, H_2.

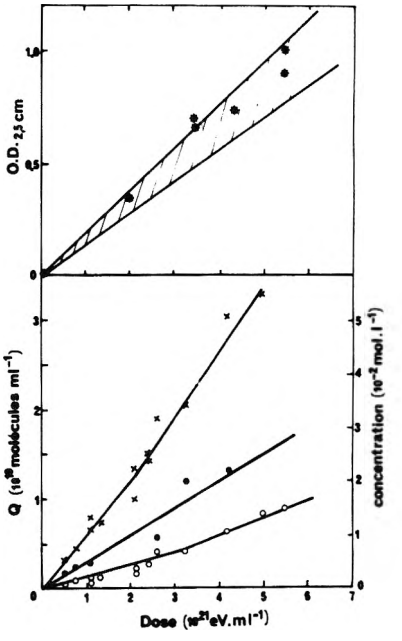

Figure 6. Products of the radiolysis of liquid ammonia at high dose ($T_{irr} = -55$ °C, optical path 2.5 cm): lower curve: O, N_2; ●, N_2H_4; ×, H_2; upper curve: *, optical density (measured at 247 nm and 20 °C) as a function of dose; shaded zone: calculated optical density corresponding to the absorption of N_2H_4 (ϵ_{247nm} 15.7 ± 0.6 M^{-1} cm^{-1}).

solutions of hydrazine with our spectrophotometric method. In previous studies[5] it was difficult to prepare pure solutions of hydrazine. Also we could not precisely analyze N_3^- in the presence of N_2H_4. The quantities of azide were calculated from the formation of other products and the disappearance of hydrazine. This inaccurate method explains the dispersion of results previously obtained.

The technique we now employ gave more precise results.

TABLE I: Radiolysis of Liquid Ammonia at Low Temperatures

Doses, 10^{19} eV ml^{-1}	T_{irr}, °C	$G(H_2)$	$G(N_2)$	$G(N_2H_4)$	$G(N_3^-)$	$G(N_3^-)$ calcd	Ref
10–150	−70	0.64	0.12	0.18		0.025	11
	−26	0.61	0.16	0.07		0.02	
0.2–11.5	−75	0.51	0.17				12[a]
	−55	0.58	0.2				
3.2–20	−72	0.85 ± 0.04	0.12 ± 0.01	0.15 ± 0.02	0.05 ± 0.02	0.07 ± 0.02	4
Up to 6[b]	−72	0.80 ± 0.04	0.04 ± 0.01	0.23 ± 0.04		0.11 ± 0.03	16
2–150	−55	0.61 ± 0.02	0.11 ± 0.01	0.305 ± 0.01		0	This
150–500	−55	0.74 ± 0.03	0.18 ± 0.01	0.26 ± 0.03	$\leq 3 \times 10^{-3}$	0	work

[a] Values obtained from Figure 1 of this reference. [b] Pulse radiolysis by 13-MeV electrons.

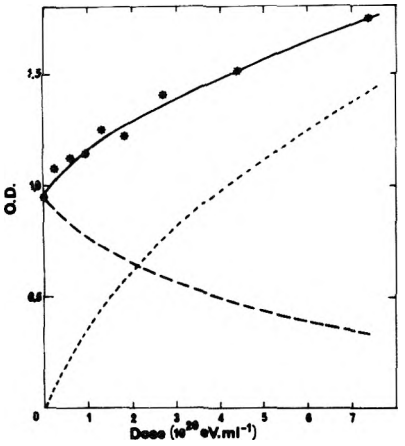

Figure 7. Radiolysis at 20 °C of a 2.3 × 10^{-2} M solution of N_2H_4 in liquid ammonia (optical path 2.5 cm): *, OD_{247nm} as a function of dose; ——, $OD_{N_2H_4}$ calculated from decomposition curves determined by chemical analyses; ·····, difference between the preceding curves, attributed to N_3^-.

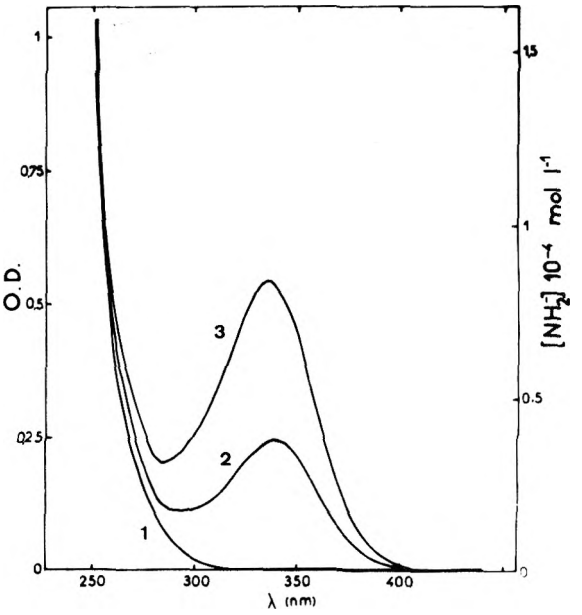

Figure 8. Radiolysis at 20 °C of a 1.1 × 10^{-2} M solution of NaN_3 in liquid ammonia (optical path 0.1 cm): (1) spectrum before irradiation; (2) spectrum after irradiation, dose 1.8 × 10^{20} eV ml^{-1}; (3) spectrum after irradiation, dose 3.6 × 10^{20} eV ml^{-1}.

As previously mentioned, ammonia irradiated at low temperature accumulates hydrazine and by this means we prepared solutions of very pure hydrazine in liquid ammonia. After irradiation at −55 °C the gases were extracted and the sample tube sealed off again. Then the spectrophotometric method allowed us to observe directly the formation of N_3^-, the extinction coefficient of which is two orders of magnitude higher than that of N_2H_4. We then used the sample which had already been studied at low temperature (Figure 6b) and for which the concentration of N_2H_4 had been measured as 2.34 × 10^{-2} M from its absorption at zero dose (Figure 7). This sample was irradiated at 20 °C. The absorption at 247 nm is given as a function of dose on Figure 8. The shape of the spectrum is similar to those of N_2H_4 and N_3^-.

Chemical analysis of other samples prepared in the same way show that hydrazine is destroyed during the radiolysis according to our previous results.[5] The value of $\epsilon_{N_2H_4}$ at 247 nm enables us to calculate the contribution of hydrazine to the absorption. Thus we obtain the broken line curve which subtracted from the line directly observed gives the dotted curve representing a species other than hydrazine and which increases with dose.

If we assign this absorption to the N_3^- ion, the quantities calculated using $\epsilon_{N_3^-}$ have values leading to a satisfactory material balance of the decomposition of N_2H_4 and the formation of the gases H_2 and N_2. Hence we can admit that azide ions are formed during the radiolysis of solutions of hydrazine and this occurs with an initial yield much higher ($G_{N_3^-}$ = 0.17 ± 0.02) than in the solvent alone, confirming the formation of azide from hydrazine. We then understand why, during the radiolysis of ammonia at 20 °C, $[N_3^-]$ is higher when more hydrazine has accumulated. In preceding papers[4,9] we have proposed the following mechanism which is the only one which can account for the invariance of $G(N_2)$ and $G(H_2)$ when azide ions begin to be formed in the pure solvent. At weak doses, the NH radicals in the triplet state (^{T}NH) insert themselves into NH_3 giving N_2H_4 and then react progressively with N_2H_4 which accumulates.

$$^T\text{NH} + NH_3 \rightarrow N_2H_4 \quad (2)$$

$$^T\text{NH} + N_2H_4 \rightarrow N_2H_2 + NH_3 \quad (3)$$

$$2N_2H_2 \rightarrow N_4H_4 \rightarrow N_3^- + NH_4^+ \quad (4)$$

Studying the radiolytic decomposition products of N_2H_4 we have found that their yields were constant in the range 2 × 10^{-3} to 2 × 10^{-2} M N_2H_4 which is that given in Figure 7. Hence the capture of ^{T}NH according to reaction 2 would be total giving a yield $G_{^T\text{NH}} = 2G(N_3^-) = 0.34 \pm 0.04$. This value is in excellent agreement with those obtained using other reducing scavengers[5,13] and provides strong support of the mechanism given above for the formation of azide.

The possible intermediate species (diimide, tetrazene, . . .) are unfortunately too unstable to be observed at room temperature.[14] Furthermore, as described above, no transient spectrum has been observed after irradiation at low temperature but this result is consistent with the absence of N_3^- under these conditions and implies that reaction 2 is predominant compared to reaction 3 even at high N_2H_4 concentration.

C. *Azide–Ammonia Solutions Irradiated at Room Temperature.* These results led us to examine the radiolysis of azide solutions which were prepared by dissolving crystals of NaN_3 in liquid ammonia. Figure 8 presents the spectra at 20 °C of a 1.1×10^{-2} M solution before and after irradiation. We see the appearance of a new uv band corresponding to the formation of the amide ion for which the spectrum has a maximum at 345 nm (ϵ_{345nm} 2600 M^{-1} cm^{-1})[15] and with a yield $G(NH_2^-) = 0.50 \pm 0.10$ up to doses as high as 7×10^{20} eV ml^{-1}.

Chemical analyses made on solutions irradiated with 3 to 25×10^{19} eV ml^{-1} gave the molecular yields $G(H_2) = 1.15$, $G(N_2) = 1.05$, and $G(N_2H_4) = 0$. The charge balance can be written $G(-N_3^-) = G(NH_2^-)$ and one obtains a satisfactory material balance

$$G(H_2) + 4G(-N_3^-) = 3G(N_2) + G(N_2H_4) \quad (5)$$

An experiment was done to observe the conjugate action of scavengers: sodium azide (2×10^{-2} M) as reducing agent and copper (II) perchlorate (6×10^{-3} M) as oxidizing agent. The results show that the capture yields are lower than with solutions containing only one of the scavengers, suggesting a higher proportion of back reaction in the case of the mixture.

D. *Radical Yields at Low Temperatures.* By comparing the results obtained at low temperature in the absence and presence of reducing scavengers we have found[13] the following values of primary yields: $G_{H_2} = 0.56$, $G_{N_2H_4} = 0.40$, and $G_{^TNH} = 0.13$. As at room temperature, we conclude that the ^TNH inserts into the solvent molecule to give N_2H_4 (reaction 2) unless it is scavenged by a strongly reducing solute such as Cu^+ or e_{am}^-.

If we represent the formation of primary species by

$$NH_3 \rightsquigarrow H_2, H, e_{am}^-, NH_4^+, N_2H_4, NH_2, {}^TNH \quad (0)$$

the material balance gives

$$2G_{H_2} + G_H + G_{e_{am}^-} = 2G_{N_2H_4} + 2G_{^TNH} + G_{NH_2} \quad (6)$$

The reaction of hydrogen atoms H

$$H + N_2H_4 \rightarrow H_2 + N_2H_3 \quad (7)$$

becomes more and more important when the concentration of N_2H_4 increases, i.e., in ammonia irradiated to a high dose (Figure 6b). One then obtains $G(H_2) = 0.74$ constant from 2 to 5×10^{-2} M N_2H_4. Assuming a total capture of H atoms one finds $G_H = 0.18$. Pulse radiolysis studies[6] have shown that the yield of solvated electrons at low temperatures is close to $G_{e_{am}^-} = 3.0$. Hence $G_{NH_2} = 3.2$. From these results at low temperature the yields of all the primary species of reaction 0 have been obtained.

To conclude, the direct observation by spectrophotometry has allowed us to reexamine problems which were not possible to solve due to limitations imposed by the analytical methods. We were able to determine the azide ion in the presence of hydrazine spectrophotometrically and to find new evidence which supports certain mechanisms. We have been able to complete the list of yield values.

Acknowledgment. We wish to thank Mrs. M. Miñana for her technical assistance. We are indebted to Dr. J. Sutton for his fruitful remarks and discussions throughout this investigation.

References and Notes

(1) J. Belloni, *J. Chim. Phys.*, **9**, 1281 (1966).
(2) J. W. Sutherland and H. Kramer, *J. Phys. Chem.*, **71**, 4161 (1967).
(3) A. Blum and R. K. Broszkiewicz, *Radiochem. Radioanal. Lett.*, **12**, 15 (1972).
(4) A. Blum and R. K. Broszkiewicz, *Radiochem. Radioanal. Lett.*, **14**, 309 (1973).
(5) J. Belloni, *Actions Chim. Biol. Radiat.*, **15**, 47 (1971).
(6) J. Belloni, P. Cordier, and J. Delaire, *Chem. Phys. Lett.*, **27**, 241 (1974).
(7) J. Belloni, *Int. J. Radiat. Phys. Chem.*, **1**, 449 (1969).
(8) J. Belloni and E. Saito, "Electrons in Fluids", J. Jortner and N. R. Kestner, Ed., Springer-Verlag, Berlin, 1973, p 461.
(9) C. Willis and R. A. Back, *Can. J. Chem.*, **51**, 3605 (1973).
(10) I. Burak and A. Treinin, *J. Chem. Phys.*, **39**, 189 (1963).
(11) Yu. A. Sorokin, V. I. Tsivenko, and S. Ya. Pshezhetskii, *Zh. Fiz. Khim.*, **37**, 1871 (1963).
(12) F. S. Dainton, T. Skwarski, D. Smithies, and E. Wezranowski, *Trans. Faraday Soc.*, **60**, 1068 (1964).
(13) M. O. Delcourt and J. Belloni, *Radiochem. Radioanal. Lett.*, **13**, 329 (1973).
(14) R. A. Back and C. Willis, *Can. J. Chem.*, **52**, 2513 (1974).
(15) J. Belloni and J. Fradin de la Renaudiere, *Int. J. Radiat. Phys. Chem.*, **5**, 23 (1973).
(16) A. Blum, *J. Chem. Soc. Faraday Trans. 1*, **71**, 2299 (1975).

Carbon-13 Spin–Lattice Relaxation Study of the Molecular Dynamics of 10-Methylnonadecane

J. R. Lyerla, Jr.,* and T. T. Horikawa

IBM Research Laboratory, San Jose, California 95193 *(Received January 7, 1976)*

Publication costs assisted by IBM Corporation

Carbon-13 spin–lattice relaxation times (T_1) have been measured for the 11 magnetically distinct carbons of 10-methylnonadecane over the temperature range ca. 10–90 °C. Effective correlation times, τ_{eff}, have been determined from the T_1 data and used to discuss the motional features of the C_{19} alkane chain. The τ_{eff} values for the methylene carbons of 10-methylnonadecane follow a temperature dependence defined by "apparent" activation energies that range from 5.1 to 5.5 kcal/mol. The methyl carbons' τ_{eff} values have a temperature dependence associated with lower activation parameters, and the reorientation rates of these carbons have been shown to be related to the potential barriers to methyl rotation. Collectively, the temperature dependence of the τ_{eff} data and the comparative values of τ_{eff} along the chain are consistent with a model of molecular motion in which overall and various internal reorientational modes contribute to the carbon relaxation in a 19-carbon alkane.

Introduction

It was well established[1-5] that carbon-13 spin–lattice relaxation times (T_1) can be used to obtain information on the molecular dynamics of compounds in the liquid state. However, like other methods for assessing molecular motion, the rotational correlation times derived from the T_1 data, in general, yield a quantitative description of the molecular dynamics only for rigid spherical systems or rigid axially symmetric ellipsoidal systems. For the case of a rigid spherical molecule, a single rotational correlation time, τ_r, characterizes the isotropic reorientation of a C–H vector and is equated with the rotational diffusion coefficient of the sphere via the relationship $\tau_r = (6D)^{-1}$. For the rigid ellipsoid, τ_r can be related to rotational diffusion constants parallel and perpendicular to the unique axis.

With enhanced flexibility in the molecular system, the description of the reorientational motion of the C–H vector becomes quite complex as multiple internal as well as overall molecular motions contribute to the reorientation process. Thus, for a complex molecular system such as a polymer chain, a distribution of correlation times (τ_K)[6,7] is required to describe the motion of a C–H vector. In such instances, the correlation time determined experimentally from the T_1 value for a given carbon is designated an "effective correlation time" (τ_{eff}) and must be viewed as a weighted average of the correlation times for the individual motions that reorient the C–H vector of concern, i.e., $\tau_{eff} = \Sigma_K C_K \tau_K$, where the C_K are orientation and probability dependent coefficients. Rigorous interpretation of τ_{eff} is, therefore, dependent upon detailed models of chain motion.

One approach to providing the framework for structuring models of chain motion is the qualitative assessment of ^{13}C relaxation data in appropriate model compounds for trends which reveal the general features of chain molecular dynamics. Thus, the n-alkanes, which serve as models for understanding the segmental motion in the backbone of polymer molecules and as models for side-chain motion in biological structures (e.g., the alkyl chains of lecithin vesicles[8]), have been the subject of several investigations by ^{13}C relaxation.[9-11] To date, T_1 data on the linear hydrocarbons through eicosane ($C_{20}H_{42}$) have been obtained in the temperature range 30–40 °C. From these results important features of alkyl chain motion have been delineated; however, additional T_1 results on such compounds are required to complete even a qualitative description of the molecular dynamics. In particular, temperature-dependent relaxation studies, which can provide information on activation energies for various types of motions of the alkyl chain, are required. In addition, information on the reorientation process for C–H vectors of carbons in the central part of the alkane chain for compounds larger than decane is still required because methylene carbons beyond carbon three from the end methyl are not magnetically distinct in the n-alkanes.

In an attempt to provide information on the thermal behavior of ^{13}C relaxation times for alkane compounds, we have determined the T_1 values of 10-methylnonadecane over the temperature range ca. 10–90 °C. The rationales for studying this compound are twofold. First, the 19-carbon chain is of sufficient length that short-order segmental motions similar to those occurring in a polymer chain may be present. Secondly, the chemical shift perturbation caused by the methyl branch allows resolution of carbon resonances over the length of the chain and thus enables temperature-dependent relaxation data to be ascertained at each carbon site along the alkyl chain.

Results

Figure 1 shows the proton-decoupled ^{13}C spectrum and chemical shift assignments for neat 10-methylnonadecane. The resonance assignments were obtained straightforwardly from (1) C–H multiplet structure in the coupled spectrum, (2) the regressional analysis parameters derived by Grant and Paul[12] for linear and branched alkanes, and (3) the results of Carmen et al.[13] on ^{13}C chemical shifts of branched alkanes. The ^{13}C spin–lattice relaxation times at ca. 10° intervals over the 80° temperature range were determined from inversion-recovery Fourier transform spectra[14] for each of the 11 resolved carbons and are listed in Table I.

To complement the relaxation measurements, ^{13}C-{^1H} nuclear Overhauser enhancements (NOE) were also determined for each resolved carbon line, with the result that a

TABLE I: Temperature Dependent ^{13}C Spin–Lattice Relaxation Times[a] for 10-Methylnonadecane

	Carbon in chain										
Temp, °C	1,19	2,18	3,17	4,16	5,15	6,14	7,13	8,12	9,11	10	10-Me[b]
10	2.0	1.0	0.67	0.48	0.41	0.37	0.30	0.27	0.22	0.37	0.60
17	2.5	1.3	0.94	0.64	0.51	0.45	0.41	0.32	0.28	0.46	0.73
31	3.3	2.0	1.4	0.96	0.80	0.72	0.58	0.53	0.45	0.72	1.0
38	3.8	2.4	1.7	1.2	0.96	0.86	0.74	0.63	0.52	0.85	1.2
50	4.8	3.3	2.4	1.6	1.4	1.2	1.1	0.90	0.83	1.1	1.6
61	5.9	4.3	3.1	2.2	1.7	1.5	1.4	1.3	1.0	1.5	2.0
70	6.8	5.2	3.6	2.6	2.3	2.0	1.8	1.5	1.2	1.9	2.4
80	7.9	6.1	4.4	3.2	2.6	2.3	2.0	1.8	1.5	2.4	2.8
90	10.0	7.8	5.3	3.8	3.2	2.9	2.6	2.4	1.9	3.1	3.2

[a] In seconds. [b] Internal methyl carbon.

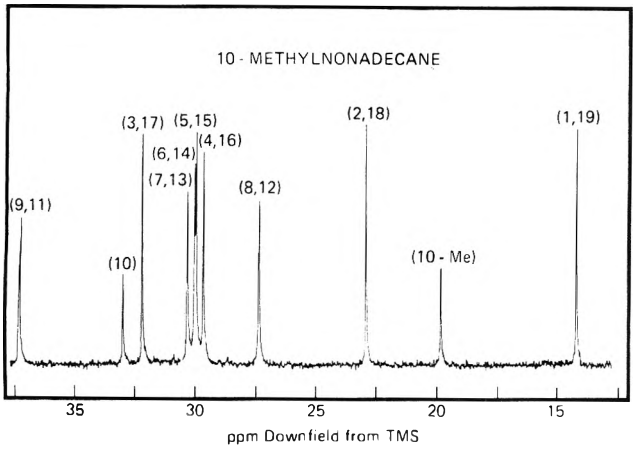

Figure 1. The Fourier transform proton-decoupled carbon-13 spectrum of 10-methylnonadecane at 38 °C. Chemical shifts are given in ppm downfield from external TMS. Assignments of the resonance lines to carbons in the alkyl chain are given in parentheses above the respective resonance lines.

maximum NOE[15] (2.98 ± 0.15) was found for all carbons at each temperature. The NOE results are consistent with the domination of the carbon spin–lattice relaxation in 10-methylnonadecane by the C–H heteronuclear dipolar mechanism[2-4] and indicate that rotational reorientation is such that the extreme narrowing condition is valid, i.e., $(\omega_H + \omega_C)^2\tau_r^2 \ll 1$ where ω_H and ω_C are the respective Larmor frequencies. Under these conditions the effective rotational correlation time, τ_{eff}, for the vector connecting the directly bonded C and H atoms is given by[11,16]

$$\tau_{eff} = r_{CH}^6/KT_1N_H \quad (1)$$

where r_{CH} is the internuclear distance (1.09 Å), T_1 is the spin–lattice relaxation time from Table I, N_H is the number of attached protons, and K is a constant equal to 3.56×10^{10} Å^6 s^{-2}. Values of τ_{eff} calculated from eq 1 for the C–H vectors of 10-methylnonadecane are presented in Table II.[17]

The several obvious trends in the τ_{eff} data include: (1) At each temperature, there is a progressive decrease in τ_{eff} values from the central methine carbon outward to the chain ends; (2) For a given carbon of the chain, the τ_{eff} value decreases with increasing temperature; (3) Over the 80° temperature differential, the τ_{eff} values for end-chain methyl and internal methyl decrease by factors of 5 and 6, respectively, while the τ_{eff} changes for each methylene and the methine carbon fall into the range of an 8.0–8.5 decrease; (4) The τ_{eff} values for the various methylene carbons and the methine carbon appear to maintain a consistent relationship over the temperature range studied, e.g., the ratio of τ_{eff} values for methine and first methylene of the chain is about 5.2 at each temperature.

To determine if the thermal behavior of τ_{eff} (over this limited range of temperature) could be represented by an Arrhenian-type dependence, i.e.

$$\tau_{eff} = \tau_0 e^{\Delta E/RT} \quad (2)$$

(where τ_0 is a preexponential factor), the τ_{eff} results have been plotted vs. reciprocal temperature. Figure 2 displays the semilog plots for the methylene carbons and the methine, while Figure 3 shows the corresponding plots for the methyl carbons of the compound. In all cases, the data have been found to fit reasonably well to a temperature dependence defined by eq 2,[18] and the values of ΔE derived from least-squares analysis are given in Table III and Figure 3. As evidenced by the nearly parallel plots for the methylene carbons and methine carbon, the range of activation energies found for these carbons is quite limited (5.1–5.5 kcal/mol). However, the τ_{eff} data for the two methyl carbons were found to follow a temperature dependence governed by activation energies (given in Figure 3) about 1.0–1.5 kcal/mol lower than the methylene carbons.

To assist in the interpretation of the 10-methylnonadecane relaxation times and their temperature dependence, T_1 results on several other 20-carbon alkanes, which differed in the number and placement of methyl branches, were collected. Temperature-dependent T_1 and τ_{eff} data for n-eicosane above its melting temperature are given in Table IV. At all corresponding temperatures, the τ_{eff} data for the four end-chain carbons of n-eicosane are seen to mirror the behavior of their counterparts in 10-methylnonadecane. Additionally, T_1 and τ_{eff} data have been determined at 38 °C for the 20-carbon branched alkane, 2,6,11,15-tetramethylhexadecane (whose C-13 spectrum is presented in Figure 4).[19] The T_1 and τ_{eff} results for this compound along with τ_{eff} data on n-eicosane and 2-methyl- and 10-methylnonadecanes, at a comparable temperature, are listed in Figure 5 below the appropriate carbon of the skeletal diagram for each compound.

Discussion

In the studies on the n-alkanes, the correlation times (at 39 °C) were found (1) to increase from chain ends toward the center in each alkane, (2) to increase progressively for a given carbon as the chain length increases, and (3) to increase proportionately less at chain ends as the chain length increases.[9-11] These trends in the data suggested[11] a simplified

TABLE II: Calculated τ_{eff} Values[a] for 10-Methylnonadecane

	Carbon in chain										
Temp, °C	1,19	2,18	3,17	4,16	5,15	6,14	7,13	8,12	9,11	10	10-Me[b]
10	8.0	23.5	35.0	49.2	58.5	65.3	79.9	85.6	105	127	26.2
17	6.2	17.3	25.2	36.1	46.3	51.7	57.4	72.4	84.2	100	21.6
31	4.8	11.8	17.2	24.4	29.4	32.8	40.6	44.6	52.2	65.0	15.4
38	4.1	9.8	14.1	19.6	24.6	27.4	31.8	37.6	45.1	55.3	13.2
50	3.2	7.2	9.8	14.4	17.4	19.4	21.9	26.2	28.5	41.4	9.9
61	2.7	5.5	7.6	10.7	13.7	15.3	17.3	18.6	23.5	31.2	7.8
70	2.3	4.6	6.6	9.2	10.6	11.8	13.0	15.7	19.0	24.8	6.6
80	2.0	3.8	5.3	7.4	9.2	10.2	11.9	13.5	15.7	19.9	5.6
90	1.6	3.0	4.4	6.2	7.2	8.0	8.9	10.0	12.4	15.0	4.8

[a] In picoseconds. [b] Internal methyl carbon.

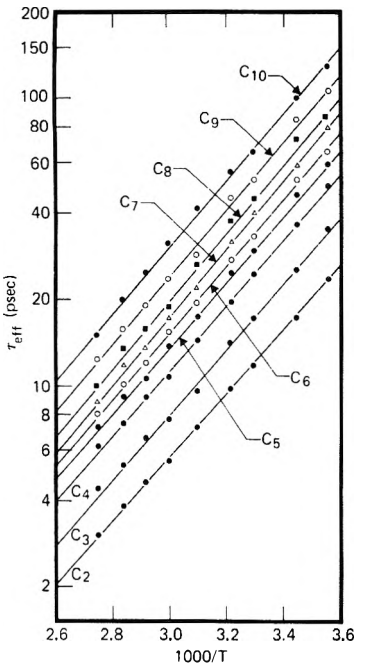

Figure. 2. Plot of the τ_{eff} values (in ps) for the methine and various methylene carbons of 10-methylnonadecane vs. reciprocal temperature.

model for alkane motion which provides a self-consistent framework for the analysis of the τ_{eff} data. In this model, the reorientation of a C–H vector is dependent upon an overall rotation of the molecule (considered rigid) with average rotational rate $(\tau_0)^{-1}$ and internal motion due to rotations about individual C–C bonds in the chain with rates $(\tau_i)^{-1}$. The effective rotation rate for a C–H vector is then given by

$$(\tau_{eff})^{-1} = (\tau_i)^{-1} + (\tau_0)^{-1} \quad (3)$$

where τ_i is understood to contain all internal reorientational modes. The overall motion (which is assumed independent of internal modes and vice versa) is a function of molecular weight and viscosity and subject to chain-length dependent, intermolecular barriers. In comparison, the internal motions originate from conformational changes and internal rotations within a conformation and are largely determined by intramolecular potential barriers that are independent, to a first approximation, of chain length.

A similar model of alkane motion is the basis for the more quantitative characterization of the *n*-alkane τ_{eff} data by Levine et al.[20] In this instance, calculations were carried out for a C–H vector subject to multiple internal motions and attached to an axially symmetric prolate ellipsoid (i.e., an all trans conformation was assumed). In the calculations, internal modes were considered to be independent of neighboring in-

TABLE III: Apparent Activation Energies[a] for Methylene and Methine Carbon Reorientation in 10-Methylnonadecane

Carbon	ΔE, kcal/mol	Carbon	ΔE, kcal/mol
C-2	5.1	C-7	5.5
C-3	5.2	C-8	5.5
C-4	5.2	C-9	5.4
C-5	5.3	C-10[b]	5.3
C-6	5.5		

[a] From least-squares analysis of temperature-dependent τ_{eff} data. [b] Methine carbon.

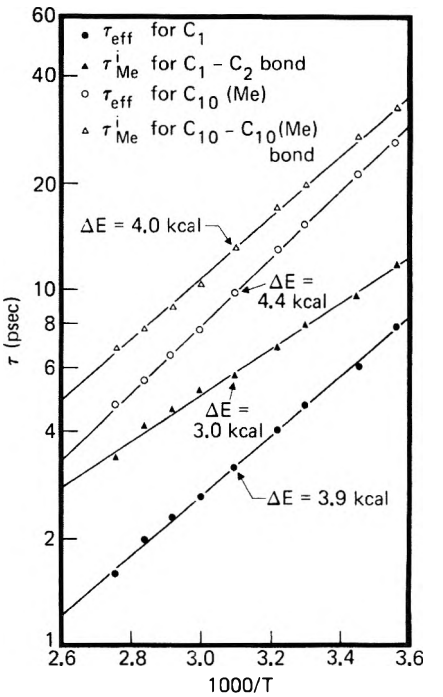

Figure 3. Plot of τ_{eff} values (in ps) for end-methyl and the internal-methyl carbons of 10-methylnonadecane vs. reciprocal temperature. Also plotted are the values of τ_{Me}^{i} for these carbons.

TABLE IV: Temperature Dependent ^{13}C Spin–Lattice Relaxation Times and τ_{eff} Values for Eicosane

Temp, °C	Carbon in chain									
	1,20		2,19		3,18		4,17		5–16	
39[a]	3.6[b]	(4.3)[c]	2.3	(10.4)	1.6	(14.4)	1.1	(21.4)	0.80	(29.5)
50	4.8	(3.3)	3.3	(7.1)	2.4	(9.8)	1.6	(14.4)	1.1	(21.4)
60	5.8	(2.7)	4.2	(5.6)	3.1	(7.6)	2.1	(11.2)	1.3	(18.6)
70	7.1	(2.2)	5.4	(4.4)	3.7	(6.4)	2.7	(8.7)	2.0	(11.9)
80	8.1	(1.9)	6.1	(3.9)	4.6	(5.1)	3.1	(7.6)	2.1	(11.2)
90	10.1	(1.6)	7.9	(3.0)	5.2	(4.6)	3.7	(6.4)	2.9	(8.1)

[a] Data taken from ref 11. [b] T_1 in seconds. [c] τ_{eff} in picoseconds.

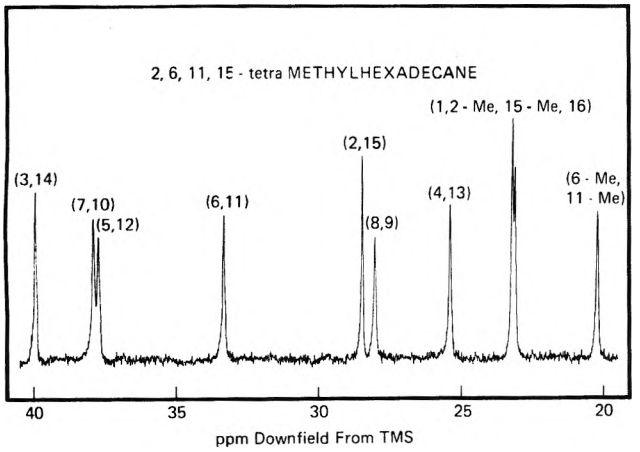

Figure 4. The Fourier transform proton-decoupled carbon-13 spectrum of 2,6,11,15-tetramethylhexadecane at 38 °C. Chemical shifts are given in ppm downfield from external TMS. Assignments of the resonance lines to carbons in the alkyl chain are given in parentheses above the respective resonance lines.

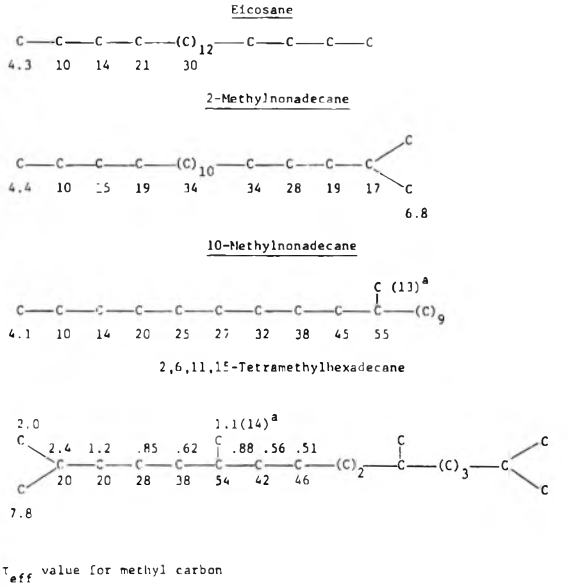

Figure 5. The τ_{eff} values for several 20-carbon alkanes at 38–39 °C. The τ_{eff} values (in ps) are listed below the respective carbon at each position in the skeletal structure of the alkane. The T_1 values in seconds for each carbon in 2,6,11,15-tetramethylhexadecane are listed above each carbon in this compound's skeletal structure.

teractions and to be governed by a stochastic rotational diffusion process. Calculations were also carried out for independent and correlated jump processes with the result that, while absolute values of internal rates differ from the stochastic model, trends in the values of the internal rates were unaffected.

In the context of eq 3, the gradation in τ_{eff} data along the length of the 10-methylnonadecane chain suggests that even in the central portion of the alkane chain there are internal reorientational motions of a comparable time scale to that for overall reorientational motion. However, as evidenced by the relative spacings of the plots in Figure 2, the gradient in τ_{eff} is not constant over the length of the chain. Instead, τ_{eff} increases rapidly for the first three methylene units of the chain, increases more slowly for carbons C_5 through C_7, and then increases sharply at C_9 and C_{10}. The small variation in effective correlation time for C_5 through C_7 may indicate that the τ_{eff} values for the central methylene units of an intermediate length alkane chain tend to plateau. The τ_{eff} results for 2-methylnonadecane (Figure 5) provide some support for this viewpoint. Unlike in *n*-alkanes, the C_5 carbon (at the substituted end of the chain) is resolvable from the other methylene carbons. The equivalence of the τ_{eff} value for this carbon with the "average" τ_{eff} for the ten nonresolved internal methylene units (C_6–C_{15}) is consistent with the correlation times of each of the nonresolved carbons being about equal. In addition, the experimental τ_{eff} value of 34 ps for these respective methylene units in 2-methylnonadecane is in accord with the 25–38-ps range for the C_5–C_8 carbons of 10-methylnonadecane. However, in 10-methylnonadecane the presence of the methyl branch apparently changes the reorientational characteristics at C_9 and C_{10} so that the leveling-off of τ_{eff} is not reached in this compound.

As isotropy of overall motion is assumed in eq 3, an estimate of τ_0 can be found from the Gierer–Wirtz[21] modification (the "microviscosity" correction) to the Stokes–Einstein formulation of rotational diffusion constants (D)

$$\frac{1}{6\tau_0} = D = \frac{1.15 \times 10^{10} \rho T}{M_w \eta} \qquad (4)$$

Assuming the viscosity and density data for *n*-eicosane[22] at 40 °C are not too different than that of either 2-methyl- or 10-methylnonadecane, a value of τ_0 = 72 ps is calculated[23] from eq 4. When this value is compared to the experimental τ_{eff} value of 34 ps, the result indicates that each C–H vector in the central portion of the C_{19} chain experiences not only the same degree of overall motion but also a similar degree of internal motion. The implied near equality in $(\tau_i)^{-1}$ values (see eq 3) for these methylene units could be explained by a scheme in which short segments of the chain participate in a cooperative internal reorientational process. Such chain lengths

could be as short as the so-called "crankshaft" segment.[24] The probability of any given methylene unit in the central portion of an n-alkyl chain being part of the crankshaft would be the same, and thus, on the average, the internal motion arising from this type of mechanism would be equivalent for each CH_2 unit.

In 10-methylnonadecane, the increase in τ_{eff} at the branch point of the chain and the neighboring methylene sites can be rationalized by a decrease in internal motion resulting from a reduced probability of forming a "kink" in the chain that must include the branched methyl carbon. An increased τ_{eff} value relative to those for neighboring methylene units is also found for the internal-methyl substituted carbon of 2,6,11,15-tetramethylhexadecane (Figure 5). Interestingly, the effective correlation time for this methine carbon at position six of the alkyl chain is the same as that for the methine carbon of 10-methylnonadecane which is at position ten. Such a result is also consistent with there being cooperative internal reorientation modes for methylene units in the central portion of the C_{19} alkane chain, as the probability change in formation of a "kink" in the chain would be independent of the position of methyl substitution (provided the substitution is not at the first few methylene units of the chain). Finally, the result that the ΔE values for the temperature dependence of τ_{eff} for carbons C_6 through C_{10} in 10-methylnonadecane are about the same is in accord with the relaxation of these carbons being controlled by the same types of reorientational processes.

The C–H vectors of methylene carbons near the chain ends, i.e., C_2–C_4, will undergo reorientation due to the motions discussed above, but also should have significant contributions to the relaxation by additional internal modes. Indeed if, as calculated above, τ_0 is equal to ca. 72 ps at 40 °C, then in 10-methylnonadecane, the τ_{eff} values for methylenes C_2 and C_3 are only slightly influenced by τ_0. This result is in accord with the calculations of Levine et al.[10] which indicate that in a large alkane the decay of the autocorrelation function (and therefore τ_{eff}) for end chain carbons is virtually independent of overall reorientation rate. In fact, the relatively large changes in τ_{eff} for carbons C_2 through C_4 indicate that the relaxation for these carbons is strongly influenced by rotational motion about the individual C–C bonds. Presumably, such rotations of end chain segments can occur in a smaller swept-volume of solution than that required for the cooperative internal rotational motion that dominates the $1/\tau_i$ contribution to $1/\tau_{eff}$ for the more internal methylenes. If the facility of rotation about the C–C bonds decreased to a great extent from the first methylene inward into the chain, such an effect might be evident in different thermal behavior of the τ_{eff} values along the nonadecane chain. There is a trend toward smaller ΔE values (Table III) for the temperature dependence for the first methylene relative to that for more interior CH_2 units; however, the effect is less than 0.5 kcal. Nonetheless, the influence on relaxation of rotations about the individual bonds at the chain end is evident when the effect of an isopropyl end group on the τ_{eff} values for carbons C_2 through C_4 of an alkyl chain is compared to the corresponding τ_{eff} data for a straight chain system. The result is the τ_{eff} value for the C_2 and C_3 carbons at the substituted chain end of 2-methylnonadecane are approximately equal to the τ_{eff} values for C_3 and C_4 carbons of n-eicosane and 10-methylnonadecane. This apparent correlation of τ_{eff} to the mass of the segment to be reoriented about the C–C bond argues strongly for the influence of such internal motions on the relaxation of the end methylene units of an alkyl chain.

The temperature dependence (Figure 3) of the τ_{eff} data for the two methyl carbons in 10-methylnonadecane are governed by ΔE values of 3.9 and 4.4 kcal/mol for end methyl and internal methyl, respectively. The different temperature dependence of the methyl carbons relative to the methylene carbons presumably arises from the fact that motion about the methyl–methylene or methyl–methine bond can take place within the molecular volume. Such internal motion would then depend only on the V_3 intramolecular potential barrier for methyl group reorientation. The values of the V_3 potential for methyl carbons in alkane compounds are usually less than the 5.1–5.5 kcal/mol ΔE values that characterize all the other reorientational motions in 10-methylnonadecane that can affect the reorientation of a methyl C–H vector. Thus, a lower value for the apparent activation energy would be expected when methyl reorientational motion affects the methyl relaxation. The different temperature dependence for the end-chain methyl relative to that of the methylenes is also consistent with Levine's et al.[10] result that a value for internal diffusion constant about the C_1–C_2 bond different than that of the other C–C bonds of an alkane chain was required to fit their relaxation data.

The above conclusions concerning the τ_{eff} data for the methyl carbons of 10-methylnonadecane can be in part substantiated by considering the following qualitative arguments. In the model of motion manifest in eq 3, the differences in effective rotational rates, i.e., $(\tau_{eff})^{-1}$, between terminal methyl and terminal methylene unit should reflect differences in internal reorientation rates for the respective C–H vectors (as it is assumed that overall motion is effectively isotropic). Because the methyl carbon is subject to the internal rotations that affect its neighboring methylene plus additional rotation about the C_1–C_2 bond, the difference in effective rotational rates, defined as $(\tau_{Me}{}^{i})^{-1}$, should reflect (to a first approximation) the rate of methyl group reorientation alone.[11] The values of $(\tau_{Me}{}^{i})^{-1}$ calculated[25] for the various methyl carbons from the data on the four 20-carbon alkanes given in Figure 5 are listed in Table V. There is excellent agreement in $(\tau_{Me}{}^{i})^{-1}$ values between the various types of methyls, i.e., end chain, isopropyl, and internal methyl, of the four compounds. The slower reorientation rates for isopropyl and internal methyls is consistent with the larger V_3 potential barrier to methyl rotation found for branched methyls, e.g., the barrier of 3.9 kcal/mol for 2-methylpropane,[26] relative to those (2.6–3.2 kcal/mol) found for end-chain methyls of n-alkanes.[27,28] When temperature-dependent $\tau_{Me}{}^{i}$ values are computed from the τ_{eff} data of 10-methylnonadecane and plotted against reciprocal temperature (Figure 4), ΔE values of 3.0 kcal/mol for end-methyl rotation and 4.0 kcal/mol for internal-methyl rotation are found. Although the arguments are qualitative, the good agreement of these ΔE values to established barriers for V_3 potentials is indicative that the general picture of reorientation of the C–H vectors of methyl carbons is correct. In addition, the temperature data tend to confirm the results of Lyerla et al.,[11] who found the values of $\tau_{Me}{}^{i}$ calculated for the alkanes C_7–C_{20} at 39 °C were approximately independent of chain length and, when compared to the correlation time for a free-methyl rotor at 39 °C, were consistent with an activation energy of ca. 2.6 kcal.

While the temperature results on the τ_{eff} of the methyl carbons can be demonstrated to have a relationship to the methyl rotational potential barrier, no direct physical significance can be attached to the ΔE values for methylene carbons since separation of reorientational processes involving various internal and overall motions of the molecule is not straightforward. However, that the ΔE values determined for

TABLE V: Reorientation Rates[a] for Methyl Carbon C–H Vectors, $(\tau_{Me}^{i})^{-1}$, about Methyl–Methylene and Methyl–Methine Bonds

Compound	$(\tau_{Me}^{i})^{-1}$
n-Eicosane	13[b]
10-Methylnonadecane	
End methyl	14
Internal methyl	5.9
2-Methylnonadecane	
Isopropyl methyl	8.8
End methyl	13
2,6,11,15-Tetramethylhexadecane	
Isopropyl methyl[c]	7.8
Internal methyl	5.3

[a] At 38 °C. [b] Values are given in units of 10^{12} s^{-1}. [c] It should be noted that the isopropyl methyl carbons in the hexadecane compound are nonequivalent. This result is in accord with the findings of Carmen et al. (ref 13), who have reported nonequivalent isopropyl methyl carbons in 2,5,8-trimethylnonane and 2,4,6-trimethylheptane. The magnitude of the shift differences between methyl resonances in the above two compounds was 0.22 and 1.07 ppm, respectively. The separation in the case of 2,6,11,15-tetramethylhexadecane is 0.08 ± 0.02 ppm, which is consistent with the predicted decrease in the magnitude of the effect as the number of methylene units is increased between interacting methyls. The origin of this effect has been attributed to differences in the spatial relationship between isopropyl and internal methyls as a function of the rotational conformation. For a fuller discussion, the reader is referred to ref 13; for our purposes it is sufficient to note that the two resonance lines have the same T_1 value.

the methylene τ_{eff} data in the temperature range studied here are reasonable is supported by comparison to ΔE values for light scattering data. Although direct comparisons of the NMR relaxation data and that obtained from depolarized light scattering require various assumptions, both techniques measure the relaxation of the second-order spherical harmonics.[29] Thus, it is of interest that the temperature dependence of the collective relaxation time from light scattering[30] in *n*-$C_{15}H_{32}$ and *n*-$C_{16}H_{34}$, over a similar temperature range, is governed by an apparent activation energy of 5.0 kcal. For a C_{19} alkane chain, the value might be even closer to the range of values obtained in 10-methylnonadecane.

It is somewhat surprising that the methylene τ_{eff} data follow a temperature profile defined by a single activation parameter since it would seem unlikely the activation energies for overall motion and internal modes would be approximately equivalent. If the temperature range of the measurements was extended, deviations from linearity may then occur. Nonetheless, it is interesting that the temperature dependence of η/T for eicosane,[22] which may be taken as a measure of the thermal behavior for overall motion, yields an activation energy of 5.0 kcal. The ΔE values found for segmental motion in several polymer backbones are 6.7, 6.5, and 5.7 kcal/mole in bulk polyethylene,[31] polypropylene oxide (PPO),[32] and polyisobutylene (PIB),[32] and 5.0, 4.4, and 4.3 kcal for solutions of PPO,[32] PIB,[32] and polystyrene,[33] respectively. That the ΔE values for local internal cooperative chain segmental motions may be similar to that for η/T dependence in 10-methylnonadecane suggests that internal and overall reorientational modes may have similar thermal behavior in this compound. Such a result would correlate with the recent studies of Heatley[32] on molecular motion in PIB and PPO, where dilution effects on T_1 indicate that segmental reorientation is not entirely intramolecular, but depends on the local environment. In addition, Heatley's results indicate that chain segmental motion loses correlation in about two–three monomer units, which would correspond to about six methylene units. This finding is in accord with the "five-bond" correlation found necessary by Jones et al.[35] to fit the NMR relaxation data in poly(*p*-fluorostyrene) and poly(*m*-fluorostyrene). In turn, these results are consistent with the ideas advanced here on the length of chain segments that give rise to intramolecular reorientation away from chain ends.

In summary, the ^{13}C relaxation data on 10-methylnonadecane and related 20-carbon alkanes have provided information on (1) the variation in C–H vector reorientation rates along a linear alkyl chain, (2) the magnitudes of the activation parameters governing C–H vector reorientation along a C_{19} or C_{20} alkyl chain, and (3) the effect of methyl branching on the backbone motion in an alkyl chain. The model of molecular motion for a 19- or 20-carbon chain suggested by (and consistent with) these collective results is one in which: (1) The reorientation of C–H vectors results from internal and overall molecular motions; however, reorientation for carbons near the chain end are controlled by internal motions. (2) The internal motion for methylene units approximately four carbons removed from the chain end are largely controlled by reorientations involving segments of the chain (six carbons or greater), and thus rates of internal motion about the C–C bonds in this portion of the chain are about equal. (3) The methylene units near the chain end have additional internal reorientational modes, for the volume required to be swept-out for reorientation of molecular segments near the end of the chain is smaller than that necessary for the segment controlling motion further into the chain. (4) The end-methyl reorientation is subject to the internal modes above, but because it can undergo reorientation about the methyl–methylene bond within the molecular volume, the reorientation is greatly influenced by the V_3 potential barrier for rotation about the bond.

The above model of motion is not unique, and other models can be proposed that are in qualitative agreement with the trends in the data. In order to provide additional information on the molecular dynamics of alkane chains and thus (hopefully) define more clearly a model of molecular motion, we are extending the temperature range of the T_1 experiments on 10-methylnonadecane and carrying out T_1 studies as a function of dilution of the neat hydrocarbon. We are also embarking on a program of computing NMR relaxation times from theoretical models of chain motion via isomeric state calculations.[34]

Experimental Section

A. *Spin–Lattice Relaxation Times.* Experiments were performed on a Varian CFT-20 pulse Fourier transform spectrometer operating at 20.0 kG. The CFT-20 variable temperature probe (8-mm o.d. sample tubes) and associated temperature controller were employed for temperature control and variability. The pulse power delivered to the single coil probe was sufficient to rotate the ^{13}C magnetization by 90° in 14 μs. Spectra were obtained using a spectral width of 1 kHz, 4 s acquisition time and 8K Fourier transformation (via the Varian 620l-16K-computer), thus yielding a digital resolution of ca. 0.25 Hz.

Relaxation experiments were carried out using the standard 180–τ–90 pulse sequence with a $(5T_1 + \tau)$ repetition rate. Fifty free induction decays (FID) were accumulated for each value of τ in the relaxation experiment sequence (7–10 values of τ

were employed to determine T_1). T_1 values were determined by least-squares analysis of either the time-dependent peak heights or integrated peak intensities when homogeneity degraded during the experiment, and were reproducible to ±6%. $^{13}C-\{^1H\}$ NOE values were evaluated from comparison of integrated line intensities of spectra obtained under continuously proton-decoupled and appropriately decoupler-gated (i.e., proton decoupler on only during FID acquisition) conditions.

Temperature was monitored with a thermocouple placed in the sample tube.

B. *Sample Preparation.* The hydrocarbons were obtained from commercial sources and were of >95% purity. Samples for T_1 determination were prepared by vacuum degassing the liquid and sealing in a Wilmad precision glass sample bulb. These bulbs have a flat botton, a height of ca. 8–9 mm, and fit very precisely in a flat-bottom 8-mm tube. The 8–9 mm height of the bulb is quite convenient in that the corresponding coil dimension of the NMR probe is ca. 9 mm. Thus the volume of the bulb fits in the coil and ensures the sample is confined to the volume of the coil. D_2O was placed in the interface between the 8-mm o.d. tube and the bulb to serve as the deuterium source for the internal lock system.

References and Notes

(1) E. Breitmaier, K.-H. Spohn, and S. Berger, *Angew. Chem., Int. Edit. Engl.*, **14**, 144 (1975).
(2) A. Allerhand, D. Doddrell, and R. Komoroski, *J. Chem. Phys.*, **55**, 189 (1971).
(3) G. C. Levy, *Acc. Chem. Res.*, **6**, 161 (1973).
(4) J. R. Lyerla, Jr., and D. M. Grant, *Phys. Chem., Ser. One, 1972*, **4**, Chapter 5 (1972).
(5) J. R. Lyerla, Jr., and G. C. Levy, *Top. Carbon-13 NMR Spectrosc.*, **1**, 79 (1974).
(6) T. M. Connor, *Trans. Faraday Soc.*, **60**, 1579 (1963).
(7) J. Schaefer, *Macromolecules*, **6**, 882 (1973).
(8) Y. K. Levine, P. Partington, G. C. K. Roberts, N. J. M. Birdsall, A. G. Lee, and J. C. Metcalfe, *FEBS Lett.*, **23**, 203 (1972).
(9) N. J. M. Birdsall, A. G. Lee, Y. K. Levine, J. C. Metcalfe, P. Partington, and G. C. K. Roberts, *J. Chem. Soc., Chem. Commun.*, 757 (1973).
(10) Y. K. Levine, N. J. M. Birdsall, A. G. Lee, J. C. Metcalfe, P. Partington, and G. C. K. Roberts, *J. Chem. Phys.*, **60**, 2890 (1974).
(11) J. R. Lyerla, Jr., H. M. McIntyre, and D. A. Torchia, *Macromolecules*, **7**, 11 (1974).
(12) D. M. Grant and E. G. Paul, *J. Am. Chem. Soc.*, **86**, 2984 (1964).
(13) C. J. Carmen, A. R. Tarpley, Jr., and J. H. Goldstein, *Macromolecules*, **6**, 719 (1973).
(14) R. L. Vold, J. S. Waugh, M. P. Klein, and D. E. Phelps, *J. Chem. Phys.*, **48**, 3831 (1968).
(15) K. F. Kuhlmann, D. M. Grant, and R. K. Harris, *J. Chem. Phys.*, **52**, 3439 (1970).
(16) D. Doddrell, V. Glushko, and A. Allerhand, *J. Chem. Phys.*, **56**, 3683 (1972).
(17) It should be noted that this calculation ignores the ca. 1–2% contribution to the relaxation from nondirectly bonded protons.
(18) All data sets gave least-squares correlation coefficients greater than 0.998. The values of the "preexponential" factor range from 2.6×10^{-15} to 1.1×10^{-14}. The value of this parameter for the temperature dependence of the proton relaxation in polyethylene is 3.3×10^{-15} (see ref 31). Other than to indicate the values of τ_0 are in the range found for methylene relaxation in similar studies, no physical significance can be attached to this parameter at this time.
(19) The chemical shift assignments in 2,6,11,15-tetramethylhexadecane follow from the same procedures used to assign the 10-methylnonadecane resonances. In addition, it should be noted that a maximum NOE was found for each resolved carbon in this compound and in *n*-eicosane.
(20) Reference 10 and references listed therein.
(21) V. A. Gierer and K. Wirtz, *Z. Naturforsch. A*, **8**, 532 (1953).
(22) Data taken from "Selected Values of Physical and Thermodynamic Properties of Hydrocarbons and Related Compounds", American Petroleum Institute Research Project 44, 1953.
(23) For a molecule of this size, the microviscosity correction factor of $\frac{1}{6}$, as is implicit in eq 4, may be too severe, but in this manner the computed value of τ_0 may be taken as the lower limit for τ_0, i.e., overall rotation rate may be slower than $(72 \text{ ps})^{-1}$.
(24) M. B. Clark in "Dielectric Properties of Polymers", F. E. Karasz, Ed., Plenum Press, New York, N.Y., 1972, pp 73–97.
(25) That is, from the relationship

$$(\tau_{Me}{}^{1})^{-1} = (\tau_{eff})_{C_1}{}^{-1} - (\tau_{eff})_{C_2}{}^{-1}$$

where C_1 is the methyl carbon and C_2 the carbon to which the methyl is attached.
(26) J. P. Lowe, *Prog. Phys. Org. Chem.*, **6**, 1 (1972).
(27) J. E. Anderson and W. P. Slichter, *J. Phys. Chem.*, **69**, 3099 (1965).
(28) K. van Putte, *J. Magn. Reson.*, **2**, 216 (1970).
(29) D. R. Bauer, J. I. Brauman, and R. Pecora, *Macromolecules*, **8**, 443 (1975).
(30) J. V. Champion and D. A. Jackson in "Molecular Motions in Liquids", J. Lascombe, Ed., Reidel Publishing Co., Boston, Mass., 1974, pp 585–595.
(31) U. Haeberlen, *Kolloid Z. Z. Polym.*, **225**, 15 (1968).
(32) F. Heatley, *Polymer*, **16**, 493 (1975).
(33) A. T. Bullock, G. G. Cameron, and P. M. Smith, *J. Phys. Chem.*, **77**, 1635 (1973).
(34) R. L. Jernigan in "Dielectric Properties of Polymers", F. E. Karasz, Ed., Plenum Press, New York, N.Y., 1972, pp 99–128.
(35) A. A. Jones, K. Matsuo, K. F. Kuhlmann, F. Gény, and W. H. Stockmayer, *Polym. Prepr., Am. Chem. Soc., Div. Polym. Chem.*, **16**, 578 (1975).

Equilibrium Studies by Electron Spin Resonance. 15. The Effect of Solvent Polarity Changes by the Addition of Secondary Solvents upon Ion Pair Dissociation

A. E. Alegria, Felipe Fontanez, and Gerald R. Stevenson*

Department of Chemistry, University of Puerto Rico, Rio Piedras, Puerto Rico 00931 *(Received November 3, 1975)*

Publication costs assisted by the University of Puerto Rico

The dissociation constant for the ninhydrin anion radical ion pair in hexamethylphosphoramide (HMPA) containing added water was found to increase linearly with increasing percentage of water in the solvent media, up to about 24% water. Extrapolation of this trend to 100% water predicts a dissociation constant of about 2 compared with the value of 0.014 found in pure HMPA. In contrast to these results, the addition of ammonia (a polar solvent) or hexane (a nonpolar solvent) to an equilibrium mixture of *p*-benzosemiquinone in HMPA results in an increase in the concentration of the ion pair with respect to that for the free ion. For the case of the ammonia addition this can be ascribed to the formation of the hydrogen bonded ion pair. The decrease in the ion pair dissociation constant with the addition of hexane was found to be due to an increase in the enthalpy of dissociation, while the entropy term varied only slightly. The unexpected increase in the enthalpy of dissociation is explained in terms of the special solvation properties of HMPA.

Recently the actual single ion enthalpies and free energies of solution have been determined by Parker et al.[1] for a number of cations in a series of solvents that are commonly used as solvents for anion radicals. For the alkali metal cations they found that the general order of solvation is hexamethylphosphoramide (HMPA) > dimethyl sulfoxide > dimethylformamide ≫ water > acetonitrile > methanol. In view of the fact that the bulk dielectric constant for water (78.3) is larger than that for HMPA (30.5)[2] it is surprising that the free energy of the alkali metal cations is more negative in HMPA than it is in water. However, it can be readily explained in terms of solvent–solvent interactions that exist in water and not in HMPA and other chemical properties of the two solvents.[3]

HMPA is one of the most powerful solvents for alkali metal cations known,[4] and a wide variety of anion radicals can be generated in this solvent that are free of ion pairing. However, due to the fact that the anion radicals in HMPA remain practically unsolvated, the addition of alkali metal salts to anion radical solutions in HMPA often results in the formation of ion pairs.[5] On the other hand, water is a strong solvator of both anions and cations.[6] Its ability to solvate anions is explained by the fact that water can act as a proton donor to form hydrogen bonds.

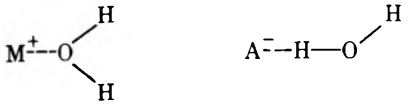

Although water is a poorer solvator of cations than is HMPA, ion pairs are essentially unknown in this solvent. Since a variety of organic anions is formed in biological systems where the concentrations of alkali metal cations (K^+ and Na^+) are quite large, it is presumably true that ion pairing, if it exists, may play an important role in the thermodynamic stability of biologically important anions.

It is our intention here to report free energies of ion pairing in mixtures of HMPA and water with the hope of extrapolating these results to estimate the free energies of ion pair dissociation in pure water. HMPA is particularly well suited to the experimental determination of ion pair dissociation constants since the equilibrium between the ion pair (β) and the free ion (α) can be described by the two-site model expressed in[7]

$$\beta \rightleftarrows \alpha + M^+ \qquad (1)$$

The major obstacle to any ESR study of anion radicals in H_2O is the fact that the vast majority of anion radicals are not stable in this solvent. Russell and Young[8] have reported one of the most stable anion radicals, that of ninhydrin. The ninhydrin radical anion is stable enough for continued observation in an aqueous media, and is particularly well suited to this study due to the fact that the charge localization in the oxygens should lead to facil ion pair formation.

Results and Discussion

Solutions (10^{-2} to 10^{-4} M) of ninhydrin in HMPA will dissolve small amounts of potassium metal to yield a solution of the very stable ninhydrin anion radical. Upon ESR analysis this solution yields a nine-line pattern consisting of two triplets, each due to two equivalent protons with coupling constants of 0.93 and 1.18 G. These values are completely consistant with those reported in dimethyl sulfoxide.[8] Addition of KI or $KClO_4$ to the anion radical solution results in a change in both of the coupling constants. The total line width (distance between the first and last ESR line) changes even more dramatically with the addition of salt. These changes in total line width (ΔW_t) and in the coupling constants are due to the formation of ion pairs which exist in rapid equilibrium with the free ion

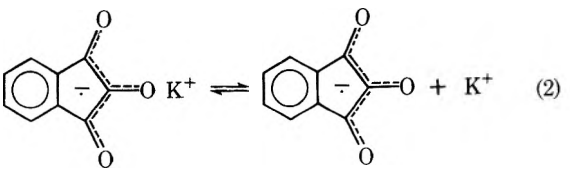

(2)

Since the observed value for ΔW_t decreases smoothly with increasing salt concentration, it must be a weighted average between the total line width for the free ion (ΔW_t^0) and that for the ion pair ($\Delta W_t'$).[9]

It has been demonstrated previously that weighted average total line widths can be used along with eq 3 for the determi-

$$1/(\Delta W_t - \Delta W_t^0) = K_{eq}/(K^+)(\Delta W_t' - \Delta W_t^0) + 1/(\Delta W_t' - \Delta W_t^0) \quad (3)$$

nation of ion pair dissociation constants.[9] If the two-jump model expressed in eq 2 (ion pair to free ion) is correct, a plot of $1/(\Delta W_t - \Delta W_t^0)$ vs. $1/(K^+)$ should give a straight line and have an intercept of $1/(\Delta W_t' - \Delta W_t^0)$ and a slope of $K_{eq}/(\Delta W_t' - \Delta W_t^0)$. Treated in this manner our data did yield a straight line, Figure 2. From the slope and intercept of this line $\Delta W_t'$ and K_{eq} were found to be 4.07 G and 0.014, respectively.

Unlike most of the other anion radicals studied in HMPA, we were not able to assume that the anion radical generated in the absence of added salt was free of ion pairing. Upon close examination of the ESR spectrum obtained before the addition of salt, some asymmetry can be observed in the line amplitudes. That is, the high-field lines have larger amplitudes than do the low-field lines due to the fact that both the ion pair and free ion exist in solution, and they are rapidly interconverting. Since the two species have different coupling constants and g values,[10] an asymmetry is expected.[5a] Being unable to generate a solution containing only free ion, ΔW_t^0 had to be obtained indirectly by extrapolating a plot of the total measured line width vs. the ratio of line amplitudes for the first and last line for systems reduced with different amounts of potassium metal to one for this ratio. The value obtained for ΔW^0 (4.39 G) is only slightly different than that observed before the addition of salt.

Addition of water to the HMPA solutions without added salt results in the disappearance of the asymmetry, Figure 1, which is certainly due to the dissociation of the ion pair. Thus, for anion radical solutions containing more than 1% water, ΔW_t^0 can be taken from the ESR spectrum of the solution before any salt is added. In general it was found that the larger the concentration of water in the anion radical solution the larger the portions of added salt had to be in order to observe a change in the total line width. For all of the water concentrations studied a linear plot was obtained when the data were treated according to eq 2, Figure 2. The results from these experiments are given in Table I for water concentrations varying from 0 to 25 wt % H_2O. For concentrations of water larger than 25% copius quantities of $KClO_4$ had to be added to observe a change in the total line width making it impractical to study these solutions.

Even though the ion pair dissociation constant could not be measured in pure water, it can be estimated from an extrapolation of the results reported in Table I. A plot of the weight percent of water in the HMPA solution vs. K_{eq} is essentially linear (Figure 3). Extrapolation of this plot to 100% H_2O yields a K_{eq} of 2.1. It is certainly not certain that this plot will remain linear all the way to 100% water, but even with considerable curvature K_{eq} is not likely to be less than one. All of this indicates that ion pair dissociation constants are very large in pure water.

In order to compare these results to systems of biological interest, it is helpful to review some of the ion pair dissociation constants for other anion radicals in HMPA (Table II).

Several compounds found in biological systems have the potential of acting as radical scavengers and may pull an electron off of an undesired radical to form the anion radical of the scavenger molecule. If this is the case the thermodynamic stability of the resulting anion radical will be of immense importance to the biological system, and ion pairing

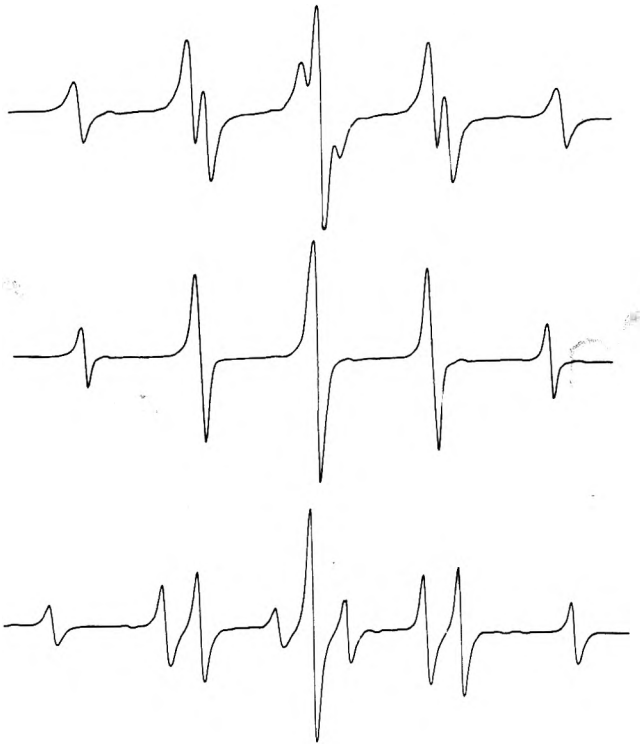

Figure 1. ESR spectra of the ninhydrin–HMPA–K system: (top) containing added potassium perchlorate (0.05 M); (middle) containing 15.2% H_2O; (bottom) no salt or water added. Note the asymmetry in the amplitudes of the first and last ESR lines.

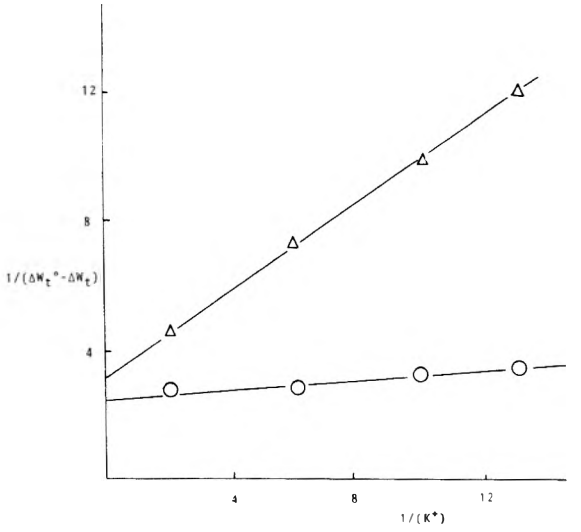

Figure 2. Plots of $1/(\Delta W_t^0 - \Delta W_t)$ vs. $1/(K^+)$ for the ninhydrin anion radical in HMPA (O) and in HMPA containing 6.8% H_2O (Δ).

is an important factor influencing this thermodynamic stability. The list of possible radical scavengers includes coenzyme Q (I) and vitamine K (II) both of which have quinoidlike structures.[10]

In HMPA the ion pair dissociation constant for our model compound (ninhydrin) is several times smaller than those for compounds with structures similar to I and II. It follows then that since there is little ion pairing of the ninhydrin anion radical in water, ion pairing is probably of little importance in biological systems for the anion radicals of I and II in an aqueous environment.

TABLE I: Equilibrium Constant for Reaction 2 in HMPA with Added Water; $\Delta W_t'$, ΔW_t^0, and the Slope of the Line Shown in Figure 2

% H_2O	Slope	ΔW_t^0, G	$\Delta W_t'$, G	K_{eq}	X_{H_2O}
0.00	0.042	4.39[a]	4.07 ± 0.04[b]	0.014 ± 0.002[b]	0
1.55	0.21	4.12	3.86 ± 0.04	0.054 ± 0.006	0.13
2.02	0.16	4.08	3.85 ± 0.06	0.037 ± 0.05	0.17
5.10	0.35	4.03	3.79 ± 0.06	0.084 ± 0.02	0.35
6.82	0.66	3.96	3.66 ± 0.06	0.15 ± 0.02	0.41
12.4	0.84	3.83	3.60 ± 0.04	0.19 ± 0.03	0.58
17.5	2.97	3.59	3.44 ± 0.06	0.45 ± 0.03	0.68
24.7	6.55	3.67	3.59 ± 0.06	0.52 ± 0.03	0.77

[a] The error in ΔW_t^0 is 0.03 G. [b] These errors were propagated from a computer calculation of the standard deviation in the best slope and intercept. [c] These are the mole fractions of H_2O.

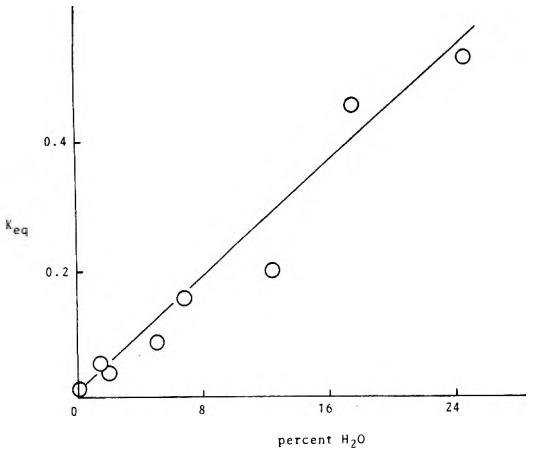

Figure 3. Plot of the ion pair dissociation constant for the ninhydrin anion radical ion pair in HMPA vs. the percent of added water.

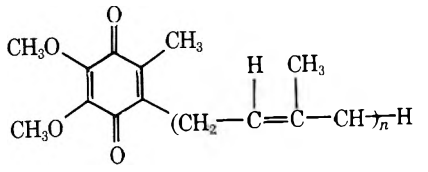

I

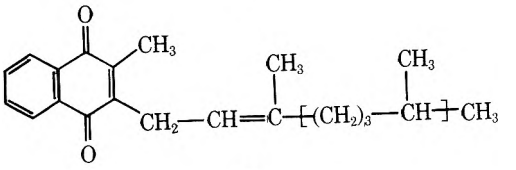

II

It is clear that the addition of water shifts the ion pair dissociation to the right because of specific interactions between the water and the ions and not just due to an increase in the polarity of the solvent medium. However, it would be predicted that the addition of a nonpolar secondary solvent (hexane) would lead to a shift to the left.

The ion pair and free ion of the ninhydrin anion radical cannot be observed individually, as only the time-averaged species is seen. For the anion radical of benzoquinone in HMPA both the free ion and ion pair are observed simultaneously, and the ion pair dissociation constant can be obtained from their respective line intensities.[5a] The observation of both the ion pair and free ion yields more information concerning the structure of the ion pair.

TABLE II: Ion Pair Dissociation Constants at 25 °C in HMPA for Anion Radicals Ion Paired with Potassium

Anion radical	K_{eq}	Anion radical	K_{eq}
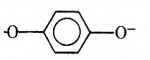	0.036[a]	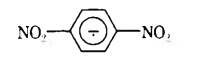	0.25[b]
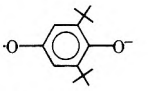	0.075[a]	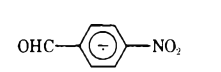	0.060[b]
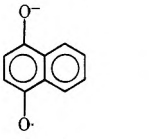	0.29[a]	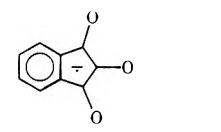	0.014[c]
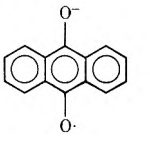	0.14[a]		

When small amounts of hexane (0.1 to 2 M) were added to solutions of benzosemiquinone in HMPA with added KI, the equilibrium constant for the ion pair dissociation was found to decrease. The effect of increasing the free energy of a reaction in which charge is created by decreasing the polarity of the solvent has been observed many times, and is normally due to the entropy term.[11] A nonpolar solvent undergoes much more ordering than does a polar solvent upon charge creation.

As can be seen in Figure 4, the shift to more positive free energies in the dissociation of the *p*-benzosemiquinone ion pair (eq 1) is due to an increase in the enthalpy term and not a decrease in the entropy. In fact, the entropy for eq 1 undergoes a slight increase upon addition of hexane to the solvent system (Table III). These results can be explained in terms of the special solvation properties of HMPA. HMPA is a polar solvent; but, due to the large steric interaction around the electropositive phosphorus center, there is little dipole–dipole ordering of this solvent. However, since HMPA is one of the most powerful cation solvators,[4] it is strongly bound to the cation (free of ion pairing). Thus the enthalpy of ion pair dissociation is negative. The addition of hexane to the system decreases the polarity of the solvent medium, but does not change the ordering of the solvent in the absence of ions. However, when the ion pair dissociates HMPA must compete with hexane in the solvation of the newly formed cations. Since the interaction between the cation and hexane cannot be as strong as that between the cation and HMPA, both the entropy and the enthalpy increase with the addition of hexane. It should be noted here that the splitting due to the ^{39}K nucleus in the ion pair (0.30 G) does not vary with the

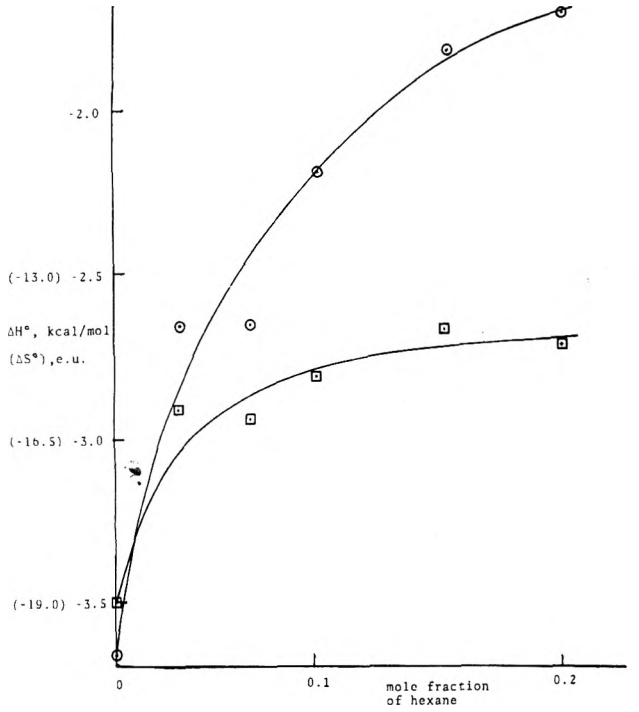

Figure 4. Plots of the enthalpy and entropy of ion pair dissociation vs. the mole fraction of added hexane. The entropy values are given in parentheses, and the plot is represented by □. The enthalpy plot is represented by O. The data for this plot were taken at 25 °C for the *p*-benzoquinone–HMPA–K system.

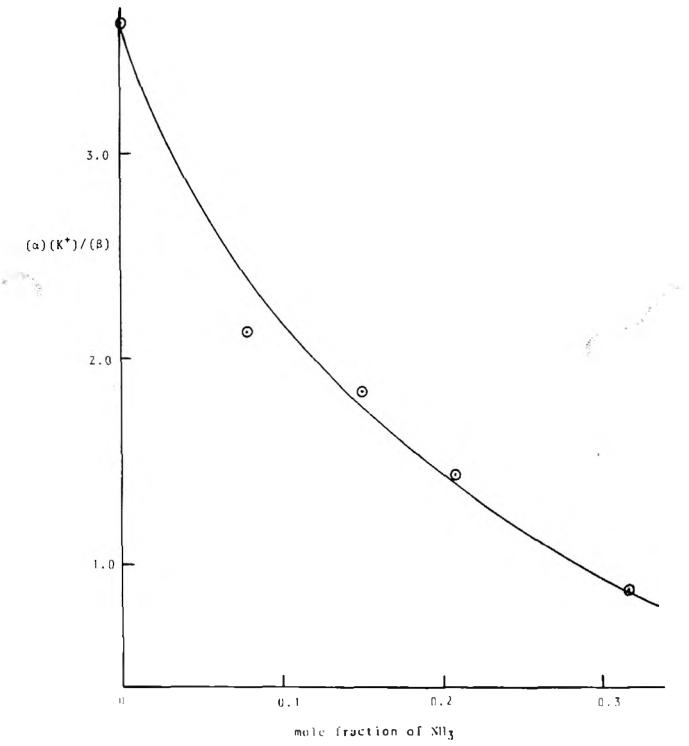

Figure 5. A plot of the free ion concentration (α) times the potassium ion concentration divided by the ion pair concentration (β) vs. the mole fraction of added ammonia.

TABLE III: Thermodynamic Parameters Controlling the Dissociation of the Potassium *p*-Benzosemiquinone Ion Pair in HMPA with Added Hexane

Mole fraction of hexane	K_{eq}	ΔH°, kcal/mol	ΔS°, eu
0	0.036[a]	−3.68 ± 0.1[b]	−19.0
0.033	0.028	−2.66 ± 0.06	−16.0
0.068	0.025	−2.65 ± 0.02	−16.2
0.102	0.016	−2.18 ± 0.1	−15.5
0.165	0.012	−1.80 ± 0.1	−14.8
0.225	0.0095	−1.71 ± 0.06	−15.0

[a] The relative error in the equilibrium constants is 0.001. This small relative error is due to the fact that the sample without any added hexane, for which the K_{eq} is known,[5] was used as a standard. Samples were taken from the same anion radical solution after various quantities of hexane were added and compared to the standard. [b] These errors represent standard deviations in the slope.

addition of hexane up to 0.2 M suggesting that the nature of the ion pair does not change with the addition of small amounts of hexane.

The addition of a polar or protic solvent to the system *p*-benzoquinone–HMPA–K with added KI would be expected to have the opposite effect upon the ion pair dissociation equilibrium from that due to the addition of hexane. That is, the free ion concentration should increase relative to that for the ion pair with the addition of ammonia.

Again, the opposite of the expected result is obtained experimentally. Small additions of NH_3 to the free ion–ion pair equilibrium mixture result in an increase in the concentration of ion pair relative to that for the free ion (Figure 5). The only way a negative slope for a plot of K_{eq} vs. the concentration of added NH_3 can be interpreted is to assume an exothermic interaction between the ion pair and ammonia, which is most probably due to the formation of a hydrogen bonded ion pair. A similar effect upon the ion pair dissociation equilibrium for the nitrobenzene anion radical in HMPA was observed when NH_3 was added to the system,[12] and was shown to be due to the formation of a hydrogen bonded ion pair for which a structure was proposed.[12] Hydrogen bonded ion pairs have also been reported by Hirota et al.[13]

No change in the metal splitting was observed for additions of NH_3 to the benzosemiquinone ion pair. However, at higher concentrations of NH_3(4 M) a decrease in A_K is observed due to the displacement of the cation by the hydrogen bonding ammonia molecules. These two similar (both can form hydrogen bonds to an anion and both can coordinate an alkali metal cation) solvents (water and ammonia) act in an opposite manner in their effect upon ion pairing. The hydrogen bonded ion pair formed upon ammonia addition is stabilized presumably by simultaneous hydrogen bonding to the anion and interaction of the lone electron pair on the nitrogen with the cation. The anion radical of benzoquinone is not sufficiently stable for study in solutions containing water.

Experimental Section

All of the organic compounds used were purchased from Aldrich Chemical Co. and recrystallized before use. Potassium iodide and potassium perchlorate were dried in a vacuum oven at 100 °C for 48 h prior to use.

The method of reduction of the neutral molecule to form anion radicals and the purification of HMPA has been previously described.[7b] Quantitative addition of NH_3 to the anion radical solution was carried out by the use of a toepler pump connected to a gas buret as previously described.[12] Hexane and water were added to the anion radical solutions via break seals in the manner previously described.[14]

The ESR spectra were recorded on an x-band E-9 ESR spectrometer. The temperature was controlled with a Varian V-4557 variable-temperature controller calibrated with an iron constantan thermocouple. The method used to determine the thermodynamic parameters for the dissociation of the *p*-benzosemiquinone ion pair (eq 1) was exactly the same as previously described.[7a]

Care must be taken in the handling of HMPA, since it has been found to be a possible carcinogen.[15]

Acknowledgment. The Authors are grateful to the National Institute of Health for support of this work. This NIH support was from Grant No. RR-8102 from the Division of Research Resources.

References and Notes

(1) G. R. Heding, D. A. Owensby, and A. J. Parker, *J. Am. Chem. Soc.*, **97**, 3888 (1975).
(2) J. E. Dubois and H. Vill, *J. Chim. Phys.*, **62**, 699 (1965).
(3) (a) R. S. Drago and B. B. Wayland, *J. Am. Chem. Soc.*, **87**, 3571 (1965); (b) R. H. Erlich, E. Roach, and A. I. Popov, *ibid.*, **92**, 4989 (1970); (c) R. H. Erlich and A. I. Popov, *ibid.*, **93**, 5620 (1971).
(4) (a) G. Levin, J. Jaugar-Grodzinski, and M. Szwarc, *J. Am. Chem. Soc.*, **92**, 2268 (1970); (b) H. Normant, *Angew. Chem., Int. Ed. Engl.*, **6**(12), 1046 (1967).
(5) (a) G. R. Stevenson and A. E. Algebria, *J. Phys. Chem.*, **77**, 3100 (1973); (b) G. R. Stevenson, A. E. Alegria, and A. M. Block, *J. Am. Chem. Soc.*, **97**, 4859 (1975).
(6) R. L. Benoit and S. Y. Iam, *J. Am. Chem. Soc.*, **96**, 7385 (1974).
(7) (a) G. R. Stevenson and L. Echegoyen, *J. Phys. Chem.*, **77**, 2339 (1973); (b) G. R. Stevenson, L. Echegoyen, and L. R. Lizardi, *ibid.*, **76**, 1439 (1972); (c) G. R. Stevenson and A. E. Alegria, *ibid.*, **78**, 1771 (1974).
(8) G. A. Russell and M. C. Young, *J. Am. Chem. Soc.*, **88**, 2007 (1966).
(9) A. E. Alegria, R. Concepcion, and G. R. Stevenson, *J. Phys. Chem.*, **79**, 361 (1975).
(10) For a brief review on the possible biological actions of these radical scavengers see W. A. Pryor, *Chem. Eng. News*, 34 (June 7, 1971).
(11) A. Frost and R. G. Pearson, "Kinetics and Mechanism", 2d ed, Wiley, New York, N.Y., 1961, Chapter 7.
(12) L. Echegoyen, H. Hidalgo, and G. R. Stevenson, *J. Phys. Chem.*, **77**, 2649 (1973).
(13) K. Nakamura, B. F. Wong, and N. Hirota, *J. Am. Chem. Soc.*, **95**, 6919 (1973).
(14) G. R. Stevenson and H. Hidalgo, *J. Phys. Chem.*, **77**, 1027 (1973).
(15) J. A. Zapp, Jr., *Science*, **190**, 422 (1975).

Proton Diffusion and Activity in the Presence of Electrolytes

Noel K. Roberts

Chemistry Department, University of Tasmania, Hobart, Tasmania, Australia 7001 *(Received August 28, 1975)*

Proton diffusion in pure water and in the presence of electrolytes is of particular importance in biological systems. In pure water the rate-determining step is the rotational or librational freedom of the water molecule. The tunneling of the proton in the H bond is very rapid and has a low activation energy. In the presence of most electrolytes the rotational and librational freedom of the water molecules is only slightly affected. In the case of structure breakers the water molecules are freer than in pure water. However, the highly polarizable H bond in which the proton tunnels is strongly polarized by the presence of electrolytes and the potential well deformed with increasing electrolyte concentration. Consequently as the concentration of electrolyte increases the Grotthus mechanism is suppressed and the hydrodynamic mechanism becomes more important. Another consequence of the polarization of the H bond and its final dehydration by ion–dipole interaction is the increase in activity of the hydrogen ion in the presence of electrolytes owing to its increased localization. Tetraalkylammonium salts, where alkyl is propyl and butyl, do not polarize the H bond as much as the surrounding water molecules, and the decrease in proton diffusion appears to be due to the reduced orientation time of the water molecule. The activity of the hydrogen ion is less in the presence of these electrolytes and reflects the decreased localization of the hydrogen ion.

Introduction

It is well established that proton and deuteron diffusion[1] in normal and heavy water solutions of electrolytes is very sensitive to the presence of electrolytes, Figure 1a and 1b.[2-7] The aim of this paper is to consider critically the present theories of proton diffusion in water and to ascertain the mechanism in the presence of electrolytes. Our recent work on proton diffusion and activity in the presence of electrolytes is briefly summarized and the interpretation is considerably extended in the light of recent infrared investigations of acid solutions containing electrolytes. The results are of importance for aqueous biological systems where hydrogen ion mobility and activity are markedly affected by the type of electrolytes present.

Mechanism for Proton Diffusion

The currently accepted mechanism for proton mobility in aqueous solutions is that advanced by Conway, Bockris, and Linton in 1956,[8] and most text books quote it as the only likely mechanism. However, Eigen[9] in 1958 postulated a slightly different mechanism and pointed out some of the shortcomings in the treatment by Conway, Bockris, and Linton. Both groups of workers agreed that the proton tunneled through a hydrogen bond rapidly and that this process had almost no activation energy, however, they disagreed on the rate-determining step. Conway et al. considered that the rate-determining step in proton mobility was the rotation of hydrogen bonded water molecules in the field of H_3O^+ ion (preceded and succeeded by fast tunneling protons). Eigen[9] maintained

that Conway et al.'s treatment contained some questionable approximations among which was the assumption that the normal rotation of water molecules in the absence of the field of the H_3O^+ ion was too slow ($\tau_0 \approx 10^{-6}$ s) to explain the high mobility of the hydrogen ion. Eigen remarks that this figure was estimated from the dielectric relaxation in ice; in liquid water he maintains that the orientation time $\approx 10^{-11}$ s. This much lower value for the thermal rotation of the water molecule in liquid water is confirmed by recent work on the NMR of electrolyte solutions.[10] Furthermore he points out the H_3O^+ is hydrated in solution and the protonic field is reduced so that the charge is distributed over a certain average region [the proton tunneling in the $H_5O_2^+$ group (see below) also contributes to this averaging] consequently the field assisted rotation of H_2O molecules in the neighborhood is considerably less than assumed by Conway et al.

Eigen postulated the rate-determining step as the structural diffusion of the $H_9O_4^+$ complex by the formation and decomposition of H bonds at its periphery. More recently Zundel,[11] from a consideration of the ir spectra of aqueous solutions, has expressed this structural diffusion more explicitly. He has shown that the proton tunnels only in the bond in the $H_5O_2^+$ grouping. Since the H_3O^+ fluctuates in the $H_5O_2^+$ grouping with the tunneling frequency, the center of the $H_9O_4^+$ complex shifts too. This is in contrast to Eigen's conception of the proton fluctuating in the three bonds of the $H_9O_4^+$ grouping—instead the $H_9O_4^+$ complex itself fluctuates in the aqueous solution. In general the proton tunnels only in one of the three hydrogen bonds as the other two are usually too bent as shown from a consideration of the ir spectrum of the hydrogen ion which means that the barrier is relatively high and the proton rarely transfers. When one of the bent H bonds becomes linear, in the course of the thermal movements of the water molecules, this is no longer distinguishable from the tunneling bond in $H_5O_2^+$. When the H nucleus in one of the previously bent bonds tunnels and when the bond in which the proton has tunneled previously becomes bent, structure diffusion has taken place. The rate-determining step, then, according to Eigen and Zundel, is the structure diffusion of the excess proton.

If the thermal orientation time for liquid water is of the order of 10^{-11} s, there is not such a vast discrepancy between the number of protons arriving at each water molecule per second and the rate of *thermal* reorientation of water molecules.

For example, Conway et al. calculate[8] that for 0.1 N HCl, 4.9×10^{10} protons arrive at each water molecule per second. Using the angular rotation of *free* water molecules as 2.5×10^{13} radians sec^{-1} and the Arrhenius relation $2.5 \times 10^{13} \exp(-\Delta H^{\circ\ddagger}/RT)$, where $\Delta H^{\circ\ddagger}$ is the heat of activation for rotation and consequent H-bond breakage, to calculate the angular rotation of *hydrogen-bonded* water molecules, they obtain the average rate of thermal rotation of water molecules as 1.4×10^6 radians s^{-1} corresponding to a rotational time of 5×10^{-6} s. However, $\Delta H^{\circ\ddagger}$ is estimated from dielectric measurements in *ice* rather than in *liquid* water. If the accepted thermal orientation time of pure water as determined from recent nmr measurements is used, i.e., 10^{-11} s, the angular rotation (due to thermal motion) of water molecules becomes $2\pi \times 10^{11}$ radians s^{-1}, which is more than adequate to cope with 4.9×10^{10} protons arriving at each water molecule per second for a 0.1 N HCl solution.

A new mechanism for proton mobility in ice and water has recently been proposed in which the role of proton–proton interactions in the proton transfer process are considered.[20]

Mechanism for Proton Diffusion in the Presence of Electrolytes

In the presence of electrolytes it becomes clear that the rate-determining step cannot be the thermal orientation of the water molecules and is unlikely to be the bent H bonds becoming linear in the course of the thermal movements of water molecules, so that they are no longer distinguishable from the tunneling bond in $H_5O_2^+$. Since both these rate-determining steps depend on the freedom of movement of water molecules, one would expect to observe some correlation between a measure of the freedom of water molecules, e.g., self-diffusion of water, viscosity, thermal orientation of water, and proton mobility. An inspection of Figure 1a and 1b,[7] and Table I shows that the viscosity of the solution and the thermal rotation of water molecules bear no relation to the diffusion coefficient of the proton either in magnitude or direction. The results shown in Figure 1a and 1b were obtained from dc polarography. The most pronounced change in D_{H^+} occurs between 0 and 1 *m*, the very region in which the viscosity and the thermal rotation of water (even in the primary hydration sphere) are changing slowly and in some cases changing in the opposite direction to D_{H^+}. So it seems that the rate-determining step cannot be the field rotation of water molecules since this would follow the same trend as the thermal rotation. In agreement with our observations, Hertz and Klute[12] concluded from an ^{17}O NMR study of aqueous solutions containing electrolytes, which reduce the viscosity of water and lower the rotational time of the water molecule, that proton exchange of the water molecule is *slower* than in pure water. The slowing down of proton exchange was less marked with structure makers. Franks, however, seems to draw an incorrect conclusion from these results. He states,[13] "A comparison of ionic transport properties in water and ice shows that any influence which promotes water 'structure' would, on the one hand, reduce the mobility of alkali metal ions, and, on the other, enhance the mobility of protons and hydroxyl ions. The slowing down of proton exchange in aqueous solutions containing ions which break up water structure has been established."

It is clear from Hertz and Klute's work, Zundel's, and ours, that "structure" making ions *also* reduce proton mobility. Evidently Franks has also identified structure making with the formation of icelike structures, for which there is no evidence.

That the rate-determining step cannot be the rotational freedom of the water molecule is further confirmed by the work of Zundel. Zundel[14,15] has shown from a consideration of the effect of neutral salts on the ir continuum of hydrogen ions that there is a marked change of the potential well due to the polarization of the hydrogen bond in which the proton tunnels by the local fields of the ions. The energy barrier to proton tunneling is very sensitive to the O–O distance and the electric field strength at the H bond in which the proton is tunneling.[16] The hydrogen bond in the absence of electrolytes is highly polarizable and the energy barrier to tunneling is extremely small. However, as the field strength increases, owing to the presence of electrolytes, the hydrogen bond in $H_5O_2^+$ becomes polarized and hence the Grotthus mechanism is increasingly hindered by the ion fields as the concentration of electrolyte increases.

For example, in a 1 *m* univalent electrolyte solution the average distance between ions is 9.4×10^{-8} cm.[17] If we consider the hydrogen bond in which the proton tunnels as situated equidistantly from the ions, the field strength at the H

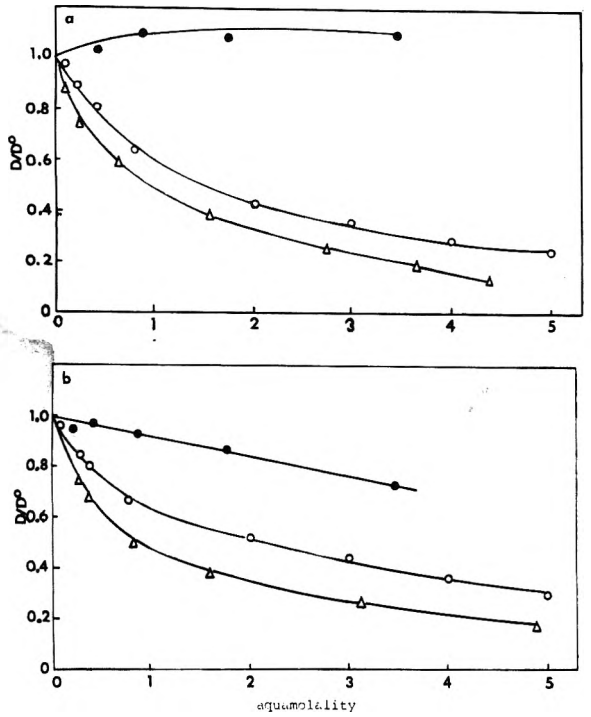

Figure 1. Tracer diffusion coefficients of the unneutralized proton and deuteron (i.e., uncompensated charge) in (a) potassium bromide and (b) sodium chloride solutions at 25 °C: (○) H^+; (△) D^+; (●) the self-diffusion ratio for normal water at 23 °C.

TABLE I:[a] Thermally Induced Orientation Times of the H_2O and D_2O Molecule in the Primary Hydration Layer of Various Diamagnetic Ions

	$\tau_\pm/\tau^b$	
Ion	(1)	(2)
Na^+	2.1	1.4
K^+	1.0	1.0
$(CH_3)_4N^+$	1.6	1.6
$(C_2H_5)_4N^+$		2.1
$(C_3H_7)_4N^+$		3.1
$(C_4H_9)_4N^+$		2.9
Cl^-	1.0	1.0
Br^-	0.6	0.8
I^-	0.35	0.6

[a] Reference 10. $\tau_\pm$ is the orientation time of a H_2O or D_2O molecule in the primary hydration sphere; τ is the orientation time of a H_2O or D_2O molecule in pure H_2O and D_2O, respectively ($\sim 10^{-11}$ s). (1) is the results for water solutions; (2) is the results for heavy water solutions. *Note that:* (a) $\tau_\pm(K^+)/\tau = \tau_\pm(Cl^-)/\tau$ because the longitudinal relaxation time of KCl solutions up to ~4 *m* equals that for pure water; (b) the ratio $\tau_\pm/\tau$ depends on the value assumed for the hydration number of the ion.

bond may be calculated approximately in the following manner. In I only a positive and a negative ion are considered.

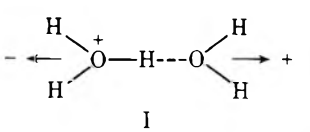

I

The field strength at the H bond is given by[18]

$$E = \frac{1}{4\pi\epsilon_0\epsilon}\frac{q}{(r/2)^2}$$

where E = field strength, q = charge on the ion, r = ionic separation, ϵ_0 = permittivity constant, ϵ = permittivity of water; if $r \simeq 10^{-7}$ cm, E becomes $\sim 7 \times 10^6$ V cm^{-1}. This value will be increased by the presence of other ions farther away.

At a field strength of 7×10^6 V cm^{-1}, the potential well in $H_5O_2^+$ becomes deformed and the fluctuation frequency is decreased.[16]

Consequently the change in mechanism of proton diffusion from Grotthus to hydrodynamic mechanism arises as a result of the polarization of the H bond in which the proton tunnels. The change in mechanism cannot arise from a change in the rotational time of the water molecule for the reasons outlined previously.

Increase in Activity of Hydrogen Ion in the Presence of Electrolytes

The polarization of the H bond can also account for the increase in activity of the hydrogen ion in the presence of these electrolytes. In earlier publications[2,3] polarographic evidence was adduced to show that the activity of the hydrogen ion is increased in the presence of most electrolytes. Zundel has also produced spectroscopic evidence for the increase in activity of the hydrogen ion. We explained the increased activity at high concentration of electrolyte as being the result of the dehydration of the hydrogen ion (possibly $H_9O_4^+$, which has been shown to be present in aqueous solutions in the presence of sufficient water). This explanation is in keeping with the shift in half-wave potential of the hydrogen ion to more positive potentials. Zundel has suggested that the polarization of the H bond and the consequent localization of the tunneling proton is responsible for the increased activity. This explanation is in keeping with the ^{17}O NMR study by Hertz and Klute, who showed that proton exchanges slowed down in the presence of the electrolytes, i.e., the proton is more localized. It seems clear that both processes contribute to the increased activity. The localization process would predominate at low concentrations of electrolyte and the dehydration process at high concentrations. The two processes are, however, related as the polarization of the H bond by electrolyte passes over into the removal of water from the H bond by strong ion–dipole interactions between the ions and dipolar water molecules. Consequently the phenomena of increased hydrogen ion activity and reduced anomalous proton diffusion are the result of the same process, namely, the polarization of the H bond in which the proton tunnels. At very high concentrations of electrolyte the hydrogen ion is almost completely dehydrated to H_3O^+ and no tunneling is possible. Under this condition the hydrogen ion has its maximum activity as shown by our polarographic work.[2,3]

Special Case of Tetraalkylammonium Salts, where Alkyl is Higher than Ethyl

The tetraalkylammonium salts, where alkyl is C_3H_7 and C_4H_9, seem to present a different case. The H bond in which the proton tunnels seems to be less polarized in the presence of these electrolytes than in the presence of water. Zundel[11,19] has shown that the ir continuum of acid solutions containing these salts is increased in contrast with the ir continuum of acid solutions containing simple electrolytes which is decreased. This indicates that the H bond is less polarized in the presence of the tetraalkylammonium salts (where alkyl = C_3H_7 and C_4H_9) than in pure water. He visualizes the effect as being due to the displacement of water molecules by the

large tetraalkylammonium ion, the induction effect of which is less than the water molecule. Consequently the energy barrier to tunneling is less than in water. However, proton diffusion decreases markedly on the addition of these salts.[7] Erdey-Grúz[21] has also observed a similar reduction in the addition of dioxane to aqueous solutions of HCl. Consequently it appears that in this case the reduced orientation time of the water molecule must be responsible for the lower diffusion coefficient. This explanation is likely when we consider Table I showing thermally induced orientation times of the water molecule, e.g., $\tau_{\pm}/\tau \simeq 3.0$ for $N(C_3H_7)_4^+$ and $N(C_4H_9)_4^+$ compared with $\tau_{\pm}/\tau \simeq 1.0$ for K^+.

Decreased Activity of the Hydrogen Ion in the Presence of $N(Alkyl)_4^+Br^-$ where R = C_3H_7 and C_4H_9

Our polarographic work[3b] indicated that the activity of the hydrogen ion as measured by the half-wave potential is increased in the presence of $N(CH_3)_4^+Br^-$, remains constant in $N(C_2H_5)_4^+Br^-$, and progressively decreases in $N(C_3H_7)_4^+Br^-$ and $N(C_4H_9)_4^+Br^-$ solutions. Zundel's results[19] are in agreement with our findings. This is a result of the H bond in which the proton tunnels becoming less polarized as the size of the alkyl group increases. Consequently the decreased activity of the hydrogen ion can be identified with an increased delocalization of the proton in the H bond in which it tunnels.

References and Notes

(1) It is more correct to refer to the process as "diffusion of the unneutralized proton" or "diffusion of uncompensated change", as this gives a clearer picture of the molecular dynamic processes which are relevant. However in this paper the more commonly used wording "proton diffusion" is adopted.
(2) N. K. Roberts and H. van der Woude, *J. Chem. Soc. A*, 940 (1968).
(3) (a) N. K. Roberts and H. L. Northey, *J. Chem. Soc. A*, 2572 (1971); (b) *ibid.*, 2640 (1971).
(4) N. K. Roberts and H. L. Northey, *J. Chem. Soc., Faraday Trans. 1*, **68**, 1528 (1972).
(5) N. K. Roberts and H. L. Northey, *Nature (London)*, **237**, 144 (1972).
(6) N. K. Roberts, *Nature (London)*, **249**, 594 (1974).
(7) N. K. Roberts and H. L. Northey, *J. Chem. Soc., Faraday Trans. 1*, **70**, 253 (1974).
(8) B. E. Conway, J. O'M. Bockris, and H. Linton, *J. Chem. Phys.*, **24**, 834 (1956).
(9) M. Eigen and L. De Maeyer, *Proc. R. Soc. London, Ser. A*, **247**, 505 (1958).
(10) H. G. Hertz and M. D. Zeidler, *Ber. Bunsenges. Phys. Chem.*, **67**, 774 (1963); **68**, 821 (1964). See also "Water, A Comprehensive Treatise", F. Franks, Ed., Plenum Press, New York, N.Y., 1973.
(11) G. Zundel, *Prak. Allg. Chem.*, **21**, 329 (1970).
(12) H. G. Hertz and R. Klute, *Z. Phys. Chem. (Frankfurt am Main)*, **69**, 101 (1970).
(13) M. J. Tait and F. Franks, *Nature (London)*, **230**, 91 (1971).
(14) G. Zundel, Euchem Conference, Montpelier, May 1974.
(15) Dag. Schiöberg and G. Zundel, *J. Chem. Soc., Faraday Trans. 2*, **69**, 771 (1973).
(16) R. Janoschek, E. G. Weidemann, H. Pfeiffer, and G. Zundel, *J. Am. Chem. Soc.*, **94**, 2387 (1972).
(17) R. A. Robinson and R. H. Stokes, "Electrolyte Solutions", 2d ed, Butterworths, London.
(18) R. Resnick and D. Halliday, "Physics", Wiley, New York, N.Y., 1966.
(19) G. Zundel, private communication; D. Schiöberg, Doctoral thesis, University of Munich, 1975.
(20) J. K. Fang, K. Godzik, and G. L. Hofacker, *Ber. Bunsenges. Phys. Chem.*, **77**, 980 (1973).
(21) T. Erdey-Grúz and I. M. Czako, *Acta Chim. (Budapest)*, **67** (3), 283 (1971).

Effect of Tetraalkylammonium Salts on the Hydrophobic Interaction

R. Tenne and A. Ben-Naim*

Department of Physical Chemistry, The Hebrew University of Jerusalem, Jerusalem, Israel

(Received November 10, 1975)

Data on the solubilities of methane, ethane, and propane in aqueous solutions of tetraalkylammonium salts are used to estimate the strength of the hydrophobic interaction in these solutions. It is found that the effect of these salts on the hydrophobic interaction is similar to the one, reported earlier, for the simple salts.

I. Introduction

It is well known that tetraalkylammonium ions (TAN^+) exhibit some unusual properties in aqueous solutions.[1] This phenomenon has traditionally been interpreted in terms of the effect of TAN^+ ions on the structure of water.

We have recently investigated the effect of various solutes (electrolytes and nonelectrolytes) on the strength of the hydrophobic interaction (HI).[2] This report extends that investigation to include TAN^+ ions as well. Our main source of data is a recent paper by Wen and Hung[3] who measured the solubilities of some low molecular weight hydrocarbons in aqueous solutions of TAN^+ salts. The conversion of their solubility data into information on HI is described in the next section. In section III we report on a sample of computed results on the effect of TAN^+ ions, as well as its concentration dependence on the strength of the HI.

II. Processing of the Solubility Data

Wen and Hung[3] report their measurements of the solubilities of methane, ethane, propane, and butane in aqueous solutions, in terms of the volume of the gas at standard conditions (1 atm and 0 °C) dissolved in 1000 g of water. In order to use these data for our purpose we have to transform them into the Ostwald absorption coefficients, which we denote by γ. The conversion relation is

$$\gamma = \frac{\text{volume of gas dissolved at } T}{\text{volume of liquid at } T} = s^{WH}\frac{T\rho_{sol}}{273.15(1000 + Mm_a)} \qquad (2.1)$$

where s^{WH} is the solubility coefficient as reported by Wen and Hung, ρ_{sol} is the solvent density (in g/cm^3), M is the molecular

weight of the solute a, and m_a its molality [in computing the total weight of the solvent in (2.1) we have taken into account only the weight of the water and of the salt a. The contribution of the gas dissolved to the total weight of the solution may be neglected].

Since the densities of the appropriate solutions are not available we have used the following procedure to estimate the volume of the solvent V_1 containing 1000 g of water and m_a moles of solute

$$V_1 = m_a \bar{V}_a + \frac{1000}{18.016} \bar{V}_w \approx m_a \bar{V}_a^0 + 1000 \rho_w^{-1} \quad (2.2)$$

where $\bar{V}_a$ and $\bar{V}_w$ are the partial molar volumes of the salt a and the water w, respectively. $\bar{V}_a^0$ is the limit of $\bar{V}_a$ for infinitely dilute solution and ρ_w is the density (in g/cm^3) of pure water at that temperature.

The approximation used in (2.2) has been based on the following consideration. The partial molar volumes of the relevant salts has been reported by Wen and Saito.[4,5] In principle from the concentration dependence of $\bar{V}_a$ one can compute $\bar{V}_w$ through the Gibbs–Duhem relation

$$N_a \frac{\partial \bar{V}_a}{\partial N_a} + N_w \frac{\partial \bar{V}_w}{\partial N_a} = 0 \quad (2.3)$$

which, after integration, yields

$$\bar{V}_w = \bar{V}_w^0 - \int_0^{N_a} \frac{N_a'}{N_w} \left(\frac{\partial \bar{V}_a}{\partial N_a'} \right) dN_a' \quad (2.4)$$

where $\bar{V}_w^0$ is the molar volume of pure water. From the concentration dependence of $\bar{V}_a$ as reported by Wen and Saito we have numerically computed the integral in (2.4) and found that for all the concentrations considered in this article the correction to $\bar{V}_w^0$ in (2.4) produces a negligible change in our results for γ or for $\Delta\mu_s^0$ (see below).

Therefore we feel that the "ideality assumption" introduced into (2.2) is sufficient for all the purpose of this work.

As a measure of the strength of the HI we use the following approximate relation:[6,7]

$$\delta G_2^{HI} = \Delta\mu_{ET}^0 - 2\Delta\mu_{Me}^0 \quad (2.5)$$

where δG_2^{HI} is the indirect part of the work required to bring two methane molecules from infinite separation to a distance R = 1.533 Å within the liquid at constant temperature and pressure. $\Delta\mu_{ET}^0$ and $\Delta\mu_{ME}^0$ are the standard free energies of solution of ethane and methane, respectively. These are related to the Ostwald absorption coefficient γ_i for any solute i through

$$\Delta\mu_i^0 = -RT \ln \gamma_i \quad (2.6)$$

We shall not dwell on the nature of the approximation involved in (2.5) since this topic has been discussed in great detail elsewhere.[6,7] We note also that a simple generalization of (2.5) is possible which relates the HI between three methane molecules to the standard free energies of propane and methane, namely

$$\delta G_3^{HI} = \Delta\mu_{Pr}^0 - 3\Delta\mu_{Me}^0 \quad (2.7)$$

Thus the solubility data from Wen and Hung are first converted into γ_i and then to $\Delta\mu_i^0$ by (2.1) and (2.6). These results are used in (2.5) and (2.7) to estimate the HI in various aqueous solutions. The dependence of $\Delta\mu_i^0$ on the salt concentration was obtained by fitting a second degree polynomial to the computed values of $\Delta\mu_i^0$ at various salt concentrations. Once we got values of $\Delta\mu_i^0$ and δG^{HI} for a given salt concentration we could fit another second degree polynomial to obtain the temperature dependence of these quantities, from which an estimate of the entropy and enthalpy of the HI is derived.

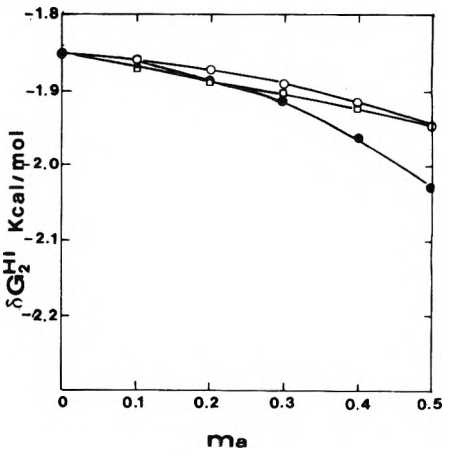

Figure 1. Values of δG_2^{HI} as a function of the molality, m_a, of the salts at 0 °C: ●, $(C_4H_9)_4NBr$; O, $(C_3H_7)_4NBr$; □, $(EtOH)_4NBr$.

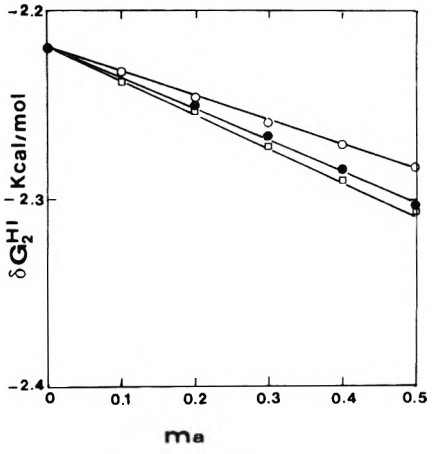

Figure 2. Values of δG_2^{HI} as a function of the molality, m_a, of the salts at 30 °C: ●, $(C_4H_9)_4NBr$; O, $(C_3H_7)_4NBr$; □, $(EtOH)_4NBr$.

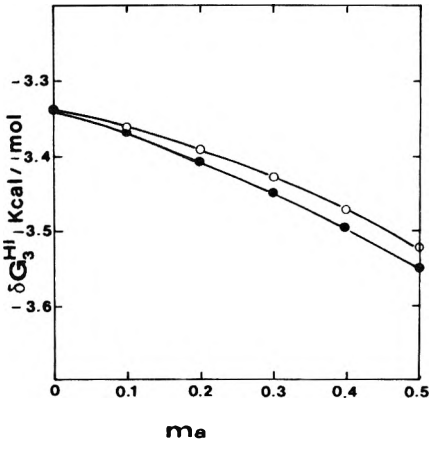

Figure 3. Values of δG_3^{HI} as a function of the molality, m_a, of the salts at 0 °C: ●, $(C_4H_9)_4NBr$; O, $(C_3H_7)_4NBr$.

III. Results and Discussion

All the computed results of δG_2^{HI} and δG_3^{HI} are presented in Figures 1–4. The values of δG_2^{HI} and δG_3^{HI} are reported at two temperatures: 0 and 30 °C.

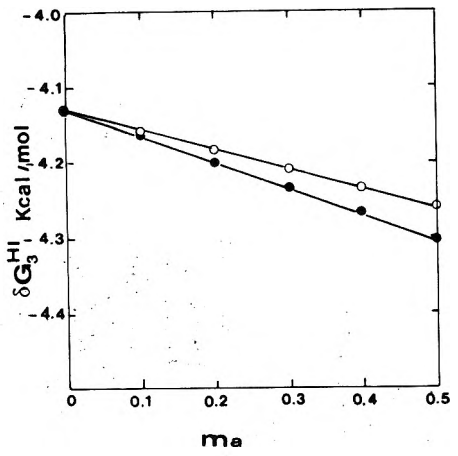

Figure 4. Values of δG_3^{HI} as a function of the molality, m_a, of the salts at 30 °C: ●, $(C_4H_9)_4NBr$; O, $(C_3H_7)_4NBr$.

TABLE I: A Qualitative Correlation between Change of the "Structure of Water" and the Change of the Strength of the Hydrophobic Interaction

Effector	Change of the structure of water	Change of the hydrophobic interaction	Ref
Raising the temperature (0–70 °C)	Decrease	Increase	6,7,9
Changing from H_2O to D_2O	Increase	Decrease	10
Addition of simple electrolytes	Decrease	Increase	2
Addition of small quantity of ethanol ($x \lesssim 0.05$)	Increase	Decrease	8
Addition of large quantity of ethanol ($0.05 \lesssim x \lesssim 0.25$)	Decrease	Increase	8

Perhaps the most striking finding of this work is the fact that the strength of the HI, at least in the sense of δG^{HI}, *increases* with the addition of the TAN^+ salts. This is quite surprising since if one assumes that TAN^+ have a stabilization effect on the structure of water, one would have expected that the effect of these salts on the HI would be different from the effect of simple salts.[2] This comment deserves further elaboration.

In a recent article[8] we have noted that there seems to exist a qualitative correlation between changes of the "structure of water" and changes in the "strength of the HI". We stress that the observed correlation not only is tentative and speculative, but also is based on an ill-defined concept of the "structure of water" on the one hand, and on one particular measure of the concept of the HI on the other.

TABLE II: Values of δS_2^{HI} and δH_2^{HI} for Two Methane Molecules in Various Solutions of Tetrabutylammonium Bromide at 10 °C

Solvent	δS_2^{HI}, eu	δH_2^{HI}, kcal/mol
Pure water	12	1.6
0.1 *m*	13.4	1.79
0.2 *m*	13.3	1.75
0.3 *m*	12.5	1.48
0.4 *m*	10.8	0.98
0.5 *m*	8.3	0.5

In spite of its qualitative nature we believe that this correlation, as summarized in Table I, deserves further considerations and deeper study on molecular grounds. The findings of this article may serve to indicate that either the correlation stated above is not valid in general, or that the TAN^+ salts, examined here, do not have a net stabilizing effect on the structure of water.

We end with a comment on the entropy of the HI which is formally defined by[7]

$$\delta S^{HI} = -\partial(\delta G^{HI})/\partial T \qquad (3.1)$$

and was estimated by fitting a second degree polynomial to the temperature dependence of the values of δG^{HI}.

It is well known that δS^{HI} is of the order of 12 eu in water (at 20 °C and 1 atm), a value which is distinctly larger than the corresponding values in nonaqueous solvents. In Table II we present some values of δS_2^{HI} and δH_2^{HI} for a series of aqueous solutions of tetrabutylammonium bromide at 10 °C. Both values of the entropies and the enthalpies of the HI seem to increase initially and then decrease as a function of the molality of the salt.

A similar observation has been reported for other aqueous solutions,[2] but at present we cannot offer any explanation for this behavior.

References and Notes

(1) Wen-Yang Wen in "Water and Aqueous Solutions, Structure, Thermodynamics and Transport Processes", R. A. Horne, Ed., Wiley-Interscience, New York, N.Y., 1972.
(2) A. Ben-Naim and M. Yaacobi, *J. Phys. Chem.*, **78**, 170 (1974).
(3) Wen-Yang Wen and J. H. Hung, *J. Phys. Chem.*, **74**, 170 (1970).
(4) Wen-Yang Wen and S. Saito, *J. Phys. Chem.*, **68**, 2639 (1964).
(5) Wen-Yang Wen and S. Saito, *J. Phys. Chem.*, **69**, 3569 (1965).
(6) A. Ben-Naim, *J. Chem. Phys.*, **54**, 1387 (1971).
(7) A. Ben-Naim, "Water and Aqueous Solutions, Introduction to a Molecular Theory", Plenum Press, New York, N.Y., 1974.
(8) M. Yaacobi and A. Ben-Naim, *J. Solution Chem.*, **2**, 425 (1973).
(9) H. A. Scheraga, G. Nemethy, and I. Z. Steinberg, *J. Biol. Chem.*, **237**, 2506 (1962).
(10) A. Ben-Naim, J. Wilf, and M. Yaacobi, *J. Phys. Chem.*, **77**, 95 (1973).

Journal of Chemical and Engineering Data

APRIL 1976, Vol. 21, No. 2

TABLE OF CONTENTS

CONTENTS

■Supplementary material for this paper is available separately by direct order (please consult the masthead page). It will also appear following the paper in the microfilm edition of this journal.

* In papers with more than one author, the asterisk indicates the name of the author to whom inquiries about the paper should be addressed.

PUBLISHED: November 1975

ANNUAL REVIEW OF PHYSICAL CHEMISTRY

VOLUME 26

This series is of great value to teachers, graduate students, and research workers in the field of physical chemistry. The articles in this latest volume maintain the high standard of scholarship, interest, and readability already set by Volumes 1 through 25. Each review is written by a well-known expert and all include extensive references to the literature, further enhancing the high quality of these volumes.

Editor: Henry Eyring *Associate Editors:* C. J. Christensen, H. S. Johnston

CONTENTS:

Clothbound **Author, Subject, and Cumulative Indexes** 428 pages

---

***PRICE POSTPAID: $15.00 (USA); $15.50 (elsewhere) U.S. dollars**
(California residents subject to sales tax.)

Other ANNUAL REVIEWS of interest:

- **FLUID MECHANICS**
  Vol. 8 / Jan. 1976 / 418 pp
  *$15.00 USA; $15.50 elsewhere
- **MATERIALS SCIENCE**
  Vol. 5 / Aug. 1975 / 418 pp
  *$15.00 USA; $15.50 elsewhere
- **NUCLEAR SCIENCE**
  Vol. 25 / Dec. 1975 / 614 pp
  *$18.50 USA; $19.00 elsewhere

---

*Effective July 1, 1976, the price for all ANNUAL REVIEWS will be increased $2.00 per copy, inclusive of back volumes. Shipments made after July 1, 1976 will be billed at the new rate.

Publisher:
ANNUAL REVIEWS INC.
(a nonprofit corporation)
4139 El Camino Way
Palo Alto, California 94306, USA

For complete information on prices, student rates, reprints, available back volumes, and a listing of the topics and authors for all our publications, please send for a free copy of our 1976 PROSPECTUS.